

# **STUDY AND DEVELOPMENT OF HIGH POWER PULSED Nd:YAG LASERS AND THEIR MATERIAL PROCESSING APPLICATIONS**

*By*

**AMBAR KUMAR CHOUBEY**

(Enrolment No. PHYS 03200704014)

**Solid State Laser Division  
Raja Ramanna Center for Advanced Technology  
Indore 452013, India**

*A thesis submitted to the  
Board of Studies in Physical Sciences  
In partial fulfilment of requirements  
for the Degree of*

**DOCTOR OF PHILOSOPHY  
of  
HOMI BHABHA NATIONAL INSTITUTE**



**September, 2014**

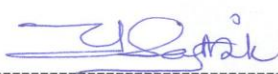
# Homi Bhabha National Institute

## Recommendations of the Viva Voce Board

As members of the Viva Voce Board, we certify that we have read the dissertation prepared by Ambar Kumar Choubey entitled "Study and development of high power pulsed Nd:YAG lasers and their material processing applications" and recommend that it may be accepted as fulfilling the dissertation requirement for the Degree of Doctor of Philosophy.

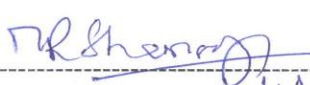
  
----- Date: 10/4/2015  
(Dr. P.D. Gupta, Chairman)

  
----- Date: 10/04/2015  
(Dr. S.M. Oak, Guide)

  
----- Date: 10/4/2015  
(Dr. P.A. Naik, Member)

  
----- Date: 10/4/2015  
(Dr. D.J. Biswas, Member)

  
----- Date: 10/4/2015  
(Dr. B.N. Upadhyaya, Technical Advisor)

  
----- Date: 10/4/2015  
(Prof. M.R. Shenoy)

Final approval and acceptance of this dissertation is contingent upon the candidate's submission of the final copies of the dissertation to HBNI. I hereby certify that I have read this dissertation prepared under my direction and recommend that it may be accepted as fulfilling the dissertation requirement.

Date: 10 April 2015  
Place: Indore

  
Signature 10/4/2015  
Guide

## **STATEMENT BY AUTHOR**

This dissertation has been submitted in partial fulfilment of requirements for an advanced degree at Homi Bhabha National Institute (HBNI) and is deposited in the Library to be made available to borrowers under rules of the HBNI.

Brief quotations from this dissertation are allowable without special permission, provided that accurate acknowledgement of source is made. Requests for permission for extended quotation from or reproduction of this manuscript in whole or in part may be granted by the Competent Authority of HBNI when in his or her judgment the proposed use of the material is in the interests of scholarship. In all other instances, however, permission must be obtained from the author.



(Ambar Kumar Choubey)

## **DECLARATION**

I, hereby declare that the investigation presented in the thesis has been carried out by me. The work is original and has not been submitted earlier as a whole or in part for a degree /diploma at this or any other Institution / University.

A handwritten signature in blue ink, appearing to be 'Ambar', with a horizontal line extending to the right.

(Ambar Kumar Choubey)

## List of Publications arising from the thesis

### Journals

- 1) “Studies on pulsed Nd:YAG laser cutting of thick stainless steel in dry air and underwater environment for dismantling applications”, Ambar Choubey, R.K. Jain, Sabir Ali, Ravindra Singh, S.C. Vishwakarma, D.K. Agrawal, R. Arya, R. Kaul, B.N. Upadhyaya, S.M. Oak, *Optics & Laser Technology*, **2015**, *71*, 6-15.
- 2) “Generation of 415 W of *p*-polarized output power in long pulse operation of Nd:YAG laser using z-fold resonator geometry”, Ambar Choubey, Shyamal Mondal, Ravindra Singh, B.N. Upadhyaya, P.K. Datta, S.M. Oak, *Optics & Laser Technology*, **2014**, *60*, 41-48.
- 3) “Enhancement of *p*-polarized average power in long pulse operation of single rod Nd:YAG laser using a tilted 90° quartz rotator”, Ambar Choubey, Shyamal Mondal, Ravindra Singh, B.N. Upadhyaya, P.K. Datta, S.M. Oak, *Optics Communications*, **2014**, *330*, 61-70.
- 4) “Study and development of 22 kW peak power fiber-coupled short pulse Nd:YAG laser for cleaning applications”, Ambar Choubey, S.C. Vishwakarma, D.M. Vachhani, Ravindra Singh, Pushkar Misra, R.K. Jain, R. Arya, B.N. Upadhyaya, S.M. Oak, *Optics and Lasers in Engineering*, **2014**, *62*, 69-79.
- 5) “Study on GRADIUM lens based fiber imaging for reduction of debris during Nd:YAG laser cutting and dismantling”, Ambar Choubey, R.K. Jain, Ravindra Singh, D.K. Agrawal, S.C. Vishwakarma, B.N. Upadhyaya, S.M. Oak, *Materials Focus*, **2014**, *3*, 149-155.

- 6) “Efficient delivery of 60 J pulse energy of long pulse Nd:YAG laser through 200  $\mu\text{m}$  core diameter optical fiber”, Ravindra Singh, Ambar Choubey, R.K. Jain, S.C. Vishwakarma, D.K. Agrawal, Sabir Ali, B.N. Upadhyaya, S.M. Oak, *Pramana: Journal of Physics*, **2014**, 82, 211-216.
- 7) “Performance study of highly efficient 520 W average power long pulse ceramic Nd:YAG rod laser”, Ambar Choubey, S.C. Vishwakarma, Sabir Ali, R.K. Jain, B.N. Upadhyaya, S.M. Oak, *Optics & Laser Technology*, **2013**, 51, 98-105.
- 8) “A highly efficient and compact long pulse Nd:YAG rod laser with 540 J of pulse energy for welding application”, Ambar Choubey, S.C. Vishwakarma, Pushkar Misra, R.K. Jain, D.K. Agrawal, R. Arya, B.N. Upadhyaya, S.M. Oak, *Review of Scientific Instruments*, **2013**, 84, 0731081-0731088.
- 9) “Performance Improvement of long pulse Nd:YAG laser using advanced diffuse ceramic reflectors”, Ambar Choubey, R.K. Jain, S.C. Vishwakarma, B.N. Upadhyaya, S.M. Oak, *Materials Focus*, **2013**, 2, 362-368.
- 10) “Nd:YAG laser assisted drilling and spallation of rocks”, Ambar Choubey, R.K. Jain, S.C. Vishwakarma, B.N. Upadhyaya, S.M. Oak, *Advanced Science, Engineering and Medicine*, **2013**, 5, 905-911.
- 11) “Study on effective cleaning of gold layer from fused silica mirrors using nanosecond pulsed Nd:YAG laser”, Ambar Choubey, Amol Singh, M.H. Modi, B.N. Upadhyaya, G.S. Lodha, S.M. Oak, *Applied Optics*, **2013**, 52(31),7540-7548.
- 12) “Efficient depolarization-loss-compensation of solid state lasers using only a Glan-Taylor polarizer”, S. Mondal, S.P. Singh, K. Hussain, Ambar Choubey, B.N. Upadhyaya, P.K. Datta, *Optics & Laser Technology*, **2013**, 45, 154-159.

- 13) “Development of underwater laser cutting technique for steel and zircaloy for nuclear applications”, R.K. Jain, D.K. Agrawal, S.C. Vishwakarma, Ambar Choubey, B.N. Upadhyaya, S.M. Oak, *Pramana: Journal of Physics*, **2010**, 75, 1253-1258.
- 14) “A highly efficient 5 kW peak power Nd:YAG laser with time-shared fiber optic beam delivery”, B.N. Upadhyaya, S.C. Vishwakarma, Ambar Choubey, R.K. Jain, Sabir Ali, D. K. Agrawal, A.K. Nath, *Optics & Laser Technology*, **2008**, 40, 337-342.

### **Other Journal papers during the Ph.D. work**

- 1) “Cleaning of carbon layer from the gold films using a pulsed Nd:YAG laser”, Amol Singh, Ambar Choubey, Mohammed H. Modi, B.N. Upadhyaya, S.M. Oak, G.S. Lodha, S.K. Deb, *Applied Surface Science*, **2013**, 283, 612-616.
- 2) “Study on effective laser cleaning method to remove carbon layer from a gold surface”, Amol Singh, Ambar Choubey, M.H. Modi, B.N. Upadhyaya, G.S. Lodha, *Journal of Physics: Conference Series*, **2013**, 425, 152020(1)-15202(4).



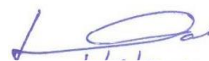
(Ambar Kumar Choubey)

## **Certificate of the guide**

This is to certify that the work entitled “Study and Development of high power pulsed Nd:YAG lasers and their material processing applications” is a piece of research work done by *Shri Ambar Kumar Choubey* under my supervision, for the degree of *Doctor of Philosophy (Physical Science)* of Homi Bhabha National Institute, at RRCAT, Indore, a Constituent Institution of HBNI, Mumbai.

To the best of my knowledge and belief, the thesis:

1. embodies the work of candidate himself,
2. the work has been duly completed to my satisfaction,
3. fulfils the requirements of the Ph.D. degree of HBNI, and
4. is up to the international standard, both, in respect of contents and language, for being referred to the examiner.



(Signature of the Guide)

Dr. S.M. Oak

## ACKNOWLEDGEMENTS

I am extremely thankful to **Dr. P.D. Gupta**, Distinguished Scientist, Senior Professor and Director, Raja Ramanna Centre for Advanced Technology (RRCAT) as a Chairman of Board of Studies, HBNI at RRCAT for permitting me to pursue my Ph. D. and their keen interest in my research work. His valuable instructions inspired me and guidance to generate the novel ideas that are presented in this piece of scientific work. My deepest regards and gratitude is due to **Dr. S.M. Oak**, Outstanding Scientist, Senior Professor and Head SSLD, RRCAT for his valuable guidance, constant support and encouragement. Their way of teaching always encouraged me to think over new ideas and made this entire journey a memorable learning experience throughout the study of this work. I am particularly thankful to **Dr. Brahma Nand Upadhyay** who with his ever-helping nature, keen interest, deep involvement and utmost cares throughout my research work, motivated me to work hard and keep patience under difficult circumstances. I would like to express my gratitude to **Dr. P.A. Naik** and **Dr. D.J. Biswas** (BARC), members of my doctoral committee and also to Dr. K.S. Bindra, Dr. S.C. Mehandale, Dr. S.B. Roy, Dr .G.S. Lodha, Dr. M.H. Modi, Shri R. Kaul, Shri R. Arya and Shri R.K. Khare for thier valuable suggestions. I acknowledge Shri S.C. Vishwakarma, Shri R.K. Jain, Shri D.Agrawal, Shri Rajpal, Shri B. Saini, Shri Ekka, Shri Vishal, Shri Sabir Ali, Shri P. Misra, Shri Ashutosh Sharma, Shri R. Sundar, Shri Vacchani, Shri Amol Singh and Shri Ravindra Singh for their dedicated support. I also acknowledge my association and work with Shri S. Mondal and Dr. P.K. Datta (IIT, Kharagpur). Finally, I would like to express my special gratitude to my teacher Dr. G.K. Upadhyay (Vikram University), my brother Anshuman, and father Late Shri B.K. Choubey who have been my source of encouragement. Finally, this thesis would not have been possible without the unconditional support and encouragement of my wife Rupali and daughter Yukta Choubey.

# CONTENTS

<b>SYNOPSIS</b>	<b>xiv</b>
<b>LIST OF FIGURES</b>	<b>xx</b>
<b>LIST OF TABLES</b>	<b>xxxi</b>
 <b>THESIS CHAPTERS</b>	
 <b>CHAPTER 1. Nd:YAG laser : An overview</b>	 <b>1</b>
1.1 Introduction	1
1.2 Scope of work	7
1.3 Construction of pulsed Nd:YAG laser	9
1.4 Optical fiber coupling	13
 <b>CHAPTER 2. Study and development of high power long pulse Nd:YAG lasers</b>	 <b>17</b>
2.1 Introduction	17
2.2 Analysis of laser pump chamber and resonator	20
2.2.1 Laser pump chamber design	21
2.2.2 Laser resonator design	26
2.3 Experimental set-up of long pulse Nd:YAG laser	29
2.4 Study on optical fiber coupling and time-shared beam delivery	32
2.5 Results and discussion	37
2.5.1 250 W average power laser	37

2.5.2 500 W average power laser	41
2.5.3 1 kW average power laser	46
2.6 Conclusions	50
<b>CHAPTER 3. Performance study of ceramic Nd:YAG rod for generation of long pulse and high average power laser output</b>	<b>52</b>
3.1 Introduction	52
3.2 Laser pump chamber and resonator design	58
3.3 Experimental details	63
3.4 Results and discussion	65
3.5 Conclusions	72
<b>CHAPTER 4. Study and development of short pulse Nd:YAG laser</b>	<b>74</b>
4.1 Introduction	74
4.2 Design of short pulse Nd:YAG laser system	77
4.2.1 Laser pump chamber and resonator design	77
4.2.2 Laser power supply	80
4.3 Experimental set-up	83
4.4 Results and discussion	86
4.5 Conclusions	91
<b>CHAPTER 5. Study on novel birefringence compensation schemes for single and dual rod long pulse Nd:YAG laser resonator</b>	<b>93</b>
5.1 Introduction	93
5.2 Theoretical background	96



6.5.2 Results and analysis	171
6.6 Conclusions	174
<b>CHAPTER 7. Study on laser cleaning with short pulse Nd:YAG laser</b>	<b>176</b>
7.1 Introduction	176
7.2 Laser cleaning of marble, stones, zirconium, and inconel	182
7.2.1 Experimental work	183
7.2.2 Results and analysis	184
7.3 Study on cleaning of carbon layer from gold surface	191
7.3.1 Experimental work	192
7.3.2 Results and analysis	193
7.4 Study on laser cleaning of gold layer from fused silica surface	196
7.4.1 Experimental work	197
7.4.2 Results and analysis	198
7.5 Conclusions	206
<b>CHAPTER 8. Summary and scope for future work</b>	<b>208</b>
8.1 Summary of the important results	209
8.2. Scope for future work	213
<b>REFERENCES</b>	<b>215</b>
<b>APPENDIX-1</b>	<b>237</b>
<b>APPENDIX-2</b>	<b>240</b>

## **SYNOPSIS**

The emergence of high power continuous wave (CW) and pulsed Nd:YAG lasers have opened many new applications and opportunities in the area of laser material processing. Some of the potential benefits of Nd:YAG lasers are high brightness beam delivery through optical fiber, and strong absorption in most of the metals and alloys. During laser material processing, pulsed Nd:YAG lasers with high energy and high peak power provide certain advantages over CW lasers such as lower distortion and lower heat affected zone. However, high peak power Nd:YAG lasers with long and short pulse durations still depend on flash lamp pumping technique instead of diode laser pumping, since the high peak power operation of laser diodes is restricted due to the thermal run away problem. Further, flash lamps are much more rugged and cost effective than the diode lasers in industrial environment. Hence, in the present scenario, study and development of flash lamp pumped pulsed Nd:YAG lasers are still important for laser material processing applications.

In this thesis, we have carried out an extensive study on the development of highly efficient, fiber coupled pulsed Nd:YAG laser systems with good beam quality and high peak power for laser material processing applications. Present study on pulsed Nd:YAG laser has been divided into three parts. The first part is devoted to the study and development of optical fiber coupled lamp pumped long and short pulse Nd:YAG lasers of high peaks and high average power. The second part is devoted to the investigation of the issues related to the birefringence compensation in lamp pumped Nd:YAG lasers and generation of linearly polarized light. Third part is on the study and evaluation of performance of these Nd:YAG lasers for laser material processing applications.

For the generation of high peak power and pulse energy, study on use of ceramic Nd:YAG laser rod in place of single crystal Nd:YAG rod has been performed with pulse duration in the range of 2-20 ms. A compact and robust laser pump chamber along with resonator has been designed to achieve this high average and peak power. We have further carried out a detailed study on the development of short pulse Nd:YAG laser system for cleaning applications. It is well known that thermal problems in the Nd:YAG laser material limits the efficiency of the laser system and degrades the beam quality. Thus, for efficient heat removal from the Nd:YAG rod laser systems, a study on the optimization of water flow rate in laser pump chamber has also been performed. Moreover, thermal problems in the Nd:YAG laser rod also generate stress induced birefringence. This stress-induced birefringence limits the generation of linearly polarized output power. For laser material processing, polarization state of the laser beam has a strong influence on its absorption in the material. In a single rod resonator, we have proposed a novel optical scheme using a  $90^\circ$  quartz rotator (QR) placed at Brewster's angle in the laser resonator between the output mirror and the laser rod to enhance the  $p$ -polarized power.

Similarly, in dual rod Nd:YAG laser, experimental investigations of z-fold resonator geometry was performed for birefringence compensation and generation of high average power linearly  $p$ -polarized laser beam. Study and analysis of z-fold resonator geometry to improve the performance of long pulse  $p$ -polarized laser operation in terms of average power, peak power, depolarization losses, beam quality, pulse-to-pulse stability, and misalignment sensitivity has also been performed.

Further, study of these long and short pulse Nd:YAG lasers have been performed for the following material processing applications, i.e., (a) laser cutting of SS in dry air and under water

environment having potential applications in dismantling and maintenance work of nuclear facilities and shipping industry, (b) laser welding of aluminium, titanium, stainless steel and other materials for automotive, heavy machinery, and vacuum industry, (c) laser drilling of rocks and concrete for use in petroleum and natural gas wells, and (d) laser cleaning of carbon contamination and removal of gold layer in beamline mirrors of synchrotron radiation sources, laser cleaning of marble for the conservation of art work, and cleaning of inconel and zirconium for nuclear applications.

### **Summary of the research work and the organization of proposed thesis:**

In the context of the above background on the development of long and short pulse Nd:YAG lasers along with material processing applications, the proposed thesis entitled “Study and development of high power pulsed Nd:YAG lasers and its material processing applications”, focuses on the following research problems:

- Study and development of high peak power long (millisecond duration) and short pulse (microsecond duration) lamp-pumped Nd:YAG lasers with efficient heat removal and optimization of resonator configurations for better beam quality.
- Performance study of long pulse fiber coupled ceramic Nd:YAG rod laser.
- Study of birefringence compensation in single and dual rod long pulse Nd:YAG rod laser using simple optical scheme for enhancement of *p*-polarized output power.
- Study and comparison of pulsed laser cutting of thick stainless steel in dry air and underwater environment using long pulse Nd:YAG lasers.
- Study on laser drilling of rocks using pulsed Nd:YAG laser.

- Study on effective cleaning of gold and carbon layer deposited on beam line mirrors using nanosecond pulsed Nd:YAG laser and its analysis using SEM and XPS methods.

The proposed thesis contains eight chapters and it has been organized as below:

**Chapter 1:** This chapter contains an introduction to the study and development of high peak power and high average power pulsed Nd:YAG lasers with short and long-pulse duration along with its potential material processing applications.

**Chapter 2:** This chapter provides results related to the study and development of high power long pulse (ms) Nd:YAG lasers to achieve high efficiency, good beam quality, and high average power with emphasis on the design of resonator and laser pump chamber. Further, it provides details about the study on fiber-coupled 250 W, 500 W, and 1 kW average power long-pulse Nd:YAG lasers for material processing applications [48-50]. The slope-efficiencies and pulse-energies of these indigenously developed laser systems are higher as compared to other world-wide reported long-pulse lamp-pumped Nd:YAG lasers. The study, analysis and design of laser systems were performed to improve the laser beam quality so that it can be coupled to 400  $\mu\text{m}$  and 600  $\mu\text{m}$  core diameter optical fibers with power transmission efficiency of  $\geq 90\%$ .

**Chapter 3:** It deals with performance study of ceramic Nd:YAG rod in place of single crystal Nd:YAG rod for the generation of 520 W average power in pulsed Nd:YAG laser system [69]. Single crystal Nd:YAG rod is the most widely used laser media. But, Nd:YAG single crystals grown by the conventional Czochralski method have certain disadvantages such as, relatively high cost and limitations on the maximum size and doping concentration of  $\text{Nd}^{3+}$  ions. The experiments using ceramic Nd:YAG laser are carried out to demonstrate the potential ability of this material to replace single crystals for the generation of high peak power and large pulse energy in long pulse operation. Novel ceramic media combines the advantages of single crystals

and glasses. The ceramic rods have good thermal, mechanical and spectral properties (like crystalline materials) and can be made in large sizes with high doping concentrations (like laser glasses). Further, this material is less expensive as compared to single crystals.

**Chapter 4:** In this chapter, we have focused our attention on the study and development of fiber coupled short pulse Nd:YAG laser system for laser cleaning application. It contains a detailed investigation of the laser pump chamber and resonator design to obtain good beam quality to couple the laser beam through 200  $\mu\text{m}$  core diameter optical fiber for cleaning of objects with high accuracy [184].

**Chapter 5:** It describes detailed study of birefringence compensation in single and dual rod, long pulse Nd:YAG lasers using simple optical schemes. Some novel optical schemes have been developed to enhance the linearly  $p$ -polarized output power in single rod Nd:YAG laser for the long pulse laser operation. A brief analysis of these novel schemes using quartz rotator has been provided and verified experimentally [114]. For a dual Nd:YAG rod laser resonator, the design of a  $z$ -fold resonator configuration for effective birefringence compensation in place of linear resonator configuration has also been provided. With this configuration, linearly  $p$ -polarized average output power of 415 W has been generated [120]. This is highly useful for second harmonic generation and material processing applications.

**Chapter 6:** In this chapter, some important material processing applications of long pulse Nd:YAG lasers such as cutting, welding and drilling have been discussed. The laser cutting of thick stainless steel sheets (thickness 4 mm to 20 mm) in dry air and underwater environment for dismantling of structures in nuclear facilities has been investigated [155]. The important process parameters have been optimized such as laser spot overlapping, pulse repetition rate, and pulse duration. Laser welding of titanium and aluminium using long pulse Nd:YAG laser has also been

performed [50]. The application of long pulse Nd:YAG laser for rock drilling has also been investigated [157].

**Chapter 7:** It has been devoted to the study and analysis of laser cleaning using short pulse Nd:YAG laser. In order to understand the effect of laser pulse duration and spot overlapping on laser cleaning process, a detailed study of various factors responsible for thermal ablation is described. Demonstration of effective and efficient laser cleaning of gold and a carbon layer of fused silica mirrors using pulsed Nd:YAG laser has been described [205]. Further, an analysis of laser cleaned surface has been carried out using SEM, XPS, and reflectivity methods. Laser cleaning of inconel tubes, zircaloy tubes, and marble samples using short pulse Nd:YAG laser is also described [184].

**Chapter 8:** In this chapter, we have summarized all the results of this thesis and have concluded with discussion on further scope for future research work.

## List of Figures

Figure 1.1: Energy level diagram of Nd:YAG crystal	2
Figure 1.2: Absorption spectrum of Nd:YAG crystal	3
Figure 1.3: Power losses during lamp pumping of Nd:YAG crystal	4
Figure 1.4: Absorption characteristics of different metals as a function of wavelength	6
Figure 1.5: Schematic of laser pump chamber (front view)	10
Figure 1.6: Emission spectrum of Krypton flash lamp	11
Figure 1.7: A schematic view of optical fiber	13
Figure 1.8: Beam addition of three fiber coupled laser beams on work piece	14
Figure 2.1: A schematic diagram of the laser pump chamber used in experiment	21
Figure 2.2: A schematic of laser pump chamber (front view) and reflector geometry	21
Figure 2.3: Schematic of the shapes of ceramic and gold-coated reflectors	25
Figure 2.4: A schematic of the laser resonator of 1 kW average power long pulse laser using two Nd:YAG rods	27
Figure 2.5: A schematic of the equivalent resonator using two Nd:YAG rods	27
Figure 2.6: Schematic of the fiber input end with coupling lens	32
Figure 2.7: Schematic of focusing by (a) standard fused silica (b) GRADIUM lens	33
Figure 2.8: A view of the input end optical fiber holder and lens mount	34
Figure 2.9: A view of two port motorized time shared fiber port selection mechanism	35
Figure 2.10: Schematic of Nd:YAG laser with time shared fiber optic beam delivery	36
Figure 2.11: A view of 250 W average power laser system with two time shared fiber optic port for beam delivery	37
Figure 2.12: Average output power as a function of average input pump power for single rod 250 W laser	39
Figure 2.13: Variation of BPP as a function of average input pump power	40

Figure 2.14: A view of 500 W average power laser system and experimental set-up (left) and ceramic reflector (right).	41
Figure 2.15: Variation of $M^2$ as a function of input pump power for gold and ceramic reflector based 500 W average power Nd:YAG laser	42
Figure 2.16: 3D view of laser beam profile (a) ceramic reflector based Nd:YAG laser shows smoother profile (b) gold-coated elliptical reflector based Nd:YAG laser shows some peaks	43
Figure 2.17: Variation of average output power with average input pump power for ceramic and gold coated reflector based Nd:YAG lasers	44
Figure 2.18: Two different cooling schemes of ceramic reflector based Nd:YAG laser	45
Figure 2.19: Output power variation with input power for ceramic reflector in scheme A & B	45
Figure 2.20: A table-top view of 1 kW average power pulsed Nd:YAG laser system	46
Figure 2.21: Variation of measured and calculated thermal focal length ( $f$ ) with variation in average input pump power for the Nd:YAG rod	47
Figure 2.22: Variation of $g_1g_2$ -parameter of the resonator with variation in average electrical input pump power showing stability of resonator	47
Figure 2.23: Variation of average output power with average input pump power for different values of heat transfer coefficients ( $h$ ) for dual rod Nd:YAG laser resonator	48
Figure 2.24: (a) Temporal evolution of the laser beam, and (b) Spatial profile of the laser beam	48
Figure 2.25: Variation of single shot pulse energy with pulse duration at 300 A of flash lamp current	49

Figure 3.1: Energy level diagram of ceramic Nd:YAG with description of (a) conventional (b) direct and (c) hot-band direct pump transitions	54
Figure 3.2: Absorption spectra for 1 at.% single crystal Nd:YAG and 4.8 at.% ceramic Nd:YAG in the range of 780 nm and 840 nm	55
Figure 3.3: A comparison of emission spectra of 1 at.% single crystal Nd:YAG and 6.6 at.% ceramic Nd:YAG in the range of 1050 nm and 1080 nm	55
Figure 3.4: A schematic diagram of the single flash lamp pumped laser pump chamber (side view)	59
Figure 3.5: A schematic diagram of the close coupled gold coated elliptical reflector (front view)	60
Figure 3.6: Symmetric plane-plane resonator with d:2d:d configuration	61
Figure 3.7: A table-top view of dual rod lamp pumped ceramic Nd:YAG resonator	64
Figure 3.8: Variation of calculated values of fundamental mode radius ( $w_0$ ) with input pump power for the ceramic and single crystal Nd:YAG rods	66
Figure 3.9: Output average power variation with input pump power for different values of heat transfer coefficient for dual ceramic rod resonator	67
Figure 3.10: Variation of average output power with average input pump power for dual rod resonator of ceramic and single crystal Nd:YAG rods	68
Figure 3.11: Measured value of beam quality factor ( $M^2$ ) as a function of input pump power variation for dual rod resonator configuration of ceramic and single crystal Nd:YAG rods	69
Figure 3.12: Beam profile of the ceramic Nd:YAG laser (a) 2D and (b) 3D view	70
Figure 3.13: Beam profile of the single crystal Nd:YAG laser (a) 2D and (b) 3D view	70
Figure 3.14: Measured value of single shot pulse energy of dual rod resonator	71

configuration of ceramic and single crystal Nd:YAG rods

Figure 4.1: A schematic view of (a) Gaussian and (b) top hat spatial profile (profile intensities are not at the same scale)	76
Figure 4.2: Schematic of laser pump chamber (front view) and reflector geometry	78
Figure 4.3: A schematic of hemispherical resonator with dual flash lamp pumped Nd:YAG rod	78
Figure 4.4: A Schematic diagram of the pulsed power supply system for flash lamp pumping which shows PFN and simmer-trigger unit	81
Figure 4.5: Flash lamp discharge current ( $I_{DISCH}$ ) with $V_0$ set at (1) 1200V (2) 1000V, (3) 800V and (4) 600V. X – Scale: 20 $\mu$ s/div, Y - Scale: 100A/div	82
Figure 4.6: Table-top view of 1.25 J pulse energy short pulse Nd:YAG laser	83
Figure 4.7: A view of focusing nozzle	85
Figure 4.8: A view of the focusing nozzle mounted on CNC machine	85
Figure 4.9: Variation of beam quality factor ( $M^2$ ) with R.O.C. of the rear mirror	87
Figure 4.10: Variation of beam quality factor ( $M^2$ ) with input pump power for 8 meter R.O.C. of rear concave mirror	88
Figure 4.11: Variation of output single pulse energy with input single pulse pump energy	88
Figure 4.12: A view of temporal shape of current pulse (yellow), flash lamp pump pulse (pink) & laser output pulse (blue)	89
Figure 4.13: Spatial profile of the laser beam 2D (left) and 3D (right) view (a) Before fiber input end (direct laser beam) shows some hot spots (b) After fiber exit end beam profile becomes more smoother	90
Figure 5.1: A schematic view of experimental set-up for the recording of conoscopic pattern	98

Figure 5.2: The experimentally recorded birefringence pattern of single crystal Nd:YAG rod for 1,3 and 5 kW pump power respectively from left to right	99
Figure 5.3: Relationship of angle $\theta$ , $\phi$ and $\gamma$ with polarization direction and rod cross section in x-y plane, beam propagates in z-direction	100
Figure 5.4: The crystal orientation and ray propagation in Glan-Taylor polarizer	101
Figure 5.5: Glan-Taylor polarizer tilted with respect to the x-axis of laboratory frame	101
Figure 5.6: Experimental set-up of resonator for compensation of birefringence	105
Figure 5.7: Output power versus input pump power of single Nd:YAG rod resonator with different optical components GTP, $\lambda/4$ -wave plate and plate polarizer	106
Figure 5.8: Depolarization loss versus heat dissipation in the rod. Theoretical values of losses are shown by solid and dotted line. Experimental values are shown by closed circle and closed square	107
Figure 5.9: A simulated cross section view of non-uniform pumped Nd:YAG rod on placing it in pump chamber with an elliptical gold-coated reflector	110
Figure 5.10: A $90^\circ$ QR was placed between plate polarizer and Nd:YAG rod	110
Figure 5.11: A $90^\circ$ QR was placed at Brewster's angle ( $\theta_B=55.4^\circ$ ), it works both as a polarizer as well as rotating element. A HR re-entering mirror provides feedback for the rejected beam.	111
Figure 5.12: Experimental scheme for the measurements of depolarization loss using Glan-Taylor (GT) polarizer and analyzer	113
Figure 5.13: Experimental set-up using $\lambda/2$ -wave plate for the recording of conoscopic pattern	114
Figure 5.14: Conoscopic pattern of Nd:YAG rod for different angle $\gamma$ using gold coated and ceramic reflector. The pattern were recorded for 3 kW and 5 kW average input pump powers	115
Figure 5.15: Variation of output power with input pump power using different optical components in resonator	116

Figure 5.16: Variation of depolarization loss with input pump power, before compensation (with polarizer) and after compensation (with 90° QR)	118
Figure 5.17: Variation of $M^2$ as a function of pump power with and without 90° QR	118
Figure 5.18: Laser beam profile placing only a polarizer in the laser resonator shows distortion in the beam shape	119
Figure 5.19: Laser beam profile after placing a 90° QR at Brewster's angle shows reduction in distortion of beam shape	119
Figure 5.20: An equivalent schematic diagram of the z-fold resonator having two Nd:YAG rods with thermal focal lengths ( $f$ ) and two concave mirrors for rod imaging	121
Figure 5.21: Ray tracing diagram to show astigmatism of a concave mirror with $f_S$ and $f_M$ as the focal lengths for tangential and sagittal rays and $\theta$ as the incident angle of the input rays with respect to optic axis	124
Figure 5.22: Variation of the ratio $f_S/f_M$ as a function of angle $\theta$	124
Figure 5.23: A table-top view of the experimental set-up of z-fold resonator	125
Figure 5.24: A schematic view of birefringence compensation scheme of z-fold resonator having two concave mirrors, two Nd:YAG rods, a polarizer, a 90° QR, and a re-entering HR mirror	126
Figure 5.25: A schematic view of experimental set-up for measurement of depolarization losses using Glan-Taylor (GT) polarizer and analyzer.	127
Figure 5.26: Variation of $g_1g_2$ for z-fold resonator as a function of average electrical input pump power	128
Figure 5.27: Variation of average output power as a function of average input pump power using different optical components in z-fold resonator	129
Figure 5.28: Variation of $M^2$ as a function of average input pump power before and after birefringence compensation. Standard deviation of the data is presented as error bar in the curve	130

Figure 5.29: Variation of measured value of depolarization loss as a function of average input pump power using polarizer, 90 <sup>0</sup> QR, and re-entering feedback mirror in the resonator	132
Figure 5.30: Comparison of spatial profile of laser beam for dual-rod z-fold resonator at different values of average input pump power	132
Figure 6.1: A schematic view of cut front during laser cutting by melting	137
Figure 6.2: A chart showing important process parameters affecting the quality of laser welding	140
Figure 6.3: Temporal shape of pulse from 500 W average power Nd:YAG laser	144
Figure 6.4: Variation of laser pulse energy with pulse duration	144
Figure 6.5: A schematic view of laser cutting objective used for cutting of thick section of steel.	145
Figure 6.6: A view of local dry cavity in underwater environment	146
Figure 6.7: A schematic diagram of local dry cavity	146
Figure 6.8: Variation of single shot effective spot diameter on melt surface with increase in pulse duration for dry air and underwater environment	149
Figure 6.9: Variation in required spot overlapping with variation in oxygen gas pressure for cutting of 8 mm thick SS304	150
Figure 6.10: Variation in cutting speed per Hz with reduction in spot overlapping in the pulse duration range of 4ms-8ms for 8 mm thick SS sample	151
Figure 6.11: Variation in cutting speed per Hz with reduction in spot overlapping in the pulse duration range of 12ms-14ms for 12 mm thick SS sample	151
Figure 6.12: Variation in cutting speed per Hz with reduction in spot overlapping in the pulse duration range of 13ms-16ms for 15 mm thick SS sample	152
Figure 6.13: Variation in cutting speed per Hz with reduction in spot overlapping in the pulse duration range of 14ms-20ms for 20 mm thick SS sample	152

Figure 6.14: (a) A sequence of drilled holes on the surface of 20 mm thick SS with reduction in spot overlapping factor below 40% showing separated holes, and (b) Continuous cut kerf on the surface at 40% of spot overlapping	153
Figure 6.15: A view of laser cutting of 20 mm thick steel in (a) dry air, and (b) underwater	153
Figure 6.16: (a) Cut surface of 20 mm thick SS304 in dry air, and (b) underwater	154
Figure 6.17: Metallographic cross section of laser cut surface of 12 mm thick steel in (a) dry air, and (b) underwater	154
Figure 6.18: SEM image of HAZ of SS304 in underwater laser cut sample	154
Figure 6.19: Variation of HAZ in dry air and underwater with change in spot overlapping from 80% to 40% and change in pulse duration from 14 ms to 20 ms for a peak power variation from 8.9 kW to 6.25 kW with a constant value of pulse energy of 125 J	155
Figure 6.20: A schematic view of laser cutting nozzle, designed for half-imaging lenses	158
Figure 6.21: (a) A schematic view of (a) 1:1 image of fused silica and (b) half-image of GRADIUM lenses	159
Figure 6.22: A comparison of kerf width for cutting of 4 mm thick stainless steel sample using nozzles of 1:1 and half imaging optics	160
Figure 6.23: A view of debris ejection during pulsed Nd:YAG laser cutting with 1:1 imaging nozzle	161
Figure 6.24: Temporally shaped Nd:YAG laser pulses having (a) rectangular (b) ramp down (c) ramp up and (d) mixed or center-up shape for 70 J pulse energy and 20 ms pulse duration	163
Figure 6.25: Fiber coupled focusing nozzle mounted on CNC	164
Figure 6.26: Experimentally observed weld geometry for (a) rectangular (b) ramp down (c) ramp up and (d) mixed pulse shapes(dimensions shown in figure are in mm)	165
Figure 6.27: (a) Weld bead on Al sample (b) Microstructure of the weld bead on Al sample	166
Figure 6.28: (a) Weld bead on Ti sample (b) Microstructure of the weld bead on Ti sample	166

Figure 6.29: Schematic view of laser drilling experimental set-up	169
Figure 6.30: Schematic and table top view of laser drilling nozzle	170
Figure 6.31: Comparison of drilled depth for different pulse duration at 200 J pulse energy and five number of laser shots	171
Figure 6.32: Comparison of drilled hole diameter for different pulse duration at 200 J of pulse energy and five number of laser shots	171
Figure 6.33: (a) Drill on the upper surface of shale (b) Stress generates cracking in the shale rock (c) Stress breaks the shale rock (d) Laser drilled glassy hole in the shale rock	172
Figure 6.34: Variation in laser drill depth with number of laser shots for different rock	173
Figure 6.35: Back reflected signal variation with laser shots for different rock samples at 500 J pulse energy	173
Figure 7.1: A view of laser cleaned surface of marble, zircaloy, and inconel	186
Figure 7.2. SEM images of the surface of the marble sample, (a) before laser cleaning and (b) after laser cleaning	186
Figure 7.3. SEM images of the surface of the stone (berea gray sand stone) sample (upper part shows uncleaned and lower part shows laser cleaned surface.	187
Figure 7.4. SEM images of the surface of the inconel sample, (a) before laser cleaning and (b) after laser cleaning	187
Figure 7.5 Surface of the marble sample shows a clear difference between unclean and laser cleaned surface. After laser cleaning the substrate colour is becomes similar to the native substrate material.	188
Figure 7.6. Surface of the inconel sample shows a clear difference between unclean and laser cleaned surface. After laser cleaning the substrate colour is becomes similar to the native substrate material.	188
Figure 7.7. Surface of the zircaloy sample shows a clear difference between unclean and laser cleaned surface. After laser cleaning the substrate colour is becomes	189

similar to the native substrate material.	
Figure 7.8. Surface of the berea gray sand stone sample shows a slightly colour difference between the laser cleaned surface and native substrate surface.	189
Figure 7.9: XPS spectrum of inconel shows the peaks of Fe increases after laser cleaning	189
Figure 7.10: XPS spectrum of inconel shows the peaks of carbon reduces after laser cleaning	190
Figure 7.11: Schematic layout of experimental set-up for laser cleaning of carbon	192
Figure 7.12: Schematic diagram of the sample used for laser cleaning experiments: (A) intact gold film, (B) carbon coated gold film, (C) carbon removed gold film after laser treatment	193
Figure 7.13: XPS measurements of the three regions of the sample: (a) intact gold film (b) carbon coated gold film (c) gold film after carbon removal with laser treatment	194
Figure 7.14: Measured and fitted SXR spectra of (a) intact gold film, (b) carbon coated gold film and (c) gold film after carbon removal are shown. Critical angle corresponding to total external reflection region are distinctly different for pure gold film and carbon coated gold film as shown in highlighted area in the figure. After carbon film removal with laser treatment the reflectivity curve of intact gold film and that of laser cleaned film are similar as shown in inset of the figure. For the sake of clarity the curves are vertically shifted	195
Figure 7.15: Schematic of experimental set-up. (1. Laser pump chamber 2. AO Q-switch 3. X-Y scanner 4. Flat field lens 5 & 6. Optical windows, 7. Sample 8. Tilting screws 9. Suction system)	197
Figure 7.16: A view of laser cleaned gold-coated mirror in selected areas	199
Figure 7.17: Variation of ablation depth as a function of laser fluence with number of laser pulses as parameters	200
Figure 7.18: A plot of cleaning efficiency versus laser fluence with number of laser pulses as parameters	200

- Figure 7.19: SEM image of single laser pass cleaned surface of the sample, upper part shows cleaning in the presence of the suction system, and lower part shows image of the cleaned surface without suction system 201
- Figure 7.20: (a) Microscope image of the cleaned surface, when it was cleaned from the front surface. It shows a good cleaned surface in the upper part and lower part shows gold coated uncleaned surface 202  
(b) Microscope image of the cleaned surface, when it was cleaned from rear surface. Some gold particles remain on surface (upper part) and lower part shows gold-coated uncleaned surface
- Figure 7.21: Variation of gold layer cleaning efficiency as a function of angle of incidence 203
- Figure 7.22: Optical microscope image showing the difference in cleaned layer for the normal incidence (left) and cleaned layer at 30° angle of incidence (right) with single pass of laser beam. 203
- Figure 7.23: Soft X-ray reflectivity (SXR) spectra of the sample before and after gold layer cleaning by using 130Å wavelength. Open circles represent the experimental data whereas continuous lines are corresponding to the best fit obtained using parameters given in Table 3. Curves are vertically shifted in the y-axis for clarity. The vertical lines mark positions of the critical angle for Au film and fused silica substrate 205
- Figure 7.24: XPS spectrum of the gold layer shows that the peaks of gold disappear after laser cleaning process 206

## List of tables

Table 1.1: Some important physical and optical properties of Nd:YAG crystal	2
Table 2.1: Some important physical properties of Sintox AL ceramic	25
Table 2.2: Pulse-to-pulse stability and output pulse energy for different configuration of resonator of 250 W average power Nd:YAG laser	38
Table 2.3: Calculated and measured values of thermal focal length for gold-coated and ceramic reflector based Nd:YAG rod ( $\phi$ 8 mm $\times$ 150 mm) for different input pump power	42
Table 3.1: Calculated and measured values of thermal focal length in meters	66
Table 4.1: Specifications and component list of power supply	81
Table 4.2: Variation of $M^2$ , PTPS and misalignment sensitivity of the laser resonator with R.O.C. of the rear mirror at maximum pump power	87
Table 5.1: Parameters of the z-fold resonator geometry	131
Table 5.2: A comparison of resonator geometry and results of the earlier reported work and present work	133
Table 6.1: Important specifications of the long pulse Nd:YAG laser deployed for cutting operation	144
Table 6.2: List of optimized process parameters for the laser cutting of SS 304 samples of different thickness	147
Table 6.3: List of measured kerf width, HAZ and percentage variation in HAZ of different thickness sample at maximum cutting speed	156
Table 6.4: Composition of the rock samples and its important physical properties	167
Table 6.5: Parameters of the long pulse Nd:YAG laser used for the rock drilling	169
Table 7.1: Experimentally measured values of ablation and damage threshold during Nd:YAG laser cleaning experiment with important thermal properties of various sample	185
Table 7.2: A list of process parameters and results of laser cleaning experiment on different samples	188
Table 7.3: Chemical composition (wt%) of inconel -600 sample	190
Table 7.4: Thermo-physical parameters of gold and fused silica	199
Table 7.5: Comparison of surface roughness obtained by angle-dependent SXR spectra of gold coated mirror sample before and after cleaning (For $0^0$ to $70^0$ incidence angle and 13 nm wavelength of soft X-ray)	204

# Chapter 1

---

## Nd:YAG laser : An overview

### 1.1 Introduction

Neodymium-doped yttrium aluminium garnet (Nd:YAG) laser was discovered almost fifty years ago at Bell Labs in 1964. It has undergone enormous evolution over the years and is now being used widely in both basic research and technological applications in a variety of fields like nuclear engineering, heavy machinery industry, automobile, aerospace, artwork conservation, geo-science, space and bio-medical sciences [1-6].

Pure YAG ( $Y_3Al_5O_{12}$ ) is a colourless, optically isotropic crystal that possesses cubic structure characteristics of garnets. Neodymium is the dopant material substituted for yttrium in YAG host. Some important physical and optical properties of Nd:YAG crystals are given in Table 1.1. Nd:YAG laser is a four-level system as depicted by a simplified energy level diagram in Fig. 1.1. Neodymium ions define the energy levels and thus the characteristics of this laser. Laser transition at a wavelength of 1064.1 nm originates from  $R_2$  component of the  ${}^4F_{3/2}$  level and terminates at the  $Y_3$  component of the  ${}^4I_{11/2}$  level. According to Boltzmann's law at room temperature, only 40% of the  ${}^4F_{3/2}$  population is at level  $R_2$  while rest 60% remains at the lower

sublevel  $R_1$  [7]. Lasing takes place only by ions at  $R_2$  level and population at this level is replenished from  $R_1$  by means of thermal transitions.

**Table 1.1:** Some important physical and optical properties of Nd:YAG crystals [7]

Chemical formula	Nd:Y <sub>3</sub> Al <sub>5</sub> O <sub>12</sub>
Weight % Nd	0.725
Atomic % Nd	1.0
Nd atoms/cm	$1.38 \times 10^{20}$
Meting point	1970° C
Knoop hardness	1215
Density	4.56g/cm <sup>3</sup>
Rupture stress	$1.3\text{-}2.6 \times 10^6$ kg/cm <sup>2</sup>
Modulus of elasticity	$3 \times 10^6$ kg/cm <sup>2</sup>
Thermal expansion coefficient	$8.2 \times 10^{-6}$ °C <sup>-1</sup> , 0-250° C
Line width	120 GHz
Stimulated emission cross section	
$R_2 - Y_3$	$\alpha = 6.5 \times 10^{-19}$ cm <sup>2</sup>
${}^4F_{3/2} - {}^4I_{11/2}$	$\alpha = 2.8 \times 10^{-19}$ cm <sup>2</sup>
Fluorescence lifetime	230 μs
Photon energy at 1064 nm	$1.86 \times 10^{-19}$ J
Index of refraction	1.82 (at 1064 nm)

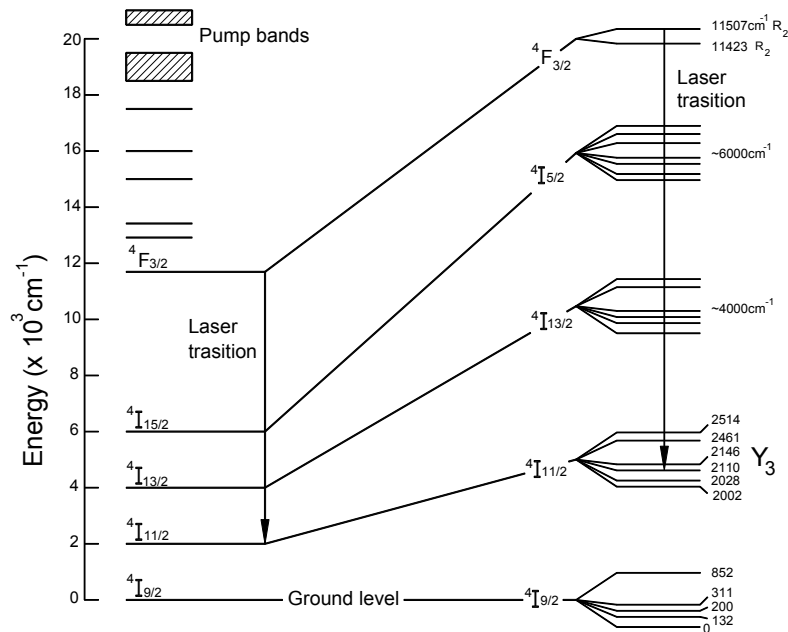


**Fig. 1.1.** Energy level diagram of Nd:YAG crystal [7].

The ground level of Nd:YAG is  $^4I_{9/2}$  level. Since the terminal laser level is not populated thermally, it is easy to reach the threshold condition for lasing. Under normal operating conditions at room temperature, Nd:YAG laser oscillates on the strongest  $^4F_{3/2} \rightarrow ^4I_{11/2}$  transition at 1.0641  $\mu\text{m}$ . However, it is possible to achieve laser oscillation at other wavelengths also either by operating at different temperatures or by using some intra-cavity optical elements like etalons or dispersive prisms. Figure 1.2 shows absorption spectra of Nd:YAG crystal. It shows strong absorption peaks near 0.57-0.59  $\mu\text{m}$ , 0.73-0.76  $\mu\text{m}$ , 0.79-0.82  $\mu\text{m}$ , and 0.86-0.89  $\mu\text{m}$  bands in the visible and near infrared region [8].

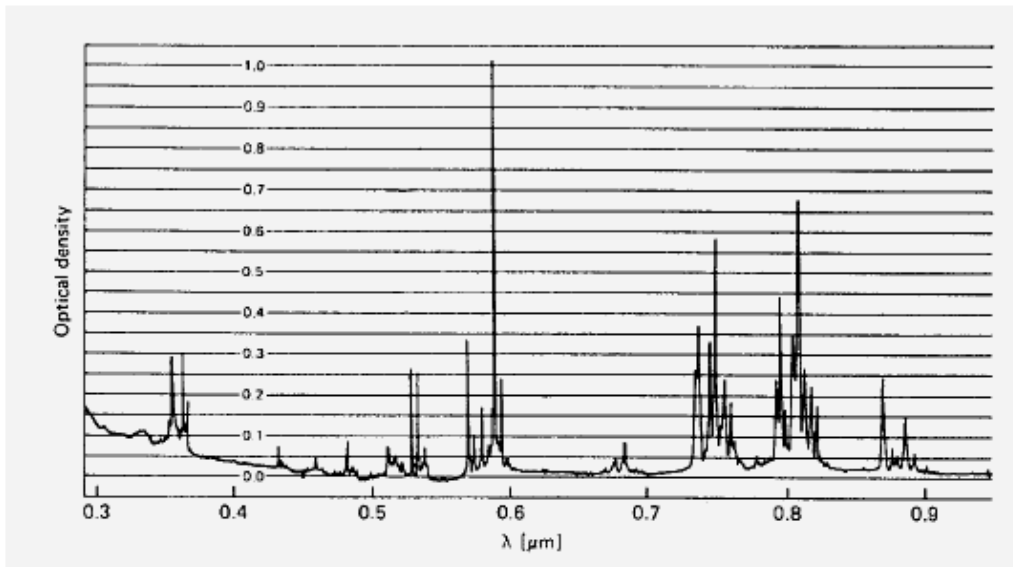


**Fig. 1.2.** Absorption spectrum of Nd:YAG crystal [7].

The most important component of an Nd:YAG laser system is the Nd-doped laser crystal which is responsible for the generation of the high power laser beam under optical pumping. Nd:YAG crystals have good thermo-physical and mechanical properties as compared to other solid state laser crystals [7]. It has a high figure of merit, large value of thermal shock parameter, and broad absorption band in visible and infra red regions [7-9]. The quality of the laser crystal is evaluated by its performance to generate maximum laser output power with good beam quality

and high efficiency. Higher efficiency (~30%) can be achieved in the Nd:YAG lasers by pumping the crystal using semiconductor diode lasers having an emission wavelength close to the absorption band of Nd:YAG. On the other hand, flash and arc lamps are also used widely for the pumping of the Nd:YAG crystal. The electrical to laser conversion efficiency in this case is poor (~4.5%). The major loss in efficiency with lamp pumping is due to the broad band emission from lamps and thermal effects, which are associated with heat removal from the laser crystal and lamps [9]. A flow diagram of the power losses during lamp pumping of Nd:YAG laser material is as shown Fig. 1.3.

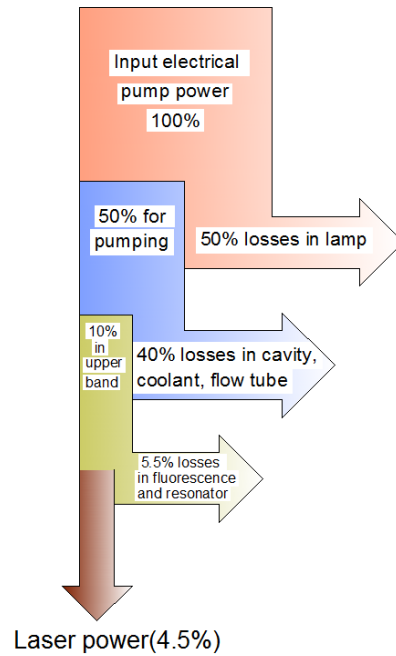


**Fig. 1.3.** Power losses during lamp pumping of Nd:YAG crystal.

However, inspite of low laser efficiency, lamp pumped Nd:YAG lasers have become the most versatile laser systems in use with over 30 years in operation. It has widespread acceptance in different areas, such as in manufacturing, where it serves a wide variety of functions, which includes welding, cutting, and drilling of different materials.

The main advantages of Nd:YAG lasers are its compactness and beam delivery using flexible optical fibers. It also provides other advantages over conventional mechanical tools during processing of materials such as non-contact nature, selectivity, easy automation, higher processing speed, reliability, well controlled beam characteristics, and repeatability. However, some of the disadvantages include inability to process non-metals and plastics, higher processing cost, and handling only by trained persons. Efficient and reliable operation of an Nd:YAG laser is necessary for its exploitation in already established fields and emerging applications.

In general, Nd:YAG lasers are operated in continuous wave (CW) and pulsed mode. Pulsed operation of Nd:YAG laser in free running (FR) mode provides millisecond (ms) and microsecond ( $\mu$ s) duration pulses [10], whereas pulses in nanosecond (ns) duration are generated by passive or active Q-switching (QS) techniques [11]. In order to generate pulses in the picosecond (ps) and femtosecond (fs) duration, Nd:YAG laser has to be operated in the mode-locking (ML) regime [12]. For thick material processing it is necessary to generate high-energy pulses with high values of average and peak powers. For high energy pulse generation, output of Nd:YAG laser oscillator is further amplified using amplifier stages of various configurations involving master oscillator and power amplifier (MOPA), zigzag slab geometry, multiple amplification media, or hybrid solid-state system [7,11,12]. However, with these amplification techniques, in many cases, the laser beam quality is degraded and it becomes difficult to couple the laser beam through optical fibers [7]. Thus, in order to obtain high energy and high average power Nd:YAG laser pulses with good beam quality, multi-rod oscillator configuration is used. With the multi-rod oscillator, pulse energy is enhanced without degradation of the beam quality even with several laser rods arranged optically in series in a well designed resonator [7,8]. Long pulse Nd:YAG laser with pulse duration in the order of ms is preferred for welding of thicker

materials. Similarly, ms and  $\mu$ s duration pulses of YAG laser are used for cutting of thick metal sheets. Pulses of  $\mu$ s, ns, ps and fs time duration are used for micro-machining and cleaning applications.

Now-a-days, laser cutting of metals is widely performed in various industries. With continuous enhancement in available output power and improvement in beam quality of laser systems, the scope of laser cutting applications has also increased to cover larger work-piece thicknesses. However, it is necessary to have good knowledge and understanding of pulsed Nd:YAG laser cutting parameters in order to successfully tailor the cutting process. A detailed description of laser material processing can be found in the literature [8, 13-15]. The basic characteristics of Nd:YAG laser radiation, which is beneficial for cutting and welding of metal includes: power density, depth of focus, absorption of metal surfaces, and possibility for fibre optic beam delivery. When a focused laser beam of high intensity strikes the surface of a metal work-piece, some part of the radiation is reflected, and some part of it is absorbed. Some amount of absorbed energy is also lost from the interaction zone due to conduction of heat through the substrate.

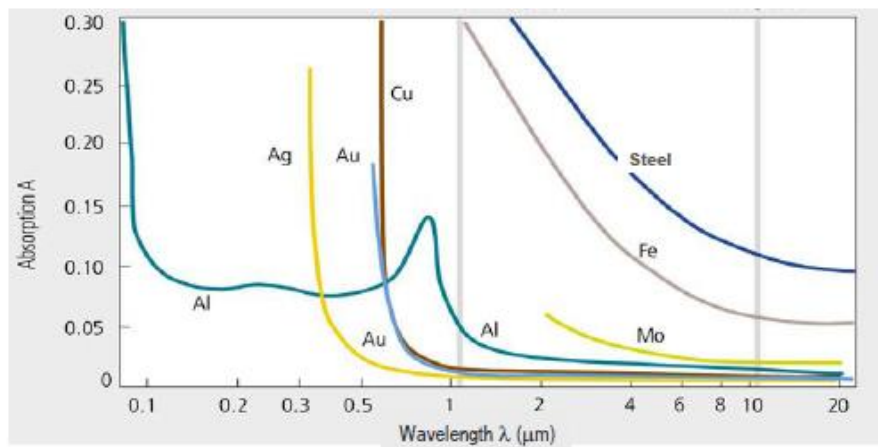


**Fig. 1.4.** Absorption characteristic of different metals as a function of wavelength [8].

Absorption of some important metals for a wide range of wavelengths is given in Fig. 1.4. Apart from the wavelength, polarization and angle of incidence, the actual absorbed power also depends on surface roughness, material type, temperature, and phase of the material. On a microscopic scale the absorption mechanism can be described as follows. The free electrons of the material absorb photons of the incident laser radiation. The absorbed energy sets the free electrons in forced vibrational motion very quickly, which is transferred to the lattice increasing lattice vibrations. On a macroscopic scale, this corresponds to the observation of increase in temperature of the substrate. If sufficient laser energy is absorbed, thermal vibrations become so intense that the metallic or molecular bonding are over stretched to an extent that the lattice is no longer capable of exhibiting mechanical strength. This results in melting of the metal at the interaction zone. With further increase in the laser intensity or power density, much stronger vibrations result in further weakening of bonds. The resultant temperature or energy of the molecules is high enough for the evaporation of the material. Fourier's law of heat conduction describes the flow of heat in the metal work-piece [8]. Melting efficiency increases with increase in the absorptivity of the material. For a particular laser, melting efficiency is defined as the ratio of absorbed laser power utilized in melting of the kerf volume to the total incident laser power.

## **1.2 Scope of work**

Motivation for this thesis was conceptualized from the requirement of pulsed Nd:YAG lasers of different pulse durations to investigate the performance of these lasers for a variety of material processing applications. Hence, the purpose of this work is to study and development of highly efficient fiber coupled pulsed Nd:YAG lasers to perform material processing. This study also aims to investigate the performance of long and short pulse Nd:YAG laser in laser

cutting, welding and cleaning to determine the appropriate processing parameters for achievement of high speed and good quality.

Although, several reports have been published towards the study and development of Nd:YAG lasers, a majority of them are related to high power (~kW) continuous wave (CW) operation [13-15]. Pulsed Nd:YAG lasers with high peak and high average power are useful in material processing and provides the advantage of localized heating in the material with minimum distortion and the heat affected zone as compared to CW lasers [16-18]. Long and short pulse high peak power free-running Nd:YAG lasers still depend on flash lamp pumping in place of diode laser pumping as the high peak power operation of laser diodes is limited to only a few hundreds of watts [19]. Most of the commercially available [20-24] lamp pumped long pulse Nd:YAG lasers provide maximum pulse energy in the range of 50 J to 150 J. With this limited pulse energy, the application areas of these lasers for deep penetration cutting, welding and drilling are also limited for most of the metals. Therefore, it is of interest to develop a ms pulse duration Nd:YAG laser system with high peak power in the range of 5-20 kW and high pulse energy in the range of 100 J to 500 J for processing of thicker materials. This research work deals with design and development of pulsed Nd:YAG laser system of different pulse durations up to 20 kW peak power and up to 500 J pulse energy with good laser beam quality for efficient fiber optic beam delivery. Research and development is required for the improvement in pulse-to-pulse stability and efficiency of pulsed Nd:YAG laser and enhancement in its output powers to the required level for material processing of thicker materials.

For laser material processing, the polarization state of the laser beam has a strong influence on its absorption in the material [25]. In view of this, some novel optical schemes have been used for the generation of high power long pulse linearly *p*-polarized laser beam.

These high peak power pulsed Nd:YAG lasers have been successfully used for several material processing applications. Detailed studies were performed on: (a) laser cutting of thick section of stainless steel in dry air and in under water environment for dismantling and maintenance work in nuclear facilities and shipping industry, (b) laser welding of aluminium, titanium and stainless steel for automotive, heavy machinery, and vacuum industry, (c) laser drilling of rocks for use in petroleum industry, and (d) laser cleaning of carbon contamination and removal of gold layer in beamline mirrors of synchrotron radiation, (e) laser cleaning of marble for the conservation of art work, and cleaning of inconel and zirconium for nuclear applications. This study also aims to provide a comprehensive view of the laser material processing and highlights the benefits of high power pulsed Nd:YAG laser. The thesis includes the description of experimental methods as well as analysis of optimization of the process parameters to achieve the above objective.

### **1.3 Construction of pulsed Nd:YAG laser**

Major components of a pulsed Nd:YAG laser system are Nd:YAG rod, flash lamp, laser pump chamber, laser resonator, optical fiber for beam delivery, power supply for flash lamps and cooling system. For the generation of high-energy laser pulses, high doping concentration of Nd<sup>3+</sup>-ions in YAG host is favourable [26]. In general, thermal problems in Nd:YAG laser material limits the efficiency of the laser system and degrades the beam quality. To achieve higher slope efficiency, the important factors which need to be considered during the design of laser pump chamber are the efficient cooling of the laser rod and design of reflectors for efficient transfer of pump light to laser rod. A schematic view of laser pump chamber with the laser rod, flash lamp, reflector, and flow tube is shown in Fig. 1.5. Different types of reflector geometries

are used for pumping of laser crystals. The single or double elliptical type reflectors are more efficient and hence more preferred. The reflectors are generally, either gold-coated metallic (specular reflection) reflectors or ceramic (diffuse reflection) reflectors. Several different types of optical resonator geometries are also used in Nd:YAG laser.

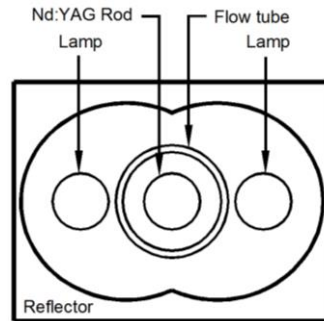


**Fig. 1.5.** Schematic of laser pump chamber (front view).

For single rod Nd:YAG lasers of low to medium power range (1W-200W), hemispherical resonators are preferred [27], since with these resonators one can obtain stable output power for the entire pumping range with relatively non-critical mechanical adjustments. However, for the high average power multi-rod type long pulse laser systems, a plane-plane symmetric resonator is the choice due to its stability for a large range of thermal focal lengths. For example, two Nd:YAG rods can be arranged optically in series with  $d:2d:d$  (lens like imaging) configuration in the plane-plane symmetric resonator. This optical resonator operated in the stable region, for the entire pumping range with the limited divergence of the laser beam. This fact can be expressed by a resonator stability criterion  $0 \leq g_1 g_2 \leq 1$ .

Flash and arc lamps used for Nd:YAG rod pumping are essentially long arc devices designed so that the plasma completely fills the tube. A gas filled flash or arc lamp consists of a linear quartz tube, two electrodes that are sealed into the envelope. These lamps are typically

filled with inert gas (Xe or Kr) at a fill pressure of 300 to 700 torr at room temperature. The emission spectra of Kr filled lamp has better spectral matching with the absorption band of Nd:YAG as compared to the Xe filled lamp. In Fig. 1.6 the spectral emission of a Kr flash lamp is plotted for two current densities. A high current density shifts the spectral output toward the shorter wavelengths, which is not desirable as the absorption bands in this wavelength are weak, and hence the pumping power is not efficient.

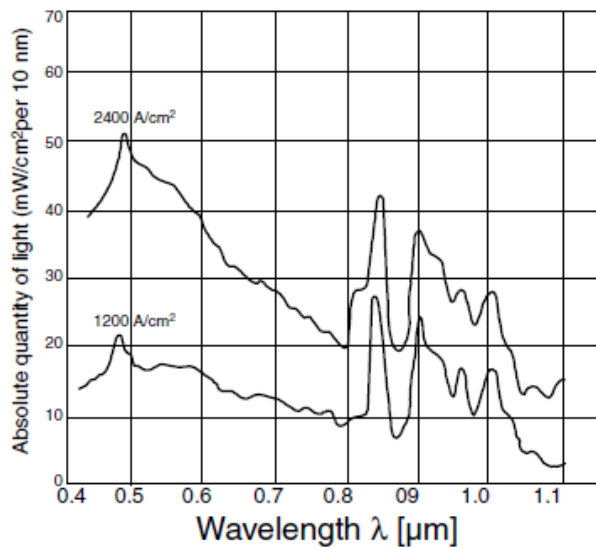


**Fig. 1.6.** Emission spectrum of Krypton flash lamp [8].

Impedance characteristics of a lamp determine its efficiency with which the energy is transferred from the capacitor bank to the lamp. After the arc stabilizes in the high-current regime, the voltage  $V$  becomes proportional to the square root of the current  $I$  as  $V=K_0\sqrt{I}$ , where the lamp impedance  $K_0$  depends on the arc length  $l$ , bore diameter  $D$  of the flash lamp, gas type and fill pressure  $p$ . For xenon filled flash lamps, the following relation for  $K_0$  holds [7]  $K_0=1.27(p/450)^{0.2}l/D$ , where  $p$  is the flash lamp pressure in torr. The energy delivered to the lamp is stored in the capacitor  $C$ . Discharge of the stored energy into the flash lamp is initiated

by a high-voltage trigger pulse generated by a pulse generator and a step-up transformer. The trigger pulse applied to a wire wrapped around the tube envelope creates an ionized spark streamer between the electrodes. The energy stored in the capacitor is then discharged into the lamp through the inductor  $L$ . The pulse duration and pulse shapes are determined by the time constant of the  $LC$  circuit. The lamp extinguishes after the capacitor is discharged. It has been found that the lifetime of a flash lamp can be significantly increased, and pump efficiency can be improved if the lamp is pre-ionized in simmer mode. In the so-called simmer mode, a low-current discharge is maintained between the high current pulses. The simmer mode of operation requires a switching element between the flash lamp and the pulse-forming network (PFN). A trigger pulse of approximately 20 kV [7] initially ignites the flash lamp. A low-current discharge of a few hundred milliamps is maintained in the lamp by the simmer supply. Energy storage capacitor is discharged via a switch such as an SCR. The pulse shape is determined by the PFN, the switch as well as the flash lamp. The flash lamp is turned off once the capacitor is discharged.

In Nd:YAG lasers, a closed loop water cooling system is also used for cooling of laser pump chamber with proper controls to maintain almost constant surface temperature of the Nd:YAG rod and the flash lamp. A secondary refrigeration cooling system cools the water of primary cooling system via plate type heat exchanger. The primary cooling system is directly connected to the laser pump chamber through a water pump and a water tank that supplies chilled water. A high flow rate of water through the pump chamber is achieved using a multi-stage centrifugal pump. Primary cooling also contains a water filter, a water flow switch, and a digital temperature controller. Further details of the laser power supply and cooling system can be found in references [7] and [8].

## 1.4 Optical fiber coupling

Optical fibers are used for the beam delivery of Nd:YAG lasers. Optical fiber is made of silica, central portion of the fiber is called core, which is surrounded with an outer part known as cladding, which is further surrounded by a coating, and a jacket is also applied as a protective cover as shown in Fig. 1.7.

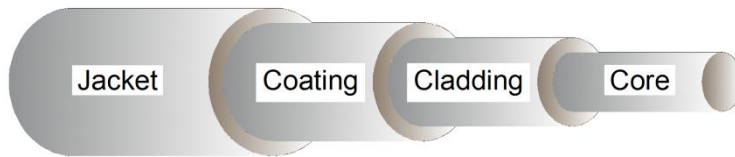


**Fig. 1.7.** A schematic view of optical fiber.

The 'sine' of the acceptance angle of optical fiber is known as the numerical aperture (NA) of the fiber which depends on the refractive index of core and clad of the fiber and is given by  $NA = \sqrt{(n_{core}^2 - n_{clad}^2)}$ . For efficient coupling of laser beam through the optical fiber, there are certain coupling conditions which are given by: (1) focused beam diameter should be equal or smaller than the core diameter, (2) full angle beam divergence should be smaller than the  $2 \times NA$  of the fiber, and (3) beam parameter product (beam radius  $\times$  half angle divergence) of the laser beam should be less than the beam parameter product of the fiber (core radius  $\times$  NA) [28]. During the beam delivery through optical fiber, the major losses, which are encountered, are (1) losses due to misalignments of focussed laser beam on fiber core, (2) Fresnel reflection losses at each end surface of about 3.5% at the interface of fused silica to air, (3) material specific losses such as scattering and absorption, and (4) fiber bending losses.

The attenuation of the beam after propagation through the fiber due to the above losses are measured in dB/km [7]. The losses due to the absorption are negligible for fiber lengths of

several meters with loss coefficient of typically less than 3 dB/km at a wavelength of 1064 nm. Bending losses are usually expressed in terms of minimum bending radius of optical fiber and can be minimized by avoiding small bending radius. In order to increase the laser power for material processing, especially for welding applications, different fiber delivery channels for beam addition are also utilized. A widely used method is to superimpose the beams of two or more independent lasers directly onto the work piece as shown in Fig. 1.8 using several independent fiber beam delivery channels.

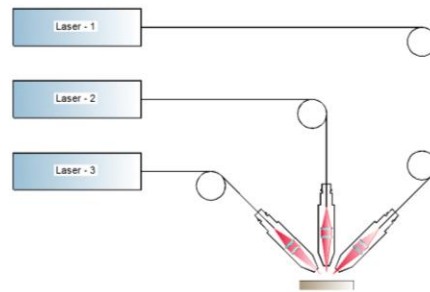


**Fig. 1.8.** *Beam addition of three fiber coupled laser beams on work piece.*

Each laser beam is coupled through a single optical fiber with a processing objective at the fiber exit end. Beam Parameter Product (B.P.P.) of the resulting beam is the sum of the individual products or more. The spot size on the work piece increases with the cosine of the tilt angle between the optics [27,28]. A deterioration of the beam quality occurs by the offset angle between the optics. The kind of beam addition may be helpful for the specific applications for example in edge welding. However, the best results for the other material processing applications are achieved by use of a single fiber in place of multiple fiber channels. Multimode single optical fibers enable efficient delivery of large laser powers with considerable higher coupling efficiency [28]. The effectiveness of fiber-optic beam delivery system is strengthened by the optimal selection of its components not only for minimizing beam quality degradation, but also for

robustness. Further, it is essential, to ensure accurate alignment of laser beam during coupling to the fiber otherwise damage of end face may occur. Coarse alignment of the beam launch conditions is carried out by checking the transmitted power through the fiber. Fine alignment can be obtained by monitoring the beam profile at the exit end of the fiber for higher order modes. Smaller core diameter ( $\sim 200 \mu\text{m}$ ) fibers tend to produce less degradation in beam quality. The spot size of the beam focused at the fiber end is determined by the quality of the laser beam, focusing optics and numerical aperture of the fiber. For short focal length lenses, selection of aberration-free optics is an important condition. This is also true for output optics, when small spot sizes or high irradiances are desired. High power handling requires special connectors that can withstand back-reflections. These high power connectors avoid the use of components such as epoxy that are susceptible to heat. Bends in the fiber-optic cable tend to produce higher order transmission losses. A variety of optics can be utilized to deliver a beam of the required shape and irradiance to the work-piece. Recent developments in optical materials allow the manufacture of aberration-free optics, which is particularly useful in the design of short focal length lenses. With the availability of GRADIUM lenses, it is now possible to obtain very small focal spots with minimum spherical aberrations and provide more intensity at focus position.

A general review of the study and development of fiber coupled lamp pumped pulsed Nd:YAG laser is carried out by various researchers [1-12]. However, most of them report the value of the slope efficiency of laser in the range of 4% to 4.5%. Thermal problems in Nd:YAG rod not only limit the efficiency of laser but also distort the beam quality in high average power multimode operation. Poor beam quality limits the beam delivery option of laser beam through optical fiber. We have focussed our attention on the design of laser pump chamber for efficient removal of heat load from the laser rod to reduce the thermal problem and enhance its slope

efficiency up to 5.5% which is on higher side for a lamp pumped pulsed Nd:YAG lasers. We have also focussed on the design of laser resonator for multi rod configuration for higher output power and good laser beam quality.

From the literature survey, it is noted that the performance of ceramic Nd:YAG has competitive advantages and the ability to replace the single crystal Nd:YAG which is currently a dominating lasing material for the high power laser development [26]. In view of this fact we have put our efforts for the development of high power long pulse ceramic Nd:YAG laser. Further, in our research work, we have also considered the problem of thermal birefringence in the single crystal Nd:YAG laser rod which degrades the beam quality. In order to compensate birefringence, some experiments have been performed using simpler and novel optical schemes for the single and dual Nd:YAG rods resonator.

The other aim of this research work was to develop a more effective and safer laser cleaning technique using short pulse duration Nd:YAG laser. For example, the cleaning of delicate and costly gold-coated optics of synchrotron radiation source and also for the cleaning of metals, stones, marble for industrial, nuclear and artwork applications. Recently, the use of lasers cleaning for conservation and restoration applications is increasing continuously because of several advantages of this non-contact cleaning method rather than the conventional cleaning methods, which carry risks of damage to the substrate material [13-16].

Finally, to achieve good quality cutting, welding or drilling, the process parameters required optimization for these specific applications. Our efforts on the laser material processing work using the high peak power pulsed Nd:YAG laser in this thesis highlights the current research area in this subject.

# Chapter 2

---

## Study and development of high power long pulse Nd:YAG lasers

### 2.1 Introduction

Lamp pumped Nd:YAG laser with fiber optic beam delivery has proved to be the most rugged and widely used laser system in industrial environments. It has been exploited commercially for various material processing applications such as cutting, welding, surface treatment and drilling [29-32]. Long pulse Nd:YAG lasers with high peak power still depend on flash lamp pumping in place of diode laser pumping as the long pulse, high peak power operation of laser diodes is limited to only few hundreds of watts due to the thermal run away problem [19]. Further, the flash lamp is much more rugged and cost effective than the diode lasers. In view of its potential laser material processing applications, high power lamp pumped, long pulse Nd:YAG laser systems are still important in the present scenario and remains an active area of research and development.

Considerable progress has been made during the past in improving the performance of lamp pumped, long pulse Nd:YAG laser systems in terms of high power scaling, beam quality, and efficiency [1,33]. Jiang *et al.* have recently demonstrated long pulse Nd:YAG laser of 2.02 kW average power and 60 J of pulse energy using four Nd:YAG rods [34]. They have used an input pump power of 58 kW with four Xe flash lamps and achieved an electrical to laser

conversion efficiency of 3.49%. Similarly, Yagi *et al.* [35] have reported the generation of 386 W average power in 5 ms pulse duration from lamp pumped Nd:YAG laser at an input average power of 16.4 kW and a slope efficiency of 2.3%. They have used a 10 mm diameter and 152 mm long 1.1% ceramic Nd:YAG rod in a samarium doped flow tube and a Xe-filled flash lamp placed in a gold coated elliptical reflector based pump chamber. The efficiency of their laser system might be poor due to the fact that they have used Xe-filled flash lamp for pumping in place of Kr filled flash lamps. Higher slope efficiency can be obtained using Kr-filled flash lamps as compared to Xe-filled flash lamps because of its better spectral matching with the Nd:YAG absorption band [7]. Most of the commercially available lamp pumped long pulse Nd:YAG lasers provide maximum pulse energy in the range of 50 J - 150 J [20-24]. With this limited pulse energy, the performance of laser, for example weld depth during laser welding is also limited to about 2-2.5 mm in most of the metals. Hence there is still a need and also scope for development of long pulse Nd:YAG lasers with higher pulse energy, better efficiency, and good beam quality.

As we have discussed in Chapter 1, the basic configuration of a long pulse Nd:YAG laser system consists of a pump chamber containing flash lamp and a Nd:YAG rod, placed in gold coated or a diffuse reflector for optical pumping. The pump chambers are kept inside an optical resonator. In general, thermal problem in the lamp pumped Nd:YAG laser rod, limits its efficiency and degrades the laser beam quality. In our studies, we had analyzed the design of cooling and pumping geometry of the pump chamber and improved it, to ensure efficient heat removal for reduction of dioptric power of the thermal lens in the Nd:YAG rod.

The dioptric power of Nd:YAG rod increases linearly with pump power and hence acts as a focusing element of variable power [8]. As the pump power increases, the stability point for

resonator moves along a straight line in the stability diagram [27]. Two most commonly used resonator geometries namely, plane-plane and hemispherical with the similar fundamental mode spot size within the rod, will provide the same beam quality. However, for a plane-plane resonator, the resonator stability point passes through the confocal point and it remains stable for a long range of pump power. Hence it preferable for high average power and long pulse operation of Nd:YAG laser with multi rod configuration.

In this Chapter, we discuss the issues related to the design and development of flash lamp pumped long pulse Nd:YAG lasers with high slope efficiency and good beam quality. The slope efficiency and the pulse energy achieved by us in these millisecond duration Nd:YAG lasers is much better than the commercially available Nd:YAG lasers of similar ratings. We have achieved this by designing a laser pump chamber with a suitable cooling scheme, and a stable resonator configuration for the entire pumping range. Further, the laser resonator was also designed to provide a good beam quality, accurate and stable alignment and better pulse-to-pulse stability, so that the laser beam would be efficiently coupled to a small core diameter ( $\sim 400 \mu\text{m}$ ) optical fiber for beam delivery. Several material processing applications using these high average power, long pulse Nd:YAG lasers such as cutting, welding and drilling have been performed. Some of the potential application areas of these long pulse lasers are the laser welding of stainless steel, titanium and aluminium for the automotive, aerospace, and vacuum components industries, and underwater cutting of thick stainless steel for dismantling applications in nuclear and shipping industries.

In this Chapter, Section 2.2 presents the analysis of laser pump chamber and resonator configurations of the long pulse Nd:YAG laser. Section 2.3 provides the details of the experimental set-up for the development of long pulse Nd:YAG laser system. Section 2.4

provides the study on efficient optical fiber coupling of laser beam and Section 2.5 presents the results and discussion on the development of long pulse Nd:YAG lasers. Finally, Section 2.6 describes the conclusion of the work.

## 2.2 Analysis of laser pump chamber and resonator

Thermal effects in laser material is a critical issue for the design of long pulse Nd:YAG laser system. The part of the pump power, which is converted to heat inside the material, is considered as a heat source term  $Q(x,y,z)$  in units of power per unit volume. The unheated surrounding, such as air, coolant or any solid-state material, cools the surface of the material, and due to the heat conductivity of the material  $k(T)$ , a temperature distribution  $T(x,y,z)$  is established, which is described by [7]

$$\rho C_p \cdot \frac{\partial T(x, y, z)}{\partial t} = \nabla \cdot [k(T) \cdot \nabla T(x, y, z)] + Q(x, y, z) \quad (2.1)$$

where  $\rho$  is the material density and  $C_p$  the specific heat at constant pressure. For high power lamp pumped Nd:YAG laser operation, effective cooling is required for the rod. This is usually done with a water coolant flowing along the pumped rod surface. The refractive index profile of the Nd:YAG rod becomes parabolic because a temperature difference is created between the rod centre and the rod surface due to the combined effect of the optical pumping and water cooling. In the simplest case, this pumped rod is equivalent to a thick spherical lens known as thermal lens. Thermal lensing of the Nd:YAG rod is depends on the design parameters of the laser pump chamber namely, the geometry of pumping reflectors and cooling scheme of the rod for heat removal.

Further, important characteristics of the laser such as beam quality factor, output power and slope efficiency is influenced strongly by the heat removal from the laser rod. In subsection

2.2.1 and 2.2.2, we focus our study on the design of the laser pump chamber and resonator for long pulse Nd:YAG laser operation with output average powers up to 1 kW. In high average power dual rod Nd:YAG laser system, with good beam quality and high slope efficiency, plane-plane symmetric resonator configuration has been used, whereas for single rod, Nd:YAG laser, hemispherical resonator configurations has been selected.

### 2.2.1 Laser pump chamber design

As discussed earlier, in order to achieve high average power and slope efficiency for pulsed Nd:YAG laser, the important factor is the efficient cooling of the laser rod. Apart from this, the pumping geometry of elliptical reflector for efficient transfer of pump light to the laser rod is also important [7].

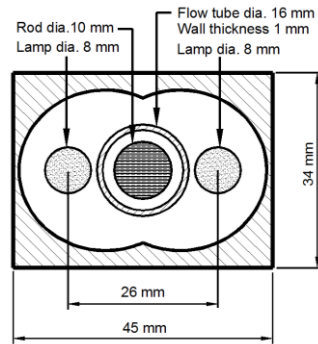


**Fig. 2.1.** A schematic diagram of the laser pump chamber used in experiments.

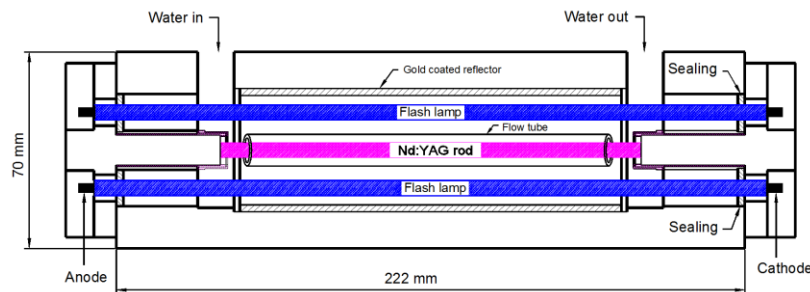


**Fig. 2.2.** A schematic of laser pump chamber (front view) and reflector geometry.

A schematic diagram of the side view of the laser pump chamber, designed for 1 kW long pulse Nd:YAG laser is shown in Fig. 2.1. The laser pump chamber consists of a 10 mm diameter and 150 mm length, 1.1% at. Nd<sup>3+</sup>-doped YAG rod and two 8 mm bore diameter Krypton filled flash lamps, placed in a double elliptical gold-coated reflector as shown schematically in Fig. 2.2.

The pump chamber is 222 mm long and 70 mm wide and is made of stainless steel (SS 304) because of its beneficial thermo physical properties like corrosion resistance, excellent toughness and low thermal expansion. The double elliptical reflector is 140 mm long and is also made of SS 304, and its surface is coated with 10 µm thick gold coating. Its major axis is  $2a=32$  mm, minor axis  $2b=28$  mm, distance between the rod and lamp  $2c=13$  mm with an eccentricity of  $e=0.4$ . In this close coupled type elliptical reflector geometry, the laser rod absorbs pump light emitted from the flash lamp directly as well as after specular reflection from the reflectors. A refrigeration cooling system with 20 kW heat load capacity has been used for cooling with proper regulation and controlling to adapt to the variation of the heat load, environmental changes, and requirements of maintaining almost constant surface temperature of Nd:YAG rod, and flash lamp. The coolant water temperature is maintained at 20<sup>0</sup>C for 20 kW heat load. The secondary refrigeration cooling system cooled the water of primary cooling system via plate type heat exchanger. The primary cooling system has been directly connected to laser pump chamber using a water pump and a water tank that supplies chilled water with a maximum flow rate of 50 lpm. Such a high water flow rate was achieved using a multi-stage centrifugal water pump (Wilo, GmbH). Water flow rate was measured using an ultra-sonic water flow meter (Endree-Hanser, Japan). Primary cooling system is also incorporated with a 10 µm size water filter (Millipore, India), a water flow switch (Switzer, India), and a digital temperature controller

(Selec, PID 528). The coolant water circulates in a closed loop in the laser pump chamber. Its heat transfer coefficient  $h$  in  $\text{W}/\text{cm}^2\text{ }^0\text{K}$  is given by [7,36].

$$h = 10.4 \times 10^{-3} \frac{(D_2 / D_1)^{0.53}}{(D_2 - D_1)(D_2 + D_1)^{0.8}} W^{0.8} \quad (2.2)$$

Where  $D_1$  is the diameter of the laser rod in cm,  $D_2$  is the inner diameter of the coolant flow tube in cm, and  $W$  is the water flow rate in  $\text{cm}^3/\text{s}$ . For the value of  $D_1 = 10$  mm and  $D_2 = 14$  mm. The constant value  $10.4 \times 10^{-3}$  in the equation (2.2) has a unit of  $\text{W} \cdot \text{s}^{0.8} / \text{cm}^{2.6} \text{ }^0\text{K}$ . The heat transfer coefficient  $h$  was varied from  $1.61 \text{ W}/\text{cm}^2\text{ }^0\text{K}$  to  $3.35 \text{ W}/\text{cm}^2\text{ }^0\text{K}$  by water flow rate variation in the range of  $20 \text{ l}/\text{m}$  to  $50 \text{ l}/\text{m}$  to optimize the heat transfer rate from the laser rod to ensure that there is no roll-off in the average output power even at the maximum average input pump power. An efficient heat transfer in the laser pump rod resulted in a higher slope efficiency.

Further, our studies showed that the pump light in the chamber is lost mainly due to the absorption at the surfaces of the metallic reflector, which results in the reduction of the transfer efficiency. It was observed that improvement in transfer efficiency is possible by changing the gold-coated metallic reflectors by diffuse ceramic reflectors. Moreover, gold-coated elliptical reflectors are based on specular reflection and provide highly directional reflectance and therefore tend to create ‘hotspots’ in the laser output. On the other hand, in a diffuse ceramic reflector the diffuse reflection of the flash lamp light, averages out the pump light and provides uniform pumping. During last two decades, several reports have been published concerning Nd:YAG laser operation using ceramic reflectors, but most of these are related to CW operation of Nd:YAG lasers [37,38].

We report studies and development of ceramic reflector based, long pulse fiber coupled Nd:YAG laser system with  $494 \text{ W}$  of average output power and  $10 \text{ kW}$  of peak power. The

ceramic reflectors used in laser pump chambers are made of an advanced material called ‘Sintox AL Alumina’, (Supplied by Morgan Ceramics, UK) which is a high purity ceramic material (99.7% Alumina) that works particularly well for pumping of Nd:YAG laser rod. Sintox AL alumina shows reflectance figures in excess of 98% over the wavelength range of 500 nm-2000 nm [39]. These reflectors are also glazed to enhance the reflectivity and to seal the porosity. A comparison between ceramic and gold-coated reflector based laser pump chambers for similar input pump power is also carried out. For ceramic reflectors, no corrosion/erosion problems were found to occur and it is expected to provide longer lifetime of operation as compared to gold-coated reflectors although the cost of the ceramic reflectors is about 2.5 times higher than that of the gold-coated reflectors. For example, in our lab ceramic reflector is still working in long pulse Nd:YAG laser operation for more than five years without any output power degradation.

In general, in the laser pump chamber of most of the commercial flash lamp pumped Nd:YAG laser system, flash lamp and the laser rod are kept at the two foci of an elliptical gold-coated metallic reflector. As the transfer of pump light from gold-coated reflectors to the laser rod is primarily by specular reflection the transfer efficiency is proportional to the ratio of rod and lamp radii ( $r_R / r_L$ ). However, in some cases, in order to achieve a good laser beam quality, it is necessary to keep the laser rod radius is smaller than the pump lamp radius. In this case, the transfer efficiency is poor for the gold-coated reflectors. This problem of poor efficiency can be overcome in our experiment by using diffuse ceramic reflectors as the reflection of radiation by a diffuse ceramic reflector is uniform and hence the transfer efficiency does not depend on the ratio ( $r_R / r_L$ ). A schematic of the geometries of gold-coated and the ceramic reflector is shown in Fig. 2.3. A 10% samarium oxide doped glass plate is inserted between the lamp and the rod to absorb the unwanted UV radiation from the lamp, which may create colour centres in the rod. In

addition, the Samarium doped glass filter enhances pumping efficiency by absorption of UV radiation and re-emission in the pump bands of Nd:YAG rod.

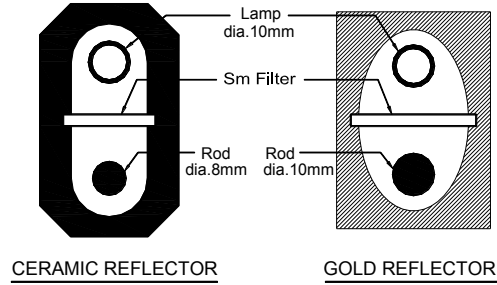


**Fig. 2.3.** Schematic of the shapes of ceramic and gold-coated reflectors.

The ceramic reflector used in the experiments has a close-coupled rectangular geometry with 30 mm  $\times$  15 mm cross-section and 7 mm wall thickness. The important physical parameters of this Sintox AL ceramic (Morgan ceramics, UK) material are listed in Table 2.1.

**Table 2.1:** Some important physical properties of Sintox AL ceramic

Physical Property	Value
Colour	White
Bulk density	3.3 g/cm <sup>3</sup>
Thermal conductivity	30 W/m <sup>o</sup> K
Specific heat capacity	0.88 J/g <sup>o</sup> C
Thermal expansion	7.9 $\times$ 10 <sup>-6</sup> / <sup>o</sup> C
Particle size	1-12 $\mu$ m
Modulus of elasticity	370-400 GPa
Fracture strength	150 MPa
Reflectance efficiency	98% at 1064 nm

In the ceramic reflector based laser pump chamber, we have designed a flooded type-cooling scheme for efficient cooling of the laser rod [40]. In this scheme, the laser rod, flash lamp, samarium filter, and reflectors are fully immersed in water. A closed-loop water chiller unit providing 50 l/m of water flow rate at 20<sup>o</sup>C has been used. Heat transfer coefficient  $h$  for the

flooded cooling scheme is calculated from the Nusselt number (Nu), which is a function of the Reynolds number (Re) as given by [41]

$$Nu = hD / k = 0.023 Re^{0.8} Pr^{1/3} \quad (2.3)$$

Here,  $k$  is the thermal conductivity of the water and  $Pr$  is the Prandtl number. The duct of the laser pump chamber for water flow was rectangular in shape and is divided in two equal rectangular subsections angle by a samarium filter as shown in Fig. 2.3. Its hydraulic diameter is calculated as  $D=4A/P_w$ . Here,  $A$  is the cross section area and  $P_w$  is the wetted perimeter of the rectangle given by  $P_w=2(a+b)$ . For the values of two half sides of rectangle  $a/2=1.5$  cm,  $b/2=0.75$  cm, the area of subsection of rectangular duct is  $A=1.12$  cm<sup>2</sup>, perimeter  $P_w=4.5$  cm and  $D=0.99$  cm. During turbulent flow of water in flooded type of laser pump chamber, the Nusselt and other calculated numbers are  $Nu=150$ ,  $Re=29870$ ,  $Pr=7.35$ ,  $k=0.569$  (W/m<sup>0</sup>K),  $h=9800$  (W/m<sup>2</sup><sup>0</sup>K). With these optimum values of different numbers, an efficient heat transfer coefficient was achieved in the laser pump chamber, which resulted in high slope efficiency. These ceramic reflectors have been tested successfully up to 5 kW pump power, as we will discuss later in section 2.5.2. Our studies show that ceramic reflectors are more cost effective as compared to the gold-coated reflectors. Their initial cost is higher but these ceramic reflectors provide a good laser beam quality with high slope efficiency and also have a longer operating life.

## 2.2.2 Laser resonator design

A plane-plane symmetric stable resonator was designed for the dual Nd:YAG rod, high average power and long pulse laser operation. The maximum output power from a single laser rod is limited by the maximum input pump power due to thermal fracture limit of Nd:YAG rod. Further output laser power can be increased by placing two or more laser rods (optically in

series) with  $d:2d:d$  (lens like imaging) configuration in the resonator. The distance ( $d$ ) between the plane mirror and the principal plane of the rods was optimized such that the resonator remains stable for the whole range of input pump power. For 1 kW average power Nd:YAG laser, the arrangement of the laser pump chamber in the laser resonator is shown schematically in Fig. 2.4. The rear mirror was taken as reference for round trip ABCD matrix calculations, which is given as

$$\begin{pmatrix} A & B \\ C & D \end{pmatrix} = \begin{pmatrix} 1 & d \\ 0 & 1 \end{pmatrix} \begin{pmatrix} 1 & 0 \\ -1/f & 1 \end{pmatrix} \begin{pmatrix} 1 & 2d \\ 0 & 1 \end{pmatrix} \begin{pmatrix} 1 & 0 \\ -1/f & 1 \end{pmatrix} \begin{pmatrix} 1 & d \\ 0 & 1 \end{pmatrix} \begin{pmatrix} 1 & d \\ 0 & 1 \end{pmatrix} \begin{pmatrix} 1 & 0 \\ -1/f & 1 \end{pmatrix} \begin{pmatrix} 1 & 2d \\ 0 & 1 \end{pmatrix} \begin{pmatrix} 1 & 0 \\ -1/f & 1 \end{pmatrix} \begin{pmatrix} 1 & d \\ 0 & 1 \end{pmatrix}$$

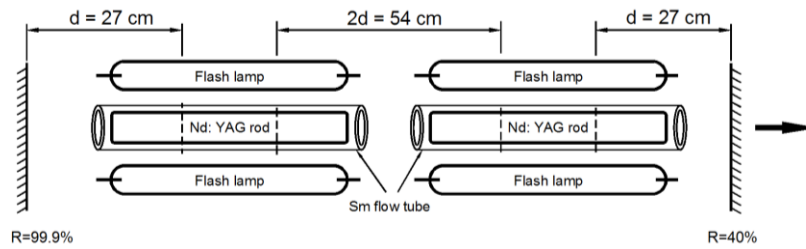


**Fig. 2.4.** A schematic of the laser resonator of 1 kW average power long pulse laser using two Nd:YAG rods.

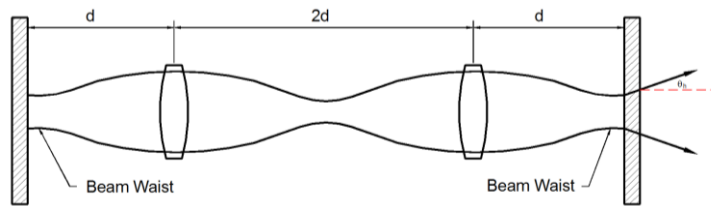


**Fig. 2.5.** A schematic of the equivalent resonator using two Nd:YAG rods.

The equivalent resonator consists of two flat mirrors with two internal lenses of focal lengths ( $f$ ) as shown in Fig. 2.5. The stability condition for the resonators with the resonator

parameters  $g_1$  and  $g_2$  can be expressed by  $0 < g_1 g_2 < 1$ . The value of  $g_1 g_2$  is related with the elements of round trip matrix by

$$g_1 g_2 = (A + D + 2) / 4 \quad (2.4)$$

It was observed that for an optimum distance of  $d = 27$  cm, for 1 kW average power and  $d = 20$  cm for 500 W average power, the resonator remains stable for the whole range of input pump power. The thermal refractive power ( $D_f$ ) or the overall thermal focal length ( $f$ ) of the uniformly pumped laser rod can be calculated by [7]

$$f = \frac{1}{D_f} = \frac{kA}{P_h} \left( \frac{1}{2} \frac{dn}{dT} + \alpha C_{(r,\phi)} n_0^3 + \frac{\alpha r_0 (n_0 - 1)}{L} \right)^{-1} \quad (2.5)$$

where,  $P_h$  is the thermal power dissipated in the laser rod of cross sectional area ( $A$ ) and length  $L$ ,  $n_0$  is the index of refraction,  $k$  is the thermal conductivity of the laser rod and  $r_0$  is the rod radius,  $\alpha$  is the coefficient of thermal expansion.  $C_r$  and  $C_\phi$  are the radial and tangential polarization dependent elasto-optical coefficients of Nd:YAG rod. Thermal power dissipation in the rod ( $P_h$ ) is proportional to the electrical input power ( $P_E$ ) from the flash lamp as given by  $P_E = K_0 I^3 t_p f_p$ , here,  $K_0$  is the lamp impedance parameter having a value of 18 for the flash lamps used in our experiments,  $I$  is lamp current,  $t_p$  is pulse duration and  $f_p$  is pulse repetition rate. It has been mentioned in reference [42] that the value of  $P_h$  can be in the range of 5-10%. Thus, in order to calculate the thermal focal length in the laser rods, the value of  $P_h$  was selected as 10% of  $P_E$ . The experimental value of thermal focal length matched well with the calculated focal length for this value of  $P_h$ . The lamp current ( $I$ ), pulse duration ( $t_p$ ), and repetition rate ( $f_p$ ) can be varied using a microcontroller based power supply. For a plane-plane symmetric resonator, the beam radius ( $w_0$ ) of the fundamental mode is related with the distance ( $d$ ) and the thermal refractive power of the laser rod ( $D_f$ ) by [42,43]

$$w_0^2 = \frac{2d\lambda}{\pi} \cdot \frac{1}{\sqrt{dD_f(2-dD_f)}} \quad (2.6)$$

Measured value of  $w_0$  is slightly higher than calculated values for different values of pump power since it depends on thermal focal length  $f$  and experimentally measured value of  $f$  are slightly higher than the calculated values as per Eq. (2.5). This may be due to samarium filter flow tube/plate, which reduces the effective heat load in the laser rod by cutting-off the UV radiation of the flash lamp and increases the value of  $f$  and subsequently  $w_0$ . The beam quality factor ( $M^2$ ) of the laser beam in a plane-plane symmetric resonator can be calculated by using the following expression [42]

$$M^2 = \left( \frac{r_0}{w_0} \right)^2 = \frac{\pi r_0^2}{2\lambda d} \cdot [dD_f(2-dD_f)]^{1/2} \quad (2.7)$$

The pulse-to-pulse stability (PTPS) is also an important factor in the laser resonator design with respect to laser welding applications and is given by

$$PTPS(\%) = \frac{E_{\max} - E_{\min}}{E_{\text{avg}}} \times 100 \quad (2.8)$$

The PTPS gives for a given number (for example 1000 pulses in our experiment) of pulses the percentage spread in energy difference of the highest and lowest value normalized to the average energy in these pulses. A small spread in the pulse energy from the average value demonstrates a good and stable resonator and is beneficial for laser material processing.

### 2.3 Experimental set-up of long pulse Nd:YAG laser

A dual rod laser system was made using two identical laser pump chambers arranged in a single laser resonator. Each pump chamber contains a 1.1% atomic doped Nd:YAG rod (Laser

Material Inc., USA). Both the ends of the Nd:YAG rod are plane-parallel and antireflection (AR) coated for 1064 nm wavelength, whereas cylindrical rod surface is grounded. The YAG rod is pumped over a length of 136 mm by two-cerium doped, Kr-filled flash lamps (Heraeus Noblelight, UK) for 1 kW average power laser and by a single flash lamp for the 500 W average power laser. The cerium doped flash lamps absorb UV and re-emits blue fluorescence. These lamps operate in simmer mode and are triggered by individual power supplies and serial transformers. However, after triggering, all the lamps are fired synchronously by a single controller for generation of high-energy laser pulses. Expected lifetime of the lamps, as calculated from data sheet of Heraeus Noblelight is  $2 \times 10^9$  shots at the maximum pump pulse energy of 3740 J with 40 ms pulse duration. The laser rods were kept in 10% samarium doped glass flow tube (Kigre, USA) of 16 mm outer diameter and 1 mm wall thickness. The resonator consists of ~99.8% reflective plane rear mirror and 40% plane output mirror. An aperture of 10 mm diameter has been placed between the two laser rods to filter out higher order modes. The laser pump chambers were cooled with identical closed-loop de-ionized water chillers having water flow rate of 50 *l/m* at 20°C temperature.

For 500 W and 1 kW average power lasers two modules and four modules of pulsed power supplies were used, respectively. A single controller was used in each case to synchronously drive the flash lamps. All these flash lamps have been connected electrically in parallel. The pulse power supplies can provide maximum average electrical input pump power of 5, 10 and 20 kW for 250 W, 500 W and 1 kW laser, respectively. The current variation from 100-300 Amp, pulse duration varies from 1-40 ms and repetition rate from 1-100 Hz with rectangular current pulse shape. Although the average electrical input to each lamp is rather large, care was taken that the absorbed pump power per unit length of laser rod in our laser

system is less than 150 W/cm, which is the maximum pump power limit of Nd:YAG before fracture [9].

For experimental measurement of thermal focal length  $f$  of each rod, an expanded and collimated He-Ne red laser was passed through the Nd:YAG rods under the flash lamp pumping. The minimum focal spot of the thermal lens was measured using a CCD camera. The distance between the one of the principal plane of the laser rod to the location of this focal spot is defined as the thermal focal length  $f$ . The beam quality factor  $M^2$  was measured using a standard knife-edge method [27]. The knife edge was moved through the laser beam by means of a translation stage. The positions  $x_1$  and  $x_2$  of the translation stage at which the average power becomes 90% and 10% of the total average output power are recorded. The beam diameter  $d_0$  is then calculated using the relation  $d_0 = 1.561 |x_1 - x_2|$ . The  $M^2$  was calculated by focusing the laser beam using a plano-convex lens of focal length 200 mm. The measured beam diameter near the focal plane was plotted to calculate the  $M^2$  at various locations. The  $M^2$  measurements were carried out by measured a 4% reflection of the laser beam using a wedge plate. Further, the average output power was measured by expanding the beam to a diameter of ~20 mm. The output power up to 500 W was measured using an air cooled thermocouple based power meter FL500A-LP1 (Ophir, Israel). The further higher output power (> 500 W) was measured using another water cooled high rating power meter W-6000 (Laser point, Italy). The single pulse energy of the laser beam was measured by means of an energy detector QE50ELP-H-MB-DO (Gentec, Canada). For this a fraction of the laser pulse energy was used which was obtained using a 50% reflectivity mirror at 45° angle of incidence in the beam path and then further taking ~4% sample of the reflected beam energy using a wedge plate.

## 2.4 Study on optical fiber coupling and time-shared beam delivery

For an ideal single mode Gaussian beam the value of  $M^2$  is equal to 1, while for a multimode beam the value of  $M^2$  is  $\geq 1$ . The beam quality factor ( $M^2$ ) characterizes, in general by the smaller the value of  $M^2$  the smaller is the focal spot diameter of the laser beam. The Beam Parameter Product (B.P.P.) is related with  $M^2$  by [27]

$$B.P.P.(w_m, \theta_m) = (\lambda / \pi) . M^2 \quad (2.9)$$

Here,  $w_m$  is the beam radius and  $\theta_m$  is the half angle divergence for the multimode beam. It is essential that the laser beam quality of long pulse Nd:YAG should be such that it can be efficiently transmitted through a small core diameter silica-silica optical fibers, which is possible only if the laser beam parameter product is smaller than the fiber parameter product (core radius  $\times$  NA) [28] where, NA is the numerical aperture of the fiber. Thus, selection of the fiber for fiber optic beam delivery depends on laser beam quality. The optical damage threshold of pure silica is about 10 GW/cm<sup>2</sup>, but it was observed experimentally that the damage threshold depends on fiber end surface preparation (polishing) on both ends. Due to this in general the surface damage threshold is lower than the bulk damage threshold. In order to launch the light beam into the fiber core, the maximum permissible angle between the light ray and the fiber axis is determined by the acceptance angle  $\theta_{max}$  as shown in Fig. 2.6.

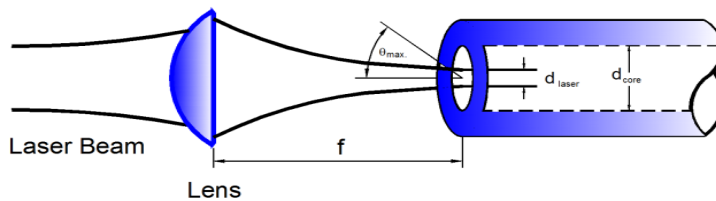


**Fig. 2.6.** Schematic of the fiber input end with coupling lens.

The sine of the acceptance angle is related with the numerical aperture (NA) of the fiber and is given by  $\theta_{\max}=\sin^{-1}(\text{NA})$ . The laser beam quality obtained in our lasers was adequate to ensure efficient coupling of 1 kW, 500 W and 250 W long pulse Nd:YAG laser beams to the 600, 400 and 200  $\mu\text{m}$  core diameter fiber respectively. Because as we increases the pump power of laser rod for higher output power exit, the laser beam quality degrades due to higher value of thermal focal power of the rod and its difficult to couple high power laser beam in to smaller core optical fiber (Eq. 2.7). The measured power transmission efficiency of this fiber coupling is as high as 90%. These optical fibers are step index type having a value of numerical aperture of 0.22. For the fiber coupling in 600 and 400  $\mu\text{m}$  core diameter fiber, fused silica plano-convex lens of focal length 35 mm is used in our experiment. In case of standard spherical lenses, due to the spherical aberrations, tight focusing of laser beam is difficult. As a result, the coupling efficiency is reduced. Further, it is difficult to launch high power laser beams through smaller core diameter optical fibers due to coupling of light in cladding region and hence damage of outer coating and jacket. To overcome this issue, for the efficient and damage free coupling of high power laser beam in small core diameter (200  $\mu\text{m}$ ) optical fiber, GRADIUM lens (manufactured by Light Path Technologies, USA) were used in place of standard spherical fused silica lenses.

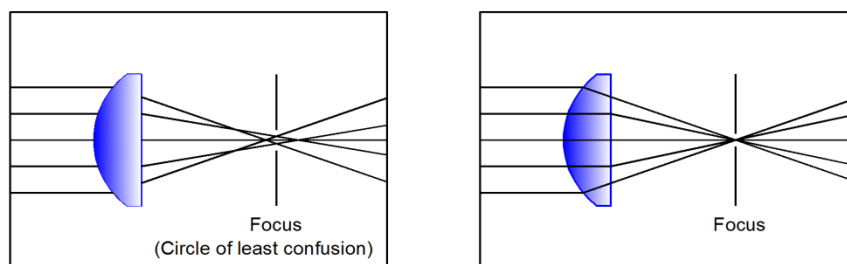


**Fig. 2.7.** Schematic of focusing by (a) standard fused silica (b) GRADIUM lens.

The GRADIUM lenses are made from axial gradient index glass and reduce spherical aberrations as well as focal spot diameter as compared to the fused silica lens shown schematically in Fig. 2.7. The material of GRADIUM lens is doped with lead oxide. The lead oxide concentration varies within the glass to create a smoothly variable refractive index gradient between 1.65 and 1.8 across the profile and thus corrects the spherical aberrations. The large range in  $\Delta n$  provides a substantial ability to correct aberrations, especially spherical. In our experiment, for the fiber coupling of 250 W average power laser beam a GRADIUM lens of 22 mm focal length and 12.5 mm diameter have been used. The optical fiber was a step index type with 200  $\mu\text{m}$  core diameter and 0.22 NA. The optical fiber input and output end face was prepared using a multimode fiber cleaver (Vytran, USA) to avoid damage of the fiber end face at high pulse energies. The input end of the optical fiber was held in a water cooled fiber holder mount having alignment facilities in  $x$ ,  $y$  and  $z$  direction, as shown in Fig. 2.8.

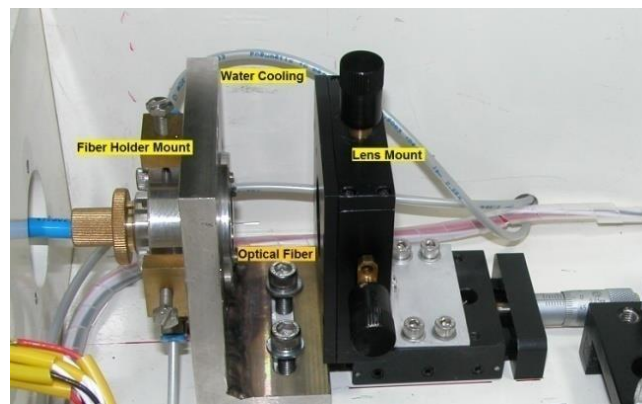


**Fig. 2.8.** A view of the input end optical fiber holder and lens mount.

Two such optical fibers were used in two separate fiber holders for the beam delivery on time-sharing basis. In industry, it is often required to carry out different material processing applications at various locations or workstations. For example, at one workstation it may be required to go for profile cutting on a CNC table and at another for spot welding. In such

applications, a single laser system with two or more time-shared fiber optic ports is highly useful and economical. Just by switching the laser beam to different fiber ports, different applications can be easily performed without changing the material processing nozzle or using another laser system. Time-shared fiber optic beam delivery in many commercial laser systems uses either mirror rotation to switch the beam to different fiber ports or a manual plug-in and pre-aligned technique for port selection [44,45]. Mirror rotation technique requires a precise control on angular movement of mirror and accuracy in positioning the mirror for port selection. We have developed a simple electronically controlled fiber port selection method, which does not require precision motors for mirror positioning and costly optics.

A beam alignment system, consisting of a kinematic mount and bending mirror holder is designed for the time-sharing operation. The design ensures that the alignment of mirror for best coupling of the laser beam with the fiber and does not change even after repetitive removal and replacement of the kinematic mount. The electronic control for fiber port selection consists of a mechanical slide on which a  $45^{\circ}$  bending mirror has been mounted. These mechanical slide is rigidly fixed on a laser head base as shown in Fig. 2.9. The schematic of 250 W average power Nd:YAG laser system with time shared fiber optic beam delivery using  $45^{\circ}$  bending mirror is shown in Fig. 2.10.

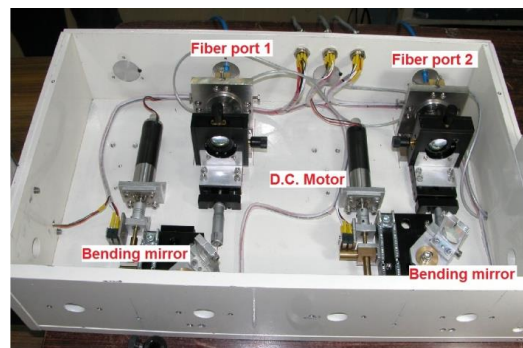


**Fig. 2.9.** A view of two port motorized time shared fiber port selection mechanism.

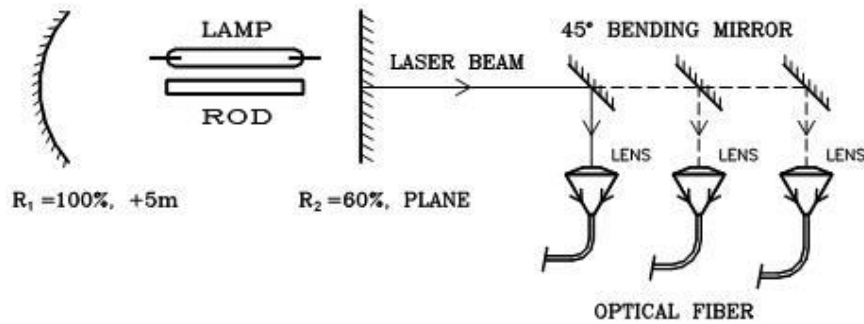


**Fig. 2.10.** Schematic of Nd:YAG laser with time shared fiber optic beam delivery.

A DC motor is used to move the slide in forward and reverse directions as shown in Fig. 2.9. Linear slide has a straight-line accuracy of  $10\ \mu\text{m}$  with a repeatability of  $2\ \mu\text{m}$ . Roller bearing of linear slide moves in a double V-groove to achieve high accuracy both in the linear and angular movements. At the time of port selection, a shutter automatically blocks the beam path in the resonator for safety and as soon as the port is selected, it can be opened to allow the beam. Total time for positioning of any of the mirrors in the beam path is 30 s. The stability of the alignment of different time-shared fiber optic ports was recorded by switching the laser beam to different ports for a number of times and measuring the output at the exit fiber end. It was found that power stability between different fiber ports was better than 1.5% indicating reliable switching between the fiber ports. For the comparison of the performance and reliability of the different time-shared fiber optics ports, some material processing experiments was also performed. This motorized port selection technique is highly useful in remote operations, at different locations, when the laser is kept far away from the workstations.

## 2.5 Results and discussion

### 2.5.1 250 W average power laser

In this section, we will discuss the experimental results for the development of long pulse Nd:YAG lasers of different average power levels. Fig. 2.11 shows a view of 250 W average power pulsed Nd:YAG laser system using a single Nd:YAG rod and single flash lamp. The performance of this 250 W average power laser was evaluated with and without samarium spectral filter between the rod and lamp. It was observed that, without samarium filter the measured thermal lens power was 0.4 Dioptre/kW and with samarium spectral filter, the measured thermal lens power was reduced to 0.34 Dioptre/kW which is better for improving the laser beam quality. For the whole range of input pump power (from 0- 5 kW) the resonator remains within the stability region. The power of thermal lens of laser rod changes from 0 to 1.7 Diopter in this pumping range.



**Fig. 2.11.** A view of 250 W average power laser system with two time shared fiber optic port for beam delivery.

The pulsed power supply used to pump the flash lamp is able to provide a maximum average electrical input power of 5 kW with a temporary rectangular current pulse in the range 50-300 Amp, pulse duration in the range 1-20 ms and repetition rate in the range 1-200 Hz. Electrical

input pump energy to the flash lamp is given by  $E_{elec}=K_0I^{3/2}t_p$ , where  $K_0=18$  is flash lamp constant,  $I$  is electrical current and  $t_p$  is pulse duration. Three different resonator configurations were studied with the same fundamental mode spot size of 0.55 mm within the rod in each case and hence the same expected beam quality. The three studied cases are as below:

**Case1:**  $R_1=3m$ ,  $R_2=\infty$ ,  $d_1=55$  cm,  $d_2=13.5$  cm, with passive resonator g-values  $g_1=0.817$ ,  $g_2=1$

**Case2:**  $R_1=5m$ ,  $R_2=\infty$ ,  $d_1=50$  cm,  $d_2=13.5$  cm, with passive resonator g-values  $g_1=0.9$ ,  $g_2=1$

**Case3:**  $R_1=\infty$ ,  $R_2=\infty$ ,  $d_1=45$  cm,  $d_2=38$  cm, with passive resonator g-values  $g_1=1$ ,  $g_2=1$

Table 2.2 shows the pulse-to-pulse stability and output laser energy for all the three cases with different electrical input pump energy. The output laser energy and pulse-to-pulse energy stability were measured using a pyro-electric energy meter and a display, which is able to hold data for 500 pulses.

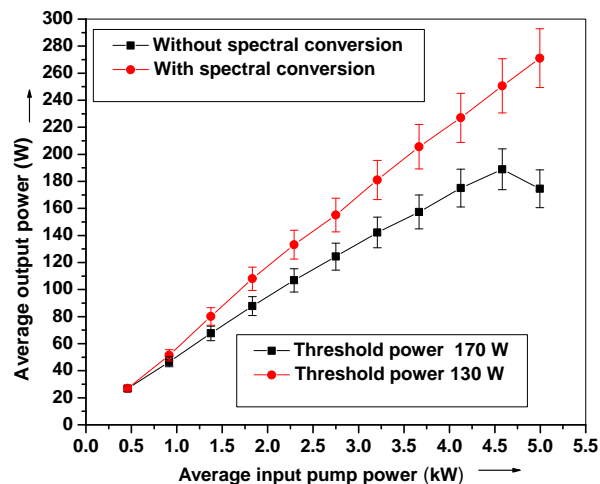
**Table 2.2:** Pulse-to-pulse stability (energy stability) according to Eq. 2.8 and average output pulse energy for different configuration of resonator of 250 W average power Nd:YAG laser.

Sr. no.	Electrical input pump parameters	Parameter	Case 1	Case 2	Case 3
1	200 A, 2 ms, 1 Hz (102J)	Output pulse energy	5.85 J	4.97 J	3.45 J
		Energy stability	3.36%	4.20%	13.4%
2	300 A, 2 ms, 1 Hz (187J)	Output pulse energy	10.05 J	9.65 J	7.77 J
		Energy stability	3.74%	6.06%	18.95%
3	200 A, 9 ms, 1 Hz (458 J)	Output pulse energy	28.5 J	27 J	26.5 J
		Energy stability	4.45%	6.13%	8.68%
4	300 A, 9 ms, 1 Hz (842J)	Output pulse energy	49.5 J	49 J	46.7 J
		Energy stability	3.22%	4.32%	9.80%

It is observed from the Table 2.2 that the laser pulse energy and pulse-to-pulse stability is best in case 1 (hemispherical configuration) and worst in case 3 (plane-plane symmetric configuration). It is expected because stability points in the gstability diagramme lie near the marginal stable region in the plane-plane resonator as compared to hemispherical resonator [7]. Hence, hemispherical resonator configuration with one curved mirror is preferred for the single rod resonator in place of plane-plane symmetric resonator for better pulse-to-pulse stability.

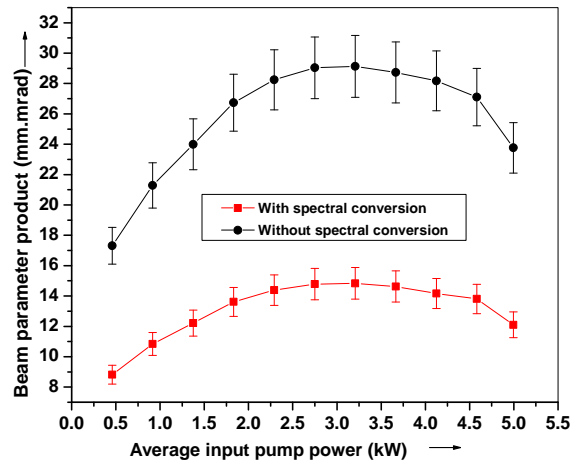
Thus, for the material processing applications of 250 W average power laser, where pulse-to-pulse energy stability is important, the resonator design should ensure that its stability point is well within the stable region in the hemispherical resonator [46,47].

Fig 2.12 shows a comparison of average laser output power with and without spectral conversion of lamp radiation using samarium filter for 250 W lasers. In case of spectral conversion (with samarium filter), the output power increases linearly with pump power up to the maximum available pump power of 5 kW. A maximum average output power of 270 W has been achieved without any drop in average output power with increase in pump power. The threshold average input pump power was 130 W in this case. However, in the absence of a samarium filter (no spectral conversion) a drop in the output power is observed beyond an average output power of 174 W indicating that in this case, the resonator reaches its limit of stability earlier due to higher thermal load. The threshold average input pump power in this case is 170 W. Composite effect of spectral conversion of flash lamp radiation and water flow optimization resulted in an improved beam quality from 30 mm.mrad to 15 mm.mrad.



**Fig. 2.12.** Average output power as a function of average input pump power for single rod 250 W laser.

Fig. 2.13 shows a variation of the measured beam parameter product with an increase in the input pump power. The Beam Parameter Product (BPP) is maximum and the beam quality is poorest at an input pump power of about 3 kW, and then the BPP is decreasing on both sides of this input pump power. With this beam quality, the laser output beam has been transmitted efficiently and reliably through a 150 m long 400  $\mu\text{m}$  core dia optical fiber of 0.22 NA with a transmission efficiency of more than 90% for the whole range of pump power. The 10% loss in the transmission may be accounted for 4% Fresnel reflection losses from each fiber end and about 2% as attenuation and coupling loss through a long fiber.



**Fig. 2.13.** Variation of BPP as a function of average input pump power.

For laser material processing applications, at the fiber exit end the laser beam is first collimated using a plano-convex lens and is then focused using another lens with a desired imaging ratio. The focused spot size on the job depends on the imaging ratio, i.e., the ratio of focal lengths of the collimating and the focusing lenses. We have designed focusing objectives at the exit fiber end of various diameters in the range of 40 mm to 12 mm and various imaging ratios in the range 1:3 to 1:0.5 depending on the desired application and focused spot size. Using

this 250 W average power laser system, cutting of ~14 mm thick stainless steel (SS) sheets and welding of SS with a weld depth of penetration up to 2 mm has been achieved [48].

### 2.5.2 500 W average power laser

Fig. 2.14 shows a table-top view of 500 W average power pulsed Nd:YAG laser system having two ceramic reflector based laser pump chambers in the laser resonator. Table 2.3 shows theoretically calculated values of thermal focal length of Nd:YAG laser rod (diameter 8 mm  $\times$  length 150 mm).



**Fig. 2.14.** A view of 500 W average power laser system and experimental set-up (left) and ceramic reflector (right).

A comparison of experimentally measured values of thermal focal length of Nd:YAG rod for different values of input pump power with ceramic and gold coated elliptical reflector is also shown in the Table 2.3 [49]. For the 500 W average power Nd:YAG laser, the measured values of the thermal focal length of Nd:YAG rod with gold coated reflector was found to be lower than that with the ceramic reflector. Difference in thermal focal length is due to the difference in pumping geometry for the gold-coated and ceramic reflectors. Due to the specular reflection from gold-coated elliptical reflector, optical pumping of Nd:YAG rod becomes non-uniform, which causes a slight decrease in its thermal focal length. On the other hand, with diffuse

ceramic reflector, optical pumping is uniform due to diffuse reflection results in slightly higher value of thermal focal length.

**Table 2.3:** Calculated and measured values of thermal focal length for gold-coated and ceramic reflector based Nd:YAG rod ( $\phi$  8 mm  $\times$  150 mm) for different input pump power .

Input pump power (kW)	Calculated values (meter)	Measured thermal focal length of 1.1% at. doped Nd:YAG rod	
		With gold-coated reflector(meter)	With ceramic reflector(meter)
0.5	6.34	6.42	6.56
1.0	3.58	3.69	3.78
1.5	1.36	1.54	1.62
2.0	0.69	0.82	0.93
2.5	0.52	0.60	0.71
3.0	0.37	0.49	0.59
3.5	0.32	0.41	0.49
4.0	0.29	0.34	0.40
4.5	0.24	0.30	0.36
5.0	0.22	0.27	0.32

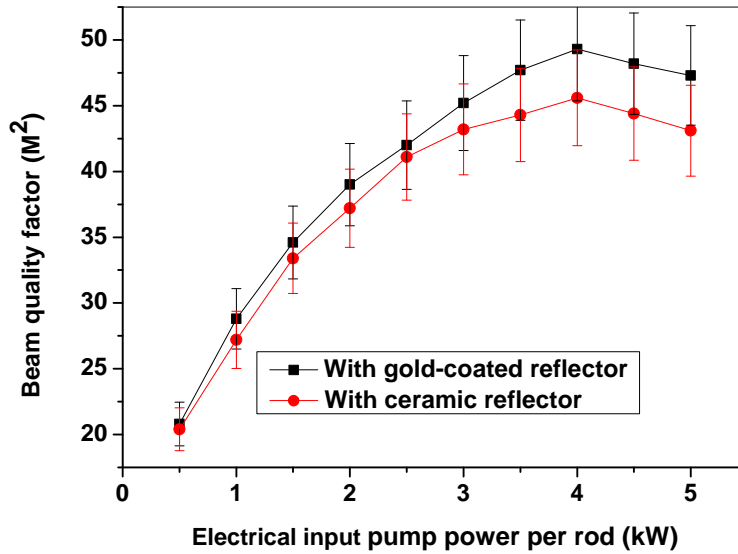


**Fig. 2.15.** Variation of  $M^2$  as a function of input pump power for gold and ceramic reflector based 500 W average power Nd:YAG laser.

Fig. 2.15 shows a variation of beam quality factor  $M^2$  as a function of input pump power for ceramic and gold-coated reflector. It is clear that the value of  $M^2$  is improved with ceramic reflector, because of lower value of thermal refractive power of laser rod with ceramic reflector. Hence, the value of fundamental mode spot size is higher with ceramic reflector as compared to that for gold-coated elliptical reflector. As we have discussed earlier, a lower value of the  $M^2$  corresponds to a better beam quality of the laser in multi mode operation. For 500 W average powers, the maximum measured value of  $M^2$  was 52 in our experiment for gold-coated reflector, which improved to a value of 45 for ceramic reflector. In addition, laser beam profile measurement using a CCD camera (Wincam-D, Gentec) at the maximum input pump power (10 kW) shows that the beam profile of Nd:YAG laser with ceramic reflectors is smoother compared to the beam profile obtained using gold-coated elliptical reflector as shown in the Fig. 2.16. This can be explained by the fact that the distribution of absorbed pump power is more uniform in case of ceramic reflectors as compared to the gold-coated reflector since in case of gold-coated reflectors hot spots may be generated due to the specular reflection.

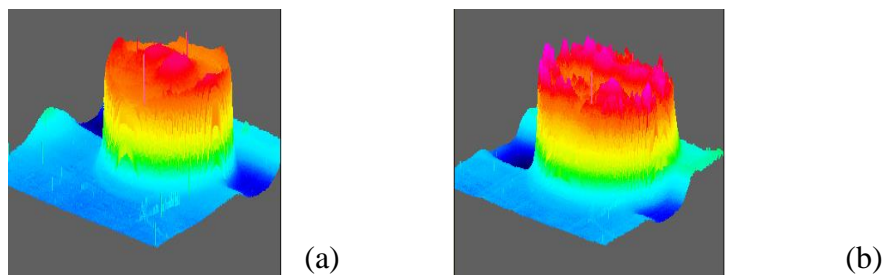


**Fig. 2.16.** 3D view of laser beam profile (a) ceramic reflector based Nd:YAG laser shows smoother profile (b) gold-coated elliptical reflector based Nd:YAG laser shows some peaks.

Figure 2.17 show variation of average laser output power as a function of electrical input pump power for the ceramic and gold-coated reflector based 500 W average power Nd:YAG lasers in the dual rod plane-plane symmetric resonator configurations. It shows that the average

output power and efficiency was slightly higher for the ceramic reflector as compared to gold-coated reflector. This is due to the fact that the gain of the laser medium is slightly higher with ceramic reflectors due to the uniform pumping and the threshold of laser was also reduced slightly. A maximum average output power of 500 W has been achieved with 5.14% slope efficiency for 10 kW average electrical input pump power (5 kW in each rod) in case of ceramic reflector based Nd:YAG laser. The threshold input average pump power was 144 W. Whereas, in case of gold coated elliptical reflector based Nd:YAG laser, a maximum average output power of 478 W was achieved for the same average electrical input pump power with a slope efficiency of 4.85%. The threshold input average pump power was 272 W.

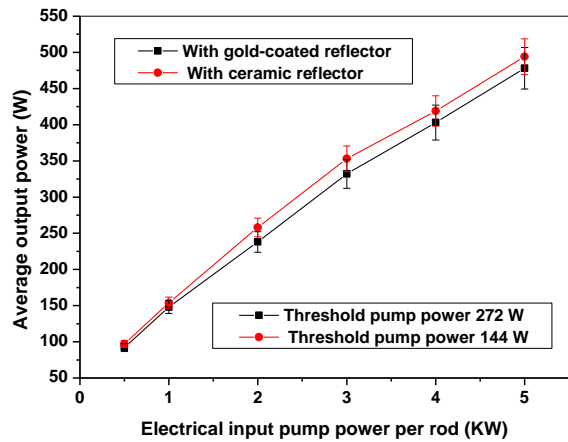


**Fig. 2.17.** Variation of average output power with average input pump power for ceramic and gold coated reflector based Nd:YAG lasers.

Further, we have compared two different water-cooling schemes in ceramic reflector based laser pump chambers as shown in Fig. 2.18. In scheme A, water flows through the rod and the flash lamp simultaneously in the pump chamber. In scheme B, water first cools the flash lamp and then goes through the rod in series. The flow pattern was made U-shaped in scheme B and it was found to cool both lamp and rod more effectively as compared to scheme A.

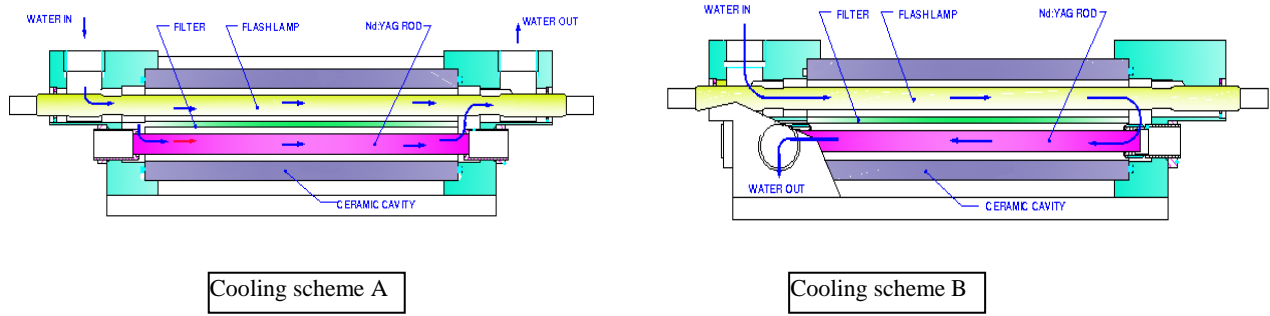


**Fig. 2.18.** Two different cooling schemes of ceramic reflector based Nd:YAG laser.

Figure 2.19 shows that because of better cooling rate in scheme B, average output power increases almost linearly with the input pump power without experiencing any drop in power as compared to scheme A, where cooling was not effective at higher pump power. Better cooling rate in scheme B is due to higher water flow rate over the laser rod, resulting in better heat removal. In scheme A the threshold input average pump power was 294 W and in scheme B the threshold input average pump power was 272 W.

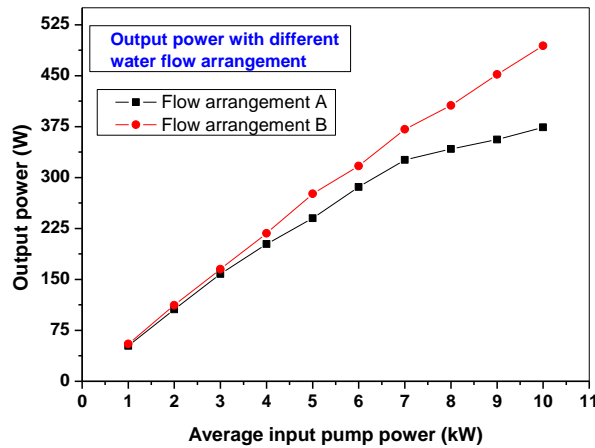


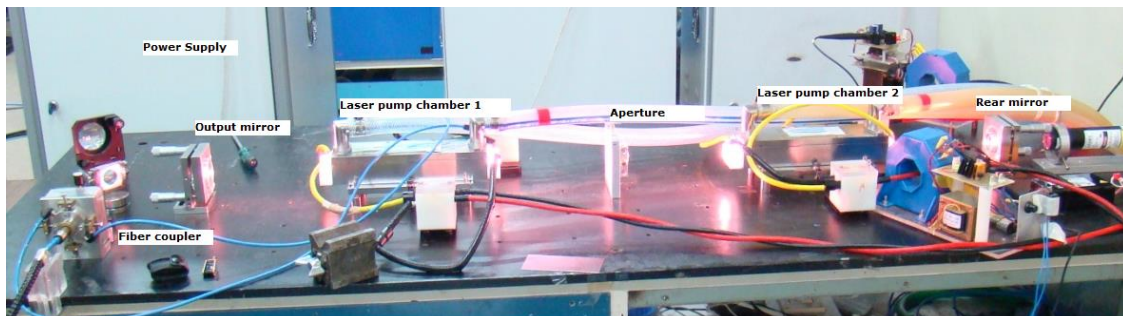
**Fig. 2.19.** Output power variation with input power for ceramic reflector in scheme A & B.

Output laser beam of the 500 W average power laser system was efficiently and reliably coupled through an optical fiber of 150 m length, 400  $\mu\text{m}$  core diameters and 0.22 NA, with a

transmission efficiency of more than 90% for the whole range of pump power. The ceramic reflector based laser is found highly suitable for material processing applications. Some of the potential applications of this 500 W average power laser are cutting of thick section stainless steel for the automotive, nuclear, shipping and heavy machinery industries.

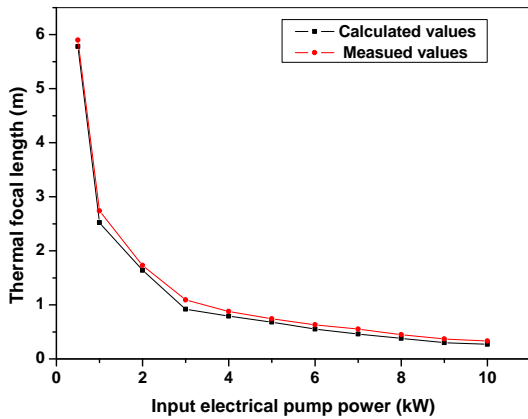
### 2.5.3 1 kW average power laser

Figure 2.20 shows a table-top view of 1 kW average power pulsed Nd:YAG laser system and Figure 2.21 shows variation of thermal focal length of the Nd:YAG laser rod (diameter 10 mm  $\times$  length 150 mm) as a function of input pump power up to 10 kW pump power for this laser.



**Fig. 2.20.** A table-top view of 1 kW average power pulsed Nd:YAG laser system.

It is found that the experimentally measured value of the thermal focal length of Nd:YAG rod is slightly higher than the calculated value. This may be due to the use of samarium filter flow tube on the rod, which reduces the effective heat load in the rod by cutting-off UV radiation from the flash lamp.



**Fig. 2.21.** Variation of measured and calculated thermal focal length ( $f$ ) with variation in average input pump power for the Nd:YAG rod.

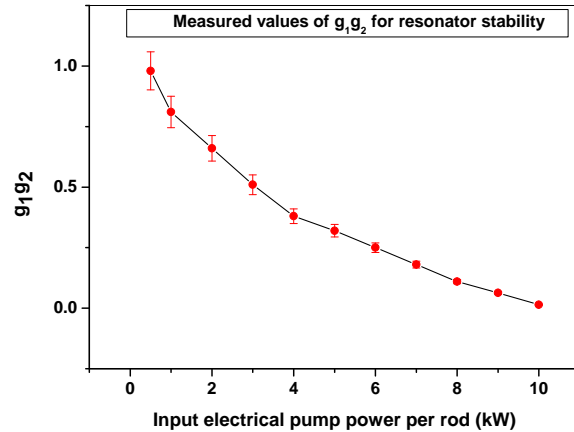


**Fig. 2.22.** Variation of  $g_1g_2$ -parameter of the resonator with variation in average electrical input pump power showing stability of resonator.

The beam quality factor  $M^2$  was measured for the maximum pump power of 10 kW per rod, and its value was  $M^2 \sim 91$  for the multimode operation. This value of the beam quality was suitable for laser beam delivery through a 600  $\mu\text{m}$  core diameter and 0.22 numerical aperture optical fiber for the entire range of pump power. Figure 2.22 shows a plot of the values of  $g_1g_2$  calculated from the ABCD round trip matrix using the measured values of thermal focal length  $f$  for different values of electrical input pump power. It shows that the resonator remains stable for a wide range of the average electrical input pump power from 0-10 kW in each rod.

The average output power of dual rod Nd:YAG laser system was measured for different values of heat transfer coefficient  $h$  as shown in Fig. 2.23. Heat transfer coefficient ( $h$ ) was varied by increasing the coolant water flow rate in the range of 20 - 50  $l/m$ . At the lower value of water flow of 20  $l/m$  providing  $h=1.61 \text{ W/cm}^2 \text{ } ^\circ\text{K}$ , the variation of laser output power did not remain linear at higher input pump power due to inefficient heat removal from the laser rod. Whereas, for the higher value of water flow rate of 50  $l/m$  providing  $h=3.35 \text{ W/cm}^2 \text{ } ^\circ\text{K}$ , the laser output

power varies almost linearly with input pump power. It indicates better heat load removal at these values of water flow rate. This flow rate was found to be optimum and safe for the operations of the laser. However, at higher flow rates of water beyond the optimum value, erosion of gold coating of elliptical reflectors was observed.

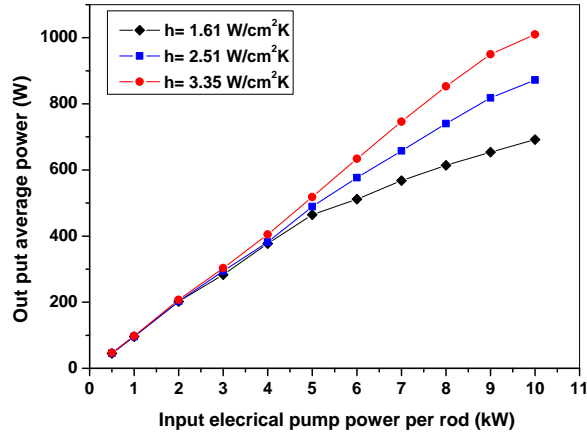
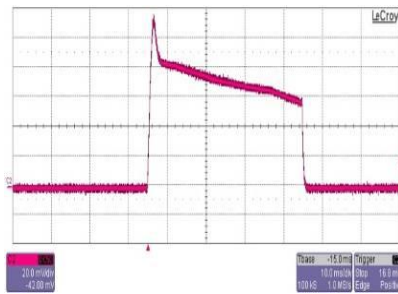
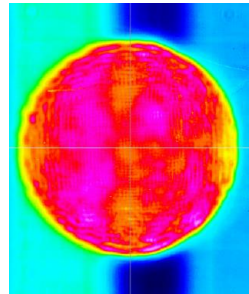


**Fig. 2.23.** Variation of average output power with average input pump power for different values of heat transfer coefficients ( $h$ ) for dual rod Nd:YAG laser resonator.



(a)



(b)

**Fig. 2.24.** (a) Temporal evolution of the laser beam (b) Spatial profile of the laser beam.

Figures 2.24 (a) and (b) show the typical temporal evolution, and spatial profile of the laser beam at the maximum average input pump power of 10 kW. The temporal evolution of the laser was measured at 40 ms pulse duration using a broadband photodiode (New focus make) with an RG 850 filter (Coherent make), and a 1 GHz oscilloscope (Lecroy make). On the other hand, the spatial laser beam profile was measured at maximum pump power using a CCD camera (Wincam-D, Gentec).

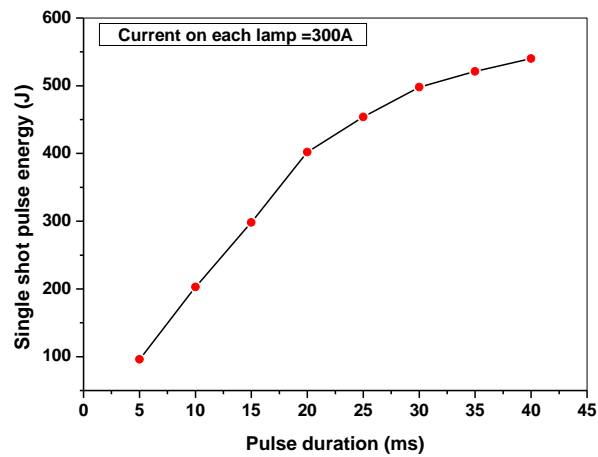


**Fig. 2.25.** Variation of single shot pulse energy with pulse duration at 300 A of flash lamp current.

Figure 2.25 shows variation of single shot pulse energy for the dual rod symmetric laser resonator, which shows a linear variation of pulse energy up to a pulse duration of ~22 ms with a some drop in the linearity for longer pulse durations (up to 40 ms). A maximum pulse energy of 540 J was achieved at 40 ms pulse duration [50]. Further, pulse energy of 402 J was measured at 20 ms pulse duration, which is equivalent to 20 kW peak power. This peak power is highly suitable for laser welding applications. The marginal saturation in pulse energy for pulses which are longer than ~22 ms is due to the fact that at higher average input pump power and higher

pulse duration, the resonator stability point moves to the boundary of the stability diagram and reaches close to marginally stable points. In this case some higher order modes filter out from the resonator, resulting in reduction in the single shot pulse energy for longer pulses ( $> 22$  ms).

Maximum average pump power to each lamp is 5 kW and each lamp has been pumped by 3740 J of maximum pulse energy in 40 ms duration to achieve 540 J of laser pulse energy in a single pulse. This corresponds to the operation of this laser at 1.4 Hz of repetition rate at the maximum pulse energy of 540 J with 40 ms pulse duration. The slope efficiency for the average power of up to 1 kW with pulse duration up to 20 ms is 5.4% (Fig. 2.25) and reduces slightly for pulses larger than 20 ms pulse duration due to filtering of higher order modes as explained earlier. Pulse-to-pulse stability was also measured for 1000 pulses and it was found that the pulse-to-pulse stability is better than  $\pm 3\%$  for maximum output pulse energy of 540 J.

Some of the potential applications of this 1 kW average power system are the laser welding of titanium and aluminium for the automotive, nuclear, aerospace, and vacuum components industries. Using this laser system, 4 mm deep penetration welding has been performed in titanium and aluminium under optimized conditions of output power, pulse energy, and pulse duration. Laser drilling in rocks is also performed with this 1 kW average power laser system that we will discuss in detail later in Chapter 6.

## **2.6 Conclusions**

In conclusion, design, fabrication and demonstration of highly efficient long pulse Nd:YAG lasers of 1 kW, 500 W, and 250 W average powers have been carried out. Improvement in laser beam quality and slope efficiency by appropriate design of the laser pump chamber and resonator with a slope efficiency of more than 5% was also achieved. This

efficiency is one of the highest achieved efficiency for lamp pumped Nd:YAG lasers operated in the long pulse duration regime. The laser beams have been efficiently transmitted through a 0.22 NA silica-silica optical fiber with a transmission efficiency of more than 90% in the whole range of operation. A simple motorized fiber port selection technique has also been developed for material processing using several time-shared work stations. This long pulse Nd:YAG laser can be effectively used for material processing applications such as cutting of thick section of stainless steel and deep penetration welding of titanium, aluminium and stainless steel.

# Chapter 3

---

## Performance study of ceramic Nd:YAG rod for generation of long pulse and high average power laser output

### 3.1 Introduction

Importance of high average power millisecond (ms) pulse duration Nd:YAG lasers in various industrial and scientific applications [2,50-53] has already been discussed in Chapter 2. In these lasers, single crystal Nd:YAG rods are the most widely used laser material. However, single crystal Nd:YAG rods are grown by conventional Czochralski (Cz) method and has its own insurmountable disadvantages such as expensive and time-consuming crystal growth process, limited size, and low doping concentration of Nd<sup>3+</sup>-ions [7]. Although, it is easy to fabricate large size of Nd:Glass with high concentration, but its thermal conductivity and gain is quite poor and hence laser efficiency is not satisfactory compared to single crystal Nd:YAG for CW or high repetition rate pulse operation. Novel ceramic Nd:YAG material combines the advantages of single crystals and glasses. Ceramic rods have good thermal, mechanical, and spectral properties (like crystalline laser materials) and can be made in large sizes with high doping concentrations (like laser glasses) [54].

However, the major advantage of ceramics over single-crystals is its simple fabrication process. To grow single crystals, the process is complicated and slow at melting temperatures

above 2000°C. Further, it can take several weeks to grow single-crystals by melting the raw materials and their growth requires expensive iridium crucibles. For ceramics, it is usually only necessary to heat up the raw materials to two thirds of the melting temperature. Further, single crystals also suffer from limited doping concentration and composition, whereas powder based processing technique for ceramic provides higher flexibility in doping concentration and composition. Thus, in comparison with single crystal Nd:YAG, these ceramic Nd:YAG laser material has several advantages, such as: (1) Ease of fabrication; (2) Less expensive; (3) Fabrication of large size and high neodymium concentration; (4) Multi-layer and multi-functional ceramic structure; (5) Mass production, etc.

In view of these advantages, polycrystalline Nd:YAG ceramic lasers have received much attention recently as the quality of Nd:YAG ceramics has been improved greatly and highly efficient laser oscillation seems to be easily possible. Thus, highly doped ceramic Nd:YAG rods appear to be a better option to replace single crystal Nd:YAG rods, if one can generate higher pulse energies (~100 J) with higher peak power (~few kW) in long pulse laser operation. Under normal operating conditions at room temperature, Nd:YAG laser generates 1064 nm of emission wavelength using strongest transition of  ${}^4F_{3/2} \rightarrow {}^4I_{11/2}$ . However, direct absorption to the upper laser level of  ${}^4F_{3/2}$  is weak as compared to higher level of  ${}^4F_{5/2}$  [7]. The parasitic quantum defect between the  ${}^4F_{5/2}$  and  ${}^4F_{3/2}$  level is of the order of  $900\text{ cm}^{-1}$  and it contributes to the reduction in performance of single crystal Nd:YAG materials [54]. Weak absorption of  ${}^4F_{3/2}$  level is due to low doping concentration (~1%) of  $\text{Nd}^{3+}$ -ions by substituting  $\text{Yb}^{3+}$ -ions. As the radii of two rare earth ions differ by ~3%, increase in doping concentration of  $\text{Nd}^{3+}$ -ion results in strained crystals with distortion in crystal lattice. Hence, increase in doping concentration of  $\text{Nd}^{3+}$ -ions in single crystals is avoided [7]. In contrast, Nd:YAG ceramics can have high doping concentration of

$\text{Nd}^{3+}$  ions and a reduction in pump quantum defect with direct transition  $Z_1 \rightarrow R_2$ , and hot-band direct pump transitions  $Z_2 \rightarrow R_1$  and  $Z_3 \rightarrow R_2$  in  ${}^4I_{9/2} \rightarrow {}^4F_{3/2}$  transition is possible. These absorption transitions are indicated as (b), and (c) in the energy level diagram of Nd:YAG ceramic shown in Fig. 3.1 [8]. Absorption transition (a) indicates transition to higher energy level  ${}^4F_{5/2}$ .

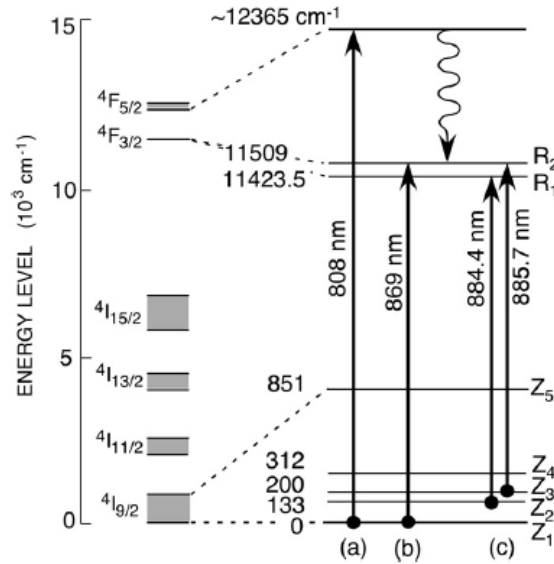


**Fig. 3.1.** Energy level diagram of Nd:YAG ceramic showing (a) conventional, (b) direct, and (c) hot-band direct pump transitions [8].

Fig. 3.2 shows a comparison of the absorption spectra in the wavelength range of 780 to 840 nm for a Nd:YAG single crystal with 1 at.% and ceramic Nd:YAG rod with 4.8 at.% doping [55]. The absorption coefficient of 4.8 at.% ceramic Nd:YAG is 4.8 times higher as compared to the 1 at.% single crystal Nd:YAG because of higher doping of  $\text{Nd}^{3+}$ -ions. Emission spectra of 1 at.% and 6.6 at.% ceramic Nd:YAG rods are similar to that of a 1 at.% Nd:YAG single crystal, as observed by Shoji *et al.* and is shown in Fig. 3.3 [56]. It indicates that ceramic Nd:YAG is a promising laser material to replace single crystal for the development of high power Nd:YAG lasers using either lamp or diode pumping.

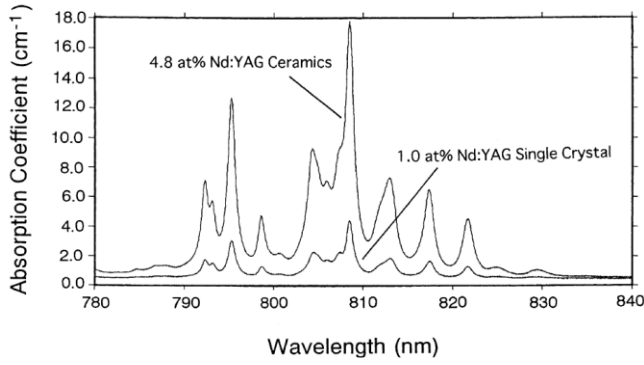


**Fig. 3.2.** Absorption spectra for 1 at.% single crystal Nd:YAG and 4.8 at.% ceramic Nd:YAG in the range of 780 nm to 840 nm [55].

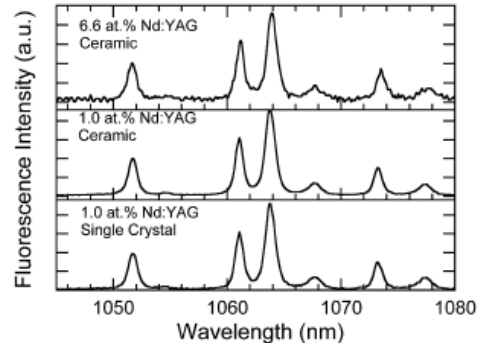


**Fig. 3.3.** A comparison of emission spectra of 1 at.% single crystal Nd:YAG and 6.6 at.% ceramic Nd:YAG in the range of 1050 nm and 1080 nm [56].

In the case of lamp pumped ceramic Nd:YAG lasers, removal of heat load from laser material is an important issue. Heat generation in flash lamp pumped laser rod is characterized by the fraction of absorbed pump power transformed into heat by non-radiative processes [7]. Optical pumping in levels above the emitting level induces a parasitic upper quantum defect between the pump energy levels and the emitting laser level, which is transformed completely into heat. If the heat load is not removed efficiently, temperature as well as the gradient of temperature in the lasing medium may rise and degrade the laser output power, efficiency, and beam quality. From the point of view of power scaling, solid-state laser medium should have high thermal conductivity and good tensile strength. Thermally induced rupture or catastrophic failure is then the primary limiting factor for the attainment of higher average power in solid-state laser material. In typical side pumped rod-type lasers, the maximum extractable power ( $P_{ex}$ ) available is given by  $P_{ex} \leq (8\pi R_T L)/\chi$ , where  $L$  is the rod length and  $\chi$  is the heating parameter defined as heat deposited per unit of stored energy [57]. It is clear that the maximum extractable power is directly proportional to the thermal shock parameter  $R_T$ , which is roughly proportional

to  $k/L\alpha^2$  ( $L\alpha$  is the thermal expansion coefficient). The value of thermal conductivity  $k$  for ceramic Nd:YAG (9 W/m<sup>0</sup>K for 6.6 at.% Nd doped) is close to the value for a single crystal Nd:YAG (10.4 W/m<sup>0</sup>K for 1 at.% Nd doped) [58].

In 1990, Sekita reported the optical properties of Nd-doped YAG ceramics fabricated by a urea precipitation method [59]. Optical properties of the YAG ceramic were almost the same as that of single crystals grown by Cz method, except for higher background absorption of 2.5-3 cm<sup>-1</sup>. The breakthrough happened in 1995, when Ikesue *et al.* [60] fabricated a highly transparent neodymium doped YAG ceramic for the first time with a solid-state reaction method. CW lasing was demonstrated in this ceramic Nd:YAG rod using a diode laser as a pump source. Laser output of ~70 mW was obtained with a slope efficiency of ~28%. This was the first laser demonstration using ceramic Nd:YAG.

In 1999, Yanagitani *et al.*[61] fabricated high quality and highly transparent ceramic laser materials using a vacuum-sintering method. Its absorption spectrum, emission spectrum and fluorescence lifetime were almost identical to the single-crystal Nd:YAG. Using this ceramic material, an output power of 357 mW was obtained with a slope efficiency of 53% using diode laser pumping, which was almost at the same level as that from single crystal Nd:YAG with a slope efficiency of 54.5%. In 2002, Lu *et al.*[62] demonstrated generation of 1.46 kW of CW output power using diode pumping of ceramic Nd:YAG rods. Since then, a tremendous amount of efforts have been made to realize high power ceramic Nd:YAG lasers suitable for various industrial and defense applications. Further, Heller *et al.*[63] demonstrated the generation of 67 kW of output power from ceramic Nd:YAG laser at Lawrence Livermore National Laboratory. Bishop *et al.*[64] demonstrated the generation of 100 kW of output power from ceramic Nd:YAG laser. However, these lasers were operated in heat capacity mode. Recently, Liu *et al.*

have generated 2.44 kW of CW output power using diode pumping in ceramic Nd:YAG disc [65]. A detailed review of ceramic laser materials has been found in references [26, 66-68]. Most of the reports on high power ceramic Nd:YAG lasers are based on diode pumping. In 2006, Yagi *et al.* [35] reported the generation of 386 W average power from lamp pumped ceramic Nd:YAG laser at an input average power of 16.4 kW with a maximum slope efficiency of 2.3%. This laser was operated with 5 ms pulse duration and up to 20 Hz repetition rate. They have used a 10 mm diameter and 152 mm long 1.1% doped ceramic Nd:YAG rod and a Xe-filled flash lamp placed in a laser pump chamber with gold coated elliptical reflectors and samarium doped flow tube. The reason for poor slope efficiency in their design seems to be the use of Xe flash lamp for pumping in place of Kr flash lamp and higher heat load due to high pumping of a single rod.

Long pulse (several tens of ms duration) and high peak power Nd:YAG lasers still depend on flash lamp pumping in place of diode laser pumping [19]. Further, flash lamp pumped lasers are more rugged and cost effective than the diode pumped lasers. Hence, lamp pumped long pulse duration Nd:YAG laser systems are still important in the present scenario for various material processing applications. The aim of this work has the following objectives: (1) to develop a lamp pumped long pulse ceramic Nd:YAG rod based laser, (2) to compare the performance of ceramic laser with single crystal laser in terms of slope efficiency, output average power, and beam quality. We have generated 520 W of average output power at an average input pump power of 10 kW using two numbers of 2 at.% doped ceramic Nd:YAG rods of size (10 mm × 152 mm) and Krypton filled flash lamps with a slope efficiency 5.4% and a beam parameter product of 16 mm.mrad ( $M^2 \sim 47$ ). This laser has been operated with pulse duration in the range of 2-20 ms and repetition rate in the range of 1-100 Hz. The laser beam was efficiently delivered through a 400  $\mu\text{m}$  diameter optical fiber. A comparison was also made

between the performance of ceramic and single crystal Nd:YAG rod of the same size. It was found that these two types of laser rods provide almost similar laser output power in long pulse operation at the same electrical pump power to flash lamps. To the best of our knowledge, this is the highest average power, pulse energy, and efficiency in long pulse operation of flash lamp-pumped ceramic Nd:YAG lasers. The potential applications of this laser include laser cutting and welding of metals for the automotive, nuclear, shipping, and heavy machinery industries.

### **3.2 Laser pump chamber and resonator design**

As discussed earlier, heat generation in flash lamp pumped laser rod is characterized by the fraction of absorbed power transformed into heat by non-radiative processes. This not only influences negatively the laser emission parameters (slope efficiency, emission threshold), but also reduces the output power range and resonator stability. In flash lamp-pumped systems, the broad spectral distribution of the pump source in visible and ultraviolet (UV) region further increases the heating of laser rod during optical pumping. In our set up, we have used a 10% doped samarium glass filter between the rod and the lamp to cut-off UV radiation from the flash lamp and hence to protect solarization of ceramic Nd:YAG rod by UV radiation [35]. In addition, samarium doped glass filter enhances pumping efficiency by absorption of UV radiation and re-emission in the pump bands of Nd:YAG rod. For the design of laser pump chamber, important factors which need utmost attention are the efficient cooling of the laser rod and close coupled pumping geometry of elliptical reflectors for efficient pumping. A schematic diagram of the single flash lamp pumped laser pump chamber used for experiments is shown in Fig. 3.4.

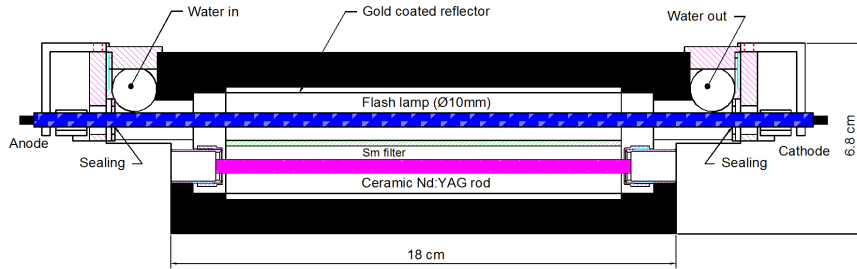


**Fig. 3.4.** A schematic diagram of the single flash lamp pumped laser pump chamber (side view).

In this pump chamber, a ceramic Nd:YAG rod of 10 mm diameter and 152 mm length has been side pumped by using a single Kr flash lamp of bore diameter 8 mm and an arc length of 136 mm. The laser pump chamber has an overall length of 180 mm with a total width of 68 mm and is made of stainless steel (SS304) because of its beneficial thermo-physical properties like corrosion resistance, excellent toughness, and low thermal expansion. The elliptical reflector has a length of 140 mm and is also made of SS304 with a 10  $\mu\text{m}$  thick gold coating. It has been designed to have a closed coupled pumping geometry [7] with major axis  $2a=28$  mm, minor axis  $2b=24$  mm and distance between the two foci  $2c=14$  mm with an eccentricity of  $e=0.5$ . Figure 3.5 shows a schematic diagram of reflector used in the experiments. With this close coupled elliptical reflector geometry; the laser rod efficiently absorbs light emitted from the flash lamp directly as well as after specular reflection from the reflector surface.

In general, the electrodes of the flash lamp in a pump chamber are cooled with de-ionized water since the normal water has a higher electrical conductivity and causes problems in triggering of the flash lamp. In our design, the electrodes are air cooled and have been kept out of water contact, and hence it is also possible to use normal water for cooling of pump cavity. It eliminates use of de-ionizer unit from the cooling system. Flash lamp has been fitted in the pump chamber in such a way that there is no need to open the complete laser pump chamber for replacement of flash lamp.

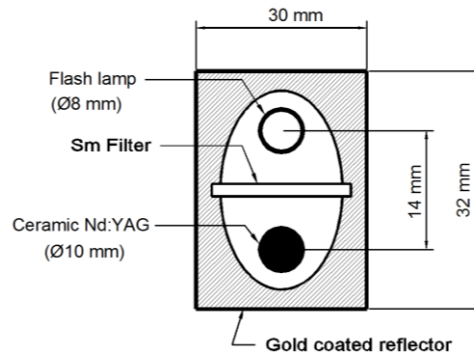


**Fig. 3.5.** A schematic diagram of the close coupled gold coated elliptical reflector (front view).

Cooling system of laser pump chamber consists of primary and secondary cooling units. Primary cooling unit is directly connected to the laser pump chamber and provides a closed loop water flow at a rate of 50 lpm with 4 bar inlet pressure using a water pump (Wilo make). Water flow rate was measured and optimized using an ultrasonic water flow meter (Endree-Hanser make). Primary cooling unit contains a 10  $\mu\text{m}$  size water filter, a water flow switch (Switzer make), and a digital temperature controller (Selec, PID 528). A secondary cooling unit with a refrigeration unit is connected with primary cooling unit via a water to water plate type heat exchanger to maintain secondary cooling unit water temperature. In the conventional cooling scheme, the laser rod surface is cooled by a water flow through a concentric flow tube. In this scheme, heat transfer coefficient  $h$  is a function of flow tube diameter, and coolant water flow rate as given in Eq. 2.2. On the other hand, in a flooded type cooling scheme, the laser rod, flash lamp, samarium filter flow tube, and reflectors are fully immersed in water [36]. The heat transfer coefficient for the flooded cooling scheme was calculated from the Nusselt number (Nu), which is a function of the Reynolds number (Re) as explained by Dalkilic *et al.* [41] and is given in Eq. 2.3 of Chapter 2.

The duct of the laser pump chamber used for water flow was not circular in shape and was divided in two equal subsections of an ellipse by a samarium filter as shown in Fig. 3.5. Its hydraulic diameter can be calculated as  $D=4A/P_w$ . Here,  $A$  is the cross section area and  $P_w$  is the wetted perimeter of the semi ellipse, and is given by  $A=(\pi ab)/2$  and  $P_w = (\pi/2)[3(a+b) - \sqrt{(3a+b)(a+3b)}]$ , respectively. For the typical values of  $2a=28$  mm,  $2b=24$  mm,  $A=2.63$  cm<sup>2</sup>,  $P=40.8$  mm and  $D=25.7$  mm, during the turbulence flow of water in flooded laser pump chamber, the Nusselt, Reynolds, Prandt and other calculated parameters are  $Nu=400$ ,  $Re=87660$ ,  $Pr=7.35$ ,  $k=0.569$  (W/m<sup>0</sup>K),  $h=9800$  (W/m<sup>2</sup> °K). With these optimum values, an efficient heat transfer was achieved in the laser pump chamber, which resulted in better heat transfer coefficient and higher slope efficiency.

A plane-plane symmetric stable resonator was designed for the high average power and long pulse laser operation [27,43]. Two ceramic Nd:YAG rods placed in two laser pump chambers were arranged optically in series with d:2d:d (lens like imaging) configuration as shown in Fig. 3.6.

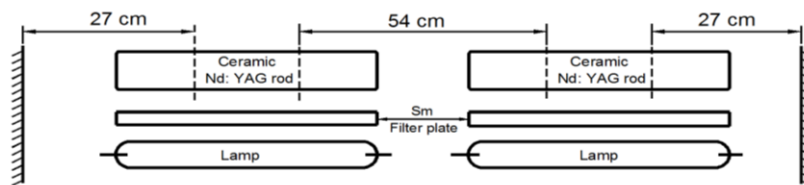


**Fig. 3.6.** Symmetric plane-plane resonator with d:2d:d configuration.

The distance ( $d$ ) between the plane mirror and principal plane of the rods was optimized such that resonator remains stable for the whole range of input pump power. As mentioned earlier, for a plane-plane symmetric resonator, beam radius ( $w_0$ ) of the fundamental mode is

related with the distance ( $d$ ) and the thermal refractive power of the laser rod ( $D_f$ ) as given in Eq. 2.6. In this case, beam quality factor ( $M^2$ ) and BPP of the laser beam can be calculated by using the expression of Eq. 2.7 and Eq. 2.9. For beam quality improvement, the distance  $2d$  in the laser resonator can be increased, but with an increase in value of  $d$ , a corresponding decrease in the range of pump power for stable resonator operation is observed [42]. We have carried out experiments for beam quality improvement with optimization of distance  $2d$  in symmetric plane-plane resonator. The optimum value of distance  $2d$  was found to be  $\sim 66$  cm for single crystal Nd:YAG rod and  $\sim 54$  cm for the ceramic Nd:YAG rod for the entire range of pump power operation from 0-10 kW. Further from Eq. (2.7), it is clear that the value of  $M^2$  depends on the value of  $w_0$  and hence on dioptric power ( $D_f$ ) of the laser rod. For good beam quality,  $w_0$  should be as large as possible but it is limited by the thermal refractive power ( $D_f$ ) of the rod. The value of fundamental mode spot radius  $w_0$  in the rod can not be increased without reducing the value of  $D_f$ . The value of  $D_f$  can be reduced by the effective heat removal from the laser rod.

As mentioned earlier, the thermal refractive power ( $D_f$ ) or the overall thermal focal length ( $f$ ) of the uniformly pumped laser rod can be calculated using Eq. 2.5 of Chapter 2. It is clear from Eq. 2.5 that for a small diameter laser rod, the thermal refractive power ( $D_f$ ) will be more as compared to large diameter rods for the same amount of heat dissipation. Hence, large diameter (10 mm) ceramic Nd:YAG and single crystal Nd:YAG rods were selected for the experiment. Further, thermal power dissipation in the rod ( $P_h$ ) is proportional to the electrical input pump power ( $P_E$ ) from the flash lamp. In order to calculate the thermal lensing in laser rods, the value of  $P_h$  was selected as 10% of  $P_E$  for the lamp pumped system. The measured value of  $K_0$  is 18 for the flash lamp used in this experiment. The lamp current ( $I$ ), pulse duration ( $t_p$ ), and repetition

rate ( $f_p$ ) can be varied using a microcontroller based power supply. Electrical average input pump power ( $P_E$ ) can be varied from 0-5 kW in each rod. The output power ( $P_{out}$ ) is given by [36]

$$P_{out} \cong \eta_s \cdot (P_E - P_{Th}) \quad \dots\dots\dots (3.1)$$

where,  $P_{Th}$  is the threshold pump power, and  $\eta_s$  is the slope efficiency.

For an efficient transmission of laser beam through a small core diameter silica-silica optical fibers, the laser beam parameter product should be smaller than the fiber parameter product (core radius  $\times$  NA) [28]. Here, NA is the numerical aperture of the fiber. Thus, the fiber selection for fiber beam delivery depends on the laser beam quality. The optical damage threshold of pure silica fiber is about 10 GW/cm<sup>2</sup> [7], but the experimentally observed damage threshold depends on fiber end preparation at both ends, as the end faces are more prone to damage by any dust particle sticking on the surface.

Further, we have performed a study on the pulse-to-pulse stability (PTPS) of laser, which is an important factor in the resonator design and is given by Eq. 2.8. It shows the percentage spread of energy between the highest and lowest values for a certain number of pulses, for example 1000 pulses. A smaller spread of the pulse energy from the average value shows a better stability of the resonator. These formulations have been used in the Results and Discussion part of this Chapter.

### 3.3 Experimental details

For experimental study, two identical laser pump chambers having a single flash lamp and a ceramic Nd:YAG rod were placed symmetrically in the laser resonator as shown in Fig. 3.6 and 3.7.



**Fig. 3.7.** A table top view of dual rod lamp pumped ceramic Nd:YAG resonator.

Both the ends of the ceramic Nd:YAG rod are antireflection (AR) coated at 1064 nm. The laser resonator consists of  $\sim 99.8\%$  reflectivity rear mirror and 30% output coupler mirror. The mirror-to-mirror distance or the geometrical length of the resonator was 152 cm. Closed-loop water chillers, with an identical and optimized water flow rate of  $\sim 50$  lit/min were connected to each pump chambers. For experimental measurement of thermal focal length  $f$  of each rod, an expanded and collimated 632 nm He-Ne probe beam of  $\sim 5$  mW power was passed through the Nd:YAG rod under flash lamp pumping. The minimum spot size of the beam due to rod thermal lens was measured using a CCD camera. The distance from the principal plane of the laser rod to the location of this minimum spot size has been taken as the thermal focal length of the rod. An 8 mm diameter aperture has been placed between the two laser rods in the resonator to cut off higher order transverse modes and improve the beam quality. The beam quality factor  $M^2$  was measured using a standard knife edge method [27] by focusing the laser beam using a lens and then plotting the measured beam diameter using knife edge near the focus at different locations near the focal plane as explained in Section 2.3 of Chapter 2.

Two modules of the pulsed power supplies have been used to synchronously drive two Kr-filled flash lamps in each pump chamber using a single controller. Both the flash lamps have

been connected electrically in parallel. These power supplies can provide maximum average electrical input pump power of 5 kW for each lamp with current variation from 100-300 Amp (rectangular pulse shape), pulse duration from 2-20 ms and repetition rate from 1-100 Hz respectively. The temporal profile of the laser was measured using a photodiode, a RG 850 filter, and a 1 GHz oscilloscope. The average output power was measured using a thermocouple based power meter with variation of average electrical input pump power to the lamp. The single pulse energy was also measured using an energy detector. The experiments were repeated with the 1.1% doped single crystal Nd:YAG rod for a comparison of its performance with respect to ceramic Nd:YAG rod. The optimum output coupler reflectivity for the single crystal was 40% as compared to 30% for ceramic Nd:YAG rod, indicating that ceramic Nd:YAG rod has a slightly higher small signal gain as compared to single crystal Nd:YAG rod. Output laser beam was focused at the optical fiber tip for beam delivery by using a plano-convex fused silica lens of 35 mm focal length. The optical fiber input and output end surface was cleaved using a large diameter fiber cleaver (Vytran make). In order to perform material processing applications, beam at the exit fiber end was first collimated using a plano-convex lens and then it was focused using another lens with a desired imaging ratio.

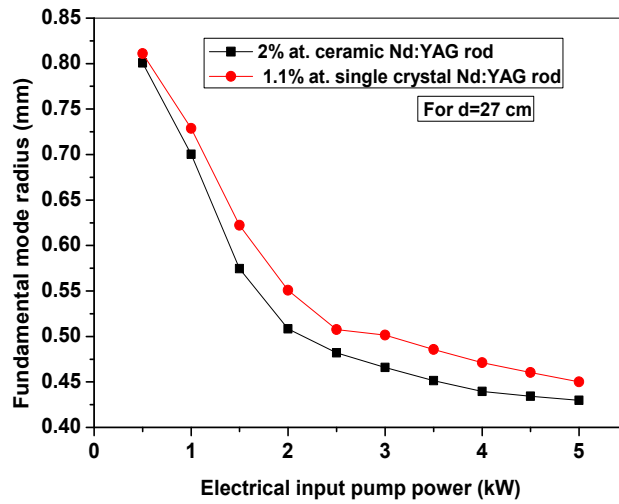
### **3.4 Results and Discussion**

Table 3.1 shows a comparison of theoretically calculated values and experimental measured values of thermal focal lengths for different values of input pump powers for 2% at. doped ceramic Nd:YAG rod and 1.1 % doped single crystal Nd:YAG rods. It was observed that experimentally measured values of thermal focal lengths of these laser rods are slightly higher as compared to the calculated values using Eq. 2.6. It may be due to the insertion of a samarium

filter between the rod and lamp, which reduces the effective heat load in the rod by cutting off the UV radiation of flash lamp as discussed earlier.

**Table 3.1:** Calculated and measured values of thermal focal length in meters.

Input pump power (kW)	2% at. ceramic Nd:YAG rod		1% at. single crystal Nd:YAG rod	
	Calculated values (m)	Measured values (m)	Calculated values (m)	Measured values (m)
0.5	6.42	6.56	6.52	6.91
1.0	3.69	3.78	4.37	4.46
1.5	1.54	1.62	2.21	2.30
2.0	0.82	0.93	1.22	1.35
2.5	0.60	0.71	0.82	0.92
3.0	0.49	0.59	0.76	0.87
3.5	0.41	0.49	0.67	0.74
4.0	0.34	0.40	0.55	0.63
4.5	0.30	0.36	0.47	0.55
5.0	0.27	0.32	0.41	0.48



**Fig. 3.8.** Variation of calculated values of fundamental mode radius ( $w_0$ ) with input pump power for the ceramic and single crystal Nd:YAG rods.

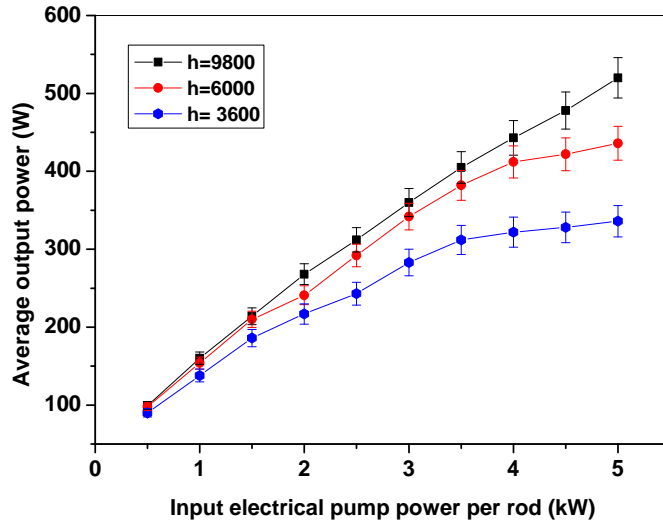


**Fig. 3.9.** Output average power variation with input pump power for different values of heat transfer coefficient for dual ceramic rod resonator.

Fundamental mode radius in the laser rod was also calculated using Eq.3.3 for different values of thermal focal lengths. Its comparison for ceramic and single crystal Nd:YAG rods is shown in Fig. 3.8. The values of  $w_0$  for ceramic and single crystal Nd:YAG rod was in the range of 0.69-0.42 mm and 0.66-0.41 mm, respectively. The value of  $w_0$  is slightly more for the single crystal as compared to that for ceramic Nd:YAG rod because of the long thermal focal length  $f$  in single crystal Nd:YAG rod. Next, the optimization of the flow rate of coolant was carried out to achieve linear variation in the output laser power for the entire pumping range. The average output power from dual ceramic Nd:YAG rod laser resonator set up was measured for different values of heat transfer coefficients ( $h$ ).

Fig. 3.9 shows variation of average output power as a function of average input pump power for three different heat transfer coefficients [69]. Three different values of  $h$  were selected in our experiment by increasing the coolant water flow rate  $W$  in the range of 20  $l/m$  to 50  $l/m$ . At

a lower value of flow rate of 20 l/m providing  $h=3800 \text{ W/m}^2\text{K}$ , the output laser power variation is not linear for the entire range of input pump power due to inefficient heat removal from the laser rod at higher input pump powers. However, for the higher value of water flow rate of 50 l/m providing  $h=9800 \text{ W/m}^2\text{K}$ , the output laser power was found to vary almost linearly with input pump power.

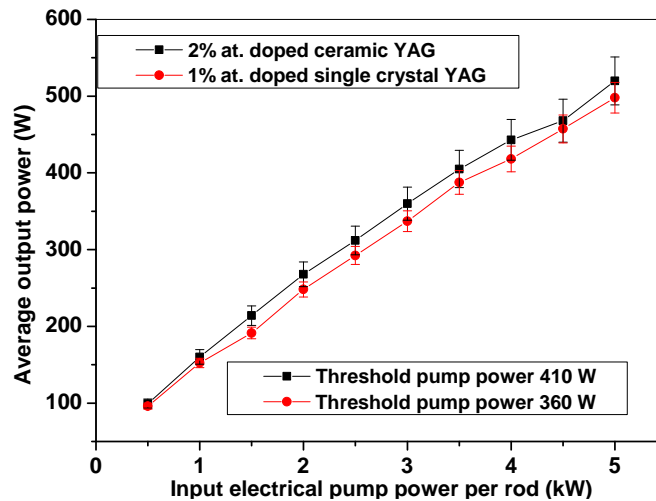


**Fig. 3.10.** Variation of average output power with average input pump power for dual rod resonator of ceramic and single crystal Nd:YAG rods.

Fig. 3.10 shows the variation of average laser output power as a function of electrical input pump power for the ceramic and single crystal Nd:YAG rod in dual rod resonator configurations, for the maximum water flow rate and heat transfer coefficient. It shows that the average output power is slightly higher for the ceramic Nd:YAG rod as compared to single crystal Nd:YAG rod, which is in accordance with the report by Lu *et al.* [62]. For dual rod ceramic resonator, the maximum average output power of 520 W was achieved with 5.4% slope efficiency for a total average electrical input pump power of 10 kW, which is the highest for such laser systems. Whereas, in case of dual rod single crystal Nd:YAG rod, a maximum average

output power of 498 W was achieved for the same average electrical input pump power with a slope efficiency of 5.1%. The efficiency of ceramic Nd:YAG laser in our experiments is much higher than that reported by Yagi *et al.*, possible reasons behind this is the efficient heat removal from the laser rods in newly designed water-cooled pump chamber and use of Kr flash lamps in place of Xe flash lamps. The measured threshold pump power for the ceramic rod was ~410 W and that for single crystal was ~360 W. The threshold pump power was slightly higher for the ceramic Nd:YAG rod since it is inversely proportional to the  $\sigma\tau$  product, where  $\sigma$  is the stimulated emission cross-section of the rod and  $\tau$  is spontaneous emission life time. Although  $\sigma$  is almost similar for ceramic Nd:YAG and single crystal Nd:YAG rods, spontaneous emission lifetime  $\tau$  has a value of 230  $\mu\text{s}$  for the 1.1% atomic doped single crystal Nd:YAG rod and 174  $\mu\text{s}$  for 2% atomic doped ceramic Nd:YAG rod [70].

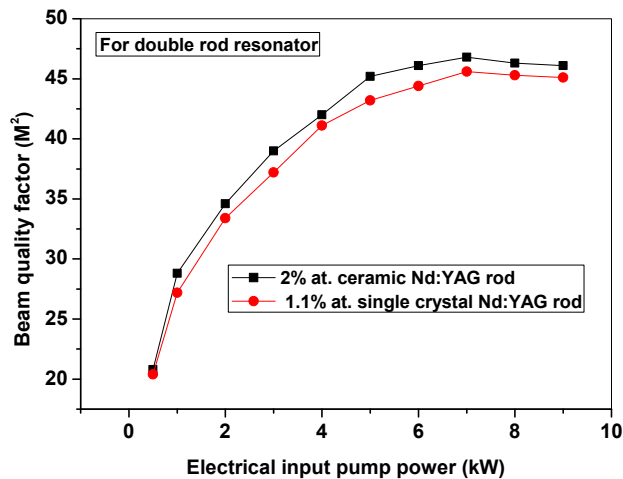


**Fig. 3.11.** Measured value of beam quality factor ( $M^2$ ) as a function of input pump power variation for dual rod resonator configuration of ceramic and single crystal Nd:YAG rods.

The variation of laser beam quality factor ( $M^2$ ) as a function of the pump power was also studied. Figure 3.11 shows measured values of  $M^2$  as a function of average input pump power for the

multimode operation with the maximum value of  $M^2 \sim 45$  for dual rod resonator of single crystal Nd:YAG, which is slightly better than that for dual rod ceramic Nd:YAG with a maximum value of  $M^2 \sim 47$ .

The reason for better  $M^2$  in the case of single crystal rod is the higher value of fundamental mode spot size within the rod as compared to fundamental mode spot size within the ceramic Nd:YAG rod (see Fig. 3.8). The beam quality of dual rod ceramic Nd:YAG was found to be suitable to couple the beam effectively through a 400  $\mu\text{m}$  core diameter optical fiber for the entire pumping range (0-10 kW).

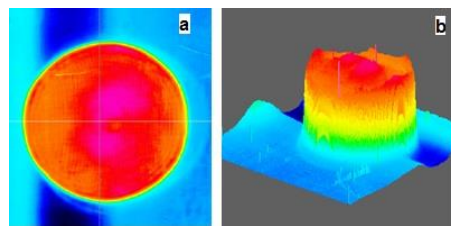


**Fig. 3.12.** *Beam profile of the ceramic Nd:YAG laser (a) 2D view, and (b) 3D view.*

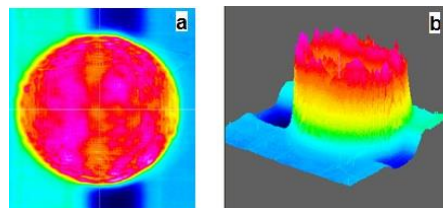


**Fig. 3.13.** *Beam profile of the single crystal Nd:YAG laser (a) 2D view, and (b) 3D view.*

Figures 3.12 and 3.13 show the beam profiles of ceramic and single crystal Nd:YAG rods, respectively using a CCD camera (Wincam-D, Gentec) at a maximum electrical pump power of 10 kW. The laser beam profile measurements show that the beam profile of ceramic Nd:YAG

laser is more smooth than for the single crystal laser. This can be explained by the fact that the absorption coefficient of 2% doped ceramic Nd:YAG rod is almost 3 times higher as compared to 1.1% doped single crystal Nd:YAG rod due to higher doping concentration of  $\text{Nd}^{3+}$  ions [55]. Hence, a more smooth multimode beam profile is obtained for ceramic Nd:YAG laser. The beam profile also shows that the real beam extracted from the laser system will actually be a mixture of the higher order cavity modes.

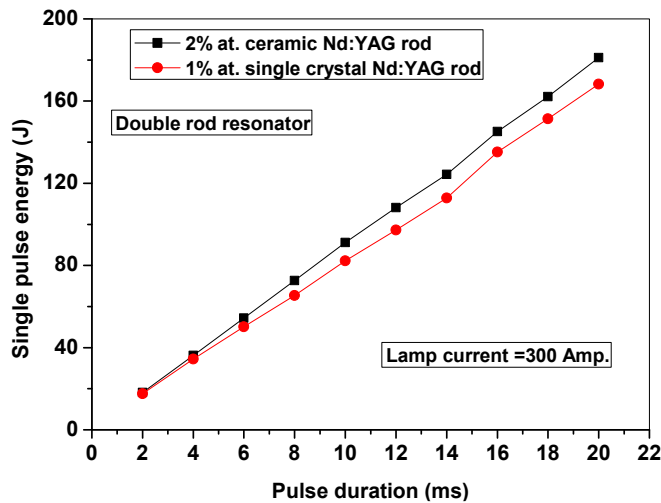


**Fig. 3.14.** Measured value of single shot pulse energy of dual rod resonator configuration of ceramic and single crystal Nd:YAG rods.

Figure 3.14 shows the single shot pulse energy for the ceramic and single crystal Nd:YAG rods, which shows a linear variation in pulse energy with variation in pulse duration from 2-20 ms. The pulse energy of ceramic Nd:YAG laser is slightly higher due to the higher doping concentration of ceramic rod. In this case, maximum single pulse energy of 180 J was achieved at 20 ms pulse duration with 9 kW of peak power, which is suitable for several material processing applications.

Finally, the laser beam from ceramic and single crystal Nd:YAG rod was efficiently and reliably coupled in a 150 m long, 400  $\mu\text{m}$  core diameter and 0.22 NA optical fiber with a transmission efficiency of more than 90% for the whole range of pump power. The transmission loss of 10% may be accounted for 4% Fresnel reflection losses from each end of fiber and about 2% attenuation and coupling losses. Pulse-to-pulse stability (PTPS) was measured for 1000 pulses and it was found that the PTPS is better ( $\pm 4\%$ ) for the ceramic Nd:YAG rod as compared to that for single crystal Nd:YAG rod ( $\pm 6\%$ ) for 20 ms pulse duration. This is due to the fact that thermal focal length is slightly lower for the ceramic Nd:YAG rod even for single shot operation, which results in better pulse stability of the resonator for the ceramic rod for single shot operation in plane-plane symmetric resonator, where the resonator stability point lies just near the limits of stability.

### **3.5 Conclusions**

In conclusion, we have studied the performance of ceramic Nd:YAG rod for high average power and long pulse laser generation. By appropriate design of the laser pump chamber and resonator, a maximum average output power of 520 W has been achieved with 5.4% slope efficiency using ceramic Nd:YAG rod. This was comparable to the generation of 498 W from single crystal Nd:YAG rod with 5.1% slope efficiency at the same electrical input pump power. The theoretical considerations and experimental results show that ceramic Nd:YAG rod can be used as a potential replacement for single crystal Nd:YAG rods for the development of high average power solid-state lasers. It is more economical to use ceramic Nd:YAG rod as compared to single crystal Nd:YAG rod because its method of fabrication is simpler as compared to single crystal Nd:YAG which reduces its fabrication cost. Ceramic rods with large diameters and sizes

with higher doping concentrations can be fabricated as compared to single crystal for generation of high average output power with good beam quality. This ceramic Nd:YAG laser can be effectively used for material processing applications such as cutting of thick section of stainless steel and deep penetration welding of the vacuum grade components like aluminium, titanium, stainless steel, and its alloy for the automotive, nuclear, shipping, and heavy machinery industries.

# Chapter 4

---

## Study and development of short pulse Nd:YAG laser

### 4.1 Introduction

Application of pulsed Nd:YAG lasers for cleaning or ablation of material surface, particularly for artworks restoration is well known. Laser cleaning has been reported as a well-established and specific technique for conservation of marble, variety of stones, and metals. It involves thermal ablation process using an Nd:YAG laser beam of short pulse duration and high energy density. Thus, Nd:YAG lasers operating either in Q-switched (QS) mode or short pulse free-running (FR) mode have been utilized for such applications. At present, both of these modes are being used for cleaning application with their own advantages and drawbacks. Although QS mode allows a higher ablation rate than FR, however, it generates intense shock waves, which may result in micro-cracking of delicate surfaces and it is also difficult to deliver QS mode lasers through optical fibers [71]. Difficulty in fiber optic beam delivery of QS regime is a major drawback, as it denies flexibility in access to work place and uniform cleaning with homogeneous beam profile at the exit from multi-mode fiber.

On the other hand, FR mode Nd:YAG lasers with pulse duration of the order of hundreds to tens of microsecond ( $\mu\text{s}$ ) can be easily delivered through optical fibers and are preferred to remove surface contaminations from different materials like marbles, stones, and other variety of

materials due to flexibility [72-76]. Surface cleaning by laser irradiation involves complex mechanisms such as photo-thermal, photo-chemical, and mechanical effects on the target material. Thus, cleaning of different materials requires different laser parameters. For example, Nd:YAG laser with pulse duration in the range of 20-50  $\mu\text{s}$  has been found to be highly suitable for marble and stones cleaning [77-79]. Similarly, 50-100  $\mu\text{s}$  duration FR Nd:YAG laser pulses have also been found to be highly suitable for cleaning of deposition, corrosion, and oxide layer from the surface of metals such as copper, bronze, carbon steel, and mild steel [73,74].

Generation of short pulses ( $\mu\text{s}$ ) from FR Nd:YAG lasers with high peak power still depend on lamp pumping in place of diode pumping, since the high peak power operation of laser diodes is restricted by thermal run away problem [19]. However, lamp pumped FR Nd:YAG lasers with pulses shorter than the upper level lifetime of 230  $\mu\text{s}$  are difficult to realize, since a higher pumping rate is required to maintain the population inversion at the upper lasing level. This requires a large value of  $dI/dt$  for lamp current  $I$  to reach the threshold of lasing and requires high peak current power supply for lamp pumping [78]. Moreover, these high peak current and shorter pulses reduce the life time of flash lamps.

In literature, flash lamp pumped FR Nd:YAG laser with pulse duration as short as 20  $\mu\text{s}$  and pulse energy of 0.5-1 J has already been reported for marble cleaning [80]. However, the laser beam was delivered through a 600  $\mu\text{m}$  core diameter optical fiber. Beam delivery using a 600  $\mu\text{m}$  fiber may not be suitable for uniform cleaning of selective area of smaller size objects with high accuracy [80,81]. It is well known that the coupling of laser beam through smaller core diameter ( $\sim 200$   $\mu\text{m}$  or less) optical fiber is difficult as it depends on laser beam quality, which in turn depends on the design of a laser pump chamber and laser resonator [27].

Wazen [81] have shown that cleaning process with a laser beam having a Gaussian shape spatial profile is less selective, inhomogeneous, and cleaning efficiency is also low in comparison with a uniform top-hat beam profile. As a result, a top-hat beam intensity distribution is preferable for uniform laser cleaning application. A schematic view of Gaussian and top-hat beam profiles is shown in Fig. 4.1 for the sake of comparison. In general, most of the commercial grade short pulse Nd:YAG lasers provide Gaussian shape spatial beam profiles with a maximum intensity at the center of the beam and an exponential decrease towards the edges [7]. In direct laser beam delivery, the top-hat beam intensity distribution can only be achieved by using expensive variable reflectivity mirrors of a super-Gaussian reflectivity profile as an output coupler mirror in the laser resonator [82].

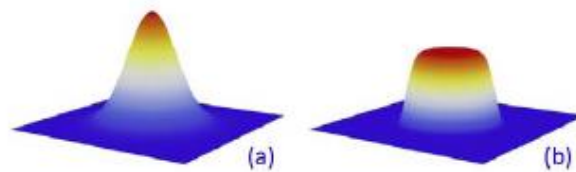


**Fig. 4.1.** A schematic view of (a) Gaussian and (b) top-hat spatial beam profiles (profile intensities are not at the same scale).

In this Chapter, we have focused on the study and development of good beam quality, fiber coupled, FR short pulse ( $\mu\text{s}$ ) Nd:YAG laser for cleaning of marble, zircaloy, and inconel materials for conservation. It contains an investigation of the design of laser pump chamber and resonator to obtain good beam quality for delivery through 200  $\mu\text{m}$  core diameter optical fiber to achieve almost top-hat uniform spatial beam profile. To the best of our knowledge, there is no other published report on  $\mu\text{s}$  pulse duration high peak power ( $\sim 22$  kW) Nd:YAG laser cleaning

system with 200  $\mu\text{m}$  fiber optic beam delivery. Further, the laser resonator has been designed to provide a better pulse-to-pulse stability for effective laser cleaning. Performance of this laser system was also evaluated successfully for cleaning of marble, stones, zircaloy, and inconel. Our results show that laser cleaning efficiency using this fiber coupled and almost top-hat uniform beam is close to 100%. The details of the laser pump chamber, resonator and power supply are given in Section 4.2. Experimental details have been provided in Section 4.3 and the results are given in Section 4.4. Section 4.5 outlines the conclusion of this work.

## **4.2 Design of short pulse Nd:YAG laser system**

As discussed earlier a well designed laser pump chamber and resonator provides good beam quality for efficient fiber coupling of the laser beam. To obtain higher pulse energy and peak power, a pump chamber with double flash lamp pumping arrangement has been used. Further, the laser pump chamber has been designed for large value of heat transfer coefficient for efficient heat removal from the laser rod, which reduces thermal lensing effect and subsequently improves laser beam quality. Moreover, a close-coupled elliptical reflector geometry in the laser pump chamber improves transfer efficiency of the useful pump radiation from flash lamp to laser rod [7]. The laser resonator designed to obtain good beam quality, pulse-to-pulse stability and alignment stability to ensure uniform laser cleaning of surface.

### **4.2.1 Laser pump chamber and resonator design**

The laser pump chamber consists of a 6 mm diameter and 85 mm long Nd:YAG rod and two 6 mm bore diameter flash lamps placed in a double elliptical gold-coated reflector as shown

schematically in Fig. 4.2. The pump chamber is 150 mm long and 60 mm wide and is made of stainless steel (SS 304). The double elliptical reflector is 90 mm long and made of SS 304 with 10  $\mu\text{m}$  thick gold coating on the internal surface. The elliptical reflector has following parameters: major axis  $2a=25$  mm, minor axis  $2b=23$  mm, distance between the rod and lamp  $2c=10$  mm with an eccentricity of  $e=0.4$ . In this close coupled elliptical reflector geometry, the laser rod absorbs pump light emitted from the flash lamp directly as well as after specular reflection from the reflectors.

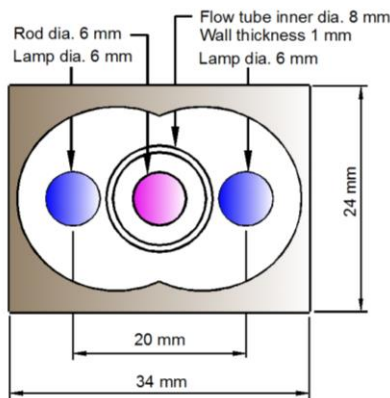


**Fig. 4.2.** Schematic of laser pump chamber (front view) and reflector geometry.

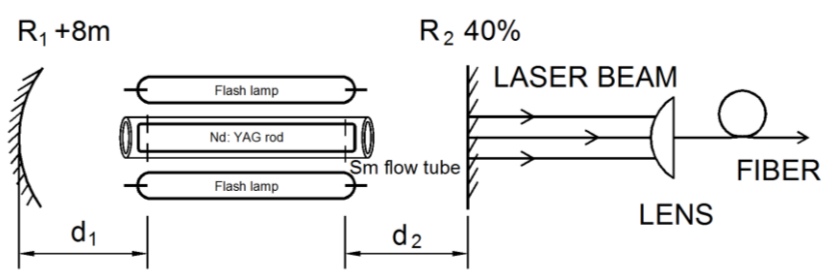


**Fig. 4.3.** A schematic of hemispherical resonator with dual flash lamp pumped Nd:YAG rod.

The laser rod is kept in a 10% doped samarium glass flow tube of 8 mm inner diameter to cut-off UV radiation from the flash lamp. In addition, the samarium doped filter enhances pumping efficiency by absorption of UV radiation and fluorescent re-emission in the pump bands of Nd:YAG rod [35]. The arrangement of laser pump chamber in laser resonator is shown schematically in Fig. 4.3.

A nearly hemispherical stable resonator was designed for the high peak power generation in the short pulse laser operation. The hemispherical resonator configuration was chosen for its better alignment stability and pulse-to-pulse stability for operation at higher as well as lower repetition rates as compared to other resonator configurations [46]. The distances  $d_1$  between the rear mirror of radius of curvature  $R_1$  and the principal plane of the laser rod and  $d_2$  between front mirror and principal plane of the laser rod was optimized in such a way that resonator remains stable for the entire pumping range. The equivalent resonator consists of one internal lens (laser rod) of focal lengths  $f$ . The rear curved mirror was taken as reference for round trip ABCD matrix which is given as

$$\begin{pmatrix} A & B \\ C & D \end{pmatrix} = \begin{pmatrix} 1 & 0 \\ -2/R_1 & 1 \end{pmatrix} \begin{pmatrix} 1 & d_1 \\ 0 & 1 \end{pmatrix} \begin{pmatrix} 1 & 0 \\ -1/f & 1 \end{pmatrix} \begin{pmatrix} 1 & d_2 \\ 0 & 1 \end{pmatrix} \begin{pmatrix} 1 & d_2 \\ 0 & 1 \end{pmatrix} \begin{pmatrix} 1 & 0 \\ -1/f & 1 \end{pmatrix} \begin{pmatrix} 1 & d_1 \\ 0 & 1 \end{pmatrix} \begin{pmatrix} 1 & 0 \\ -2/R_1 & 1 \end{pmatrix}$$

The stability condition for the resonators with the resonator parameters  $g_1$  and  $g_2$  can be expressed by  $0 < g_1 g_2 < 1$ . The value of  $g_1 g_2$  related to the elements of round trip ABCD matrix is given as [27]

$$g_1 g_2 = (A + D + 2) / 4 \quad (4.1)$$

For a hemispherical resonator, beam radius ( $w_0$ ) of the fundamental mode is given by [42]

$$w_0^2 = (2d_1 \lambda / \pi) [1 - d_1 D_f - (d_1 + d_2 - d_1 d_2 D_f) / R_1] \quad (4.2)$$

and beam quality factor ( $M^2$ ) of the multimode laser beam in a hemispherical resonator can be written as [42]

$$M^2 = (r_0^2 / w_0^2) = (\pi r_0^2 / 2d_1\lambda) / [1 - d_1D_f - (d_1 + d_2 - d_1d_2D_f) / R_1] \quad (4.3)$$

Here,  $D_f$  is the thermal refractive power of the laser rod and  $r_0$  is the rod radius. It is clear that for a hemispherical resonator, beam quality factor  $M^2$  of the multimode beam can be improved using larger values of  $d_1$  and  $R_1$  for which the resonator remains stable. The design parameters of the resonator were chosen so that the output beam quality will ensure efficient transmission through a 200  $\mu\text{m}$  core diameter optical fiber, which is possible only if the laser beam parameter product is smaller than the fiber parameter product (core radius  $\times$  NA) [28]. Although the bulk optical damage threshold of pure silica is about 10  $\text{GW}/\text{cm}^2$ , but it was observed experimentally that the damage threshold depends on fiber end preparation on both ends and is much more prone to damage by any dust particle sticking on the surface.

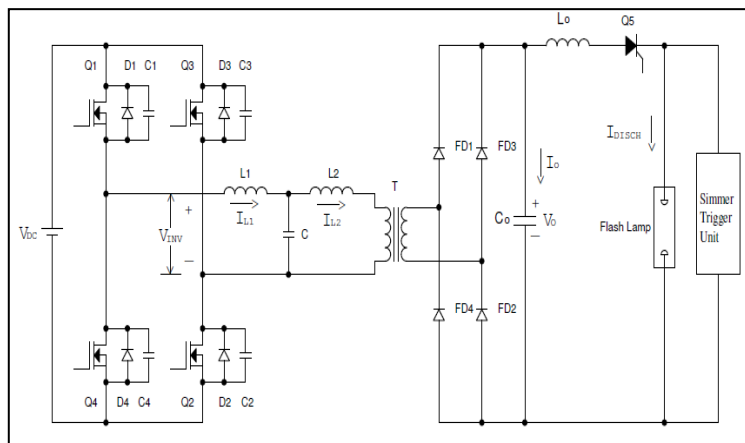
#### 4.2.2 Laser power supply

A microcontroller based double-lamp power supply was used for pumping of pulsed Nd:YAG laser. Both the flash lamps have been connected electrically in parallel. A schematic diagram of the power supply is shown in Fig. 4.4. The flash lamp power supply is a single phase, 230V, 50 Hz AC mains supply. The power supply specifications and component list is given in Table 4.1. The flash lamp works in simmer mode of operation, and uses a single-mesh inductor/capacitor ( $L/C$ ) pulse-forming network (PFN) with a capacitance value of 40  $\mu\text{F}$  and inductance value of 7.6  $\mu\text{H}$ . Capacitor voltage reaches a value of 1225 V and the peak value of the discharge current is 868 A with a pulse width of 55  $\mu\text{s}$  measured at 1/3 of the peak value. Once the PFN energy storage capacitor ( $C_0$ ) is charged to the required voltage corresponding to

the desired energy by the capacitor charging power supply, firing of SCR numbered Q5 is initiated and the stored energy of the capacitor is delivered to the flash lamp through the PFN inductor in the form of a current pulse. Profile of the current pulse was determined by the PFN capacitor and inductor values. The pump energy per pulse per lamp was 28 J (56 J total pump pulse energy). At an input voltage of 1225 V and 20 Hz repetition rate, the maximum average input pump power is 560 W per lamp (1120 W for both the lamps).

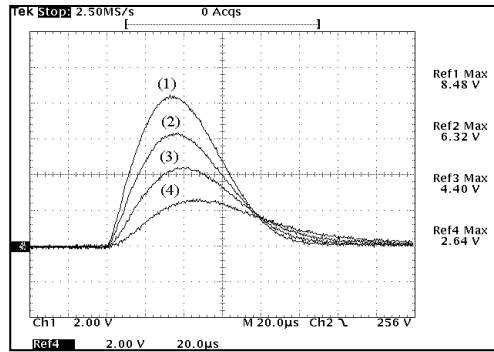
**Table 4.1:** Specifications and component list of power supply.

Parameters/Components	Value/Part No.
Charging Voltage (Max.)	1225 V
Rep. rate (Max.)	20 Hz
Charging rate	600 J/s
Switching freq.	1000 Hz
Energy/pulse (input)	28 J
HV trigger pulse	20 kV, 10 $\mu$ s
Simmer current	400 mA
Power MOSFETs, Q1 to Q4	SPW35N60CFD
Diodes, FD1 to FD4	MUR8100E
SCR, Q5	HF80TB14
PFN Inductor	7.6 $\mu$ H
Resonant Inductor, L1	28.3 $\mu$ H
Resonant Inductor, L2	22.9 $\mu$ H
Resonant Capacitor, C	89.47 nF



**Fig. 4.4.** A schematic diagram of the pulsed power supply for flash lamp pumping, which shows PFN and simmer-trigger unit.

A high simmer current is important in a short pulse flash lamp pumped laser to obtain sufficiently long lamp lifetime and increase the overall efficiency of laser. Thus, a separate simmer current power supply is used, to provide 400 mA of constant current for simmer. A touch screen type micro-controller swithes controls the voltage, repetition rate, synchronization of charge and discharge, and fires the laser at user command.



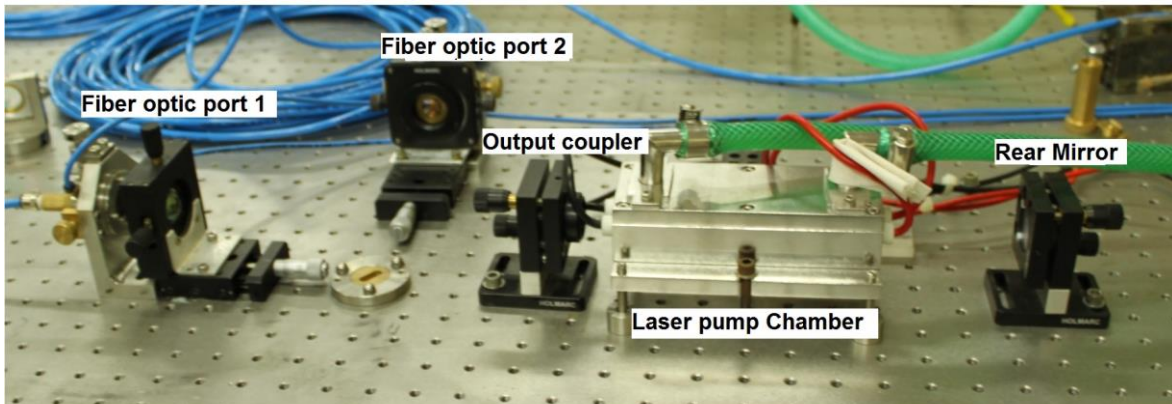
**Fig. 4.5.** Flash lamp discharge current ( $I_{DISCH}$ ) with  $V_0$  set at (1) 1200V (2) 1000V, (3) 800V and (4) 600V. X – Scale: 20 $\mu$ s/div, Y - Scale: 100A/div.

Fig. 4.5 shows the waveforms of discharge current ( $I_{DISCH}$ ) when charged capacitor voltage is 1225V. The damping parameter  $\gamma$  is given by  $\gamma=K_0/\sqrt{ZV}$  [49]. Here,  $Z=\sqrt{L/C}$  and  $K_0$  is the lamp impedance parameter. The measured value of  $K_0$  for flash lamp used in the experiment was found to be 18. The input voltage  $V$  and the pulse repetition rate ( $f$ ) can be varied in the ranges of 100-1225 V and 1-20 Hz, respectively. It is well known that  $\gamma=0.8$  corresponds to critically damped pulse at which PFN shows the best efficiency. However, a value in the range of 0.7 to 1.2 is acceptable in practical operation. An under-damped pulse beyond this value can shorten the life of the flash lamp, on the other hand over-damped pump pulse results in a low

value of output laser peak power. Input voltage for the PFN at laser threshold was 450 V with a value of  $\gamma = 1.2$  and at the maximum output laser energy, it was 1225 V with  $\gamma = 0.78$ .

### 4.3 Experimental set-up

A table-top view of in-house developed 1.25 J pulse energy short pulse Nd:YAG laser is shown in Fig. 4.6. In this set up, laser pump chamber consists of two krypton (Kr) filled flash lamps of 6 mm bore diameter and 82 mm arc length (Heraeus Noblelight, UK) and a 1.1% atomic doped Nd:YAG rod of size  $\phi 6 \text{ mm} \times 85 \text{ mm}$  (Laser Material Inc., USA). Both the ends of the Nd:YAG rod are plane-parallel to each other and is antireflection (AR) coated for 1064 nm wavelength, whereas the cylindrical rod surface is grounded. Envelope material of flash lamp is cerium doped quartz, which absorbs UV and re-emits blue fluorescence. A closed-loop water chiller, which circulates de-ionized water at a flow-rate of 20 l/m, removed the heat from the laser pump chamber.



**Fig.4.6.** Table-top view of 1.25 J pulse energy short pulse Nd:YAG laser.

The laser pump chamber was placed in a hemispherical resonator, which consists of  $\sim 99.8\%$  reflective concave rear mirror and 40% plane output mirror. The measured overall geometrical

length (mirror-to-mirror) of this hemispherical resonator was 26 cm. Experiments were performed using different radius of curvature (R.O.C.) concave rear mirrors to obtain better beam quality ( $M^2$ ), so that the laser beam can be efficiently delivered through a 200  $\mu\text{m}$  core diameter optical fiber. For experimental measurement of thermal refractive power of the laser rod, an expanded and collimated He-Ne red laser was passed through the Nd:YAG rods under the flash lamp pumping. The minimum focal spot of the thermal lens was measured using a CCD camera. The distance from the principal plane of the laser rod to the location of this focal spot was the thermal focal length  $f$  and its inverse is the thermal focal power  $D_f$ . The average output power of laser beam was measured using an air-cooled thermocouple based power meter and single pulse energy of the laser beam was measured using an energy detector. The beam quality factor  $M^2$  was measured using a standard knife-edge method as described in Chapter 3 [27]. A plano-convex fused silica lens of 30 mm focal length was used for coupling of this laser beam to a 150 m long, 200  $\mu\text{m}$  core diameter step index optical fiber having NA of 0.22. The optical fiber input and output end face was prepared using a multimode fiber cleaver (Vytran, USA) to avoid damage of the fiber end face at high values of pulse energies. Two such optical fibers were used for the beam delivery on time-sharing basis as described in Chapter 2 [48].

In order to perform laser cleaning experiment, a focusing nozzle was designed as shown in Fig. 4.7. It consist of a plano-convex fused silica collimating lens having a focal length of 40 mm and a cylindrical focusing lens of 40 mm focal length, which are mounted in the lens imaging assembly. It generates a line focus spot of size 0.2 mm  $\times$  6 mm and is more suitable for cleaning of large surface area as compared to a circular focal spot. Focus position was kept ~2 mm away from the tip of focusing nozzle. For cleaning application, this nozzle was mounted on a three-axis, computer controlled CNC machine as shown in Fig.4.8.

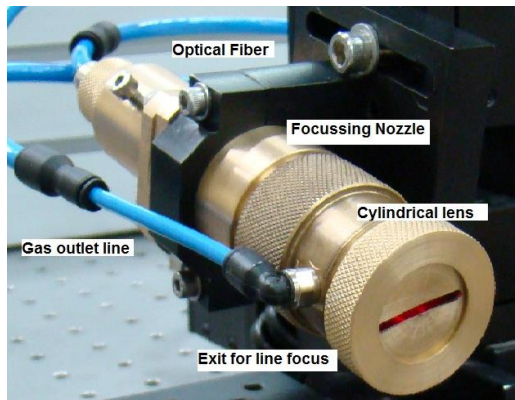


**Fig.4.7.** A view of focusing nozzle.

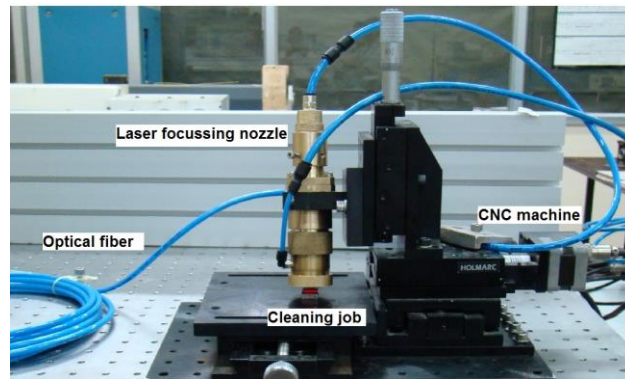


**Fig.4.8.** A view of the focusing nozzle mounted on CNC machine.

Laser focusing nozzle was kept at an angle of  $10^0$  with respect to plane of the given material to prevent the damage of optical fiber exit face due to the back reflected laser beam from the surface of the material. The focusing nozzle is equipped with a coaxial gas jet of argon gas with a constant flow rate of  $\sim 30$  l/m to protect the cleaned surface from oxidation by creating an inert atmosphere and also to protect the damage of focusing lens from the vapour of ablated material. Cleaning efficiency was evaluated by counting the surface densities of particles before and after laser cleaning in a given area of the sample using Scanning Electron Microscope (SEM) (Sigma, Carl Zeiss FE-SEM) in combination with a particle counting, image processing computer software programme. For the evaluation of the cleaning effectiveness, colour analysis was performed using an optical microscope (LEICA, GmbH). Laser cleaned surface was also studied and analyzed using X-ray photoelectron spectroscopy (XPS) before and after laser cleaning.

## 4.4 Results and discussion

Variation of thermal focal length ( $f$ ) of the Nd:YAG laser rod ( $\phi$  6 mm  $\times$  85 mm) was measured to be in the range of 11 m to 0.90 m for change of input pump power from 0.1 kW to 1.12 kW. Experimentally measured value of thermal focal length of Nd:YAG rod was slightly higher than the calculated value due to the samarium flow tube, which reduces the effective heat load in the rod by cutting-off the UV radiation from flash lamp. Further, pulse-to-pulse stability (PTPS) is also an important factor in the laser resonator design with reference to laser cleaning application and is given by  $PTPS (\%) = \pm (E_{\max} - E_{\min})/E_{\text{avg}} \times 100$ . Small deviation of the pulse energy from its average value indicates a good and stable resonator, which is highly beneficial for good quality of laser cleaning. In view of this, beam quality factor  $M^2$ , PTPS, and misalignment sensitivity were measured for maximum average input pump power of 1.12 kW by using concave rear mirrors of different ROC (1 m to 10 m) and a fixed plane output coupler mirror. The values of  $d_1$  and  $d_2$  were fixed at 50 cm and 17 cm, respectively. These optimum values of  $d_1$  and  $d_2$  were calculated from the measured value of thermal focal length, so that the resonator remains stable for the entire pumping range. Fig. 4.9 shows a plot of the beam quality factor  $M^2$  for the multimode beam with variation in R.O.C. of the rear concave mirror for the maximum average electrical input pump power of 1.12 kW. It was observed that the beam quality for multimode operation improves with increase in R.O.C. of the rear concave mirror.

However, selection of higher value of R.O.C. of the rear mirror for beam quality improvement is limited by the stability criteria of laser resonator. Results of our experimental measurements in the variation of  $M^2$ , PTPS, and misalignment sensitivity of the resonator with R.O.C. are listed in Table 4.2. It was observed that 10 m R.O.C. mirror provides best beam

quality ( $M^2 \sim 24$ ), but at the same time it has smaller value of misalignment sensitivity of only 110  $\mu\text{rad}$ , which affects the resonator stability. *PTPS* and misalignment sensitivity of the laser resonator were found to be better for lower value of R.O.C. (from 1 m to 5 m R.O.C.), but for these lower values of R.O.C., beam quality  $M^2$  was not suitable for coupling the laser beam through 200  $\mu\text{m}$  optical fiber. Finally, 8 m R.O.C. rear mirror was selected, which provided  $M^2 \sim 28$ , *PTPS* =  $\pm 2.5\%$  and misalignment sensitivity  $\sim 258 \mu\text{rad}$ . These values were found to be suitable to couple the laser beam efficiently through a 200  $\mu\text{m}$  core diameter fiber with stable operation of laser resonator for the entire pumping range.

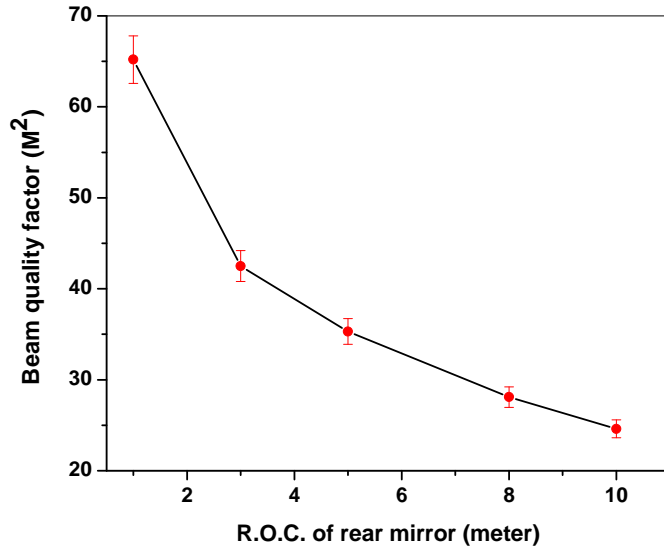


**Fig. 4.9.** Variation of beam quality factor ( $M^2$ ) with R.O.C. of the rear mirror.

**Table 4.2:** Variation of  $M^2$ , *PTPS* and misalignment sensitivity of the laser resonator with R.O.C. of the rear mirror at maximum input pump power.

R.O.C. of concave rear mirror (meters)	$M^2$	<i>PTPS</i>	Misalignment sensitivity for 10% power drop ( $\mu\text{rad}$ )
1	65.2	$\pm 2.1\%$	637
3	42.5	$\pm 2.3\%$	512
5	35.3	$\pm 2.4\%$	422
8	28.1	$\pm 2.5\%$	258
10	24.6	$\pm 2.8\%$	110

Fig. 4.10 shows the variation of  $M^2$  as a function of input pump power using 8 m R.O.C. rear concave mirror. The value of  $M^2$  varies in the range of 7 to 28 for the entire pump power range. With this beam quality, an overall power transmission efficiency of 91% was achieved. The major losses (4%) per surface of the optical fiber are due to Fresnel reflection losses. For a given pulse duration  $t_p$ , and output pulse energy  $E$ , the peak power of pulsed Nd:YAG laser can be calculated as  $P_{peak}=E/t_p$ .

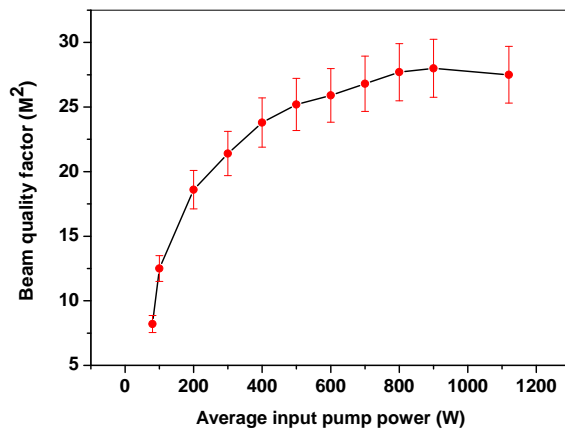


**Fig. 4.10.** Variation of beam quality factor ( $M^2$ ) with input pump power for 8 m R.O.C. of rear concave mirror.

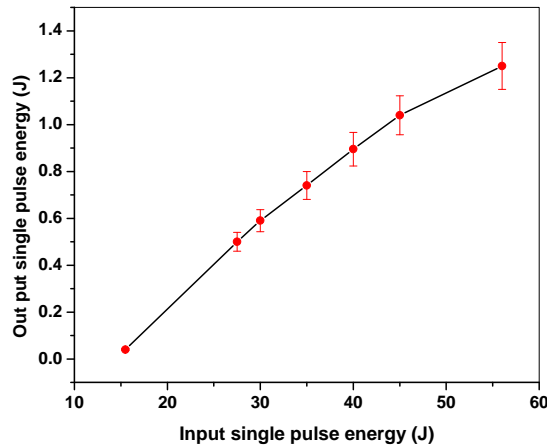


**Fig. 4.11.** Variation of output single pulse energy with input single pulse pump energy.

Fig. 4.11 shows linear variation of output single pulse energy with average input pump pulse energy to the flash lamp. Maximum single pulse energy of 1.25 J and ~ 22 kW maximum output peak power was achieved for ~56 J total pump pulse energy. Electrical-to-optical conversion efficiency of 2.23% was achieved at the maximum pump pulse energy. At the maximum input voltage of 1225 V and 20 Hz of repetition rate with an average combined input pump power of 1120 W for both the lamps (560 W per lamp), a maximum average output power of 25 W was achieved. Fig. 4.12 shows typical temporal evolution of the laser pulse at the maximum pump power. The temporal profile of the laser was measured at maximum pump power using a broadband photodiode (New focus, USA) incorporated with a RG 850 filter (Coherent, USA) and an oscilloscope (Lecroy, USA).

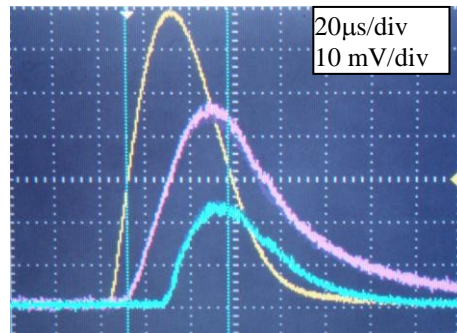


**Fig. 4.12.** A view of temporal shape of current pulse (yellow), flash lamp pump pulse (pink) & laser output pulse (blue).

Measured value of laser pulse width was 55  $\mu$ s at one third of the peak value of intensity in temporal domain. Pulse width was measured at one third of the peak value due to following reason. In a critically damped pulse forming network power supply rise time  $t_r = \sqrt{LC}$  is the time required for voltage or current to rise from zero to its maximum value. Here,  $L$  is the value of inductance and  $C$  is the value of capacitance in the pulse-forming network. Current pulse

duration  $t_p$  at 10% points is  $T$ , written as  $3T=3\sqrt{LC}$  (during this time about 97% energy has been delivered to lamp). In view of the above, it is customary to take pulse width at one third of the peak value in such lamp pumped systems instead of full-width at half maximum (FWHM). The spatial laser beam profile was also measured for maximum pump power using a CCD camera (Wincam-D, Gentec). Fig. 4.13 (a) and (b) show the typical spatial profile of direct laser beam and laser beam after exit from fiber.

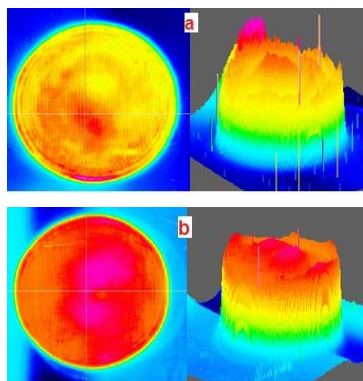


**Fig. 4.13.** *Spatial profile of the laser beam 2D (left) and 3D (right) view (a) Before fiber input end (direct laser beam) shows some hot spots (b) After fiber exit end beam profile becomes much more smooth.*

It was found that the spatial beam profile becomes much more smooth and uniform after delivery through the fiber. The hot spots in the laser beam profile get minimized at the exit fiber end as compared to the direct beam. The spatial profile of the laser beam becomes top-hat like after exit from the fiber since the fiber has a step-index profile with a constant refractive index in the core and an abrupt step transition to a different refractive index in the cladding. Total internal reflection in the fiber occurs at the core cladding interface for all modes. As the fiber used is highly multi-moded, when all the modes are filled, the output profile at the fiber end face will be a superposition of the intensity of all the modes, which results in a familiar “top-hat”

distribution. This “top-hat” distribution provides a relatively homogeneous beam with a stable spot size. The spatial profile of the output laser beam also depends on the length of the multi-mode fiber. In a long length of the fiber, all the modes get excited and mix properly resulting in almost a top-hat like beam profile as explained by Zhu *et al.* [83] in their recent study. Conversion of beam intensity to a top-hat like profile depends on several factors, which includes beam to fiber launching conditions, input spatial profile distribution, fiber inhomogeneities, and fiber bending [84].

For testing of performance and evaluation of this short pulse Nd:YAG laser for conservation applications, some experiments have also been performed to remove surface contamination on marble, stones (bera gray sand stone, and shale), zircaloy, and inconel-600. The effect of laser process parameters such as laser fluence, number of laser shots, and laser spot overlapping were also investigated. The utilization of this short pulse Nd:YAG laser for efficient cleaning of surface contaminations on marble, stones, zircaloy, and inconel materials for conservation will be explained in Chapter 7.

## **4.5 Conclusions**

In conclusion, a 200  $\mu\text{m}$ , fiber-coupled short pulse Nd:YAG laser was designed and developed for laser cleaning applications. An output peak power of 22 kW with 55  $\mu\text{s}$  pulse duration was achieved with an  $M^2$  value of  $\sim 28$  in multimode operations. This laser has been tested successfully for cleaning of surface contamination of marble for the conservation of historical buildings and artworks. It has also been tested for cleaning of the surface contamination of zircloy and inconel for potential use in different parts of nuclear facilities such as pressure tubes and steam generator tubing of PHWR (Pressurized Heavy Water Reactors). The

performance of this laser shows that it can be used for surface cleaning of contamination over a wide range of other materials also like concrete, stones, stainless steel, copper, niobium, titanium, and aluminium.

# Chapter 5

---

## Study on novel birefringence compensation schemes for single rod and dual rod long pulse Nd:YAG laser resonators

### 5.1 Introduction

Linearly polarized, high power Nd:YAG laser is used for different applications such as laser material processing, electro-optic Q-switching, and second harmonic generation (SHG) [13,85-87]. Polarization state of the laser beam has a strong influence on its absorption in the material [88]. For example, in the case of iron, percentage absorption of un-polarized light is ~35%, for *p*-polarized light it is ~65%, and for *s*-polarized light it is ~10% at  $70^\circ$  angle of incidence [89]. Thus, *p*-polarized Nd:YAG laser beam is highly beneficial for grooving and welding applications in metals due to its high absorption at a large angle of incidence [90].

Laser operation in pulsed mode is more suitable for material processing as compared to continuous wave (CW) mode in terms of minimum thermal distortion and small heat affected zone [32]. Hence, development of *p*-polarized and long pulse duration lamp pumped Nd:YAG laser is of potential importance.

In order to generate linearly polarized beam, a polarizer is generally inserted in the resonator. However, it leads to a significant reduction in the output power. This reduction in the output power occurs due to thermally induced stress birefringence in the Nd:YAG rod. It limits

linearly polarized output power by introducing depolarization losses and also distorts the laser beam spatial profile.

A number of techniques have been reported to compensate the effect of thermally induced birefringence and for enhancement of linearly polarized output power in single and dual-rod Nd:YAG lasers [91-93]. In single rod Nd:YAG lasers, most commonly used optical element for birefringence compensation is either a  $45^\circ$  Faraday rotator (FR) or a quarter-wave ( $\lambda/4$ ) plate [94-95]. A  $45^\circ$  FR located between the laser rod and the rear mirror is more effective for compensation, but FR is based on magneto-optic effect and has a bulky magnetic assembly. Moreover, a FR uses a Terbium Gallium Garnet (TGG) crystal, which has a low bulk damage threshold of  $\sim 5 \text{ J/cm}^2$  for 10ns pulses of 1064 nm. Hence, it is not suitable for commercial grade high peak power pulsed Nd:YAG lasers.

A  $45^\circ$  quartz rotator (QR) is a simple, cost effective optical element with a high damage threshold of  $\sim 20 \text{ J/cm}^2$  for 10 ns pulses. It may provide a good alternative. However, it will not be effective when it is placed between the laser rod and the rear mirror since the rotation of the polarized light is cancelled when the beam passes second time through the rotator on its way back to the rod [27]. On the other hand, a  $\lambda/4$ -plate at an appropriate location could reduce the depolarization losses and compensate the birefringence. However, it has been observed that this scheme of birefringence compensation is satisfactory for  $\text{TEM}_{00}$  mode of operation, but is not adequate in high power multimode lasers [96-97]. Thus, novel and simpler schemes of birefringence compensation in place of  $45^\circ$  FR are still required for single rod Nd:YAG laser operation. In dual rod Nd:YAG laser, a widely used birefringence compensation optical element is a  $90^\circ$  quartz rotator (QR) placed between two identically pumped rods [27,98]. Using this method, linearly polarized output power of the order of kW in diode pumped continuous wave

(CW) Nd:YAG laser operation, has already been reported [99-100]. However, there are only a few reports on the generation of linearly polarized output in pulsed operation of Nd:YAG laser with high average and peak power [101].

In this chapter, we have focused on the investigation of novel birefringence compensation schemes for single and dual Nd:YAG rod laser resonator. These schemes are based on the use of simple optical elements in the laser resonators for efficient birefringence compensation, reduction of depolarization losses, and enhancement of  $p$ -polarized output power. We have analyzed and optimized resonator configuration for long pulse operation to achieve high average power, higher slope efficiency, better alignment stability, good beam quality, and better pulse-to-pulse stability.

In single Nd:YAG rod laser resonator, as compared to conventional schemes, we have introduced a novel approach to compensate birefringence which uses a tilted Glan-Taylor polarizer (GTP) in the resonator. This innovative method is advantageous in the sense that it avoids separate use of polarizer and quarter-wave plate to compensate depolarization loss in Nd:YAG laser. It performs better than quarter-wave plate scheme in high power multimode operation. However, this scheme was found to work well only up to a limited pump power level of  $\sim 3$  kW. As cutting and welding application of thick metals require Nd:YAG lasers of much higher power and pulse energy, we have further investigated another simple and novel optical scheme for birefringence compensation in single Nd:YAG rod resonator. In this scheme, a  $90^\circ$  QR tilted at Brewster's angle has been utilized in the laser resonator between the output coupler mirror and the laser rod for effective birefringence compensation even at higher pump powers of up to 5 kW. Re-entrance of rejected beam (at Brewster's angle) in the resonator using a highly reflective (HR) plane mirror, further improves the  $p$ -polarized power in the output beam. Using

this scheme, generation of 215 W of  $p$ -polarized average output power with 4.5% slope efficiency has been demonstrated. To the best of our knowledge, this is highest reported slope efficiency in long pulse (1-20 ms), linearly  $p$ -polarized operation of a lamp pumped single rod Nd:YAG laser.

Similarly, for dual-rod laser resonator, we have introduced a folded resonator configuration with a simple optical scheme for effective birefringence compensation. Using this scheme, a maximum of 415 W of  $p$ -polarized average output power with a slope efficiency of 4.3% has been demonstrated. Some of the potential applications of this dual-rod, long pulse, linearly  $p$ -polarized Nd:YAG laser include laser welding, cutting, and grooving of titanium and aluminium for automotive, aerospace and vacuum components industries.

In Section 5.2, we describe theoretical background for birefringence and its compensation. In Section 5.3, we give the details of birefringence compensation in single rod laser resonator using tilted Glan-Taylor polarizer and  $90^\circ$  QR at Brewster's angle in subsections 5.3.1 to 5.3.4. In Section 5.4, we provide details of birefringence compensation in dual rod laser resonator in subsections 5.4.1 and 5.4.2 and in Section 5.5 we have given the conclusions.

## 5.2 Theoretical background

Heating of Nd:YAG laser rod due to broadband emission from flash lamps and quantum defect leads to a non-uniform temperature distribution in the rod. Thermal lensing and stress-induced birefringence are the two important thermal effects, which occur in the Nd:YAG laser material. Change in the refractive index of Nd:YAG rod can be separated into a temperature and a stress-dependent variation given as  $n(r) = n_0 + \Delta n(r)_T + \Delta n(r)_\epsilon$ , where  $n(r)$  is the radial variation of the refractive index,  $n_0$  is the refractive index at the center of the rod, and  $\Delta n(r)_T$ ,

$\Delta n(r)_\varepsilon$  are the temperature and stress dependent changes of the refractive index, respectively. Stresses give rise to thermal strains in the Nd:YAG laser rod which in turn generate refractive index variations via photo-elastic effect [7]. Thus, a pumped Nd:YAG laser rod behaves like a thick lens. The principal birefringence axes lie along the radial ( $r$ ) and tangential ( $\phi$ ) directions in the cross-section of cylindrically symmetric laser rod. The overall thermal focal length  $f_{(r,\phi)}$  of the rod is given by [7].

$$f_{(r,\phi)} = \frac{1}{D_{(r,\phi)}} = \frac{KA}{P_h} \left( \frac{1}{2} \frac{dn}{dT} + \alpha C_{(r,\phi)} n_0^3 + \frac{\alpha r_0 (n_0 - 1)}{L} \right)^{-1} \quad (5.1)$$

where,  $P_h$  is the thermal power dissipated in laser rod of cross sectional area  $A$  and length  $L$ .  $D_{r,\phi}$  is the thermal refractive power of the rod,  $r_0$  is rod radius,  $\alpha$  is the coefficient of thermal expansion, and  $C_{r,\phi}$  are the radial and tangential polarization dependent elasto-optical coefficients of Nd:YAG rod. Thermal power dissipation in the rod ( $P_h$ ) is proportional to the electrical input pump power ( $P_E$ ) to the flash lamp and is given by  $P_E = K_0 I^2 t_p f_p$ . Here,  $K_0$  is the lamp impedance parameter having a value of 18 for the flash lamps used in our experiments. In order to calculate thermal lensing in laser rods the value of  $P_h$  is selected as 10% of  $P_E$  for the lamp pumped system. The lamp current ( $I$ ), pulse duration ( $t_p$ ) and repetition rate ( $f_p$ ) can be varied using a microcontroller based power supply. In a cylindrical coordinate system, the photo-elastic changes in the refractive index for  $r$  and  $\phi$  polarizations are given by  $n_r = -\frac{1}{2} n_0^3 \Delta B_r$  and  $n_\phi = -\frac{1}{2} n_0^3 \Delta B_\phi$ . A considerable amount of tensor calculation is required to determine the coefficients  $\Delta B_r$  and  $\Delta B_\phi$  in a plane perpendicular to the [111]-direction of the Nd:YAG crystal. Stress or strain in the laser rod is characterized by the elasto-optical coefficients into the matrix form  $p_{nm}$  of the photo-elastic tensor ( $m, n=1, 2, 3, 4, 5, 6$ ), stress tensor  $\sigma_{kl}$  and strain tensor  $\varepsilon_{kl}$  ( $k,$

$l=1, 2, 3$ ). For Nd:YAG crystal, approximate values of the elasto-optical coefficients are given by  $p_{11}=-0.0290$ ,  $p_{12}=0.0091$ , and  $p_{44}=-0.0615$ . The induced birefringence in the Nd:YAG rod is determined from [7]

$$\Delta n_r - \Delta n_\phi = n_0^3 \frac{\alpha Q}{K} C_B r_0^2 \quad (5.2)$$

where,

$$C_B = \frac{1+\nu}{48(1-\nu)} (p_{11} - p_{12} + 4p_{44}). \quad (5.3)$$

Inserting the values of the photo-elastic coefficients and the material parameters of Nd:YAG,  $\alpha=7.5 \times 10^{-6} / ^\circ\text{C}$ ,  $K = 0.14 \text{ W/cm}^2 / ^\circ\text{C}$ ,  $\nu = 0.25$ ,  $n_0 = 1.82$  into Eq. (5.3), the induced birefringence in the Nd:YAG laser rod is given by [21]

$$\Delta n_r - \Delta n_\phi = (-3.2 \times 10^{-6}) Q r_0^2 \quad (5.4)$$

Here,  $Q$  is proportional to the absorbed pump power  $P_a$  dissipated as heat in the Nd:YAG rod of length  $L$  with total heat load  $A_0$ , and is given by  $P_a = A_0 (\pi r_0^2 L)$ . The principal axes of the induced birefringence are radially and tangentially directed at each point in the laser rod cross-section and the magnitude of the birefringence increases quadratically with rod radius. Birefringence is always zero at the centre of the rod ( $r_0=0$ ). Birefringence is also zero if the heat dissipated in the laser rod is zero.

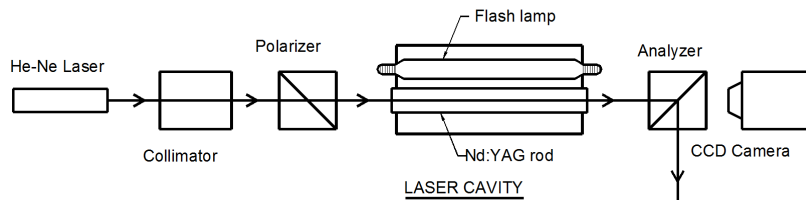


**Fig. 5.1.** A schematic view of experimental set-up for recording of conoscopic pattern.

Birefringence effects in pumped laser rods can be studied using conoscopic method in which an expanded and collimated linearly polarized beam of He-Ne laser serves as an illuminator for the observation of rod between two crossed polarizers (Fig. 5.1).

Polarized He-Ne probe beam suffers depolarization due to thermally induced birefringence in the rod and hence it is only partially transmitted by the analyzer. The transmitted beam forms the so-called isogyres, which display the geometrical locus of constant phase differences. This pattern is known as conoscopic birefringence pattern. Fig. 5.2 shows conoscopic patterns of single crystal 1.1 at.% Nd:YAG rod ( $\phi$  10 mm  $\times$  150 mm length) for different input pump powers. There are hyperbolic isogyres with cross and rings in the conoscopic pattern. Hyperbolic isogyres illustrate that single crystal rod has become biaxial and crosses correspond to those regions of the crystal where an induced (radial or tangential) axis is along a polarizer axis, so that the induced birefringence results only in a phase delay and not in a polarization rotation. Rings in the conoscopic pattern show the radial dependence of birefringence and it corresponds to an integral number of full waves of retardation.

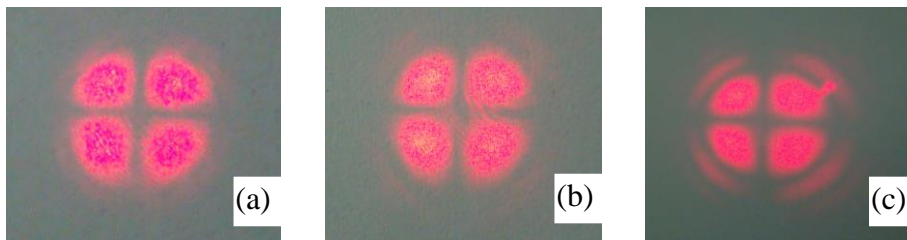


**Fig. 5.2.** The experimentally recorded *birefringence pattern of single crystal Nd:YAG rod for (a)1 kW, (b)3 kW, and (c)5 kW of average input pump power, respectively from left to right.*

When a birefringent crystal is placed between a polarizer and analyzer that are crossed, the transmitted intensity  $I_t$  is given by [7]

$$I_t = \frac{I_{out}}{I_{in}} = 1 - \sin^2(2\phi) \sin^2(\delta/2) \quad (5.5)$$

where  $\phi$  is the angle between the polarizer and one of the principal birefringent axes and  $\delta$  is the polarization phase shift of the light emerging from the crystal. A linearly polarized beam after passing through a pumped Nd:YAG laser rod, experiences a substantial depolarization. Depolarization loss is defined as the ratio of the depolarized output power to the initially linearly polarized power. The total amount of depolarization  $d_p$  at each point  $(r, \phi)$  in the plane perpendicular to the direction of the beam propagation ( $z$ -axis) in the cylindrical Nd:YAG rod is given by [102]

$$d_p = \sin^2[2(\theta - \gamma)] \sin^2\left(\frac{\delta}{2}\right) \quad (5.6)$$

Here,  $\theta$  indicates the angle between polarization direction and one of the birefringence eigenvectors  $(r, \phi)$ ,  $\gamma$  represents the angle between  $y$ -axis and the direction of initial polarization and  $\delta$  is the phase difference between radial and tangential polarization components as shown in Fig. 5.3.

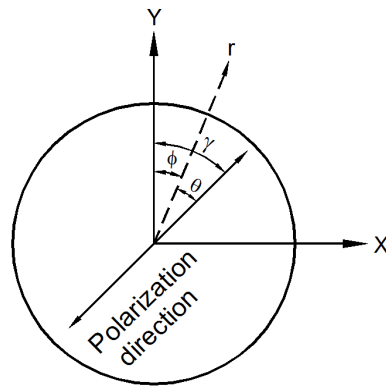


**Fig. 5.3.** Relationship of angle  $\theta$ ,  $\phi$ , and  $\gamma$  with polarization direction and rod cross-section in  $x$ - $y$  plane, beam propagates in the  $z$ -direction.

### 5.3 Birefringence compensation in single Nd:YAG rod resonator

As discussed earlier, there are only a few reports on the generation of linearly polarized beam of high average power long pulse Nd:YAG laser. For example, Bhusan *et al.* [103] have reported the generation of 100 W of average *p*-polarized output power in long pulse, single rod Nd:YAG laser operation. We have performed some experiments using simple and novel optical schemes to generate high average power *p*-polarized laser beam in single rod Nd:YAG laser resonator for long pulse operation and these schemes will be described in the following subsections.

#### 5.3.1 Study of birefringence compensation using tilted GTP

In the first scheme, a Glan-Taylor polarizer (GTP) of size 10 mm × 10 mm × 10 mm has been used for birefringence compensation in a flash lamp pumped, long pulse single rod Nd:YAG resonator. Crystal orientation and ray propagation in GTP is shown in Fig. 5.4. GTP is composed of two symmetric calcite prisms cemented with 1 mm of air gap in between. Here, GTP acts as a phase retarder and as a Brewster's plate in its tilted position. To obtain required tilt (see Fig. 5.5), the GTP is given a rotation of angle  $\theta$  with respect to face normal and another rotation by  $\phi$  with respect to an axis perpendicular to the optic axis.

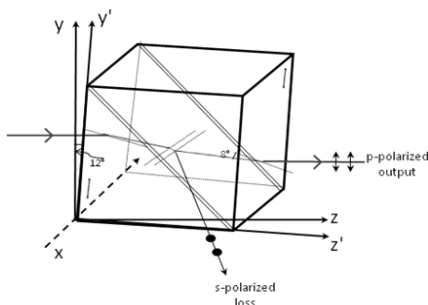


**Fig. 5.4.** Crystal orientation and ray propagation in Glan-Taylor polarizer.

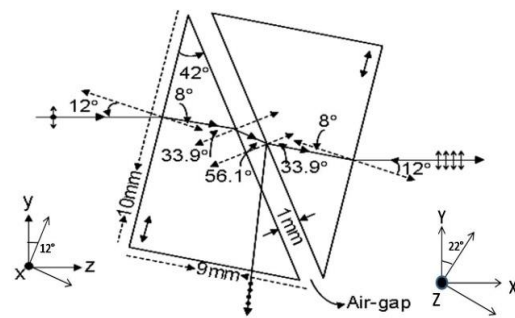


**Fig. 5.5.** Glan-Taylor polarizer tilted with respect to *x*-axis of laboratory frame.

Working of GTP can be analyzed by using Jones matrices of various components of resonator.

Jones matrix (see Appendix 1) of a GTP for transmission of a beam can be written as [104]

$$GTP_B = \begin{pmatrix} S & 0 \\ 0 & 1 \end{pmatrix} \quad (5.7)$$

At Brewster angle, all the  $p$ -polarized light will pass through GTP and  $s$ -polarized light will pass only by a factor  $S$ . For a single pass,  $S$  can be calculated by [105]

$$S = \left( \frac{2n_e(\phi)}{n_e^2(\phi) + 1} \right)^2 \quad (5.8)$$

which amounts to 0.857 for calcite crystal with  $n_e(\phi) = 1.4888$  at 1064 nm. Where,

$$\frac{1}{n_e^2(\phi)} = \frac{\sin^2 \phi}{n_e^2} + \frac{\cos^2 \phi}{n_o^2} \quad (5.9)$$

Jones matrix for phase retardation of GTP is given by

$$GTP(\delta) = \begin{pmatrix} e^{-i\delta/2} & 0 \\ 0 & e^{i\delta/2} \end{pmatrix} \quad (5.10)$$

Here, we allow only  $p$ -polarization to oscillate (in laboratory frame,  $y$ -axis) in the resonator. The phase  $\delta$  introduced by the GTP for an  $e$ -polarized (also  $p$ -polarized) normally incident beam, can be determined as [27]

$$\delta(y) = \frac{2\pi}{\lambda} (n_e(\phi) - 1)(2y - a) \quad (5.11)$$

here,  $y$  is the entrance height of the beam in the GTP,  $a$  is the length of GTP in the  $z$  direction.

Jones matrix of a pumped Nd:YAG rod with the birefringence phase difference of  $\Gamma$  is written as

$$Rod(\Gamma) = \begin{pmatrix} e^{i\Gamma/2} & 0 \\ 0 & e^{-i\Gamma/2} \end{pmatrix} \quad (5.12)$$

If  $\theta$  is the angle between the laboratory frame and the thermally induced dielectric axes in the transverse plane of the rod, the transformation matrix is given by

$$R(\theta) = \begin{pmatrix} \cos \theta & \sin \theta \\ -\sin \theta & \cos \theta \end{pmatrix} \quad (5.13)$$

According to Jones matrix formulation, the round-trip matrix starting from the output coupler to the rear mirror and back, when there is no compensating element can be written as

$$M_{unpol} = R(-\theta).Rod(\Gamma).Rod(\Gamma).R(\theta) = \begin{pmatrix} e^{i\Gamma} \cos^2 \theta + e^{-i\Gamma} \sin^2 \theta & -2i \sin \Gamma \cos \theta \sin \theta \\ -2i \sin \Gamma \cos \theta \sin \theta & e^{-i\Gamma} \cos^2 \theta + e^{i\Gamma} \sin^2 \theta \end{pmatrix} \quad (5.14)$$

Therefore, selecting  $x$ -polarization (with respect to laboratory frame) as loss by inserting an intra-cavity polarizer of matrix  $\begin{bmatrix} 0 \\ 1 \end{bmatrix}$ , the uncompensated depolarized component  $E_x^{uncomp}$  is given by

$$E_x^{uncomp} = -2i \sin \Gamma \cos \theta \sin \theta \quad (5.15)$$

And hence the uncompensated depolarization loss fraction for thermal birefringence at  $(r, \theta)$  in the transverse plane of the rod will be,

$$l_D^{uncomp} = E_x^{uncomp} \bullet E_x^{uncomp\dagger} = -\sin^2 \Gamma \sin^2 2\theta \quad (5.16)$$

The total uncompensated depolarization loss can be derived by integrating over the cross section of the rod as,

$$L_D^{uncomp} = \frac{1}{\pi r_0^2} \int_0^{2\pi} \int_0^{r_0} l_D^{uncomp} r dr d\theta = \frac{1}{4} [1 - \sin c(2C_T P_h)] \quad (5.17)$$

For compensation, the round-trip matrix  $M$  would be the multiplication of all the matrices of the components in the path taken in appropriate order with tilted-GTP as a compensating element inside the resonator placed in between the laser rod and the output coupler, which can be written as

$$M = GTP_B.GTP(\delta).R(-\theta).Rod(\Gamma).Rod(\Gamma).R(\theta).GTP(\delta).GTP_B \\ = \begin{pmatrix} e^{-\frac{i\delta}{2}} (e^{\frac{i\Gamma}{2}} \cos^2 \theta + e^{-\frac{i\Gamma}{2}} \sin^2 \theta) & e^{\frac{i}{2}(\delta+\Gamma)} (e^{i\Gamma} - 1) S \sin \theta \cos \theta \\ e^{-\frac{i}{2}(\delta+\Gamma)} (e^{i\Gamma} - 1) S \sin \theta \cos \theta & e^{\frac{i\delta}{2}} (e^{-\frac{i\Gamma}{2}} S \cos^2 \theta + e^{\frac{i\Gamma}{2}} \sin^2 \theta) \end{pmatrix} \quad (5.18)$$

Therefore,

$$E_x^{comp} = e^{2i(\delta+\Gamma)} (e^{i\Gamma} - 1) S \sin \theta \cos \theta \quad (5.19)$$

and hence the depolarization intensity loss will be

$$I_D^{comp} = E_x^{comp} \bullet E_x^{comp\dagger} = 2(1 - \cos \Gamma) S^2 \cos^2 \theta \sin^2 \theta \quad (5.20)$$

where,

$$\Gamma = \frac{C_T P_h r^2}{r_0^2} \quad C_T = \frac{2n_0^3 \alpha C_B}{\lambda K}$$

and  $\alpha$  is the thermal expansion coefficient,  $K$  is the thermal conductivity,  $P_h$  is the power dissipated from the laser rod as heat.  $C_B$  depends on Young's modulus, poisson ratio and photo-elastic tensor elements. The total depolarization loss  $L_D$  for a plane-polarized light due to the stress birefringence by the laser rod can be obtained by integrating the above equation over the cross-section of the rod and can be written as

$$L_D = \frac{1}{\pi r_0^2} \int_0^{2\pi} \int_0^{r_0} (2(1 - \cos \Gamma) S^2 \sin^2 \theta \cos^2 \theta) r dr d\theta \quad (5.21)$$

After integration and simplification of the above Eq., we get

$$L_D = \frac{S^2}{4} \left\{ 1 - \frac{\sin(C_T P_h)}{C_T P_h} \right\} \quad (5.22)$$

The calculated value of total depolarization loss using the above equation was found to be 0.1804 with the values of  $n_0=1.82$ ,  $\alpha= 6.9 \times 10^{-6}/^\circ\text{C}$ ,  $C_B= -0.0099$ ,  $\lambda=1064$  nm,  $K=14$  W/m<sup>0</sup>K,  $r_0=4$  mm,  $P_h=100$  W, and  $S=0.857$  for [111]-cut Nd:YAG rod.

In the experimental set-up, laser pump chamber contains an antireflection (AR) coated, 1.1 at. % doped Nd:YAG rod of diameter 8 mm and length 150 mm (Laser Material Inc., USA). The rod is kept in a pump chamber consisting of a close coupled gold-coated elliptical reflector and a 10 mm bore diameter and 136 mm arc length Kr-filled flash lamps. A 10% Samarium oxide doped glass filter plate with a 1 mm wall thickness is kept between the rod and lamp to absorb the unwanted UV radiation from the lamp and to re-radiate in the pump band of Nd:YAG.

A plane-plane symmetric resonator (Fig. 5.6) has been designed using a 99.9% HR (High Reflectivity) plane rear mirror and 60% plane output coupler. An aperture of diameter 4 mm was inserted to reduce the beam diameter in the cavity so that the beam is accommodated within the clear opening of the tilted GTP of size 10 mm × 10 mm × 10 mm. The average electrical input power ( $P_E$ ) of the flash lamp was varied by means of variation in pulse width from 1 to 20 ms and repetition rate from 1 to 50 Hz, respectively. The maximum value of  $P_E$  is 5 kW. GTP with antireflection coated faces at 1064 nm was placed on a Goniometer mount near the output coupler mirror within the cavity to generate polarized laser output. Experimentally, it was observed that with two angular rotations at the calculated angles with respect to the  $x$  and  $z$ -direction in the laboratory frame,  $z$ -being the resonator axis the GTP acts as a compensating element in the laser resonator. When the pump power is varied, the rotation of GTP needs to be adjusted for optimized compensation. The polarization of the output beam from the laser cavity was analyzed using another polarizer.

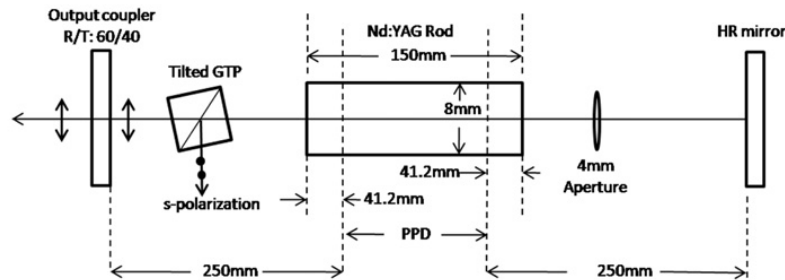


**Fig. 5.6.** Experimental set-up of resonator for compensation of birefringence.

### 5.3.2 Results and analysis with GTP in the resonator

Let  $P_1$  be the output power measured without any polarizing element or compensating element inside the cavity and  $P_2$  be the output power measured when a polarizer is introduced in

the cavity to select a particular polarization.  $P_3$  be the output power measured when both the polarizer and a compensating element is present in the resonator. Then the experimentally measured depolarization loss is calculated by

$$D_{WC} = \frac{P_2 - P_1}{P_1} \times 100 \% \text{ (Without compensation)} \quad (5.23)$$

$$D_C = \frac{P_3 - P_1}{P_1} \times 100 \% \text{ (With compensation)} \quad (5.24)$$

Output power  $P_1$  is recorded without the GTP in the resonator, and  $P_2$  is recorded with GTP in the resonator. When the GTP is placed inside the cavity with its surface normal to the cavity axis, the output power  $P_2$  reduces. Measurement of compensation was also performed using a quarter-wave plate and thin film polarizer. A comparison of compensated output power with input pump power for different optical compensating elements is plotted in Fig. 5.7.

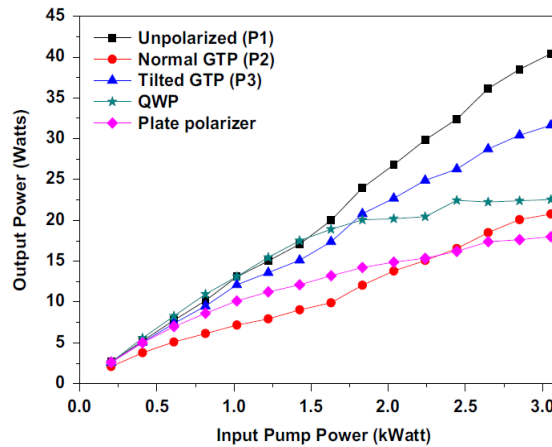


**Fig. 5.7.** Output power versus input pump power from single Nd:YAG rod resonator with different optical components GTP,  $\lambda/4$ -wave plate, and plate polarizer.

It is clear that tilted GTP compensates better than other component at high pump power. Fig. 5.8 shows that a single optical element (GTP) reduces the depolarization loss quite efficiently. This scheme reduces the depolarization loss from 29% to 13.3% at 1.83 kW of input pump power [92]. After birefringence compensation with tilted GTP, an average output power of 30 W was

achieved as compared to 17 W of average output power on using only a plate polarizer in the resonator without birefringence compensation.

At low input pump power, plate polarizer provides more output power as compared to normal GTP whereas the situation is reversed at higher input pump power. This experimental observation can be explained by considering thermo-optic effect of the polarizer's material. The plate polarizer works on the principle of Brewster's effect, whereas GTP works on the principle of total internal reflection. The variation of Brewster's angle with temperature ( $d\theta_B/dT$ ) for fused silica based plate polarizer is  $3.8 \times 10^{-6} \text{ rad/}^\circ\text{C}$ ; whereas the variation of  $d\theta_B/dT$  for calcite based GTP is  $1.3 \times 10^{-6} \text{ rad/}^\circ\text{C}$ . This clearly accounts the crossing over of the curves for normal GTP and plate polarizer, as the angular position of the polarizer has not been adjusted at each value of input pump power.

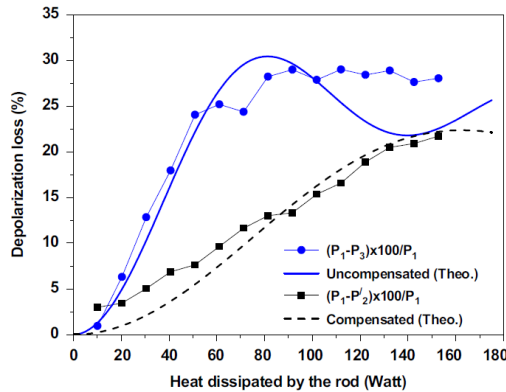


**Fig. 5.8.** Depolarization loss versus heat dissipation in the rod. Theoretical values of losses are shown by solid and dotted line. Experimental values are shown by closed circle and closed square.

Ordinary and extra-ordinary refractive indices of Calcite at 1064 nm are 1.658 and 1.47964. Using these data, calculated value of the critical angle for 'o' ray is  $\sim 37^\circ$ . Ordinary rays experience total internal reflection, when they are incident on the prism-air interface at  $\sim 42^\circ$  under normal position of GTP. When a tilted GTP was placed in the resonator, output power was

found to vary with the tilting of GTP along the axis of the beam propagation as well as perpendicular to it. It was found that when the GTP angular position corresponds to  $\theta=12^\circ$  and  $\phi=22^\circ$ , depolarization loss reduces significantly. To explain the process of depolarization compensation, we can refer to the schematic of a Glan-Taylor polarizer as shown earlier in Fig 5.5, where the polarizer has been tilted by an angle of  $12^\circ$  with respect to  $x$ -axis. This rotation helps to obtain the required Brewster's angle for the incidence beam at the interface between the air-gap and the second prism of the GTP. This tilt also suppresses the total internal reflection for the ordinary beam. Using Sellmeier's coefficients, refractive indices of ordinary and extraordinary beam were calculated including the angle  $\theta=12^\circ$  for calcite [106]. Another tilt of  $22^\circ$  with respect to the face normal of the GTP effectively contributes to obtain the required phase difference to compensate the depolarization loss due to thermal birefringence of the Nd:YAG rod. This innovative method of birefringence compensation is advantageous in the sense that it avoids separate use of polarizer and quarter-wave plate to compensate the depolarization loss in Nd:YAG laser. It performs better than quarter-wave plate scheme in high power and compensates well even for multimode operation.

### **5.3.3 Study of birefringence compensation using $90^\circ$ QR**

Koechner and Rice [107] have analyzed depolarization loss as a function of the rod axis orientation in a uniform lamp pumped single Nd:YAG rod resonator. Their investigation illustrates that the depolarization loss depends on the direction of initial polarization represented by angle  $\gamma$  as shown in Fig. 5.3 in the case of [100]-and [110]-cut Nd:YAG crystals, however, it is independent of angle  $\gamma$  in the case of [111]-cut crystal. Shoji *et al.* [108], Punken *et al.* [109], and later Tünnermann *et al.* [110] have also investigated that the depolarization loss changes

with the angle  $\gamma$  for [100]-and [110]-cut Nd:YAG crystals. They have shown that the relation  $\theta=\phi$  in any plane as given by Koechner is true only for the [111]-direction cut crystals. The relation of  $\theta$  and  $\phi$  for the [100]- and [110]- plane of Nd:YAG crystal is given by [107,108]

$$\tan(2\theta) = \frac{2p_{44}}{p_{11} - p_{12}} \tan(2\phi) \quad (5.25)$$

$$\tan(2\theta) = 8p_{44} \tan(2\phi) [3(p_{11} - p_{12}) + 2p_{44} - (p_{11} - p_{12} - 2p_{44})(2 - r_0^2 / r^2)(1 / \cos(2\phi))]^{-1} \quad (5.26)$$

Sun *et al.* [111] have found that the overall depolarization loss of the [111]-cut rod is about 2 times higher than that of the [100]-cut rod at the angle  $\gamma=\pi/4$ . Similarly, Puncken *et al.* [109] found that the depolarization could be reduced by a factor of 6 in [100]-cut crystals for a suitable value of angle  $\gamma$ . Thus, it is clear from the literature that the depolarization loss in Nd:YAG laser rod can be minimized if the beam enters the rod at a suitable angle  $\gamma$  in the case of [110]- and [100]- cut Nd:YAG crystals.

In our experiments, it has been observed that the depolarization loss can be reduced significantly with suitable angle  $\gamma$  even for the [111]-cut Nd:YAG rod if the laser rod is non-uniformly pumped, which has not been pointed out earlier [107-111]. For a single lamp pump chamber the assumption of non-uniform pumping of the laser rod is justified as the laser rod and flash lamps are kept at the two focii of the close coupled, gold-coated elliptical reflector one half of the laser rod is pumped directly by the flash lamp and the other half is pumped after reflection from the elliptical reflector. Hence, the optical pumping of the rod is non-uniform and the photo-elastic coefficient tensor of the rod and subsequently the depolarization losses are different in different directions of the rod and depend on the angle  $\gamma$ . A typical simulated cross-sectional view of non-uniform pumped [111]-cut Nd:YAG crystal rod of 8 mm diameter is shown in Fig. 5.9.

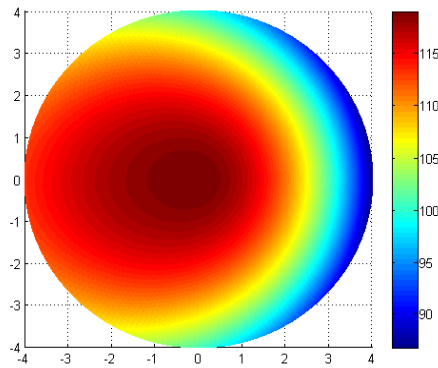


**Fig. 5.9.** A simulated cross-sectional view of non-uniform pumped Nd:YAG rod on placing it in pump chamber with an elliptical gold-coated reflector.

For experimental study, a plane-plane symmetric resonator has been designed using a plane 99.9% HR rear mirror and plane 60% output coupler mirror. The single crystal Nd:YAG rod ( $\phi$  8 mm  $\times$  150 mm long) with [111]-cut crystal direction was pumped by a Kr-filled flash lamp ( $\phi$  8 mm  $\times$  136 mm arc length). The ends of the laser rod were anti-reflection coated for 1064 nm. In the initial part of the experiment, output power was measured without placing a polarizer in the resonator.

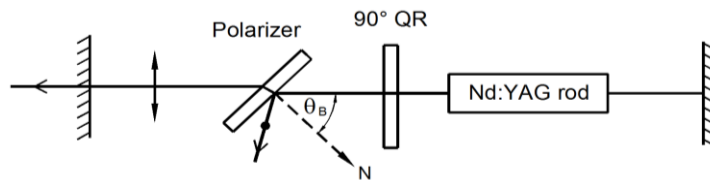


**Fig. 5.10.** A  $90^\circ$  QR placed between plate polarizer and Nd:YAG rod.

The output power was measured in four different configurations (a) First, a plate polarizer (CVI Melles Griot) with polarization extinction ratio (PER) ( $T_p/T_s$ ) of  $\sim 700:1$  at Brewster angle ( $\theta_B=55.4^\circ$ ) was inserted between laser rod and the output coupler mirror. (b) Then a 38 mm

diameter,  $90^\circ$  quartz rotator (QR) (Fujian Castech, China) was placed between the plate polarizer and Nd:YAG rod (VLOC, USA) as shown in Fig. 5.10. (c) Further, plate polarizer was removed and  $90^\circ$  QR tilted at Brewster's angle ( $\theta_B=55.4^\circ$ ) was placed in the resonator. It works both as a polarizer as well as polarization rotating element and saves an additional optical element (plate polarizer) in the resonator (Fig. 5.11). (d) Finally, a plane highly reflective (HR) re-entering feedback mirror was placed in the resonator (Fig. 5.11) for further enhancement of the  $p$ -polarized output power.

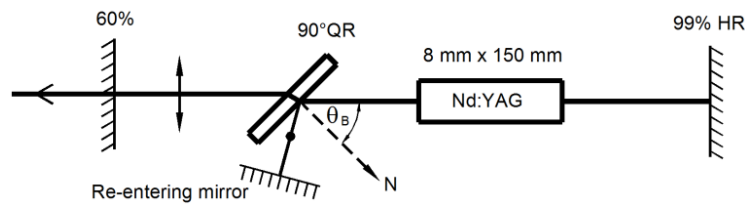


**Fig. 5.11.** A  $90^\circ$  QR placed at Brewster's angle ( $\theta_B=55.4^\circ$ ), which works both as a polarizer as well as polarization rotating element. A HR re-entering mirror provides feedback for the rejected beam.

First we consider the configuration with only a polarizer at Brewster angle in the resonator. Starting from the rear mirror, an unpolarized laser beam having two polarizations states  $s$  and  $p$  passes through the laser rod and is incident on the polarizer at Brewster's angle. According to Fresnel's relation, the polarizer rejects 15% of  $s$ -polarized part of the laser beam. Hence, 85% part of the  $s$ -polarized beam and 100% of  $p$ -polarized beam pass through the polarizer. On the return path the laser beam 100%  $p$ -polarized and 85%  $s$ -polarized after reflection from the partial (60%) output coupler mirror, again passes through the polarizer and 15% of the  $s$ -polarized part is once again rejected by the polarizer. After few round trips, only  $p$ -polarized part of the laser beam will sustain in the resonator. Without using any birefringence compensation, this  $p$ -polarized laser beam suffers significant depolarization losses by the

pumped Nd:YAG laser rod due to stress induced birefringence. Hence, in this case, only 118 W of the  $p$ -polarized laser output was obtained for 5 kW of average input pump power.

When a  $90^\circ$  QR tilted at the Brewster's angle is placed between the output mirror and laser rod in place of the plate polarizer, it works both as a polarizer as well as a polarization rotating element. Starting from the rear mirror, an unpolarized laser beam having two polarizations  $s$  and  $p$ , first passes through the laser rod and is then incident on the  $90^\circ$  QR at Brewster's angle. According to the Fresnel's relation, due to incidence of beam on QR at Brewster's angle,  $p$ -polarized part of the beam will be transmitted fully ( $\sim 100\%$ ), while 85% of the  $s$ -polarized part of the beam will be transmitted and  $\sim 15\%$  will be rejected. At the same time, transmitted  $p$ -polarized and  $s$ -polarized parts of the laser beam will also get rotated by an angle of  $\sim 100^\circ$  from the original position, as it has passed through the tilted  $90^\circ$  QR as in configuration c. In this case, 100%  $p$ -polarized part of the laser beam becomes almost 100%  $s$ -polarized part and 85%  $s$ -polarized part of the laser beam becomes almost 85%  $p$ -polarized part. After reflection from the 60% output coupler mirror, laser beam is again incident on the  $90^\circ$  QR at Brewster's angle in the return path. Now, 85%  $p$ -polarized part is converted into 85%  $s$ -polarized part after passing through the  $90^\circ$  QR. On the other hand, out of 100%  $s$ -polarized part of the laser beam, 15% of  $s$ -polarized part is rejected by tilted  $90^\circ$  QR and the remaining 85%  $s$ -polarized part is transmitted through the  $90^\circ$  QR and is converted into 85%  $p$ -polarized part. Hence, 85%  $s$ -polarized and 85%  $p$ -polarized part of laser beam will now pass through the pumped Nd:YAG laser rod. Now, the 85% part of the  $s$ -polarized laser beam (which is actually  $\sim 100^\circ$  rotated original  $p$ -polarized part of the laser beam) suffers minimum depolarization loss on passing through the laser rod. On the round trip, this  $s$ -polarized laser beam ( $\sim 100^\circ$  rotated  $p$ -polarized) becomes  $p$ -polarized before exit from the output mirror as it passes through the  $90^\circ$  QR second

time before facing the output coupler mirror. This occurs in every round trip of laser beam in the resonator and  $p$ -polarized part of the laser beam is enhanced. In this case, 198 W of the  $p$ -polarized output power was achieved for 5 kW of average input pump power. Further, when an HR re-entering feedback mirror was introduced in the resonator (configuration d as shown in Fig. 5.11), 215 W of the  $p$ -polarized output power was achieved because the rejected part of the  $s$ -polarized component now re-enters in the resonator and is converted in the  $p$ -polarized component after four passes. Jones matrix analysis for the resonator having  $90^\circ$  QR tilted at the Brewster's angle can be found in appendix at the end of this thesis.

For the round trip depolarization loss measurement, pump-probe method was used [27,108]. A collimated and linearly polarized probe beam of 1.5 W CW Nd:YAG laser was passed through the laser rod under different pumping conditions. An analyzer was placed in the crossed condition after the Nd:YAG rod and a power meter was placed behind the analyzer to measure the power of the depolarized component of the probe beam as shown in Fig. 5.12. Depolarization loss from the thermally induced birefringence in the laser rods is defined as the ratio of the depolarized power to the initially polarized power [102].

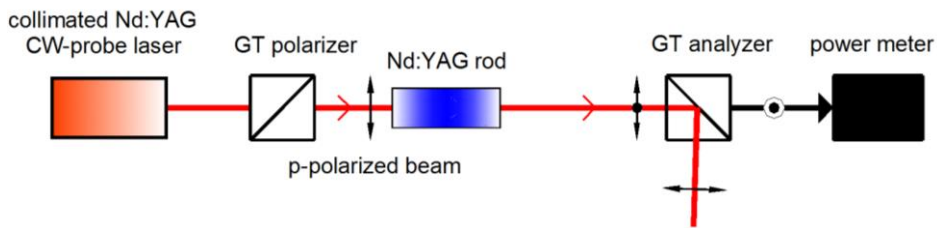


**Fig. 5.12.** Experimental scheme for the measurement of depolarization loss using Glan Taylor (GT) polarizer and analyzer.

### 5.3.4 Results and analysis with 90° QR

For the observation and comparison of conoscopic patterns of non-uniformly and uniformly pumped Nd:YAG rods, a gold-coated elliptical reflector and a circular diffuse ceramic reflector based laser pump chamber was used. Flash lamp pumped Nd:YAG rod was placed between the crossed polarizer and collimated He-Ne beam was passed through it under different pumping conditions and conoscopic pattern was recorded using a CCD camera (Watec, Japan). For the variation of angle  $\gamma$  of the polarized He-Ne laser beam, a  $\lambda/2$ -wave plate was placed between the polarizer and laser rod as shown in Fig. 5.13. The angle  $\gamma$  can be changed by rotating the  $\lambda/2$ -wave plate around its fast axis. For example, if  $\lambda/2$ -wave plate rotates by an angle  $\alpha$  with respect to fast axis, the plane of polarization of the linearly polarized beam rotates by an angle  $2\alpha$ . Hence, for the change in angle  $\alpha$  from 0 to  $\pi$ , the polarization angle  $\gamma$  changes from 0 to  $2\pi$ .

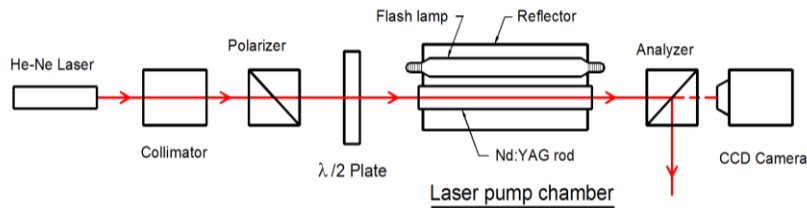


**Fig. 5.13.** *Experimental set-up using  $\lambda/2$ -wave plate for the recording of conoscopic pattern.*

Fig. 5.14 shows the conoscopic pattern of Nd:YAG rod under the uniform (with circular ceramic reflector) and non-uniform (with gold-coated elliptical reflector) pumping conditions at different angles  $\gamma$ . It shows that the conoscopic pattern for the non-uniformly pumped rod changes with variation in angle  $\gamma$ . On the other hand, no significant change is observed in the conoscopic pattern for the uniformly pumped laser rod. Hence, it is clear that for the non-

uniformly pumped rod, depolarization loss can be minimized with the selection of a suitable angle  $\gamma$  even for the [111]-cut Nd:YAG rod.

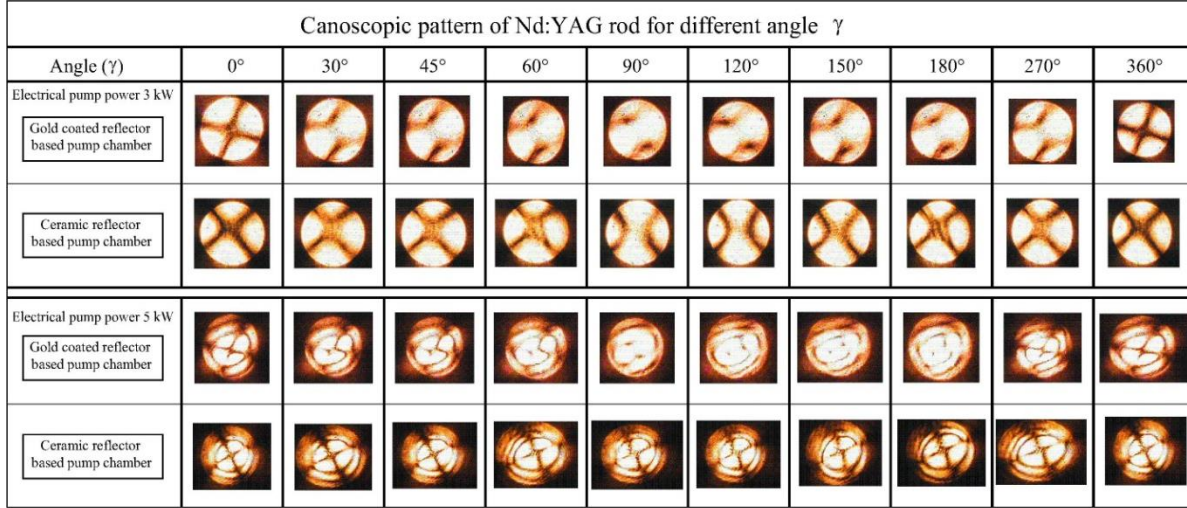


**Fig. 5.14.** *Canoscopic pattern of Nd:YAG rod for different angle  $\gamma$  using gold coated and ceramic reflector. The patterns were recorded for 3 kW and 5 kW average input pump powers.*

From the above analysis, it was found that a  $90^\circ$  QR is a good option for enhancing  $p$ -polarized output power, if it is placed at the Brewster's angle ( $\theta_B=55.4^\circ$ ) between the laser rod and output coupler mirror in the resonator. In this condition it works both as a polarizer as well as a polarization rotating element for birefringence compensation. At Brewster angle, it rotates the polarization by  $\sim 100^\circ$  before the laser light enters the laser rod during a round trip in the resonator. Rotation  $\rho$  through quartz rotator depends on the optical path length  $d$  and is expressed by the Fresnel formula [112]

$$\rho = \pi d(n_L - n_R) / \lambda \quad (5.27)$$

where  $n_L$  and  $n_R$  are the refractive indices for the left and right circularly polarized rays, respectively. For the QR used in this experiment  $d$  has a value of 14 mm and the path length becomes 16 mm, when QR is tilted at Brewster's angle. The sense of rotation is reversed, if the

propagation vector is reversed. This fact can be observed in the conoscopic pattern for different values of angle  $\gamma$  for which the linearly polarized light enters the rod during the round-trip in the laser resonator. Figure 5.14 shows that for a variation of angle  $\gamma$ , from  $90^\circ$  to  $120^\circ$ , the conoscopic pattern contains minimum isogyres, which indicates that depolarization loss in the rod becomes minimum between these angles. QR cancels the polarization rotation during the round trip of the beam in the resonator and the beam passes through QR without any significant  $p$ -polarized power losses. Further, on using a plane HR re-entering feedback mirror in the resonator, the maximum average output power in the  $p$ -component was enhanced up to 215 W from 198 W at 9 ms pulse duration and 10.9 Hz repetition rate with 4.52% slope efficiency as shown in Fig. 5.15.

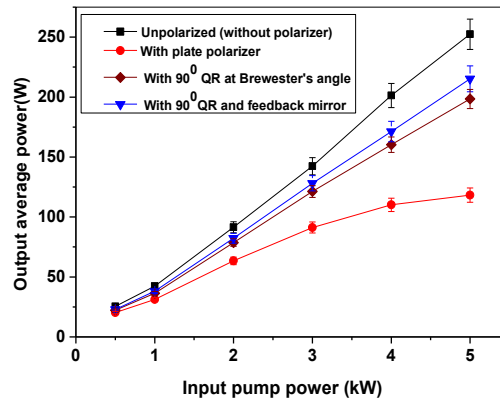


**Fig. 5.15.** Variation of output power with input pump power using different optical components in the resonator.

An increase in the  $p$ -polarized output power of more than 80% was achieved as compared with  $p$ -polarized output of 118 W with only one polarizer placed in the resonator. The maximum single pulse output energy in  $p$ -polarized beam was 80 J at 20 ms pulse duration. Experiment were also performed using  $45^\circ$  QR,  $22^\circ$  QR and a plane window ( $0^\circ$  QR) placed at Brewster's

angle in the same resonator in place of  $90^\circ$  QR. The measured enhancement in  $p$ -polarized power was only 20%, 14% and 2%, respectively for these three cases. Hence,  $90^\circ$  QR was found more suitable for  $p$ -polarized power enhancement as compared to the QR's of other angles. A detailed explanation of  $p$ -polarized output power enhancement with use of re-entering mirror is already available in literature [93,113].

It was observed that re-entering HR mirror not only enhances the  $p$ -polarized power, but it also improves the value of polarization extinction ratio (PER) of the laser beam. Polarization extinction ratio (PER) of the output laser beam was measured by transmitting the beam through a polarizer mounted on a rotating stage. When the polarizer is rotated, output power of transmitting beam is changed. If  $P_{max}$  and  $P_{min}$  are the maximum and minimum power transmission through the polarizer, then the PER (measured in dB) is given by  $PER=10 \log (P_{max}/P_{min})$ . PER of the output laser beam was measured in different conditions using two intra-cavity optical elements: (i) with  $90^\circ$  QR at the Brewster angle and (ii) with  $90^\circ$  QR and HR re-entering feedback mirror. The measured values of polarization extinction ratio (PER) in the above cases were (a) 9.8 dB and (b) 12.2 dB, respectively at the maximum average output power, which shows that the value of PER is substantially enhanced with a re-entering mirror.

Depolarization losses were measured before and after placing  $90^\circ$  QR at Brewster's angle. It was observed that the depolarization loss increases almost linearly with the pump power and reduces significantly on placing the  $90^\circ$  QR in the resonator. The depolarization loss was ~34% at the maximum pump power of 5 kW, when only a polarizer was placed in the resonator (before compensation) and it reduced significantly to a value of ~9% after placing a  $90^\circ$  QR (after compensation) as shown in Fig. 5.16 [114]. Fig. 5.17 shows the variation of  $M^2$  as a function of input pump power before and after the birefringence compensation. A lower value of

the  $M^2$  means a better beam quality of the laser in multimode operation. It was observed that the beam quality in multi mode operation was improved after placing  $90^\circ$  QR at Brewster angle. The value of  $M^2$  was found to be 52 for maximum pump power (5 kW), when only a polarizer was placed in the resonator (for the birefringence uncompensated resonator), which improved to a value of 45 when  $90^\circ$  QR was placed at the Brewster's angle (for the birefringence compensated resonator). The value of  $M^2$  improves further after placing a re-entering HR mirror in the resonator and reaches a value of 43 [114]. This improvement in beam quality is highly beneficial in laser material processing applications.

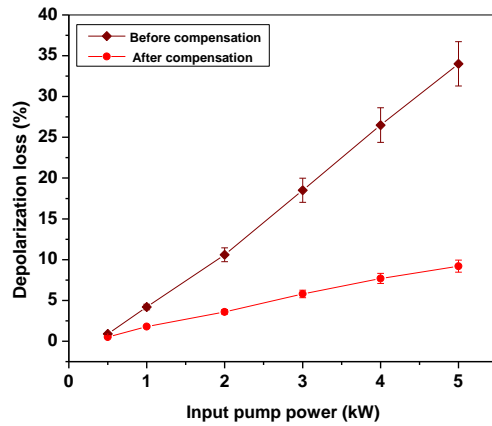


**Fig. 5.16.** Variation of depolarization loss with input pump power, before compensation (with polarizer) and after compensation (with  $90^\circ$  QR).

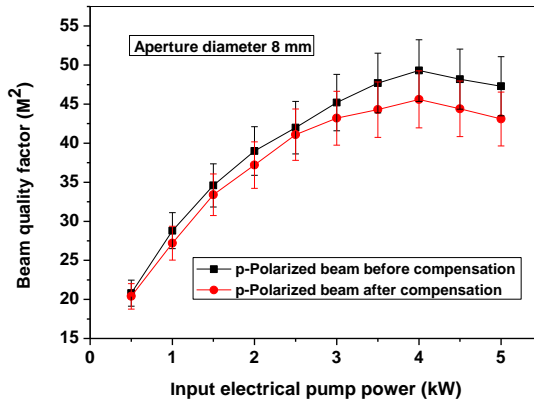


**Fig. 5.17.** Variation of  $M^2$  as a function of pump power with and without  $90^\circ$  QR.

Laser output beam profile measurements using a CCD camera (Wincam-D, Gentec) shows that after placing  $90^\circ$  QR at Brewster's angle, beam shape distortion was found to be reduced as compared to placing only polarizer in the resonator as shown in the Fig.5.18 and 5.19.

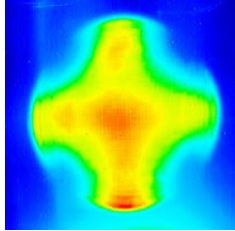


**Fig. 5.18.** Laser beam profile on placing only a polarizer in the laser resonator shows a distortion in the beam shape.

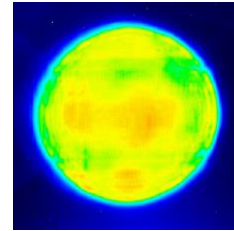


**Fig. 5.19.** Laser beam profile after placing a  $90^\circ$  QR at Brewster's angle shows reduction in distortion of beam shape.

In conclusion it was shown that the depolarization losses can be reduced significantly from a value of  $\sim 34\%$  to  $\sim 9\%$  using a tilted  $90^\circ$  QR. Further, this scheme has resulted in a significant enhancement (more than 80%) of  $p$ -polarized output power as compared to the use of only a polarizer in the resonator. It was found that laser beam quality also improves with  $90^\circ$  QR in the resonator. Thus, we have investigated a cost effective, simple and novel optical scheme for generation of high power  $p$ -polarized beam in long pulse single rod Nd:YAG laser.

#### **5.4 Birefringence compensation in dual Nd:YAG rod laser resonator**

In dual rod Nd:YAG laser resonators, a widely used birefringence compensation technique is the use of a  $90^\circ$  quartz rotator (QR) between two identically pumped laser rods. Using this technique, linearly polarized output power in diode pumped continuous wave (CW) Nd:YAG lasers in kW range has already been reported [93,99]. However, there are only a few reports on the generation of linearly polarized output in pulsed operation of dual rod Nd:YAG

laser [101]. Lu et al. [115] have demonstrated effective birefringence compensation scheme using an intra-cavity  $90^\circ$  QR and a dual lens imaging system in a linear resonator configuration for 1 ms long pulses in a lamp pumped dual rod Nd:YAG laser. This scheme was found to reduce depolarization losses significantly from a value of 26% to a value of 5% for 6 kW of electrical input pump power per rod. This effective birefringence compensation scheme has also been utilized by Moshe *et al.* [93] and Wang *et al.* [116] for efficient generation of linearly polarized output power. Using almost similar scheme, Ostermayer *et al.* [101] have demonstrated 182 W of average output power in quasi-CW operation of dual rod Nd:YAG resonator with pulse duration of 250  $\mu$ s which was operated at 980 Hz of repetition rate. However, the schemes proposed in references [93], [101] and [115] have used linear resonator geometry and the length of the resonator is long due to use of intra-cavity lens imaging system. Such a long and linear resonator geometry is affected strongly by drift in optical alignment due to the long length of support structure. This in turn affects the misalignment sensitivity of the laser resonator. One of the possible solutions to overcome this problem is the introduction of folding resonator geometry, which reduces the deflection of support structure because of its shorter length in each arm and it also improves the misalignment sensitivity and stability of the laser system.

We carried out experimental investigation of  $z$ -fold laser resonator geometry for effective birefringence compensation to generate high average power linearly polarized laser output. We have analyzed the  $z$ -fold resonator geometry in terms of average  $p$ -polarized output power, depolarization losses, beam quality, pulse-to-pulse stability, and misalignment sensitivity. For the  $z$ -fold resonator design, a simple optical scheme using concave mirrors has been utilized, which acts as a folding mirror as well as a rod-imaging configuration for birefringence compensation. These concave mirrors have been kept at small angles with respect to each other

for the minimization of astigmatism from mirrors. Average output power of  $p$ -polarized light was enhanced further by using a plane high reflectivity re-entering feedback mirror in the resonator. Using this scheme, a maximum linearly  $p$ -polarized average output power of 415 W with 150 J of pulse energy and 4.3% slope efficiency has been demonstrated. To the best of our knowledge, this is the highest average output power, pulse energy, and slope efficiency reported in long pulse (1-20 ms) linearly  $p$ -polarized operation of a flash lamp-pumped dual-rod Nd:YAG laser. This linearly  $p$ -polarized Nd:YAG laser will be highly suitable for laser material processing applications.

#### 5.4.1 Study on birefringence compensation using z-fold resonator

Design and analysis of dual-rod linear resonator geometry for generation of high average power long pulse Nd:YAG laser has already been presented in Chapter 2. This chapter describes the design of folded resonator geometry in  $z$ -fold configuration for long pulse Nd:YAG laser operation.

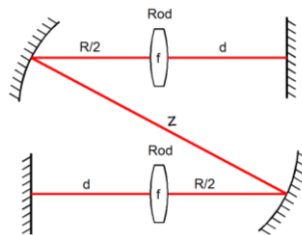


**Fig. 5.20.** An equivalent schematic diagram of the  $z$ -fold resonator having two Nd:YAG rods with thermal focal lengths ( $f$ ) and two concave mirrors for rod imaging.

The proposed  $z$ -fold resonator geometry consists of a plane output coupler and rear mirror along with two concave mirrors of radius of curvature (R.O.C.)  $R$  for folding the resonator. The distance ( $d$ ) between the plane mirrors and principal planes of the rod was

optimized such that the resonator remains stable for the whole range of input pump power. The distance between the concave mirrors ( $z$ ) were also optimized. Figure 5.20 shows equivalent  $z$ -fold resonator geometry.

For dual-rod  $z$ -fold resonator geometry, single pass ABCD matrix can be written as [117]

$$\begin{pmatrix} A & B \\ C & D \end{pmatrix} = \begin{pmatrix} 1 & d \\ 0 & 1 \end{pmatrix} \begin{pmatrix} 1 & 0 \\ -1/f & 1 \end{pmatrix} \begin{pmatrix} 1 & R/2 \\ 0 & 1 \end{pmatrix} \begin{pmatrix} 1 & 0 \\ -2/R & 1 \end{pmatrix} \begin{pmatrix} 1 & z \\ 0 & 1 \end{pmatrix} \begin{pmatrix} 1 & 0 \\ -2/R & 1 \end{pmatrix} \begin{pmatrix} 1 & R/2 \\ 0 & 1 \end{pmatrix} \begin{pmatrix} 1 & 0 \\ -1/f & 1 \end{pmatrix} \begin{pmatrix} 1 & d \\ 0 & 1 \end{pmatrix}$$

Stability condition for the resonator is expressed by  $0 \leq g_1 g_2 \leq 1$  and the value of  $g_1 g_2$  is related with the elements of round trip ABCD matrix by

$$g_1 g_2 = (A + D)^2 / 4 \quad (5.28)$$

For example, for 5 kW of input pump power per rod the values of different parameters are  $d=30$  cm,  $f=36$  cm,  $R=50$  cm,  $z=30$ . With these values, the explicit expression for the single pass ABCD matrix is given by

$$\begin{pmatrix} A & B \\ C & D \end{pmatrix} = \begin{pmatrix} -0.2933 & -38.8 \\ 0.0236 & -0.2933 \end{pmatrix}$$

Thus,  $A+D=-0.5866$ , which provides a value of  $g_1 g_2$  for the resonator as 0.08, indicating that the resonator remains stable for the chosen values of different parameters even up to the maximum input pump power of 5 kW per rod.

Long length resonators are in general strongly affected by the small misalignment or deviation of the support structure as compared to a short resonator. Misalignment in long resonator geometry may occur due to the temperature gradient or thermal expansion of opto-mechanical components. Sensitivity of the resonator to the support structure instability scales as a function of the resonator length  $L$  approximately by  $L^{3/2}$  [118]. Since a folding geometry maximizes tolerance to structural misalignment, overall resonator length and geometry is an

important factor while designing a laser resonator. Transverse displacement of the beam on imaging concave mirrors due to slight misalignment of the resonator may also change the imaging condition for birefringence compensation and thereby result in additional depolarization losses. Misalignment of one of the concave mirrors by angle  $\theta$  results in the shift in axis by an amount of  $R^2\theta/(2R-z)$ , where  $R$  is the R.O.C. of the mirrors and  $z$  is the distance between them. Overall resonator length  $L$  in  $z$ -fold geometry can be reduced if we select a smaller value of distance  $d$  or  $z$ . A smaller value of  $d$  degrades the laser beam quality, since the beam quality factor ( $M^2$ ) of the laser beam in a plane-plane symmetric resonator depends on  $d$  and is given by [69]

$$M^2 = \frac{\pi r_0^2}{2\lambda d} [dD_{(r,\phi)}(2-dD_{(r,\phi)})]^{1/2} \quad (5.29)$$

Hence, value of  $d$  should not be reduced below a certain optimized value for which the resonator remains stable for the entire pumping range of up to 5 kW per rod. The length  $L$  of the resonator can also be reduced by selecting a smaller value of  $R$  of the folding concave mirrors, but it affects the resonator stability and beam quality. Further, the distance between principal plane of the rod and the concave mirror is also fixed at  $R/2$  to meet the imaging condition. Hence, we cannot select smaller value of  $R$  of the concave mirrors for reduction of the length  $L$ . Thus, reduction in the value of distance  $z$  is the only possible way to reduce the overall length of the  $z$ -fold resonator as well as to ensure its stable operation. It is possible to reduce the value of  $z$  to a value much smaller than  $2f$ , where  $f=R/2$ . In references [101] and [115], it has been pointed out that the distance between the intra-cavity imaging lenses should be fixed at  $2f$  distance for better imaging of the laser rods. However, it has been found experimentally that the value of  $z$  smaller than  $2f$  or  $R$  in the case of concave mirror imaging system of  $z$ -fold resonator does not affect birefringence compensation and resonator stability. Thus, the value of  $z$  was reduced from

a value of 50 cm (which is equal to  $R$  in our experiment) to a value of 30 cm for the reduction of total resonator length  $L$  and also to minimize the alignment criticality of the laser system.

A major problem associated with the use of concave folding mirrors is astigmatism. It is associated with the difference in focal length of the concave mirror in tangential and sagittal planes as shown in Fig. 5.21.

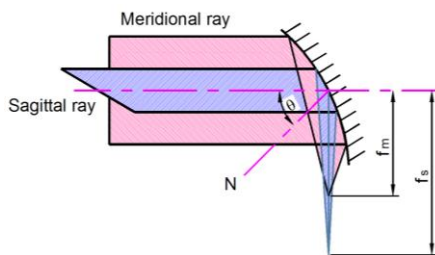


**Fig. 5.21.** Ray tracing diagram to show astigmatism of a concave mirror with  $f_s$  and  $f_m$  as the focal lengths for tangential and sagittal rays and  $\theta$  as the incident angle of the input rays with respect to optic axis.

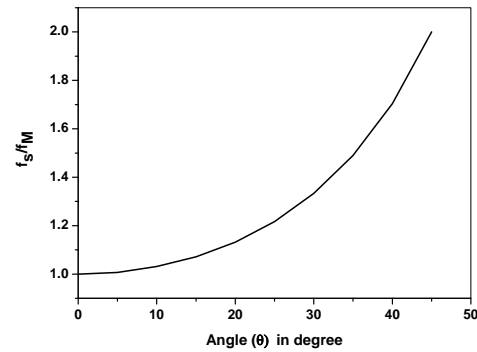


**Fig. 5.22.** Variation of the ratio  $f_s/f_m$  as a function of angle  $\theta$ .

Focal length of the concave mirror for tangential and sagittal rays are given by [119]  $f_s = R/2\cos\theta$  and  $f_m = R\cos\theta/2$ , respectively. Here,  $\theta$  is the incident angle of the input rays with respect to optical axis of concave mirror. Ratio  $f_s/f_m$  as a function of angle  $\theta$  has been evaluated and its variation as a function of  $\theta$  is as shown in Fig. 5.22. It can be seen that for values of incident angles  $\theta \geq 15^\circ$ , the ratio  $f_s/f_m > 1$ , and focused beam becomes elliptical. For  $\theta = 45^\circ$ ,  $f_s/f_m = 2$ , hence circularity of the beam is completely distorted. Hence, for minimization of astigmatism in the resonator, the value of angle  $\theta$  should be selected such that  $\theta < 15^\circ$ .

A table top view of the experimental set up of  $z$ -fold resonator for birefringence compensation is shown in Fig. 5.23. Two identical laser pump chambers have been arranged in

z-fold resonator configuration. Each pump chamber contains an 8 mm diameter and 152 mm long 1.1% at.% Nd<sup>3+</sup>-doped YAG laser rod (Laser Material Inc., USA) and an 8 mm bore diameter, Kr-filled flash lamp (Heraeus Noblelight, UK). Both the ends of the Nd:YAG rods are antireflection (AR) coated at 1064 nm. The rod and lamp have been placed in a diffuse ceramic reflector chamber having a close-coupled rectangular geometry with 30 mm × 15 mm cross-section and 7 mm wall thickness. A 10% samarium oxide doped glass filter plate having 1 mm wall thickness is kept between rod and lamp. A flooded type cooling scheme has been used for efficient removal of heat load from the laser pump chamber. In this scheme, laser rod, flash lamp, samarium filter, and reflector inner surface are fully immersed in water. A closed-loop water-cooling unit providing 50 lpm of water flow rate at 20<sup>0</sup>C has been used. Calculated value of heat transfer coefficient is  $h= 9800$  (W/m<sup>2</sup> °K). With this optimum value of  $h$ , an efficient heat transfer was achieved, which resulted in high slope efficiency.

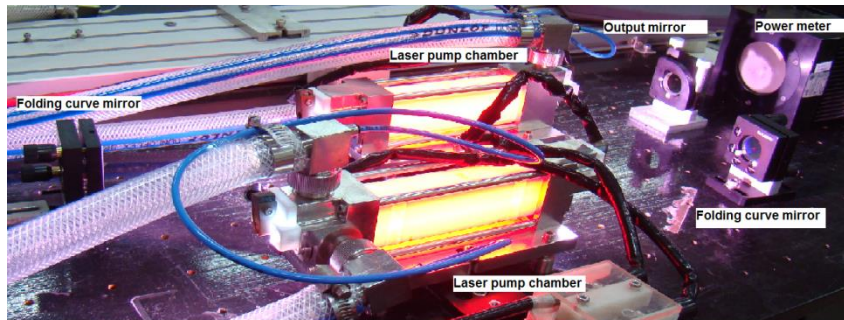


**Fig. 5.23.** A table top view of the experimental set-up of z-fold resonator.

The z-fold resonator consists of a plane rear mirror of ~99.8% reflectivity and 40% plane output coupler at 1064 nm. Two identical power supplies for flash lamps were used, which deliver maximum electrical average input pump power ( $P_E$ ) up to 5 kW per lamp with current variation in the range of 100-300 Amp., pulse duration in the range of 1-20 ms, and repetition

rate in the range of 1-100 Hz, respectively. The temporal profile of the current pulse has a rectangular shape. Two concave mirrors of 50 cm R.O.C. were used as folding mirrors in the resonator. These mirrors have been kept at angles of  $\theta=15^0$  with respect to each other. Further reduction in angle  $\theta$  was not possible in our experiment due to practical difficulties in keeping the laser pump chambers of finite width in optical path as the laser beam path is obstructed during the alignment of the resonator for angles  $\theta<15^0$ . Concave mirrors used in this experiment have  $\sim 99.8\%$  reflectivity at 1064 nm for  $15^0$  angle of incidence. For an optimum distance  $d=30$  cm, the resonator remains stable for the whole range of average input pump power from 0-5 kW per rod. The distance  $z$  between the two concave mirrors was varied from  $z=50$  cm to  $z=30$  cm. For  $z=30$  cm, the overall geometrical length of the resonator from output mirror to rear mirror was 168 cm.

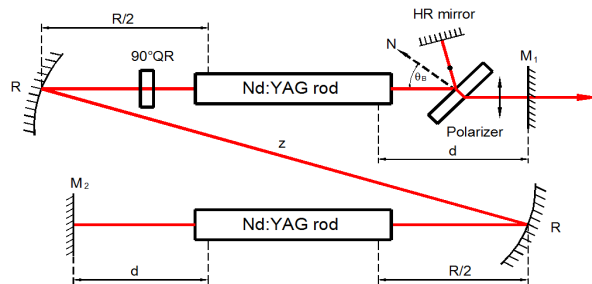


**Fig. 5.24.** A schematic view of birefringence compensation scheme of z-fold resonator having two concave mirrors, two Nd:YAG rods, a polarizer, a  $90^0$  QR, and a re-entering HR mirror.

Initially, the average output power from the resonator was measured without placing any polarizer in the resonator. Further, the output power was measured by placing different optical components in the resonator, namely; a plate polarizer having an extinction ratio ( $T_p / T_s$ ) of  $\sim 700:1$ , a  $90^0$  QR along with plate polarizer, and a plane highly reflective (HR) re-entering

feedback mirror along with plane polarizer and QR. Figure 5.24 shows a schematic of the birefringence compensation scheme in  $z$ -fold resonator configuration.

For measurement of depolarization losses, a probe beam of a collimated and linearly polarized 1.5 W CW Nd:YAG laser has been passed through the laser rods under different pumping conditions. An analyzer was placed in the crossed condition and a power meter was placed behind the analyzer to measure the power of the depolarized component of the probe beam as shown in Fig. 5.25.

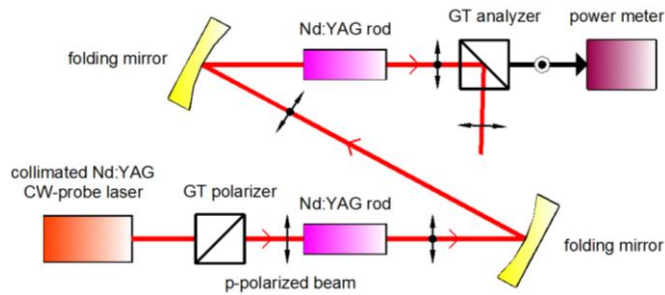


**Fig. 5.25.** A schematic view of experimental set-up for measurement of depolarization losses using Glan-Taylor (GT) polarizer and analyzer.

The power was measured, without placing a  $90^\circ$  QR (before birefringence compensation) and after placing a  $90^\circ$  QR in the resonator. The depolarization loss caused by the thermally induced birefringence in the laser rods is defined by the ratio of the depolarized power to the initially polarized power.

## 5.4.2 Results and analysis of $z$ -fold resonator

For  $z$ -fold resonator geometry, variation of  $g_{1g_2}$  as a function of input pump power using ABCD round trip matrix is as shown in Fig. 5.26. It shows that the resonator remains stable for a

wide range of average electrical input pump power in the range of 0-5 kW in each rod for two different values of distance  $z$  between the concave mirrors. For a change of the distance  $z$  from  $z=50$  cm to  $z=30$  cm, the resonator still remains stable. It indicates that a reduction in the length of  $z$ -fold resonator can be carried out without any change in its stability. A short length resonator is advantageous in terms of misalignment sensitivity and structural stability of the laser system as compared to unfolded linear resonator configuration. It was observed that for a value of  $z > 50$  cm or  $z < 30$  cm, the resonator did not remain stable over the full range of pump power. Thus, a value of  $z=30$  cm was selected in our experiments.

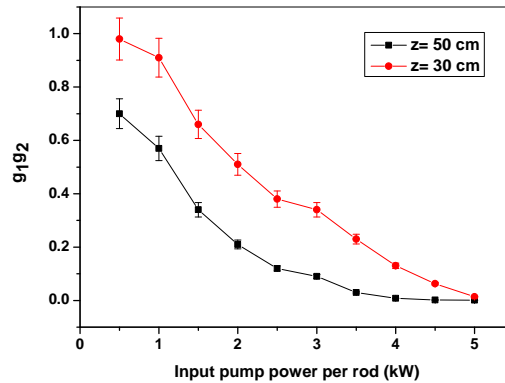


**Fig. 5.26.** Variation of  $g_1g_2$  for  $z$ -fold resonator as a function of average electrical input pump power.

Figure 5.27 shows variation of average output power as a function of average input pump power using different optical components in  $z$ -fold resonator. Without any intra-cavity polarizer, a maximum average output power of 503 W was achieved for an average input pump power of 5 kW per rod. When an intra-cavity polarizer was introduced in the resonator, output beam becomes  $p$ -polarized and the maximum average output power drops to a value of 234 W. Further, on placing a  $90^\circ$  QR between the two Nd:YAG rods,  $p$ -polarized average output power is enhanced to a value of 362 W. When a plane HR re-entering feedback mirror is introduced in

the resonator, the output power in the  $p$ -component is enhanced to a value of 415 W with 4.3% slope efficiency.

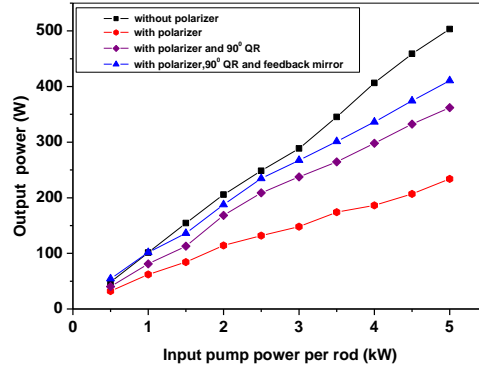


**Fig. 5.27.** Variation of average output power as a function of average input pump power using different optical components in  $z$ -fold resonator.

An increase in  $p$ -polarized average output power of more than 80% was achieved as compared to the  $p$ -polarized average output power of 234 W with only a polarizer placed in the resonator. Maximum output single pulse energy in  $p$ -polarized beam was 150 J at 20 ms pulse duration.

Pulse-to-pulse stability (PTPS) was measured for 1000 pulses and was better than  $\pm 3\%$  for the birefringence compensated  $z$ -fold resonator as compared to  $\pm 5\%$  for uncompensated resonator. This improvement in PTPS is due to the fact that before birefringence compensation, the stability zone of the resonator is divided in radial and tangential components. The overlapping part of this radial and tangential zone is small, and the stability points lie near the limit of the radial and tangential stability zones. After birefringence compensation, radial and tangential zones are merged and the stability points move slightly inside the stability zone thereby improving the PTPS stability of the resonator. It was found that before birefringence compensation, the value of misalignment sensitivity was 230  $\mu\text{rad}$  and after compensation, it improved to a value of 450  $\mu\text{rad}$ . This improvement in misalignment sensitivity is expected since

it is directly related with the losses due to the displacement of the mode axis with respect to the mode spot diameter [46]. For a plane-plane symmetric resonator, the fundamental mode spot radius  $w$  is given by [42]

$$w_{(r,\phi)}^2 = \frac{2d\lambda}{\pi} \cdot \frac{1}{\sqrt{dD_{(r,\phi)}(2-dD_{(r,\phi)})}} \quad (5.30)$$

From Eq. (5.30), it is clear that the fundamental mode spot radius within the laser rod is different for the radial and tangential polarization components and hence an uncompensated resonator is more sensitive to the misalignment. When a  $90^\circ$  QR is placed between two identical Nd:YAG rods, the polarization components are rotated by  $90^\circ$ . Hence, the radial and tangential polarization components are exchanged and the mode spot radius  $w$  in radial and tangential directions becomes equal, which improves the misalignment sensitivity of the resonator. Further, two different focal distances in the radial and tangential directions causes a split in the stability zones of the graph of fundamental mode beam size versus focusing power of the thermal lens for the uncompensated resonator as shown in Eq. (5.30).

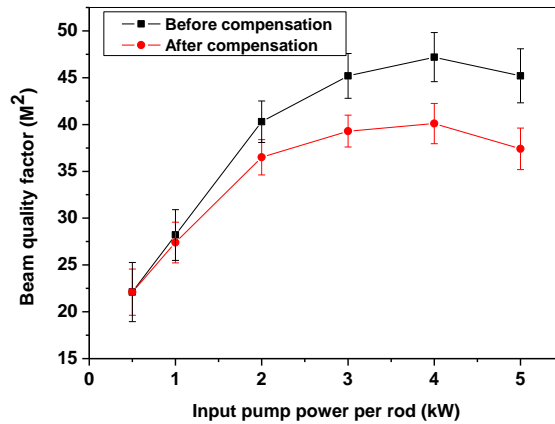


**Fig. 5.28.** Variations of  $M^2$  as a function of input pump power before and after birefringence compensation. Standard deviation of the data is presented as error bar in the curve.

After birefringence compensation, the radial and tangential zones merged and enhance the fundamental mode spot radius. It improves the beam quality factor ( $M^2$ ) of the laser beam in

multi mode operation as it is given by  $M^2 \approx (r_0/w_r, \phi)^2$ . Figure 5.28 shows the variation of  $M^2$  as a function of input pump power before and after birefringence compensation in  $z$ -fold resonator. After compensation, the measured value of  $M^2$  for maximum average input pump power was reduced to a value of 40 from a value of 47 for an uncompensated laser resonator. The polarization extinction ratio (PER) was also measured before and after birefringence compensation. The measured value of PER before birefringence compensation was 440:1 and 690:1 after compensation. A list of important measured parameters of  $z$ -fold resonator geometry is given in Table 5.1.

**Table 5.1:** Parameters of the  $z$ -fold resonator geometry.

Parameter	Value
Input electrical pump power (per rod)	5 kW
Unpolarized avg. output power (maximum)	503 W
$p$ -polarized output power (without compensation)	234 W
$p$ -polarized output power (after 90° QR)	362 W
$p$ -polarized output power (with 90° QR and re-entering mirror)	415 W
Slope efficiency (with 90° QR and re-entering mirror)	4.3%
<b>Polarization extinction ratio (PER)</b>	
(a) Before birefringence compensation	440:1
(b) After birefringence compensation	690:1
Maximum $p$ -polarized output pulse energy	150 J
Maximum $p$ -polarized output peak power	7.9 kW
$M^2$ (before compensation)	47
$M^2$ (after compensation)	40
PTPS (for 1000 pulses)	±3%
Misalignment sensitivity (10% power drop)	450 $\mu$ rad

Depolarization losses were measured using schemes as shown in Fig. 5.25. The depolarization loss increases almost linearly with the input pump power without birefringence compensation. Whereas, depolarization loss reduces significantly after placing the  $90^\circ$  QR and re-entering feedback mirror in the resonator. When only a polarizer was placed in the resonator, the measured value of percentage depolarization loss for the maximum average input pump power of 5 kW per rod was 35%, but it reduced to a value of 1.8% after placing a  $90^\circ$  QR and a HR re-entering feedback mirror in the resonator as shown in Fig. 5.29.

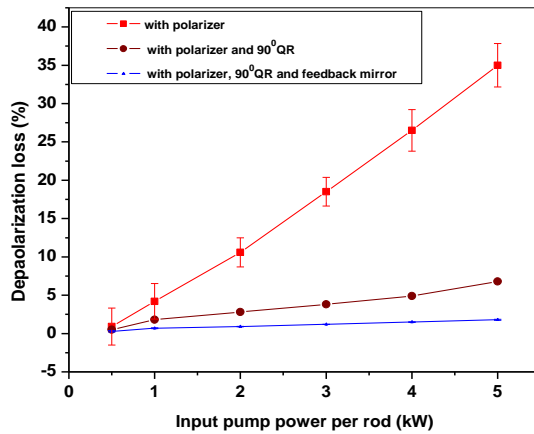


**Fig. 5.29.** Variation of measured value of depolarization loss as a function of average input pump power using polarizer,  $90^\circ$  QR, and re-entering feedback mirror in the resonator.

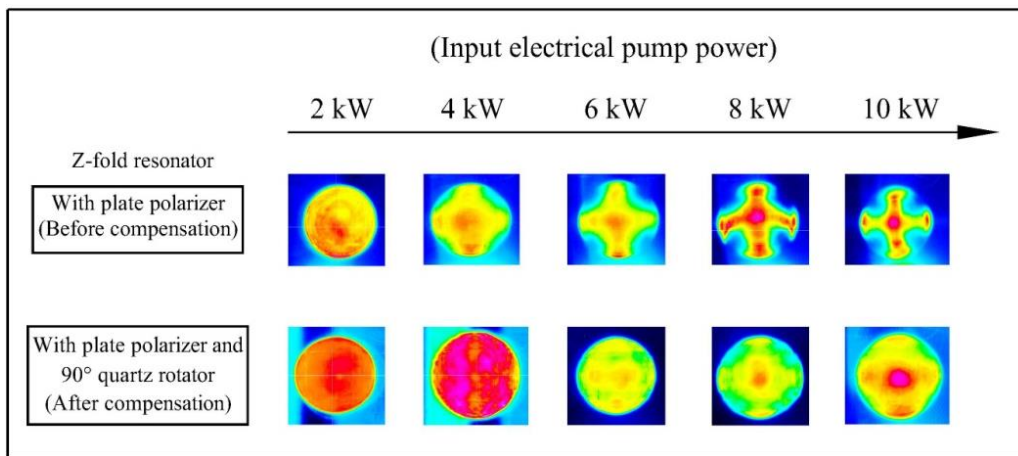


**Fig. 5.30.** Comparison of spatial profile of laser beam for dual-rod z-fold resonator at different values of average input pump power.

Spatial profile of the laser beam was also measured using a CCD camera (Wincam-D, Gentec).

**Table 5.2:** A comparison of resonator geometry and results of the earlier reported work

Method proposed by	Resonator configuration for experiment	Laser operation mode	Output power or energy	Efficiency	Depolarization losses after compensation	Beam quality factor ( $M^2$ )
Lu et al. [115] in 1996	Plane–plane resonator with linear geometry and lens imaging	Pulsed (lamp pumped)	40 J	Not reported	~5%	Multimode
Koji Yasui [121] in 1996	Concave resonator with plane folded mirror	CW (lamp pumped)	500 W	2.72% (overall efficiency)	Not reported	19
Inon Moshe [93] in 2002	Plane–plane linear resonator with re-entrance mirror and lens imaging	Pulsed (lamp pumped)	114 W	3% (overall efficiency)	~5%	Multimode
Ostermeyer et al. [101] in 2002	Plane–plane resonator with linear geometry and lens imaging	Quasi CW (lamp pumped)	182 W	7% (electro-optical efficiency)	~1%	1.2
Maik Frede et al. [98] in 2005	Plane–plane ring resonator geometry and lens imaging	CW (diode pumped)	114 W	23% (optical to optical)	Not reported	1.05
Yi-Ting Xu et al. in 2010	Convex–concave L-shaped resonator geometry	CW (diode pumped)	101.4 W	29.4% (optical to optical)	Not reported	1.14
Qing-Lei Ma In 2010 [122]	Plane-Plane resonator	CW (diode Pumped)	108 W	28.1% (slope efficiency)	Not reported	Multimode
Our present experiment	z-fold resonator with concave mirror imaging	Pulsed (lamp pumped)	415 W/ 150 J	4.3% (slope efficiency)	~1.8%	40

Figure 5.30 shows a comparison of the spatial profile of the output laser beam before and after birefringence compensation for different values of average input pump power. It shows that the shape of the beam is distorted at higher average input pump power in the rod, when a plate polarizer is introduced in the resonator [120]. However, introduction of a  $90^\circ$  QR for birefringence compensation improves the beam shape and uniformity in dual-rod  $z$ -fold resonator. Finally, we have achieved an efficient birefringence compensation in  $z$ -fold resonator geometry using a simple optical scheme consisting of concave mirrors, an intra-cavity  $90^\circ$  quartz rotator, and a re-entrant feedback mirror. This scheme resulted in an enhancement of  $p$ -polarized output power to more than 80% as compared to the  $p$ -polarized output power without birefringence compensation. Depolarization loss in the resonator has also been reduced significantly from a value of 35% to a value of  $\sim 1.8\%$  after birefringence compensation. Table 5.2 shows a comparison of our present work on the  $z$ -fold resonator geometry with the previous works in terms of  $p$ -polarized average output power, slope efficiency, depolarization losses and beam quality [120]. It can be seen that the performance of proposed  $z$ -fold resonator geometry for the birefringence compensation in dual Nd:YAG rod laser system is much better as compared to the linear resonator geometry in terms of beam quality, depolarization losses, alignment stability and pulse-to-pulse stability as proposed by Moshe *et al.* [93], Frede *et al.* [98], Ostermeyer *et al.* [101], Lu *et al.* [115], Yasui *et al.* [121] and Ma *et al.* [122].

## 5.5 Conclusions

In conclusion, we have investigated and achieved various novel and simple optical schemes for birefringence compensation and for the generation of high power  $p$ -polarized beam in long pulse operation of single and dual-rod Nd:YAG laser. An experimental verification for enhancement of  $p$ -polarized output power and reduction in depolarization loss using a GTP and

90° QR tilted at the Brewster's angle in the single Nd:YAG rod laser resonator has been performed. A single GTP at tilted angular position provides Brewster's angle at interface as well as required phase-retardation for the compensation. The compensation scheme using GTP performs better than quarter-wave plate scheme in high power multimode laser operation. This scheme has been found to work even up to 3 kW of input pump power. For further higher input pump power, tilted 90° QR is simpler, novel and cost effective method for birefringence compensation in single Nd:YAG rod. It has been verified experimentally that by using tilted 90° QR, the depolarization loss can be reduced significantly from a value of ~34% to ~9%. Further, this scheme has resulted in a significant enhancement (more than 80%) of *p*-polarized output power as compared to placing only a polarizer in the resonator.

For dual Nd:YAG rod resonator, we have achieved an efficient birefringence compensation in *z*-fold resonator configuration using a simple optical scheme consisting of concave mirrors, an intra-cavity 90° quartz rotator, and a re-entrant feedback mirror. Concave mirrors used in the resonator work as folding mirror in the resonator as well as imaging optical system for the laser rods. It was found that *z*-fold resonator geometry is a potentially good option for birefringence compensation and generation of high average power *p*-polarized beam. Using this configuration, generation of 415 W of *p*-polarized average output power with 150 J of pulse energy in long pulse operation of Nd:YAG laser was carried out. A slope efficiency of 4.3% has also been achieved, which is on the higher side for a typical lamp pumped long pulse Nd:YAG lasers. This scheme can also be applied for the enhancement of *p*-polarized output in high power diode or lamp pumped CW lasers. It has potential applications in welding, cutting, and grooving of stainless steel, titanium, and aluminium for the automotive, aerospace, and vacuum component industries.

# Chapter 6

---

## Study on some important material processing applications of long pulse Nd:YAG laser

### 6.1 Introduction

Material processing with Nd:YAG lasers is a well accepted and established technology in industry [1,8,32,51,123,124]. It is being used worldwide for cutting, drilling, welding, forming, hardening and various types of surface treatment of metals in modern industries such as automotive, aerospace, shipbuilding, and vacuum component fabrication as well as nuclear facilities. Laser material processing requires extensive empirical research and the development of accurate, robust mathematical models to understand the involved physical phenomena for example in cutting [125-127], welding [13,128-130] and drilling [131-133]. In this chapter, first part focuses on our investigation of laser cutting of thick stainless steel sheets using long pulse Nd:YAG lasers.

In laser material processing, an understanding of the fundamental absorption mechanisms in material plays a vital role in determining the optimum processing parameters and conditions. The absorptance, which is the fraction of the incident laser light, which is absorbed, depends on the laser parameters such as wavelength, polarization, the angle of incidence etc. as well as

material properties such as composition, temperature, surface roughness, oxide layer, and contamination. General treatment of laser absorption mechanisms has been given by Gamaly [134]. Bergstrom and Kaplan [135] have provided a detailed review of laser absorption mechanism in metals. During processing of metals, when the laser beam is incident on the material surface, free electrons dominate optical absorption through a mechanism known as inverse bremsstrahlung [134]. The laser energy is subsequently transferred to the lattice phonons by collisions and from there it is transferred by the molten layer. The melt surface movement and the melt ejection are driven by the pressure differences, which consist of two contributions: one from the cutting gas jet, and the other from the pressure of the evaporated or the decomposed material.

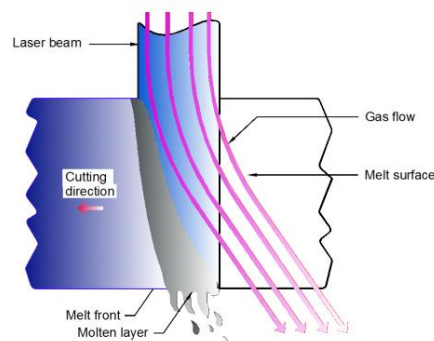


**Fig. 6.1.** A schematic view of the cut front during laser cutting by melting.

Cutting of old equipments and structures for dismantling and decommissioning is an important application in nuclear facilities and shipping industry. For dismantling work, the requirement of cutting tool is such that it should be remotely operated from a large distance either in a highly radioactive environment and/or in underwater environments. Thus, long pulse Nd:YAG laser systems with a high average and peak power, good beam quality, and fiber optic beam delivery have a great potential in dismantling work. Further, the speed of laser cutting in

underwater environment is important for dismantling of structures in nuclear facilities and ships due to several advantages in terms of the environmental, technical, and economical aspects. During the propagation of the laser beam through water it is attenuated according to Beer–Lambert’s law. For 1064 nm wavelength (Nd:YAG laser) the absorption coefficient of water is  $0.14 \text{ cm}^{-1}$ . Hence the attenuation of the beam is significant even in small propagation distances in water [136,137]. Thus, the beam delivery through an optical fiber is essential to avoid direct interaction of the beam with water. Water also provides natural and better thermal convection as compared to air, which results in reduction of the heat affected zone (HAZ), temperature gradient, and thermal stress in the material, and thereby reduces the possibility of crack formations during the laser cutting. Pulsed Nd:YAG laser cutting provides certain advantages over CW Nd:YAG lasers cutting such as minimum distortion in the material and lower HAZ. In the case of pulsed Nd:YAG laser cutting of thick sections (4 mm to 20 mm thickness) of stainless steel, millisecond (ms) duration pulses are preferable as melting time of most of the materials is of the order of a few ms [8].

For laser cutting of thicker materials, depth of focus is also an important factor. To achieve a straight cut edges without any taper angle, a large depth of focus is required. In fiber coupled Nd:YAG lasers, a dual lens imaging configuration is used at the output end of the fiber. The first lens (collimating lens) collimates the beam and the second lens (focusing lens) focuses the beam to generate an image of the fiber core at the focus point. The diameter of the focused spot ( $S$ ) is calculated with fiber core diameter  $D_{core}$  multiplied by the ratio of the focal length of the two lenses (imaging ratio) as [28]

$$S = (f_2 / f_1).D_{core} \quad (6.1)$$

where  $f_1$  is the focal length of first lens, and  $f_2$  is the focal length of the second lens. On the other

hand, when a direct laser beam (without optical fiber delivery) is focused by a single lens, the diameter  $S$  of the focus spot is given by the expression [13]

$$S = M^2 \cdot (4 / \pi) \cdot (f / D) \cdot \lambda \quad (6.2)$$

and the depth of focus (D.O.F.) for direct beam focusing is given by [13]

$$D.O.F. = \pm (8 / \pi) \cdot M^2 \cdot (f / D)^2 \lambda \quad (6.3)$$

where,  $f$  is the focal length of the focusing lens,  $D$  is the diameter of direct laser beam on the lens, and  $\lambda$  is the laser wavelength. From Eq. 2.9 (in Chapter 2), the relation of laser beam parameter product (B.P.P.) and beam quality factor  $M^2$  is given by  $B.P.P. (w_m \theta_m) = (\lambda / \pi) \cdot M^2$

For the laser beam exiting from the fiber end, its B.P.P. can be written as a product of fiber core radius ( $D_{core}/2$ ) and numerical aperture ( $NA$ ) of the fiber. Thus, the relation between B.P.P. of the beam coming out of the fiber and its  $M^2$  is given as

$$(D_{core} / 2) \cdot NA = (\lambda / \pi) \cdot M^2 \quad (6.4)$$

On using Eqs. (6.1), (6.2) and (6.3), the depth of focus for the laser beam exiting from the fiber end and imaged at focus using a dual lens imaging system with an imaging ratio of  $f_2/f_1$  can be written as

$$D.O.F. = \pm (f_2 / f_1)^2 \cdot (D_{core} / NA) \quad (6.5)$$

It is clear from the above relation that the depth of focus of laser beam exiting from the optical fiber, depends strongly on the imaging ratio. Hence, for the processing of thick materials with fiber-coupled laser, a high value of the imaging ratio is required.

During laser cutting, material loss in the form of debris is also an important issue. In general, laser cutting with Nd:YAG laser is a melt and blow process, where the laser beam melts the material and an assist gas blows out the molten material (debris) from the cut channel. If the debris are ejected into the open air, it is many times harmful for health. Hence, it is necessary to

reduce the ejection of debris in open air. One possible solution to this problem is the reduction in kerf width. With a smaller kerf width, the ejection of debris reduces significantly. In this Chapter, we describe the studies of a simple optical scheme to reduce the ejected debris by using the half imaging ratio of optical fiber. Details of the laser cutting experiments have been discussed using these schemes in section 6.2 and 6.3 of this Chapter.

We have also carried out studies on laser welding using in-house developed fiber coupled long pulse Nd:YAG lasers. Laser welding is characterised by a large number of process parameters which influence welding performance. These parameters can be grouped into a diagram, as shown in Fig. 6.2, which shows various factors affecting the quality of pulsed laser welding.

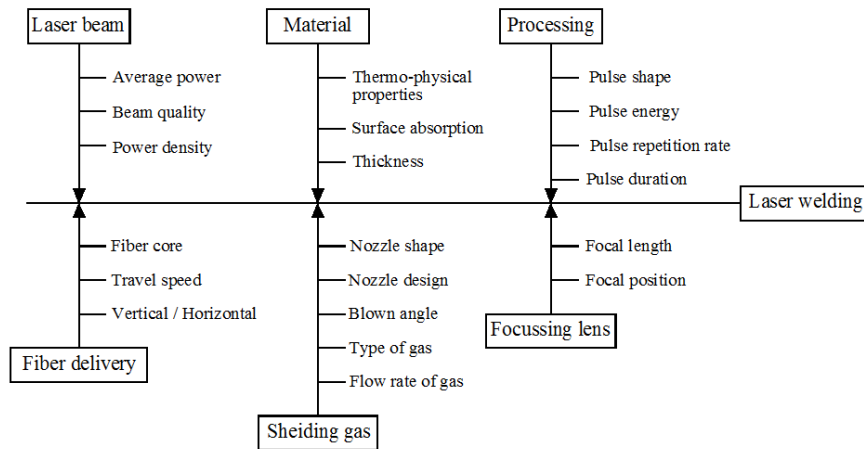


**Fig. 6.2.** A chart showing important process parameters affecting the quality of laser welding.

Laser power density or intensity is a major parameter that defines the temperature distribution in the material during the processing with near infrared lasers [8]. Other important parameters used to characterize the process of pulsed laser welding are pulse energy, peak power, average power, focal spot diameter, and pulse duration. A large depth of penetration is a

key requirement for industrial welding applications. Laser welding can be performed either in conduction mode or in keyhole mode [138-140]. It is observed that the conduction mode is characterised by a low penetration depth. However, a rapid increase in penetration depth is observed on establishing a keyhole mode of welding. Conduction mode welds are usually produced at a power density of  $\sim 10^5$ -  $10^6$  W/cm<sup>2</sup>, whereas keyhole mode welds are usually produced at a higher power density ( $\sim 10^7$  W/cm<sup>2</sup> or more). In keyhole, welding, molten metal rapidly solidifies behind the moving keyhole creating the joint between the welding parts. In laser matter interaction the keyhole is established when the laser intensity overcomes a certain value of threshold intensity. The keyhole induces two main absorption mechanisms: Fresnel absorption and plasma absorption. Jin *et al.* [141] have studied the Fresnel absorption and reflection in keyhole welding. On the other hand, Solana and Negro [142] have studied the effect of multiple reflection and plasma absorption on the keyhole profile. The stability of keyhole depends on the force balance between the vapor pressure and the surface tension pressure. The vapor pressure tends to open the keyhole, whereas the surface tension pressure tends to close it. For sustained keyhole laser welding process, kW-class continuous wave (CW) lasers are generally used. However, there are a few disadvantages in keyhole laser welding of metals using CW lasers, which include distortion, undercut on the surface and larger HAZ as compared to that with long pulse laser welding. Large HAZ modifies the base material properties, which may degrade the ductility of the material. On the other hand, the combined keyhole and conduction mode welding is possible with pulsed lasers using long duration pulses so that sufficient time is available for the diffusion of heat in the material. There is a rapid increase in weld penetration using the combination of conduction and keyhole mode of welding. We have studied long pulse Nd:YAG laser welding of titanium, aluminium, and stainless steel in the combined mode of

conduction and key hole welding. Details of our laser welding experiments and their results are illustrated in Section 6.4 of this Chapter.

Finally, we have also performed some studies on laser drilling in rocks using long pulse Nd:YAG laser. A comparison of conventional drilling techniques like rotary drilling and flame-jet spallation with laser rock drilling has been presented by Ikeda *et al.* [143]. Pulsed laser drilling provides advantage of energy deposition in the rock for a short time duration with smaller specific energy. Moreover, with the use of pulsed lasers, process parameters such as pulse duration, number of laser shots, and pulse energy can be varied in a controlled way to drill precise holes of larger depth. When rock drilling process is combined with gas purging and suction mechanism for removal of molten or vapourized material, laser beam always finds a new rock surface for interaction. The purpose of our study was to determine Nd:YAG laser process parameters to drill holes in the rocks to a maximum possible depth and the removal of maximum volume of the rock using minimum average power and laser energy. The details of the experimental work of rock drilling using long pulse Nd:YAG laser is described in Section 6.5.

## **6.2 Laser cutting of stainless steel in dry air and underwater**

Stainless steel structures are widely used in nuclear and shipping industries due to high strength and stiffness. In nuclear industry the dismantling or decommissioning of these structures is essential after a certain number of years of operation depending on their structural conditions and radiological status. The steel structures which are required to be dismantled are the vessels of the nuclear reactor, reactor internals, cooling tubes, steel fittings, steel blocks, and different steel equipments of nuclear reactor plants [144,145]. Since, most of these steel structures have a

thickness in the range of 4 to 20 mm, studies have been performed on laser cutting for this range of thicknesses.

In the shipping industry the dismantling of old ships is carried out for recycling purposes. For example, the shipyards at Alang in India recycle approximately half of all the ships salvaged around the world [146]. Dismantling of ships involves cutting of different parts such as deck and side plating, ship hulls and offshore structures, legs of production jack ups, container, oil tankers, and steel cylinders with wall thickness in the range of about 10 to 20 mm [147,148].

In this Section 6.2, our investigation is focused on the cutting of thick section of SS 304 using ms duration long pulse Nd:YAG laser in dry air and in underwater environment. Unlike laser cutting usually performed in the manufacturing industry, where cut quality such as kerf width, surface roughness, oxide layer on the surface, HAZ, etc. is an issue, there are no such quality issues in dismantling process. Performance of dismantling process is evaluated by capability to cut thick parts speedily. The aim of our work is to achieve larger cutting depth and higher cutting speed for thick section of SS 304. Study of the effect of pulse duration, spot overlapping, pulse repetition rate, and assist gas pressure on cutting speed and HAZ during cutting of SS304 in dry air and underwater environment has also been performed.

### **6.2.1 Experimental work**

Laser cutting experiments were carried out using a fiber coupled long pulse Nd:YAG laser of 500 W average power, as described in Chapter 2. Laser beam was delivered through a 400  $\mu\text{m}$  core diameter optical fiber and is focused to a diameter in the range of 0.4 mm to 1.25 mm using imaging optics. Throughout the experiments, the laser beam was focused on the upper surface of the work-piece. The important specifications of the laser system developed and

deployed for this cutting experiment are listed in Table 6.1. The temporal pulse shape of the laser is approximately rectangular with an initial peak as shown in Fig. 6.3. Variation of the pulse energy with pulse duration is almost linear as shown in Fig. 6.4.

**Table 6.1:** Important specifications of the long pulse Nd:YAG laser deployed for cutting operation.

Pumping method	Flash lamp
Average output power	500 W (maximum)
Pulse energy	300 J (maximum)
Peak power	9 kW (maximum)
Pulse duration	1-40 ms
Repetition rate	1-100 Hz
Beam delivery	400 $\mu\text{m}$ multimode fiber
Focus spot diameter	0.4 - 1.25 mm

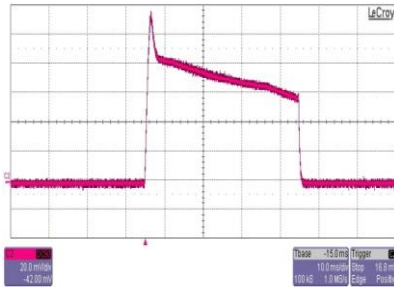


**Fig. 6.3.** Temporal shape of pulse from 500 W average power Nd:YAG laser.

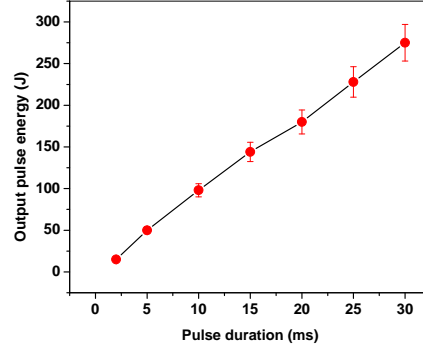


**Fig. 6.4.** Variation of laser pulse energy with pulse duration.

Stainless steel (AISI SS304) plates having thickness of 4, 8, 10, 15 and 20 mm were used as sample material for cutting experiments. For experiments in dry air, these samples were clamped in a fixture mounted on a Computer Numeric Control (CNC) table providing speed variation in a wide range of 10 mm/min to 1500 mm/min. Laser cutting fixture holds the plate in

such a way that a gap is maintained between the bottom surface of sample and top of CNC table so that it allows free flow of molten material from the kerf during laser cutting. For underwater laser cutting experiments, the samples were placed in a water jar, which was mounted on the CNC table. The samples were kept at a depth of ~300 mm from the water surface. The laser spot overlapping factor was varied in a range from 20% to 80% and the pulse duration was varied in the range of 4 ms to 20 ms for all sets of experiments. In all these experiments, oxygen was used as assist gas with outlet pressure varying in the range of 4-12 kgf/cm<sup>2</sup>. The kerf width was measured using a Starrett HB 350 optical comparator. In order to determine the HAZ, samples were cut from the cut edge and then polished to produce a cross-section of the cut edge. These samples were etched with 2% nital (a solution of methanol and nitric acid) and then imaged using an optical microscope (Leica, Germany) and also studied using a scanning electron microscope (SEM) (Philips, 30 kV).

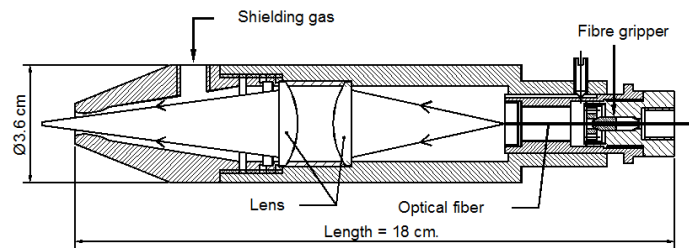


**Fig. 6.5.** A schematic view of laser cutting objective used for cutting of thick section of steel.

A water leak tight focusing objective of 180 mm length and 36 mm outer diameter was developed for cutting in dry air and in underwater environment. This focusing objective (nozzle) with 2 mm orifice diameter was tested for gas pressure in the range of 4-15 kgf/cm<sup>2</sup> corresponding to a laminar or turbulent flow pattern of the exit gas from the nozzle. The focusing objective consisted of two fused silica lenses, one of them is used for collimation and has a focal

length of 40 mm and the other one is used for focusing and has a focal length of 125 mm. With this optical geometry a focal spot diameter of 1.25 mm was achieved. The lenses were mounted in lens imaging assembly as shown in Fig. 6.5. Variation in single shot spot diameter on the material surface with different pulse duration was measured using an optical microscope. During underwater cutting the coaxial gas from the nozzle removes the water below the nozzle and forms a local dry cavity (LDC) as shown in Fig. 6.6. A schematic view of LDC is shown in Fig. 6.7.



**Fig. 6.6.** A view of local dry cavity in underwater environment.

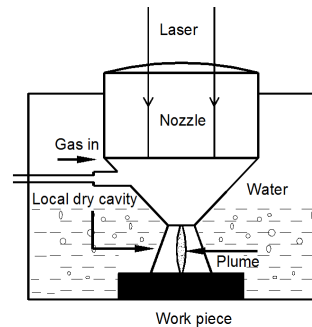


**Fig. 6.7.** A schematic diagram of local dry cavity.

For estimation of LDC, back-reflected IR signal was collected from the work-piece with the help of the same optical fiber, which has been used for beam delivery. A fraction of this back-reflected IR signal from the work piece was recorded by a photodiode (New focus, USA) and oscilloscope. A RG 850 optical filter was mounted on the photodiode to filter out the unwanted visible radiation. The stability of LDC could be determined by IR signal stability. If the LDC is unstable, the IR signal fluctuates and its value reduces when water enters the LDC. For dry air environment, the reflected IR signal was measured to be 440 mV for the SS 304 material at the optimum nozzle to work piece stand-off distance of 1.5 mm. The same value of

reflected signal was measured during the underwater laser cutting process after the formation of stable LDC. Any disturbance in the IR signal during the underwater cutting shows that LDC is not stable and the laser cutting should be stopped immediately.

## 6.2.2 Results and analysis

Pulse repetition rate ( $f$ ), laser spot diameter  $S$ , and percentage overlapping of laser focus spot determines the cutting speed ( $v$ ) during pulsed laser cutting process. For 0% spot overlapping or without spot overlapping, cutting speed is given by the relation  $v=(S \times f)$ . For  $N\%$  spot overlapping, the cutting speed can be written as  $v=(S \times f) \cdot (1-0.01N)$ . From this relation, it is clear that the cutting speed can be enhanced with an increase in pulse repetition rate  $f$ . However, the repetition rate is limited by the maximum average output power of the laser system used in the experiment. For a given pulse duration  $t_p$ , pulse energy  $E$ , and the average output power  $P_{avg}$ , the maximum value of  $f$  and the output peak power of a pulsed Nd:YAG laser are given as  $f=P_{avg}/E$  and  $P_{peak}=E/t_p$ . Using a 500 W average power Nd:YAG laser the maximum repetition rate  $f$  for cutting of five samples of SS304 with thickness 4,8,10,15 and 20 mm for the optimum value of pulse energy  $E$  were 41.6, 16.6, 9, 6.2, and 4 Hz, respectively. The optimum value of the laser pulse energy and pulse duration for different sample thicknesses is listed in Table 6.2.

**Table 6.2:** List of optimized process parameters for laser cutting of SS 304 samples of different thicknesses.

Thickness (mm)	Pulse energy (J)	Pulse duration (ms)	Maximum rep. rate for 500 W avg. power (Hz)	Minimum req. spot overlapping (%)	Single shot spot diameter in dry air (mm)	Single shot spot diameter in under water (mm)	Maximum cutting speed in dry air (mm/min)	Maximum cutting speed in under water (mm/min)
4	12	8	41	20	1.30	1.29	2620	2496
8	30	10	16	25	1.33	1.30	1029	962
12	55	14	9	30	1.34	1.32	522	504
15	80	16	6	35	1.36	1.34	341	328
20	125	20	4	40	1.53	1.51	180	172

If a 1 kW or 2 kW average power laser is deployed for this present experiment, the available repetition rate for a given pulse energy will be two to four times higher as compared to that with a 500 W average power laser. Hence, a more general expression can be given for cutting speed  $v$  for 1 Hz of repetition rate, as  $v=S \times (1-0.01N)$ . For a one minute time duration, 60 pulses are available and cutting speed  $v$  can be written in terms of cutting length ( $l$ ) per minute for sixty pulses as  $l=60 \times S \times (1-0.01N)$ . This expression explicitly shows that cutting speed can be scaled to higher values using higher repetition rates. It is clear that, if focus spot diameter  $S$  increases for a fixed laser power density ( $\sim 10^5$  W/cm<sup>2</sup>), then the minimum required spot overlapping  $N$  can be reduced and the laser cutting speed  $v$  or cutting length  $l$  per minute can be enhanced. If the pulse repetition rate increases, the numbers of pulses also increase and subsequently cutting length also increases. This is advantageous for dismantling applications in restricted and radioactive areas of nuclear facilities and underwater environment, where large speeds of cutting can reduce the time duration of operation and hence the dose for personnel.

In general, a spot overlapping of 80% has been reported in the laser cutting experiments by many researchers [149,150]. In our experiments, the calculated value of cutting speed for one Hz repetition rate using a focused laser beam diameter of 1.25 mm and spot overlapping of 80% is only  $\sim 15$  mm/min. However, we have achieved much higher cutting speed per Hz (see Table 6.2) using smaller values of spot overlapping as compared to the value of 80%. For this enhancement in cutting speed, we have studied the effect of laser pulse duration on effective laser spot diameter on melt surface of material. It was found that the effective spot diameter increases with increase in the laser pulse duration since longer pulse duration results in higher diffusion of heat on the material surface. This leads to an increase in the effective spot diameter which in turn reduces the requirement of spot overlapping and enhances the cutting speed. The

variation of effective spot diameter on the material surface was measured using optical microscope for different pulse duration at constant pulse energy of 30 J.

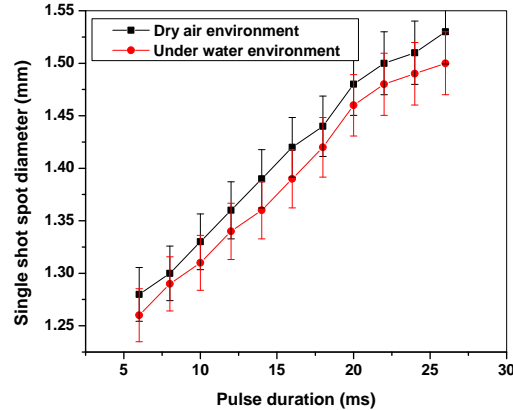


**Fig. 6.8.** Variation of single shot effective spot diameter on melt surface with increase in pulse duration for dry air and underwater environment.

Fig. 6.8 shows variation of measured value of single shot effective spot diameter on the melt surface of 8 mm thick sample as a function of pulse duration. It shows that there is an increase in effective spot diameter with increase in pulse duration. The trend of increase in spot diameter in underwater conditions was similar. However, the effective spot diameter is slightly less in underwater environment as compared to that in air since water cooling restricts heat diffusion on the surface.

Further studies were carried out on the relationship between the spot overlapping and the cutting speed. It was observed that the value of minimum required spot overlapping  $N$  for a fixed pulse duration and pulse energy can be reduced if pressure of assist gas (oxygen) is increased. It is due to the fact that extra energy is released due to the exothermic reaction in the presence of oxygen and this energy is mainly depends on the gas pressure. The amount of energy released during the exothermic reaction is of the order of kJ [151]. A variation of minimum required spot

overlapping with variation in oxygen gas pressure for 8 mm thick sample at 30 J of pulse energy and 10 ms of pulse duration is shown in Fig. 6.9.

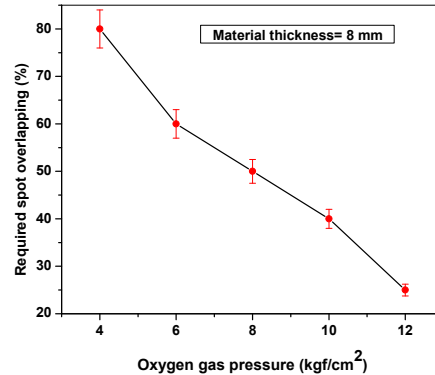


**Fig. 6.9.** Variation in required spot overlapping with variation in oxygen gas pressure for cutting of 8 mm thick SS304.

It can be seen that the spot overlapping required for the cutting reduces to a value of ~25% at 12 kgf/cm<sup>2</sup> pressure of oxygen as compared to a value of 80% for 4 kgf/cm<sup>2</sup> of gas pressure. With further increase in oxygen gas pressure beyond a value of 12 kgf/cm<sup>2</sup>, an uncontrolled blasting occurs at the cut edge of the material and results in a very poor cut surface. Hence, further experiments with increase in oxygen pressure were not carried out. It was also observed that when argon is used as assist gas in place of oxygen the above reduction in the minimum required spot overlapping to achieve laser cutting was not possible. This clearly shows that the exothermic reaction with oxygen assist gas is one of the factors which can lead to the reduction in the minimum required spot overlapping during the cutting process and enhancement in the cutting speed. The other factor is the pulse duration dependent effective spot diameter, which we have discussed earlier in this section (see Fig. 6.8). The enhancement in cutting speed is useful for dismantling work in highly radioactive and underwater environment as it reduces the

time required for particular cutting operation and thus reducing the total exposure to radioactive environment.

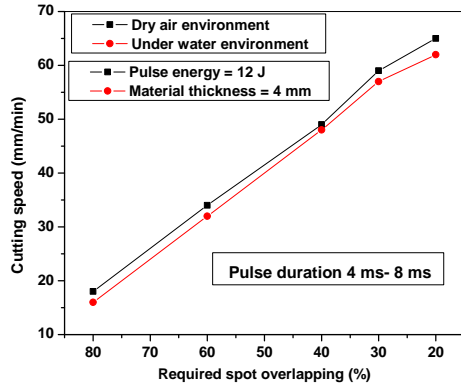


**Fig. 6.10.** Variation in cutting speed for 1 Hz with reduction in spot overlapping in the pulse duration range of 4 ms-8 ms for 4 mm thick SS sample.

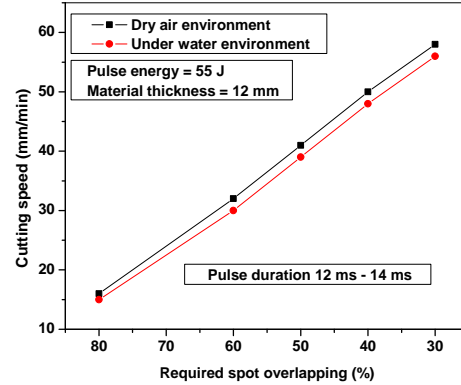


**Fig. 6.11.** Variation in cutting speed for 1 Hz with reduction in spot overlapping in the pulse duration range of 12 ms- 14 ms for 12 mm thick SS sample.

Further, it was observed that cutting of 20 mm thick plate was possible with a spot overlapping of 40% for 20 ms long pulses as compared to 80% spot overlapping required for 14 ms pulses for the same amount of pulse energy of 125 J. In this case, the measured cutting speed for 1 Hz repetition rate was 45 mm/min in dry air and 43 mm/min in underwater. Thus, it is clear that the laser cutting speed is enhanced by about three times for long duration pulses with smaller required value of spot overlapping. For SS 304 samples of different thicknesses, experimentally optimized values of minimum required spot overlapping, pulse duration, spot diameter, pulse energy, and cutting speed at 1 Hz repetition rate is listed in Table 6.2. Variation of cutting speed in mm/min for 1 Hz with required minimum spot overlapping for all the stainless steel samples (4 mm to 20 mm thickness range) are shown in Figures 6.10, 6.11, 6.12 and 6.13, respectively.

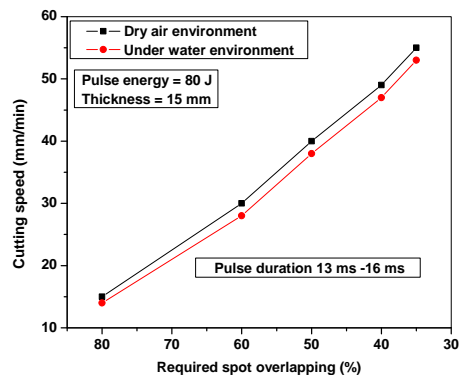


**Fig. 6.12.** Variation in cutting speed for 1 Hz with reduction in spot overlapping in the pulse duration range of 13 ms-16 ms for 15 mm thick SS sample.

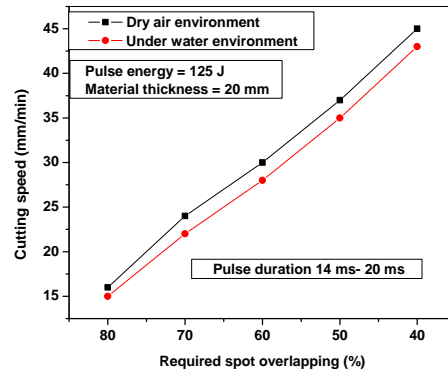


**Fig. 6.13.** Variation in cutting speed for 1 Hz with reduction in spot overlapping in the pulse duration range of 14 ms-20 ms for 20 mm thick SS sample.

All the process parameters are also listed in Table 6.3 of this chapter. These figures show that at constant pulse energy the cutting speed can be increased with reduction in spot overlapping if the pulse duration is increased. Cutting speed in underwater environment is slightly less as compared to the dry air environment due to the loss of some portion of the heat due to heat conduction by water.

The minimum spot overlapping is determined by the condition that a regular cut kerf becomes a kerf of irregular shape and finally separate drilled holes are observed on the surface in place of regular cut. Thus, further reduction in spot overlapping is not possible beyond a certain value. For example, during cutting of 20 mm thick sample, it was found that with reduction in the value of spot overlapping below 40%, the cut edges initially became irregular and later on a sequence of drilled holes appear in the cut profile in place of regular cutting as shown in Fig. 6.14. Other important cut quality parameters such as surface roughness has not been considered

here due to the presence of fine striations on the cut surface, which is expected during the cutting of thick SS section with oxygen as assist gas [152]. Although the achieved surface quality may not be acceptable for engineering applications, however it is acceptable for dismantling applications.

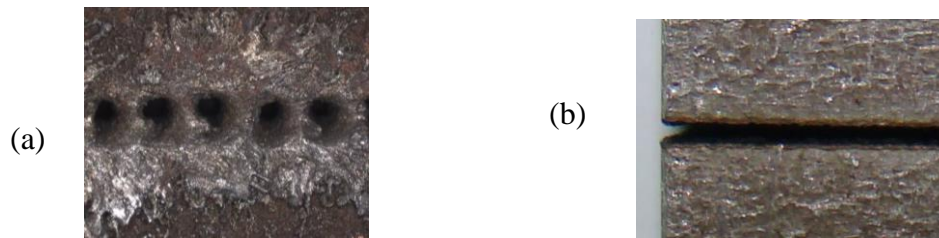


**Fig. 6.14.** (a) A sequence of drilled holes on the surface of 20 mm thick SS with reduction in spot overlapping factor below 40% showing separated holes, and (b) continuous cut kerf on the surface at 40% of spot overlapping.

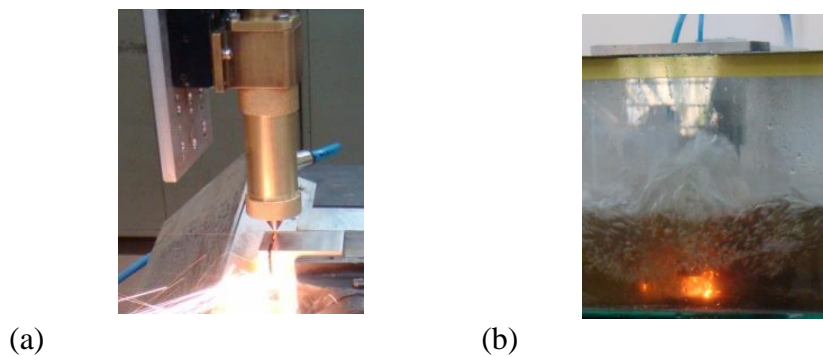


**Fig. 6.15.** A view of laser cutting of 20 mm thick steel in (a) dry air, and (b) underwater.

Fig. 6.15 (a) and (b) show a view of laser cutting process for 20 mm thick stainless steel sample in dry air and underwater environment. Figures 6.16 (a) and (b) show the laser cut surface of 20 mm thick sample in dry air and in underwater cutting. Fine striations were observed on the laser cut surface in both dry air and in underwater conditions. The cut surface was observed to be significantly smooth in underwater environment as compared to dry air. An

oxide layer is formed on the cut surface in both the cases due to exothermic reaction with oxygen.

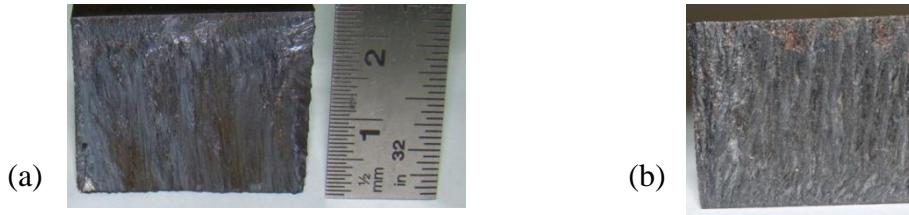


**Fig. 6.16.** (a) Cut surface of 20 mm thick SS304 in dry air, and (b) underwater cutting.

Figure 6.17 shows the metallographic cross section of the laser cut surface in dry air and in underwater environment. In the re-melting zone, there is no other noticeable change in the microstructure of the stainless steel either in dry air or in underwater cutting. Microstructure of the laser cut zone was also studied to determine the heat affected zone (HAZ).

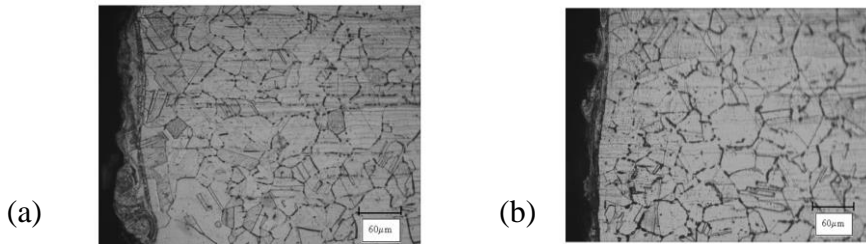


**Fig. 6.17.** Metallographic cross section of laser cut surface of 12 mm thick steel in (a) dry air, and (b) underwater cutting.

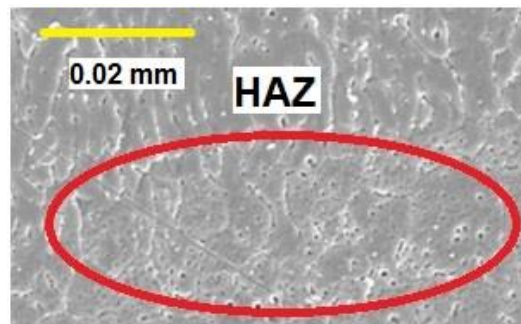


**Fig. 6.18.** SEM image of HAZ of SS304 in underwater laser cut sample.

Fig. 6.18. shows the SEM image of the grain structure near the laser cut and the grain refinement zone (re-melting zone) or HAZ. It extends into the bulk material near the laser cut portion and is very small having a value of the order of few hundreds of micrometer. For pulsed laser cutting, HAZ is given by [35]  $HAZ = 2\sqrt{\alpha(t_d - t_p)}$ , where,  $\alpha$  is the thermal diffusivity (4.2 mm<sup>2</sup>/s for stainless steel),  $t_p$  is the laser pulse duration, and  $t_d$  is the dwell time or interaction time of the laser beam of spot diameter  $S$  travelling with a speed  $v$ . Thus, HAZ can be written as [153]

$$HAZ = 2\sqrt{\alpha \left[ \left( \frac{S}{v} \right) - t_p \right]} \quad (6.6)$$

The HAZ can be related with spot overlapping by

$$HAZ = 2\sqrt{\left[ \frac{\alpha}{f} (1 - 0.01N) - \alpha t_p \right]} \quad (6.7)$$

In general, HAZ increases with increase in pulse duration, but in our experiments we have shown that there is no significant effect on HAZ due to the increase in pulse duration because of simultaneous reduction in spot overlapping. In addition, an increase in cutting speed could also be achieved. Fig. 6.19 shows variation in HAZ with change in pulse duration for 20 mm thick sample.

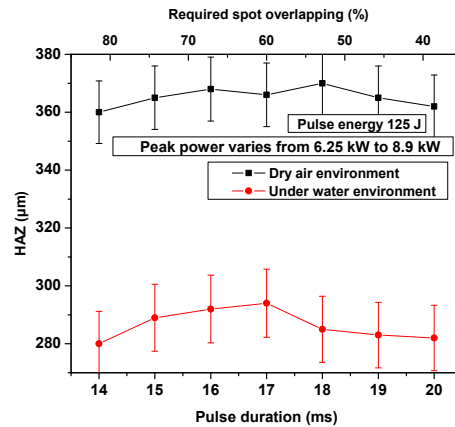


**Fig.6.19.** Variation of HAZ in dry air and underwater with change in spot overlapping from 80% to 40% and change in pulse duration from 14 ms to 20 ms for a peak power variation from 8.9 kW to 6.25 kW with a constant value of pulse energy of 125 J.

**Table 6.3:** List of measured kerf width, HAZ and percentage variation in HAZ of sample of different thicknesses at maximum cutting speed.

Thickness (mm)	Pulse energy (J)	Pulse duration variation range (ms)	Peak power variation range (kW)	Minimum req. spot overlapping variation range (%)	Measured HAZ dry air ( $\mu\text{m}$ )	Percentage variation in HAZ dry air	Measured HAZ under water ( $\mu\text{m}$ )	Percentage variation in HAZ under water	Measured kerf width(mm) dry air	Measured kerf width(mm) under water
4	12	4-8	3-1.5	80-20	230	5%	180	3%	1.32	1.30
8	30	6-10	5-3	80-25	258	8%	202	2%	1.34	1.32
12	55	12-14	4.5-3.9	80-30	302	6%	237	3%	1.38	1.35
15	80	13-16	6.1-5	80-35	328	8%	256	3%	1.42	1.40
20	125	14-20	8.9-6.2	80-40	362	8%	283	4%	1.53	1.51

It can be seen that there is no significant change in HAZ in dry air and underwater cutting when the spot overlapping was changed from 80% to 40% with simultaneous increase in the pulse duration from 14 ms to 20 ms. Table 6.3 shows measured values of HAZ and variation in the values of HAZ with variation in pulse duration and spot overlapping for samples of different thicknesses. The HAZ is smaller in underwater environment as compared to dry air environment. The increase in HAZ in dry air is ~8% as compared to ~3% in underwater conditions with increase in pulse duration from 14 ms to 20 ms with simultaneous reduction in the spot overlapping from 80% to 40%. This shows that underwater cutting minimizes the HAZ as some amount of heat is conducted through the water. The measured kerf width was also less in underwater cutting as compared to the cutting in dry air. The smaller kerf width is advantageous in terms of reduced material loss during the cutting process. During underwater laser cutting, one notable important factor was reduction in re-deposition of dross. Hence, a cleaner cut surface with minimum dross formation was observed during the underwater cutting as compared to dry air cutting.

### 6.3 Study on reduction of debris

Further study on laser cutting process for dismantling work in nuclear facilities has been carried out with a focus on the reduction of ejected debris. One of the solutions for this problem is the reduction in kerf width. In order to reduce the cut kerf, GRADIUM lenses have been utilized in place of conventional fused silica lenses in the laser cutting nozzle. The GRADIUM lenses are made from axial gradient index glass for minimization of spherical aberrations [154]. Reduction in spherical aberration reduces the focus spot diameter during imaging of the fiber and hence, can lead to smaller kerf width. This will in turn result in the reduction of ejected debris. At the exit end of the fiber, a dual lens imaging system is used and the diameter of the focused spot ( $S$ ) is given by Eq. (6.1). If two lenses have identical focal length, the imaging ratio ( $f_2/f_1$ ) will be 1:1, and the focused spot diameter  $S$  is equal to the fiber core diameter. If  $f_1 > f_2$  then the imaging ratio will be  $<1$  and the value of  $S$  will be less than the fiber core diameter. However, this reduction in imaging ratio has certain limitations due to the diameter of the lenses. Collimating lens is placed at a distance exactly equal to its focal length from the fiber exit face. The required diameter ( $A$ ) of the collimating lens is calculated by  $A=f_1 \times \tan(\theta_{max}/2)$  [8] and the value of acceptance angle is given as  $\theta_{max} = \sin^{-1}(NA)$ . For example, if  $f_1=100$  mm, and  $NA=0.22$ , it requires a lens with  $A= 50$  mm. This large diameter lens may be not be suitable for operation in areas with space limitations. In view of this, focal length of collimating lens was selected as  $f_1=25$  mm with a diameter of  $A= 11.8$  mm. Such a compact and small diameter ( $\sim 12$  mm) cutting nozzle has been found to be very useful in space restricted cutting operations during the laser cutting work in the nuclear facilities. Depth of focus depends on the square of the imaging ratio as given in Eq. (6.5). For one third-imaging ratio, depth of focus reduces drastically, and is not suitable for laser cutting of thick materials. Another limitation is related with the diameter of the

focusing lens and the cutting nozzle. Value of the diameter  $A$  of collimating lens is  $A=11.8$  mm for  $f_1=25$  mm, and that of the focusing lens is  $A=11.8$  mm for  $f_2=8.3$  mm. However, in practice, it is difficult to make a fused silica lens having focal length less than its diameter. Hence, it is difficult to reduce the imaging ratio below one-half due to the restriction in the diameter of focusing lens and depth of focus. Hence, laser cutting experiment have been performed with half-imaging of the fiber at focus. For half-imaging ratio with a  $400\ \mu\text{m}$  core diameter fiber optic beam delivery, the expected diameter of the focus spot will be  $200\ \mu\text{m}$  on the work piece.

### 6.3.1 Experimental work

Laser cutting experiment for reduction of debris has been performed using laser cutting nozzle with half-imaging optics. A schematic view of the cutting nozzle is shown in Fig. 6.20. Two leak tight cutting nozzles (1:1 and half-imaged) with outer diameter of 20 mm have been used for comparison of kerf width. These nozzles were tested at a gas pressure in the range of 5-15 kgf/cm<sup>2</sup>. Assist gas flows out through the nozzle and emerges coaxially with the laser beam during the cutting process. Focus spot diameter of laser beam at the exit from these nozzles was measured using a CCD camera (Wincam-D, Gentec). A 500 W average power long pulse Nd:YAG laser with  $400\ \mu\text{m}$  core diameter optical fiber was used in the experiments.

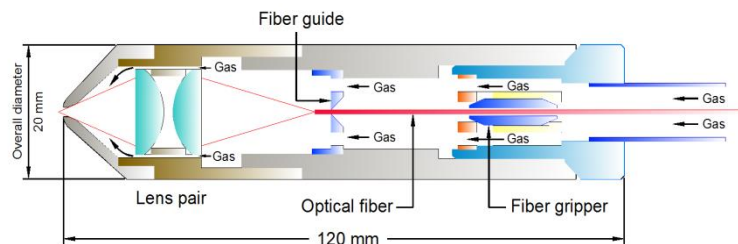


**Fig. 6.20.** A schematic view of laser cutting nozzle, designed for half-imaging lenses.

A 4 mm thick, 60 mm wide, and 100 mm long stainless steel (AISI SS 304) sample was kept on a motorized translation stage that permits a precise linear motion of the sheets. For collection of the debris ejected from the cut surface, a collection plate was placed below the cut surface. Laser cutting experiments were performed for two different assist gases: argon and oxygen. In the final cutting trials oxygen is used as an assist gas because of its advantages for high speed cutting as we have discussed in section 6.2.2 of this chapter. Kerf width was measured using an optical comparator and optical microscope (Leica, Germany).

### 6.3.2 Results and analysis

Using 25 mm focal length fused silica lenses, measured value of focus spot diameter for 1:1 imaging ratio was 445  $\mu\text{m}$  and for half -imaging ratio was 242  $\mu\text{m}$ . On the other hand, when GRADIUM lenses are used with the same focal lengths the measured diameter of focus spot was 405  $\mu\text{m}$  for 1:1 imaging ratio and 202  $\mu\text{m}$  for half-imaging ratio [155]. This reduction in focal spot diameter reduces kerf width during the laser cutting and reduces the dross ejection. A schematic view of optical scheme for 1:1 imaging and half-imaging of 400  $\mu\text{m}$  core diameter optical fiber using GRADIUM and fused silica lenses are as shown in Fig. 6.21 (a) and (b).

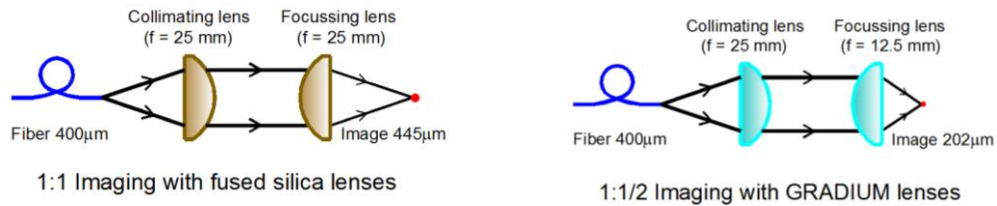


**Fig. 6.21.** A schematic view of (a) 1:1 imaging with fused silica and (b) half-image with GRADIUM lenses.

Kerf width was measured after laser cutting with oxygen as assist gas (pressure 8 kgf/cm<sup>2</sup>). It had a value of 205 μm for half-imaging optics using GRADIUM lenses as compared to 455 μm for 1:1 imaged fused silica lenses. Views of the two kerf widths are given in Fig. 6.22.

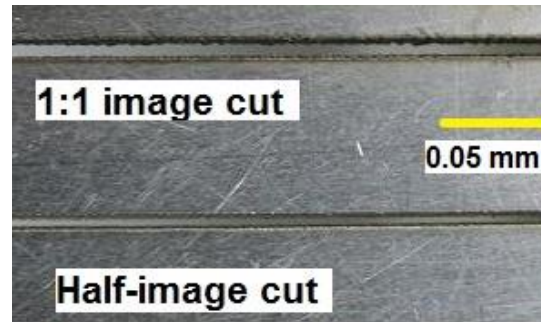


**Fig. 6.22.** A comparison of kerf width for cutting of 4 mm thick stainless steel sample using nozzles of 1:1 and half imaging optics.

The mass of material  $m$  removed in the form of debris from the cut width was calculated using the relation  $m=dLK_e\rho$ , where  $d$  is the material thickness,  $L$  is the total cut length,  $K_e$  is the kerf width and  $\rho$  is the density of the material. Calculated values of mass  $m$  of debris from 4 mm thick and 60 mm long stainless steel sheet with 445 μm kerf width was ~0.77 gm as compared to 0.38 gm for 205 μm kerf width. Quantitative measurements of mass  $m$  of stainless steel samples were also performed before and after laser cutting using a chemical balance. The difference in mass before and after laser cutting should be equal to the mass of debris ejected during the laser cutting process. However, the measured value of mass  $m$  of the collected debris was slightly less (~2%) as compared to its calculated value. It may be due to the fact that during laser cutting process, some amount of ablation and evaporation of material also occurs, which has not been collected and leads to reduction in measured mass of the debris. Further, with half imaged GRADIUM lens based nozzle, the overall mass of debris was reduced by about ~40% as

compared to 1:1 imaging nozzle with fused silica lenses [155]. A view of debris ejection during the laser cutting process is shown in Fig. 6.23.



**Fig. 6.23.** A view of debris ejection during pulsed Nd:YAG laser cutting with 1:1 imaging nozzle.

The value of required spot overlapping factor for cutting of 4 mm thick stainless steel reduces to ~60% using half-imaging with GRADIUM lens as compared to ~80% required for 1:1 imaging with fused silica lenses due to the higher power density at the focus with GRADIUM lens. Peak laser power density  $I$  at the focus for spot diameter  $S$  is given as  $I=4P/\pi S^2$ . Estimated value of laser power density for half-imaged fiber using GRADIUM lens is ~4.85 times higher than the laser power density with 1:1 imaged fiber with fused silica lenses for similar laser peak power of 7.5 kW. After performing several cutting trials of 4 mm thick stainless steel sample, optimum values of laser cutting parameters were found to be 4 ms pulse duration, 30 J pulse energy and 7.5 kW peak power with 1:1 imaging nozzle with fused silica lenses and 2 ms, 15 J and 7.5 kW peak power for half-imaging of fiber with GRADIUM lenses. The value of peak power density  $I$  was  $2.38 \times 10^7$  W/cm<sup>2</sup> for half-imaging nozzle using GRADIUM lenses with 202  $\mu$ m focus spot diameter. Maximum available pulse repetition rate  $f$  for a good quality cut was limited to 16.6 Hz for 30 J of pulse energy and 33.2 Hz for 15 J of pulse energy using 500 W

maximum average power Nd:YAG laser system. It can be enhanced further by using 1 kW or higher average power pulsed Nd:YAG laser systems. The measured cutting speed using half-imaging nozzle and GRADIUM lens was 159 mm/min as compared to 87 mm/min for 1:1 imaging nozzle with fused silica lenses. Cutting speed in the case of half-imaging with GRADIUM lens is higher since the requirement of energy is reduced to 15 J and hence the laser repetition rate could be increased to 33.2 Hz leading to increase in cutting speed. All the above experiments were carried out with oxygen as an assist gas at a pressure of 10 kgf/cm<sup>2</sup>. When the oxygen was used as assist gas, the cut surface was oxidized. However, unlike the manufacturing industry, where cut quality such as surface roughness, oxide layer on the surface, etc. is an issue, there are no such quality requirements in dismantling process hence this is acceptable for dismantling and disposal applications. The performance of dismantling system/process is evaluated by the capability to cut the parts at high speed.

In the case of cutting with argon as assist gas the measured cutting speed using half-imaging nozzle and the GRADIUM lens was 110 mm/min for 4 mm thick stainless steel sheet, which is ~33% less as compared to the cutting with oxygen for the similar gas pressure of 10 kgf/cm<sup>2</sup>. The laser cut surface with argon assist gas looks shinier and smoother and no oxidation layer was observed on it in contrast to the oxygen assisted laser cutting. It is clear that argon gas assisted laser cutting of metal parts would be preferable whenever the cut part is to be used in any subsequent operations such as welding, since no further post treatment of the cut surface is required.

## 6.4 Study on laser welding

In the next series of investigations the effect of laser process parameters of long pulse Nd:YAG laser on welding of different materials was studied which are described below.

### 6.4.1 Experimental work

First, we investigated the effect of temporal pulse shaping of long pulse Nd:YAG laser on weld depth of stainless steel (AISI SS304). The temporal shape of laser pulse could be changed by programming the flash lamp current in steps of 0.5 ms for a single long pulse and the lamp current could be varied from 100-300 Amp.

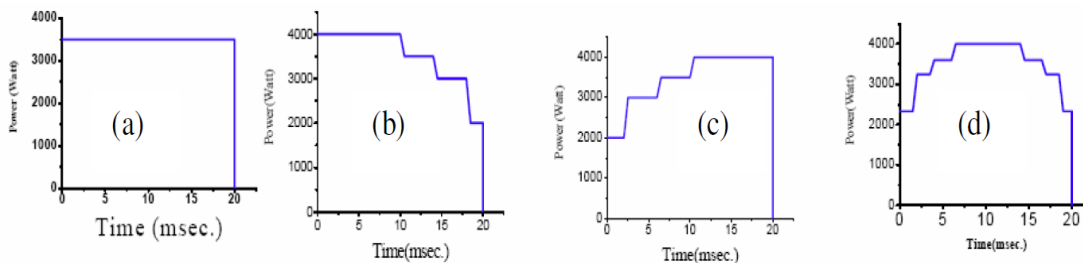


**Fig. 6.24.** Temporally shaped Nd:YAG laser pulses having (a) rectangular (b) ramp down (c) ramp up and (d) mixed or center-up shape for 70 J pulse energy and 20 ms pulse duration.

Fig. 6.24 shows four different temporally shaped Nd:YAG laser pulses namely: rectangular, ramp down, ramp up and mixed shape pulses. The energy content for all the four pulse shapes and the pulse duration were fixed at 70 J and 20 ms respectively, by varying the pulse current for each pulse shape.

Experimental studies were also performed on the effect of laser pulse energy, pulse width, peak power, and spot overlap on weld penetration in the samples of Al 1000 series and commercially pure (CP) titanium grade-4 [50]. A welding nozzle was designed with plano-convex fused silica lenses with focal lengths of 75 mm and 150 mm, respectively. The position

of the focal spot was 10 mm away from the focusing nozzle tip and the diameter of the focal spot was 1.2 mm. Focusing nozzle was mounted on a two-axis, computer controlled CNC table for laser welding of samples as shown in Fig. 6.25.

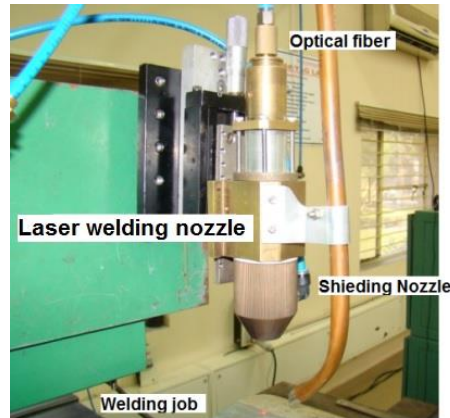


**Fig. 6.25.** *Fiber coupled focusing nozzle mounted on CNC.*

Laser focusing nozzle was tilted at an angle of  $10^{\circ}$  with respect to the plane of the sample to prevent the damage of fiber ends by the back reflected laser beam from the sample surface. The job surface was kept slightly away from the focus position to avoid sputtering of the material during the welding process. Laser spot diameter on the upper surface of the job was 2 mm. Argon gas was released coaxially through the focussing nozzle at a constant rate of  $\sim 30$  lpm to protect the weld bead from oxidation by creating an inert ambient around the welding point. The argon gas also protects the focusing lens from the weld plume and possible spatter from the sample. In order to ensure proper shielding of the weld pool from the atmosphere, another gas-shielding nozzle, which purges argon gas tangentially to the surface, was also used. The shielding gas nozzle of 12 mm diameter was kept at  $45^{\circ}$  angle with respect to the job with optimized argon gas flow rate of  $\sim 25$  lpm.

## 6.4.2 Results and analysis

Fig. 6.26 shows experimentally observed results of weld pool geometry for different temporal pulse shapes with a focused spot size of 1.2 mm, pulse duration of 20 ms and pulse energy of 70 J on AISI SS 304. This laser welding was performed in the conduction mode because power density was not sufficient to sustain keyhole mode of welding.

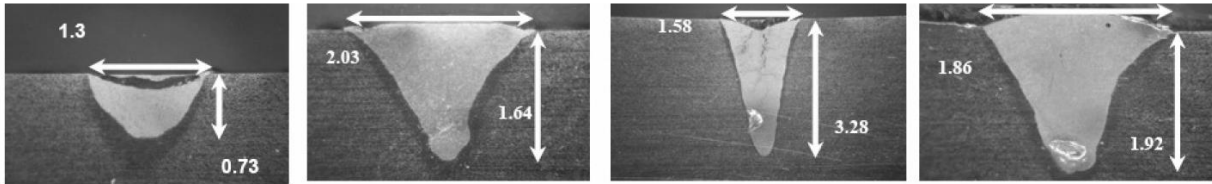


**Fig. 6.26.** Experimentally observed weld geometry for (a) rectangular, (b) ramp down, (c) ramp up, and (d) mixed pulse shapes (dimensions shown in figure are in mm).

Depth of penetration is minimum (0.73 mm) in the case of rectangular pulse shape and maximum (3.28 mm) in the case of ramp up pulse shape. The possible reason for this difference in penetration depth of different temporal pulse shapes is the difference in their pre-heating rates. Due to the energy distribution within a ramped up pulse shape, melt pool generation is more likely to occur at the end of the pulse when peak power is at its highest. The gradual increase in the laser energy pre-heats the material and reduces its reflectivity, allowing higher absorption of the pulse energy, and consequently higher depth of penetration.

In the case of welding of Al and Ti, it was observed that the pulse duration, and spot overlapping strongly influences the melting of these metals. Finally, good quality welding with 4 mm penetration depth were achieved in Al and Ti at a peak power density of  $\sim 0.5 \text{ MW/cm}^2$ , speed of 0.48 mm/s, repetition rate of 2 Hz, pulse duration of 35 ms with 380 J pulse energy, and a spot overlap of 80%. Figure 6.27 (a) shows a closer view of the weld bead on Al sample and

Fig. 6.27 (b) shows the weld bead microstructure of Al. Figure 6.28 (a) shows a closer view of the weld bead on Ti sample and Fig. 6.28 (b) shows the weld bead microstructure of Ti [50].

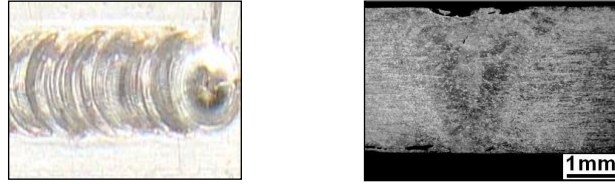


**Fig. 6.27.** (a) *Weld bead on Al sample* (b) *Microstructure of the weld bead on Al sample.*

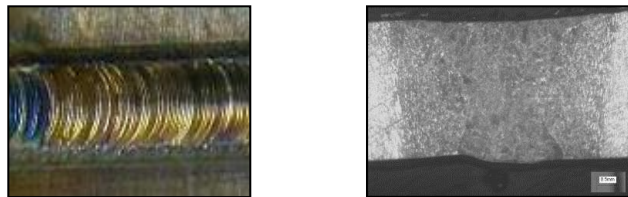


**Fig. 6.28.** (a) *Weld bead on Ti sample* (b) *Microstructure of the weld bead on Ti sample.*

The microscopic analysis which was carried out using a 1000 X microscope (Leica, GmbH), shows that the weld bead with long pulse Nd:YAG laser provides usually a good surface in both Al and Ti. Heat affected zone (HAZ) is parallel to the melt zone and has a very small width varying from 0.1 to 0.3 mm, which is very small compared with other conventional welding process. The width of the weld bead is 2 mm and the depth of penetration is 4 mm. With 80% spot overlap, weld bead was uniform and no major porosities or inclusions were observed in the welded sample. It was also found that the ultimate tensile strength of the weld joint is almost similar to that of the parent metal. Welded samples were also tested using helium leak detector for the leak rate of up to  $\sim 10^{-10}$  mbar.l/sec. These laser-welded materials can be used for the vacuum related applications.

## 6.5 Study on drilling and breaking of rock

Laser drilling and cracking (spallation) of rocks could be an innovative and economical process for petroleum industry and large construction works on hard rock strata. The purpose of this study was to determine the process parameters to drill holes in different types of rocks and stones of maximum depth as well as to crack and remove the maximum volume of the rock and stone material by laser processing. Different rock samples of sandstone, marble and shale were prepared to study the effect of laser pulse duration and number of laser shots on drilling of rocks. To break the rock, holes were drilled on the upper surface of the rock for stress generation.

**Table 6.4:** Composition of rock samples and its important physical properties.

Rock type	Composition %	Bulk density (g/cm <sup>3</sup> )	Absorption (I-R) @1064 nm (Mesured value)	Thermal diffusivity (cm <sup>2</sup> /sec)	Specific heat capacity (J/g <sup>o</sup> K)
Berea gray sand stone	SiO <sub>2</sub>	85	12%	13.6	0.88
	Al <sub>2</sub> O <sub>3</sub>	10			
	Fe	03			
	Rest	02			
Shale	SiO <sub>2</sub>	35	17%	7.5	3.2
	Al <sub>2</sub> O <sub>3</sub>	20			
	Clays	45			
Marble	CaCO <sub>3</sub>	95	8%	0.11	6.82
	H <sub>2</sub> O	02			
	Rest	03			

For a given rock, the minimum energy per unit volume for melting or vaporization can be determined as  $E = \rho[C_p(T - T_0) + L_m + L_f]$ , where  $E$  is (specific energy measured in J/mm<sup>3</sup>) required for the rock surface to reach a temperature  $T$ ,  $T_0$  is the ambient temperature,  $\rho$  is density of rock,  $C_p$  is specific heat,  $T_m$  is latent heat of melting, and  $T_f$  is the latent heat of fusion. Chemical composition, important thermal and optical parameters for different rocks used in the experiments are given in Table 6.4.

The time needed for the surface temperature (of the rocks and stones) to reach its melting point at a large intensity level of  $\sim 10^6$  W/cm<sup>2</sup> is of the order of milliseconds. Thus, it is important to select a Nd:YAG laser system of ms duration for drilling in rocks and stones. If the rock surface is smooth and planar like a mirror, then a significant portion of the incident energy is reflected, but if the surface is rough, most of the incident radiation is absorbed. The absorptivity ( $A$ ) of rock can be derived from the optical constants  $n$  (refractive index) and  $k$  (extinction coefficient). For normal incidence of the radiation, the absorptivity in the rock can be calculated by using Fresnel relation, given by [13]

$$A = 1 - \frac{(n-1)^2 + k^2}{(n+1)^2 + k^2} \quad (6.8)$$

The value of absorptivity ( $A$ ) strongly depends on the temperature and increases with increase in temperature. The high energy laser pulses absorbed on the surface of the rock raises its temperature. The temperature gradient on the surface and inside the rock generates mechanical stresses as the grains try to expand at high temperature. As these grains have no place to expand; fractures are more likely to develop in the material. The stress  $\sigma$  in the material can be calculated as  $\sigma = Y\alpha\Delta T$ , where  $Y$  is the Young's modulus of the material,  $\Delta T$  is the temperature difference between the rock surface and inside the rock and  $\alpha$  is the thermal expansion coefficient of the rock material. A detailed analysis of the stress generation in rocks has been provided by Douglas [156]. During the melting of rocks, exsolved gases in the laser drilled hole get ionized and produce a shielding effect, which reduces the transfer of laser energy to the rock and therefore penetration rate. During the laser drilling, recoil pressure  $p_r$  on the rock material can be estimated using the following equation [31]

$$p_r/I = \left[ 1.69 / \sqrt{L_v} \right] \left[ b / (1 + 2.2b^2) \right] \quad (6.9)$$

here,  $b^2 = (k_B T_S) / (m_v L_v)$ ,  $I$  is laser intensity,  $k_B$  is Boltzmann constant and  $m_v$  is the mass of the vapour molecule and  $L_v$  is latent heat of vapourization. The value of recoil pressure is of the order of several bars or atmospheric pressure and plays an important role during thermal spallation of the rock.

### 6.5.1 Experimental work

A schematic view of the experimental set-up is shown in Fig. 6.29. Important parameters of the ms pulse duration pulsed Nd:YAG laser are given in Table 6.5.

**Table 6.5:** Parameters of the long pulse Nd:YAG laser used for rock drilling experiments.

Pumping method	Flash lamp
Average output power	1 - 1000 W
Pulse energy	1 - 540 J
Peak power	20 kW
Pulse duration	1 - 40 ms
Repetition rate	1 - 100 Hz
Focus spot diameter	1 - 2 mm
Optical fiber	0.6 mm

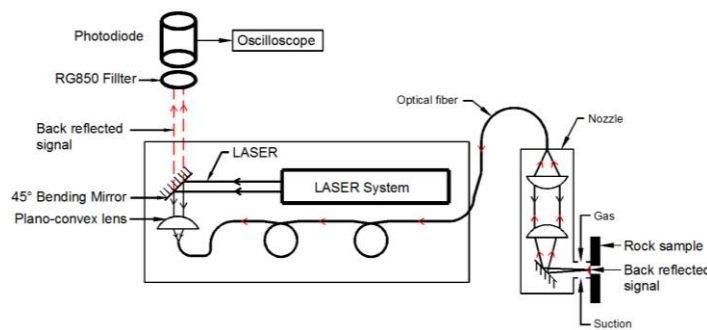


**Fig. 6.29.** Schematic view of laser drilling experimental set-up.

A microcontroller based power supply was used for the pumping of flash lamp in pulsed Nd:YAG laser and temporal pulse shape of the laser was rectangular. For rock drilling experiments, a laser focusing nozzle made of brass material with coaxial gas flow arrangement was utilized. Two plano-convex fused silica lenses having focal lengths of 75 mm and 150 mm, respectively were mounted in the nozzle along with a plane highly reflective bending mirror as shown in schematic and table-top view of nozzle in Fig. 6.30. The overall length of the nozzle was 40 cm and the width was 5 cm.

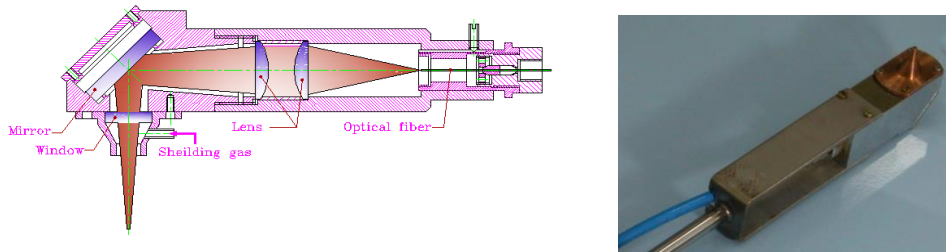


**Fig. 6.30.** Schematic and table-top view of laser drilling nozzle.

A fused silica antireflection-coated window was placed near the output tip of the nozzle to avoid the damage of lenses from the sputtered material and fumes. Further, for escape of vaporized rock particles, a suction system with a displacement rate of 200 lpm and a particle filter was also incorporated. A coaxial gas jet of compressed air at a constant pressure 15 bar was used to remove the molten rock during the drilling process. The laser focusing nozzle was tilted at an angle of approximately  $5^{\circ}$  during the drilling to avoid the entrance of back reflected beam from the glassy rock surface in to the nozzle which may lead to the damage of the optical fiber end face. Samples of different rocks like sandstone, marble and shale were prepared and were selected for this study as these are the three most common rock materials.

## 6.5.2 Results and analysis

The depth of drilling was measured for different samples with variation of laser pulse duration in the range of 10- 40 ms and 5 number of laser shots. Laser pulse energy was kept constant at a value of 200 J on the samples. Maximum depth of drilled hole was 9.8 mm for shale sample (Fig. 6.31) at an optimized pulse duration of 20 ms. Similarly, the maximum diameter of the drilled hole was 2.6 mm for Berea Grey sandstone sample (Fig. 6.32) at 40 ms pulse duration [157]. The specific melting energy for laser drilling of shale rock has a value of 2.1 kJ/cm<sup>3</sup>. It was found that the long pulse Nd:YAG laser is highly suitable to break the rock by generating stress in the material rather than melting or drilling the complete rock. Hence, use of long pulse Nd:YAG laser makes it possible to drill large holes (as shown further) which can enhance the cracking process. Mechanical properties of the rock material determine the maximum surface stress which can be tolerated prior to its fracture. If  $\sigma_{max}$  is the maximum surface stress at which fracture occurs, then the thermal shock parameter is given by  $R_s = K(1-\nu)\sigma_{max}/\alpha E$ . It is usually expressed in W/cm. For the study of stress breaking method of rock, experiments were performed using 537 J of pulse energy with 40 ms of pulse duration.

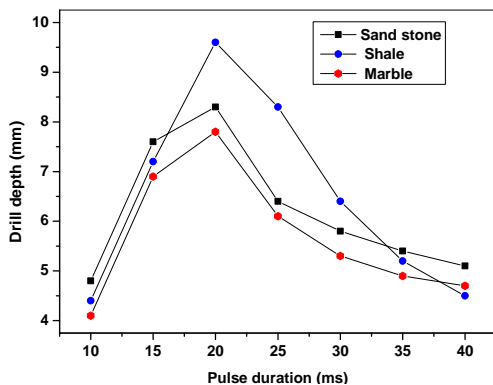


**Fig. 6.31.** Comparison of drilled depth for different pulse duration at 200 J of pulse energy and five number of laser shots.

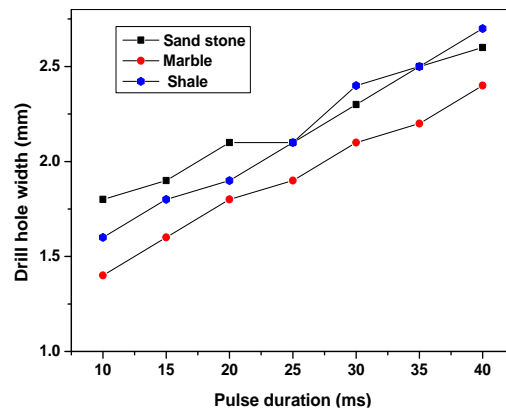


**Fig. 6.32.** Comparison of drilled hole diameter for different pulse duration at 200 J of pulse energy and five number of laser shots.

It was observed that the rock material immediately cracks after 5 laser shots due to stress generated in the rock as shown in Fig. 6.33 (a), (b), (c), and (d) for the shale rock.



**Fig. 6.33.**(a) *Drill on the upper surface of shale.*

(b) *Stress generated cracking in the shale rock.*



(c) *Stress breaks the shale rock.*

(d) *Laser drilled glassy hole in shale rock.*

A volume of  $5760 \text{ cm}^3$  of shale rock was cracked after stress generation with 2 mm diameter drilled holes [156]. In Berea grey sandstone and marble, the measured cracked volume was  $3640 \text{ cm}^3$  and  $2410 \text{ cm}^3$ , respectively. As we increase the drilled hole diameter on the rock surface, more and more stresses are generated in the rock and therefore it is possible to crack larger volumes of the rocks. The experiments clearly show that large diameter of drilled holes on the rock surface is favorable to damage the rock by this thermal spallation method. On the other hand, it seems that a large depth of drilling does not play a major role in increasing the volume of rock, which can be cracked. Depth of drilled hole was limited by the number of laser shots and it did not increase further with number of laser shots due to the insufficient material removal

capacity of suction system. As number of laser shots increase, the maximum values of measured penetration depth of drilled hole was 11 mm, 9.2 mm and 8.3 mm in the shale rock, sand stone, and marble, respectively (Fig. 6.34). This depth was measured for ten numbers of laser shots at 20 ms pulse duration and 200 J of pulse energy.

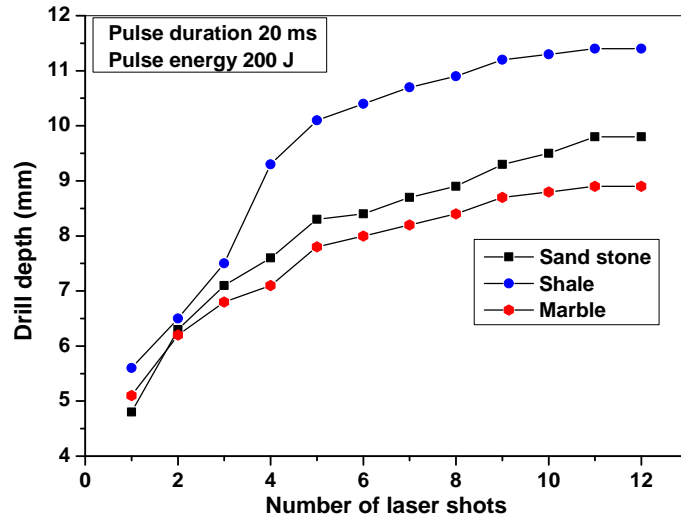


**Fig. 6.34.** Variation in laser drilled hole depth with number of laser shots for different rock.

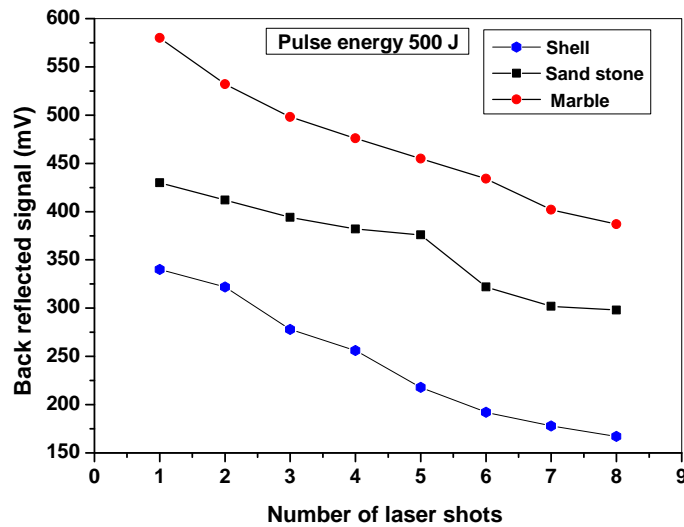


**Fig. 6.35.** Back reflected signal variation with laser shots for different rock samples at 500 J of pulse energy.

Back reflected IR signal was also measured during the drilling process with the same optical fiber which was used for the laser beam delivery. Fig. 6.35 shows a plot of the back reflected signal with number of laser shots for shale, sandstone, and marble. Higher signal was measured for marble and lower signal for shale, since shale has higher absorption as compared to the marble [157]. As the number of laser shots increase, the magnitude of the back reflected signal decreases. It clearly shows that the absorption in the material increases with the number of laser shots due to the heating of the material. Drilled depth for all the rock samples was saturated after ten number of laser shots and no further increment in the drilled depth was observed as material removal was not efficient after a depth of 10 mm. Measured diameter of drilled holes were 2.6 mm, 2.3 mm and 2.1 mm, respectively for sand stone, shale and marble samples. These dimensions of drilled holes significantly affect the behavior of fractures. It has been observed in our experiment that drilled holes of 2 mm or larger diameter have more fracturing capability as compared to holes of 1.5 mm diameter or less. Most of the molten material appears glassy near the opening of hole as seen in Fig. 6.33 (d).

## **6.6 Conclusions**

In conclusion, a study on laser cutting of thick section of stainless steel in the range of 4 mm to 20 mm using long pulse Nd:YAG laser has been performed for potential applications in dismantling work in nuclear facilities and ship breaking industry. Effect of important process parameters such as spot overlap, pulse duration, and gas pressure were investigated and optimized to achieve high cutting speed. It was found that the kerf width, HAZ, and sticky nature of dross formation are reduced in the underwater cutting as compared to dry air environment. An experimental study has been performed on laser cutting of steel to reduce the ejection of debris

using half-imaging of optical fiber. This is especially beneficial for dismantling work in nuclear facilities to reduce the contaminated debris generated during the cutting operation. It is also useful in other industrial applications to save the costly material during laser cutting process. Laser welding of stainless steel, aluminum, and titanium up to a thickness of 4 mm was also demonstrated. These results will be highly useful for the aerospace, automobile, nuclear, and vacuum components industries. Effect of laser pulse duration and number of laser shots on the rock spallation using a long pulse Nd:YAG laser was also studied. Experimental results showed that long pulse fiber coupled Nd:YAG laser can be used as a potential replacement for conventional rock drilling tools due to its ability to drill and destroy rocks more quickly. These results will be highly useful for petroleum and construction industry. In conclusion the performance of long pulse fiber coupled Nd:YAG lasers (described in Chapter 2) was tested successfully for different material processing applications.

# Chapter 7

---

## Study on laser cleaning with short pulse Nd:YAG laser

### 7.1 Introduction

Laser cleaning with short pulse Nd:YAG laser is known to be a well established technique. It involves exposure of the surface of the sample to a laser beam of short pulse duration and high energy density, to initiate the thermal ablation of the material from the surface [158-162]. As we have discussed in Chapter 6 the optical absorption for metals is dominated by free electrons and the energy transfer from photons to the lattice takes place through a physical mechanism known as inverse Bremsstrahlung. Excited electronic states transfer the absorbed energy to phonons in a time scale known as thermalization time. Hence, the interaction time of laser with material i.e., laser pulse duration is an important factor in thermal ablation process. In order to remove an atom from a solid surface by a laser radiation, one needs to deliver energy in excess of the binding energy of that atom. Short pulse lasers with pulse duration in the range of microsecond ( $\mu\text{s}$ ) to nanosecond (ns) are preferred for laser cleaning to avoid heat conduction and damage of the substrate [163-166]. For cleaning of particulates from solid surfaces, action of cleaning forces must overcome strong adhesion forces between the tiny particulates and the surface. Among these adhesion forces, the Van-der-Waals force, capillary force, and electrostatic force are of prime importance [167,168]. Laser cleaning is a selective ablation process and it

starts above a minimum fluence, called ablation threshold fluence ( $F_{th}$ ). Thermal ablation rate or evaporation rate  $R_{evap}$  and ablation depth  $d$  per pulse can be determined with the help of laser intensity and laser fluence as given by [168,169]

$$R_{evap} \cong \frac{I_a}{\varepsilon_b} \quad (7.1)$$

$$d = \frac{1}{\alpha_p} \cdot \ln\left(\frac{F}{F_{th}}\right) \quad (7.2)$$

where,  $\varepsilon_b$  is the binding energy per atom,  $1/\alpha_p$  is the effective penetration depth of laser energy and  $F_{th}$  is threshold fluence. For example, for gold target the  $\varepsilon_b=3.37$  eV per atom and  $1/\alpha=13.7$  nm [169]. The time  $t$  needed for the surface temperature to reach the vaporization temperature can be calculated by [31]

$$T_s(t) - T_0 = [2I_a / K] \cdot (kt / \pi)^{1/2} \quad (7.3)$$

where,  $T_s$  is surface temperature,  $I_a$  is the absorbed laser intensity,  $K$  is thermal conductivity of the material, and  $k$  is thermal diffusivity of the material measured in  $\text{cm}^2/\text{s}$ . From these equations, it is clear that the evaporation rate depends on the laser intensity and the ablation depth depends on the laser fluence.

In literature, marble cleaning with Free Running (FR) Nd:YAG laser with pulse duration in the range of 20-50  $\mu\text{s}$  has been found to be highly suitable [77,79]. On the other hand, for cleaning of corrosion and oxide layer from the surface of metals, such as copper, bronze, carbon steel, and mild steel, both  $\mu\text{s}$  and ns duration FR Nd:YAG laser pulses have been found to be suitable [159,161]. Laser cleaning is characterized by laser cleaning efficiency, which is given by  $\eta = 1 - (N_f/N_i)$ , where,  $N_i$  and  $N_f$  are the respective surface densities of surface layer particulates before and after laser cleaning. Maximum cleaning efficiency depends on the number of laser pulses at a single point or number of laser scan passes  $N_L$  as described by the equation [170-172]

$$\eta_N \approx 1 - (1 - \eta)^{N_L} \quad (7.4)$$

After laser cleaning, the sample surfaces were analyzed and characterized by the following methods:

**(a) Optical microscopy:** It is used for the visual observation of microstructure and deposition of sub micron size particles on the surface before and after laser cleaning. The resolution of an optical microscope is given by  $R = (0.61\lambda/NA)$  where  $\lambda$  is the wavelength of illumination and NA is the numerical aperture of the objective lens which shows the light gathering capacity of objective lens of microscope. We also need to consider the depth of focus (vertical resolution) which is given by  $DOF \approx \lambda/NA$ . The DOF shows the ability to produce a sharp image from a non-flat surface. Contrast is also an important factor defined as the difference in light intensity between the deposition and the adjacent background (substrate) relative to the overall background intensity. Image contrast, C is defined by  $C = [S(\text{deposition}) - S(\text{background})]/S(\text{background})$ , where S(deposition) and S(background) are intensities measured from the deposited particles and background. The limitation of the optical microscopy is its limited resolution. Further, if the sample is colorless, transparent, isotropic, and embedded in a matrix with similar properties, imaging with good contrast is difficult. This is because our eyes are sensitive to amplitude and wavelength differences, but not to phase differences.

**(b) Scanning electron microscopy (SEM):** The SEM is an analytical tool that uses a focused beam of electrons to form magnified images. SEM image analysis is a powerful technique for generating particle distribution profiles as well as surface characteristics with the possibility to visually re-evaluate the data by re-assessing the particles. The technique makes it possible to characterize the size (nm to  $\mu\text{m}$ ) and shape of particles with relatively wide distribution profiles. This technique is highly useful for the analysis of surfaces of conductive materials like metals.

Non-metal samples (for example marble and stones) were given a conductive coating (gold or platinum) using sputter ion coater and then examined with SEM equipped with a backscattered electron detector for imaging. In SEM, a focused electron beam is scanned over the sample in parallel lines. The electrons interact with the sample, producing an array of secondary effects, such as back-scattering, that can be detected and converted into an image. The image can then be digitalized and presented to an image analyzer, which uses complex algorithms and software program such as image processing tool to identify individual particles and record detailed information about their number, size and distribution. The limitation of SEM analysis is that it concentrates a high amount of energy in a small region and can be very destructive towards organic materials or other thermally sensitive compounds. Sometimes the particle boundaries are indistinct, and the image processing tool may interpret them incorrectly. For non metallic surface analysis a thin conductive coating is required on the surface which is a tedious job and sometimes it can modify the surface morphology.

**(c). X-ray photo-electron spectroscopy (XPS):** The XPS method uses soft X-rays (1.48 keV) for the surface analysis. The sample surface is not subjected to very high-energy fluxes unlike in the SEM. The spot size can be varied between 150 to 1000  $\mu\text{m}$ . The incident X-rays create ionized ions on the surface and the free electrons are ejected out from the surface. The energies of these free electrons are related to the binding energies of the surface atoms. The chemical elements present in the sample are identified by measuring these characteristic energies. Hence, a XPS shows intensities of photoelectrons versus binding energy. XPS provides both elemental and, to a certain extent, chemical information in the top 3-30 atomic layers (10-100 $\text{\AA}$ ) in solid samples. The sensitivity varies between 0.01-1 atom% dependent upon the element. It can do nondestructive depth profiling to 100  $\text{\AA}$  and detect all elements except H and He. XPS is

especially good for obtaining elemental surface composition of unknown materials, including conductors and insulators. An XPS spectrum consists of a series of peaks corresponding to the binding energies of the photoelectrons that produced these peaks. XPS analysis not only provides elemental information, but the technique is detecting the binding energy of emitted electrons, it can also provide some chemical bonding information. Depending on what elements the parent atom is bound to, the binding energy of the emitted photoelectrons may shift slightly. The instrument is sensitive enough to detect these electron energy shifts and use them to determine the chemical compounds. Since the analysis beam (X-rays) does not consist of charged particles, the specimen is not required to conduct away any charge buildup due to the incidence of the beam itself. XPS technique has a limitation that the largest X-ray spot (image of the beam on the sample) is only 1 mm and hence the technique is in practice is usable for analysis of small surface areas ( $\sim 1 \text{ mm}^2$ ).

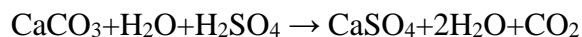
**(d) Soft X-ray reflectivity (SXR):** Angle-dependent SXR measurement with soft X-rays can be used to determine the structure of a multilayer or single-layer film and evaluate surface roughness and interface width. It can be used to study an opaque film under visible light and measure film thickness from few nm to 1000 nm. The X-ray refractive index of a substance is slightly less than 1. SXR is based on the response of a given material film to an incident X-ray, which is described by the complex index of refraction  $n=1-\delta+i\beta$ , here,  $\delta$  and  $\beta$  are the refractive and absorptive parts of the refractive index, respectively. This technique provides information about  $\delta$ ,  $\beta$ , and critical angle  $\theta_c$  for total external reflection. The value of  $\delta$  depends on the X-ray wavelength, and density of the film. The critical angle  $\theta_c$  is given by  $\theta_c=\sqrt{2\delta}$ . Thus the density of the surface film can be obtained from the angle  $\theta_c$ . The parameter  $\beta$  is expressed by the linear absorption coefficient  $\mu$  as  $\beta=\lambda\mu/4\pi$ . In our experiment, for the analysis of laser cleaned surface,

soft X-ray ( $130\text{\AA}$ ) of SR beamline of INDUS-1 synchrotron radiation source was used [173]. The X-rays undergo total external reflection when the incident angle is smaller than the critical angle ( $\theta_c$ ). X-ray reflectivity decreases rapidly with increasing incidence angle,  $\theta$  above  $\theta_c$ . The ratio of the specularly reflected X-rays decreases proportional to  $\theta^4$ . In the SXR measurements the normalized intensity ( $I/I_0$ ) is plotted on y-axis on logarithmic scale because of the wide dynamic range of the intensity  $I$  of X-ray reflectivity. Interference occurs between the X-rays reflected from the surface of the deposited film and the interface between the film and the substrate. The reflectivity profile shows oscillations caused by this X-ray interference. The oscillation depends on the film thickness: the thicker film, the shorter is the period of the oscillations. The amplitude of the oscillation and the critical angle  $\theta_c$  provides information on the density of films. The amplitude of the oscillations depends on the difference between the densities of the deposited film and substrate, the larger the difference in the film density, the higher is the amplitude of the oscillation. Thickness of contamination layer and the surface roughness of the order of a few nm can be measured using Nevot–Croce model [174]. The measured data can also be fitted to a curve using Parratt formalism [175]. Levenberg-Marquardt algorithm can be used to further refine the fitting parameters. In summary, SXR method is nondestructive and can be used for evaluating the layer structure, thickness, density and surface roughness. In SXR curve critical angle provides the value of density, the amplitude of oscillations provides the value of density contrast, the period of oscillations gives film thickness and after total external reflection, intensity decay rate of X-ray at higher angles gives the value of surface roughness. Hence, this method is highly useful for the analysis of surface before and after laser cleaning and to the best of our knowledge, this method has been used for the first time for the analysis of the laser cleaned surface of gold-coated fused silica mirrors.

In this chapter, we describe the studies carried out on laser cleaning of marble, stones, inconel, zircaloy, carbon layer from gold surface and gold layer from fused silica substrates using short pulse Nd:YAG laser. Cleaning quality and cleaning efficiency in different cases has also been analyzed. In Section 7.2, details of laser cleaning of marble, stones, zircaloy and inconel are provided. Further, in Section 7.3, laser cleaning of carbon layer from gold coated mirrors has been described. Section 7.4 is devoted to the study of laser cleaning of gold coating from fused silica substrates and Section 7.5 provides the conclusion.

## **7.2 Laser cleaning of marble, stones, zircaloy, and inconel**

Marble is an important ingredient of many buildings and monuments of historical importance. The large amount of sulphur dioxide and carbon monoxide released in the atmosphere by human activities has led to an increase in damage of monuments made of marble. The main chemical modification induced by atmospheric pollution in marble and in other limestone is associated with the formation of gypsum in the superficial layers. It is driven by the chemical reaction of calcium carbonate in the stone substrate and sulphuric acid produced by acid rains with high content of sulphur dioxide:



The gypsum layer is softer and more water soluble than marble and it is easily contaminated by hydrocarbons and other pollutants giving rise to black crust that covers most statues and monuments in urban areas [176-178]. Further, in this study we have also described laser cleaning of stones (Berea gray sandstone and Shale) using a short pulse Nd:YAG laser of microsecond pulse duration. Cleaning efficiency has been determined as a function of number of laser shots and spot overlapping.

In nuclear industry, inconel 600 is an important material used for fabrication of steam generation (SG) tubes [179]. Similarly, zircaloy is used in the fabrication of pressure tubes of Pressurized Heavy Water Reactors (PHWR). These SG tubes and pressure tubes are contaminated by radioactive nuclides, which may have a long half-life. Hence, even after decommissioning of these facilities these materials are stored and monitored over a very long period of time. Often the radioactive contaminants in these materials, are only on the surface layer or slightly deeper layer under the surface (a few micrometers to ~1mm). Since many of the structures are long and thick, it makes environmentally and economically more sense to remove a thin contaminated layer and store the material rather than to treat the entire structure as nuclear waste. Thus, surface cleaning is required to remove the oxide and other deposition layer from the surface of inconel and zircaloy to reduce nuclear waste. Current chemical and mechanical removal methods are slow and labour intensive. These methods also suffer from the dust control problem, and radiation exposure to workers. Hence, alternate methods of contamination removal without the disadvantages of the conventional methods are being investigated. In-situ laser cleaning with fiber coupled Nd:YAG lasers is one of the solutions to remove the deposition from the surface. Lasers are attractive for cleaning or decontamination purpose, since laser beam can be delivered remotely via fiber optic cables and focusing head can be manipulated by robots, thus minimizing radiation exposure to workers. We have carried out some experiments on laser cleaning with short pulse (55  $\mu$ s) Nd:YAG laser as described in the next Section.

### **7.2.1 Experimental work**

In order to perform the laser cleaning experiments, a short pulse free running Nd:YAG laser was developed with a pulse duration of 55  $\mu$ s and repetition rate 1-20 Hz. The laser

provided maximum pulse energy of 1.25 J per pulse with a peak power of ~22 kW. The laser beam was delivered through a 200  $\mu\text{m}$  fiber. A laser focusing nozzle was mounted on a three-axis, computer controlled CNC machine. The nozzle consists of a cylindrical focusing lens of 40 mm focal length which generates a focused line of 0.2 mm  $\times$  6 mm. Position of the focal line was kept 2 mm away from the focusing nozzle tip. The nozzle was tilted at an angle of  $10^\circ$  (with respect to plane of the substrate) to prevent the entry of back reflected laser beam from the job surface into the optical fiber and cause its damage. The nozzle also has provision for blowing coaxially a gas jet of argon gas at a constant flow rate of ~ 30 l/m to protect the cleaned surface from oxidation by creating an inert atmosphere and also to protect the focusing lens from the possible fumes of ablated material from the substrate surface. The experimentally measured value of ablation threshold fluence ( $F_{\text{th}}$ ) is 0.6 J/cm<sup>2</sup> for marble and 2 J/cm<sup>2</sup> for zircaloy and inconel materials. Before and after cleaning, the number of deposited particles on surface counts by SEM image acquisition materials analysis software (Avizo® Fire from Visualization Sciences Group, USA). The data obtained from SEM image, processed for cleaning efficiency measurement. For the measurement of cleaning efficiency, the surface of inconel was also studied and analyzed using X-ray photoelectron spectroscopy (XPS). Omicron EA-125 model equipped with Al source was used to perform the XPS measurements.

## 7.2.2 Result and analysis

During laser cleaning experiments the amount of ablated material  $m_{\text{avg}}$  was measured by averaging total ablated mass over the total number of laser pulses. Ablation depth per pulse is given by  $d_{\text{abl}} = m_{\text{avg}} / (s_f \rho)$ , where  $s_f$  is focus spot diameter (200  $\mu\text{m}$ ) and  $\rho$  is bulk density of the target material. Ablation rate in terms of the number of atoms ablated per pulse  $N_{\text{abl}}$  can be

calculated by  $N_{abl} = d_{abl} S_f n_a$ , where,  $n_a$  is the number density of atoms in the target [180]. For marble, measured value of ablation depth at a fluence level of 0.6 J/cm<sup>2</sup> and 55 μs pulse duration was of the order of 20-25 nm per pulse. Beyond a value of 3 J/cm<sup>2</sup> of fluence level, the substrate surface starts to damage due to high energy deposition. Hence, a careful control of laser fluence is required for damage free marble cleaning. In a single pass of laser beam, a relatively high value of cleaning efficiency of ~85% was achieved for marble as compared to ~80% for inconel material. After ten number of laser passes, the value of cleaning efficiency reaches a value as high as ~98% for marble as well as for inconel. Finally, a good clean surface was achieved for marble at a fluence level of 0.6 J/cm<sup>2</sup> and peak power density of 0.5 MW/cm<sup>2</sup>, speed of 48 mm/min, repetition rate of 20 Hz and a spot overlapping of 80%. Similarly, a good clean surface for inconel was achieved at a fluence level of 2 J/cm<sup>2</sup>, a speed of 40 mm/min, repetition rate of 20 Hz and a spot overlapping of 80%. If the fluence level is high enough, it may also damage the surface being cleaned. Surface damage threshold of various materials depend on its thermo-physical properties and surface absorption coefficient. Values of damage threshold for marble, stones, zircaloy, and inconel was measured experimentally and is listed in Table 7.1 along with other important thermo-physical properties of these materials. Fig. 7.1 shows a view of laser cleaned surfaces of marble, zircaloy and inconel obtained using 200 μm fiber coupled pulsed Nd:YAG laser.

**Table 7.1.** Experimentally measured values of ablation and damage threshold during Nd:YAG laser cleaning experiment with important thermal properties of various samples.

Sample material	Damage threshold (J/cm <sup>2</sup> )	Ablation threshold (J/cm <sup>2</sup> )	Thermal diffusivity (cm <sup>2</sup> /sec)	Melting temperature °C	Vaporization temperature °C
Marble	2.1	0.6	0.11	850	887
Berea grey sandstone	2.4	0.5	1.5	1540	1750
Shale	2.5	0.6	0.12	1215	1544
Zircaloy	4.1	2.0	0.14	2125	2620
Inconel 600	4.5	2.0	0.31	1354	2345

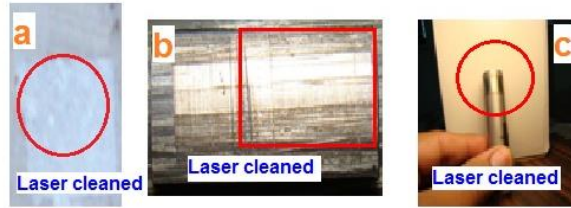


**Fig. 7.1.** A view of laser cleaned surface of marble, zicaloy, and inconel.

Further, visual and aesthetic results of any conservation process are of crucial importance. Even if the contaminated regions are not over bleached after laser cleaning, its appearance should be indistinguishable from the originally clean regions and should not diminish the authenticity of the object. Figure 7.2 (a) shows SEM image of the marble sample before laser cleaning using ten laser passes. The deposition of pollution layer on the marble surface can be clearly seen in the SEM image. Figure 7.2 (b) shows, smooth laser cleaned surface of marble. The cleaning efficiency is measured by the number of small size particles which remain on the surface after cleaning. Image of the sample clearly shows that the contamination gets removed completely from the upper surface of the marble after laser cleaning. Similarly, Fig. 7.3 shows SEM image of surface of the stone (Berea gray sand stone) sample. It shows smooth laser cleaned surface with a high cleaning efficiency as the number of small size particles, which remain after laser cleaning are negligible. Fig. 7.4 (a) and (b) shows the SEM image of the surface of inconel sample before and after laser cleaning. The laser cleaned surface is smooth and has negligible number of particles on the surface.

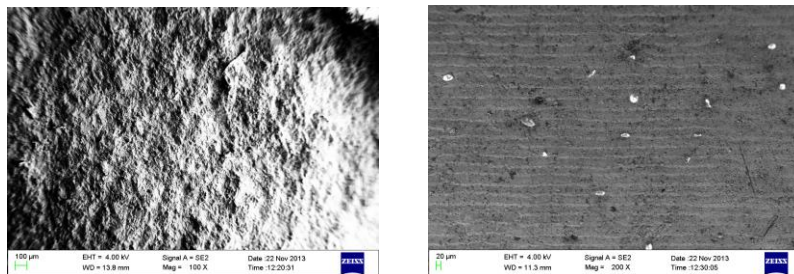


**Fig. 7.2.** SEM images of the surface of the marble sample, (a) before laser cleaning and (b) after laser cleaning,

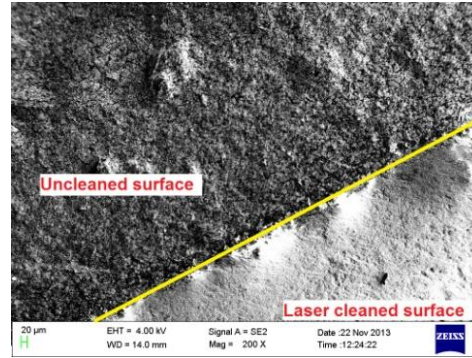


**Fig. 7.3.** SEM images of the surface of the stone (berea gray sand stone) sample (upper part shows uncleaned surface and lower part shows laser cleaned surface).

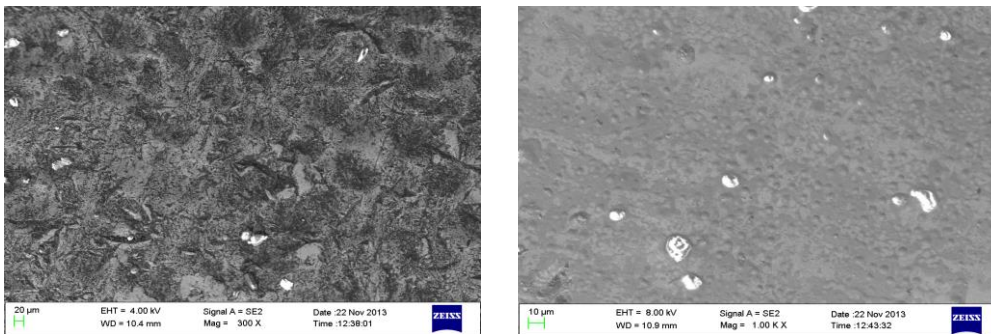


**Fig.7.4.** SEM images of the surface of the inconel sample, (a) before laser cleaning, and (b) after laser cleaning.

Further, colour analysis has also been performed for evaluation of laser cleaning [176]. For this purpose, a cleaning effectiveness parameter (CE%) is defined as  $CE\% = \left[ (\Delta E_w^* - \Delta E_c^*) / \Delta E_w^* \right] \times 100$ . Where,  $\Delta E_w^*$  is the colour difference between the surface of the native substrate material and the deposited (contaminated) surface of the same material.  $\Delta E_c^*$  is the colour difference between the surface of the native substrate material and the laser cleaned surface of the same material. When  $\Delta E_c^*$  tends to zero, the laser cleaned surface has a colour similar to the native substrate material indicating cleaning effectiveness close to 100%. Values of CE% for marble, stones, zircaloy, and inconel was measured experimentally and is listed in Table 7.2.

**Table. 7.2.** A list of process parameters and results of laser cleaning experiments on different samples.

Sample material	Density (gm/cm <sup>3</sup> )	d <sub>abl</sub> (nm)	N <sub>abl</sub> (atoms/pulse)	Process parameters			Efficiency η (%)	Cleaning Effectiveness (CE) %
				Fluence (J/cm <sup>2</sup> )	Laser shots	Overlapping (%)		
Marble	2.9	22	2.0×10 <sup>13</sup>	0.6	10	80	98	99%
Berea grey sandstone	2.15	24	3.0×10 <sup>13</sup>	0.6	10	80	98	87%
Shale	2.36	20	1.8×10 <sup>13</sup>	0.6	10	80	97	92%
Zircaloy	6.49	15	1.7×10 <sup>13</sup>	2.0	10	80	97	99%
Inconel 600	8.47	10	1.5×10 <sup>13</sup>	2.0	10	80	98	99%

Figures 7.5, 7.6, 7.7 show that after laser cleaning, marble, inconel, and zicaloy have recovered almost the same colour as the native unpolluted (without contamination) surface, whereas stones have lost some shades of original colour as shown in Fig. 7.8. Slight change in colour occurs on stone surface due to the change in the different oxidation states of Fe rich compounds.



**Fig. 7.5.** Surface of the marble sample shows a clear difference between unclean and laser cleaned surface. After laser cleaning, the substrate colour becomes similar to the native substrate material.

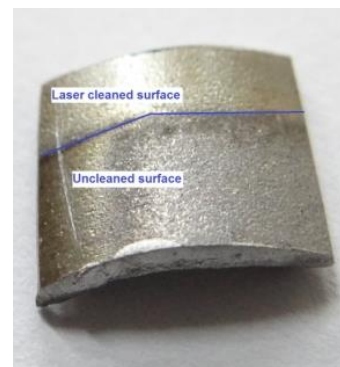


**Fig. 7.6.** Surface of the inconel sample shows a clear difference between unclean and laser cleaned surface. After laser cleaning, the substrate colour becomes similar to the native substrate material.

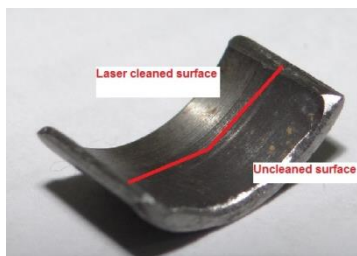


**Fig. 7.7.** Surface of the zircaloy sample shows a clear difference between unclean and laser cleaned surface. After laser cleaning, the substrate colour becomes similar to the native substrate material.



**Fig.7.8.** Surface of the berea gray sand stone sample shows a slight colour difference between the laser cleaned surface and native substrate surface.

For XPS analysis, inconel-600 sample has been selected as an example. Chemical composition of inconel-600 is shown in Table 7.3. The commonly found elements in the deposition on the surface of inconel-600 are Fe, O, C, Si, S, F and K [180-183]. However, in the XPS analysis, we have considered only Fe and C deposits due to the major contribution of these elements. Figure 7.9 shows XPS curve of the iron (Fe) peaks of inconel-600. It shows a clear difference between the Fe peaks before and after laser cleaning. After laser cleaning, although Fe deposits on the surface are removed, however, due to higher wt% of Fe (7.6 wt%) in the base material of inconel-600 as compared to that in the surface deposits, Fe peak is enhanced [184].

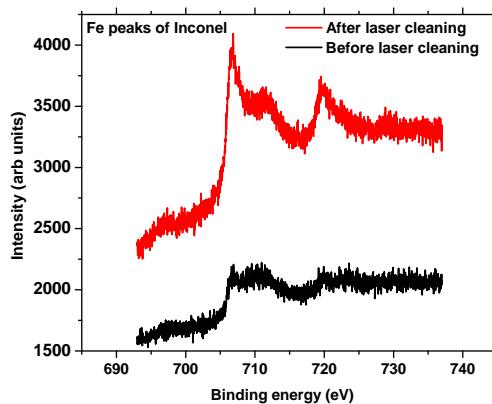


**Fig. 7.9.** XPS spectrum of inconel-600 shows the peaks of Fe increases after laser cleaning.

**Table. 7.3.** Chemical composition (wt%) of inconel-600 sample.

Ni	Cr	Fe	Si	Ti	Mo	Co	Mn	Al	C	N	S
Bal.	15.9	7.6	0.15	0.21	0.25	0.38	0.17	0.12	0.035	0.037	0.002

On the other hand, for carbon deposits the peaks are reduced after laser cleaning (Fig. 7.10). A lower peak of carbon is observed after laser cleaning as compared to the sample before cleaning due to the higher wt% of carbon in the surface deposits compared to that in Inconel-600 (the substrate) [184]. A detailed explanation and analysis of the removal of carbon layer from the metal surface, for example from the gold surface, using Nd:YAG laser based cleaning method given is in Ref. [185] and in the next Section of this Chapter.

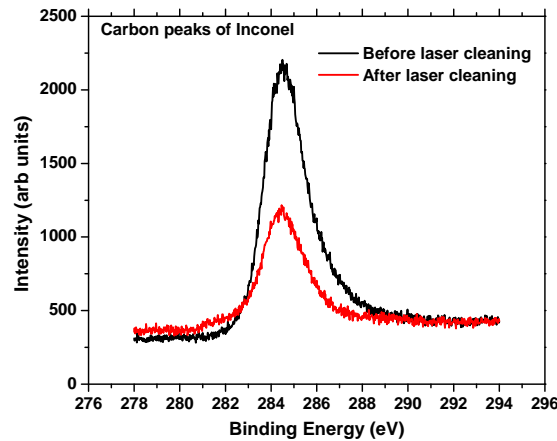


**Fig. 7.10.** XPS spectrum of inconel shows that the peaks of carbon reduce after laser cleaning.

Finally, Nd:YAG laser of  $\mu\text{s}$  pulse duration has been tested successfully for cleaning of the surface contamination from the marble. It was also used for cleaning of the surface contamination on zircaloy and inconel for nuclear industry. Performance of this laser also shows that it can be used further for effective surface cleaning of contamination over a wide range of

other materials like concrete, rocks, stainless steel, copper, niobium, titanium, and aluminium. It was also shown that the top-hat like intensity distribution obtained after the delivery of laser beam through a 200  $\mu\text{m}$  core diameter optical fiber (see Chapter 4) was also found to be useful for selective, uniform and efficient laser cleaning. In the next sections of this Chapter, laser cleaning has been studied using ns duration laser pulses.

### **7.3 Study on cleaning of carbon layer from gold surface**

Carbon contamination of optical elements in extreme ultraviolet (EUV) spectrometers and synchrotron radiation (SR) beamlines is still a big problem. The carbon containing molecules (such as oil vapors from machining process, vacuum pump oil vapors etc.) which are adsorbed on the optical surface are cracked either directly by X-rays or by free electrons created by X-rays [186-187]. After cracking, the carbon atoms stay on the surface with strong binding to the surface. Carbon molecules present in the residual gas in vacuum chambers get adsorbed on the surface and cracking process starts again. The growth rate is directly proportional to the photon flux, hence the performance of SR beamlines is seriously affected over a period of time. Carbon contaminations reduce the SR beamline flux up to two orders of magnitude near carbon K-edge (285 eV) energy. Carbon contamination reduces the signal-to-noise ratio, in experiments, particularly near C-K edge energy range. Even a 1 nm thickness of carbon layer reduces relative reflectivity ( $\Delta R/R_0$ ) of a single multi layer optical surface by 1.4% as estimated from theoretical modeling. This reduction is because of high absorption of EUV radiation by carbon, which makes this contamination layer a big source of loss. Extreme ultraviolet lithography (EUVL) scanner optics typically consists of ten such reflecting layers, where total photon flux deteriorates drastically hence replacement of costly optical elements over a period of time is a must. Since

EUV optical elements are very costly, instead of replacement with a new optical element, it is desirable to develop a technique for periodic cleaning of the carbon contamination without damage or modifications to the underneath gold film/surface. Laser cleaning has several advantages over other cleaning techniques, such as it is very fast, non-contact, dry in nature, highly localized, well controlled making it possible to carry out layer-by-layer removal of material. In the present work, we have employed a nanosecond pulsed Nd:YAG laser to remove deposited carbon layer from the gold mirror surface. It was found that the carbon layer can be removed using laser pulses at high repetition rate of 1–2 kHz. X-ray photoelectron spectroscopy (XPS) and soft X-ray reflectivity (SXR) techniques have been used to analyze the quality of laser cleaning [185].

### 7.3.1 Experimental work

A lamp pumped acousto-optic (AO) Q-switched Nd:YAG laser system, with 100 ns pulse duration, 10 mJ of pulse energy was used for laser cleaning process. Schematic diagram of laser cleaning setup is shown in Fig. 7.11. For higher cleaning efficiency sample was kept at 30° angle [171].

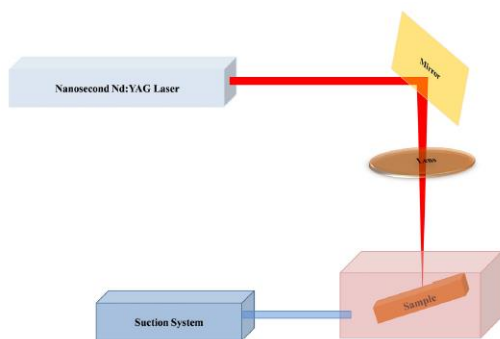


**Fig. 7.11.** Schematic layout of experimental set-up for laser cleaning of carbon.

Process parameters such as laser repetition rate, pulse duration, pulse energy, laser intensity, and focused beam area over the carbon thin film were optimized in a similar way as reported by Gamaly [169]. These optimized parameters were used in the experiments described below. We have used a test sample of 200 nm thick gold film deposited on fused silica glass for the laser cleaning experiments. A 20 nm thick carbon layer was deposited on two third portion of the gold coated test sample using electron beam evaporation technique. One third portion was kept intact for comparison after the laser cleaning.

### 7.3.2 Result and analysis

XPS measurements on three different areas of the sample marked as region A, B and C (see Fig. 7.13) are carried out near C 1s energy region and are shown in Fig. 7.12.

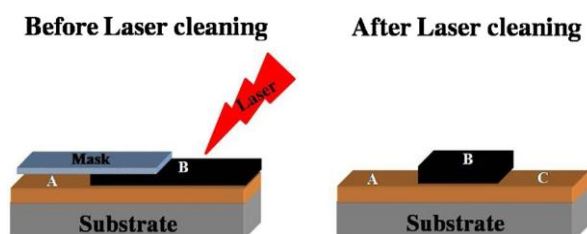


**Fig. 7.12.** Schematic diagram of the sample used for laser cleaning experiments: (A) intact gold film, (B) carbon coated gold film, and (C) carbon removed gold film after laser treatment.

The peak corresponding to C-1s binding energy has a significantly large width which indicates that different phases of carbon are present in the sample. XPS spectrum of the carbon coated gold film region (Fig. 7.13 b) shows that the experimental data can be fitted using two components, one with peak energy of 284.7 eV and the second with peak energy of 287.8 eV. After laser cleaning experiments, the carbon film is removed from the sample; however, the

presence of carbon peak in the XPS spectra seems to be originating from the residue carbon atoms or atmospheric carbon. The position of the carbon peak of the laser cleaned region ‘‘C’’ is shifted with respect to the carbon peak of the intact gold film region ‘A’ and that of carbon coated gold film region ‘B’ (Fig. 7.13). Carbon peak of region-C is fitted with two components, one with peak energy 285.3 eV, and the second with peak energy 287.4 eV. The peak at 285.3 eV corresponds to C-C sp<sup>3</sup> hybridization (diamond like) and at 287.4 eV corresponds to C-O group [188]. In the present case, the presence of 285.3 eV peak corresponding to C-C sp<sup>3</sup> bonding suggests that the residue carbon present on the sample surface after laser cleaning have undergone a phase transition induced by laser shots. However, the intensity of C peak of two areas, region-A (intact gold film) and region-C (laser treated area) are similar (Fig. 7.13). This suggests that the atmospheric carbon on region-A and sp<sup>3</sup> phase in the region-C are in similar amount. For further confirmation and quantitative study, soft X-ray reflectivity (SXR) measurements were also carried out.

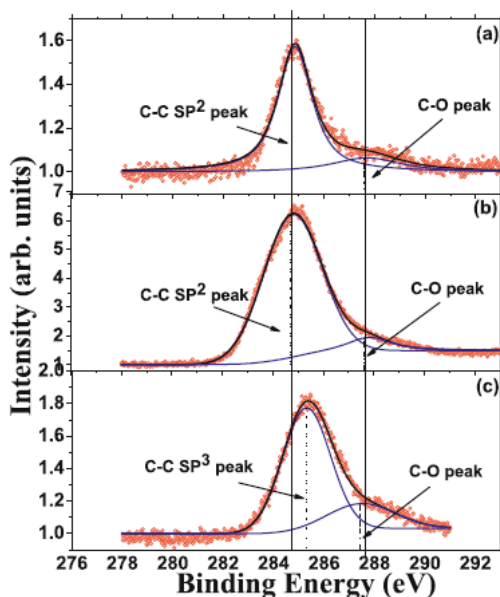


**Fig. 7.13.** XPS measurements of the three regions of the sample: (a) intact gold film, (b) carbon coated gold film, and (c) gold film after carbon removal with laser treatment.

In SXR measurements using incident wavelength  $\lambda=70 \text{ \AA}$ , the carbon coated gold film and pure gold film gives distinctly different critical angle. The carbon film shows critical angle at  $7.9^\circ$  and pure gold film at  $10.5^\circ$ . SXR data of region-A of the sample which has an intact gold film shows a single critical angle corresponding to gold layer, this is shown in Fig. 7.14(a). Since Nd:YAG laser treatment was carried out on region-C, hence this region should exhibit a single critical angle corresponding to gold film if carbon layer is completely removed. Fig. 7.14 (c) corresponding to region-C confirms that this region has a single critical angle of pure gold film. Parameters such as optical constants of the film obtained from the detailed fitting of SXR data are found to be in close agreement with the theoretical values.

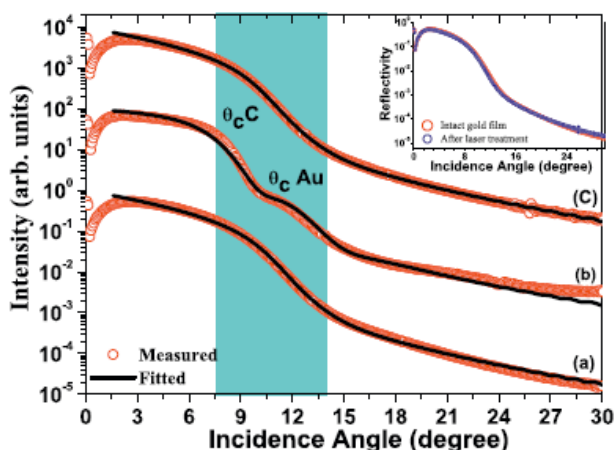


**Fig.7.14.** Measured and fitted SXR spectra of (a) intact gold film, (b) carbon coated gold film, and (c) gold film after carbon removal. Critical angle corresponding to total external reflection region are distinctly different for pure gold film and carbon coated gold film as shown in highlighted area in the figure. After carbon film removal with laser treatment, the reflectivity curve of intact gold film and that of laser cleaned gold film are similar as shown in inset of the figure. For the sake of clarity the curves are vertically shifted.

Our study on XPS and SXR analysis for carbon removal from the gold surface shows that the cleaning technique using laser can effectively remove the contaminated carbon layer from the

gold substrate. In the process of laser cleaning of carbon, the surface roughness of substrate is not changed. This is very important since the surface roughness of the gold cause's significant reduction in the intensity of reflected X-ray beam from these mirrors in SR beamline. In conclusion, it has been shown that the dry laser cleaning (laser ablation) using ns pulsed Nd:YAG laser very useful method for the cleaning of carbon from the optical components of SR beamline.

#### **7.4 Study on laser cleaning of gold layer from fused silica surface**

We have also carried out studies on laser cleaning of gold layer deposited on fused silica substrates used in beamlines of synchrotron radiation sources using nanosecond pulsed Nd:YAG laser. Synchrotron radiation (SR) is one of the important tools of investigations for material characterization, biomedical imaging, absorption measurements, and as a standard for calibrating detectors [189,190]. The continuous spectrum of electromagnetic radiation emitted by electron synchrotrons extends in the vacuum ultraviolet and X-ray regions. As we have discussed earlier in Section 7.3 of this chapter, carbon contamination on the optics surface such as on gold-coated mirrors and gratings is a major problem in the SR beamline and is responsible for the damage of reflective coatings on the optics [190-193]. The damage of coatings degrades the SR beamline performance. Generally the damage of the gold-coating is observed in the central portion of the mirrors since the grazing incident SR beam is primarily absorbed in this region by the carbon contamination. The SR mirrors are very expensive since these are large in size, have very high quality substrates of different shapes (spherical, rectangular, toroidal etc.) and have special gold coatings which are extremely uniform and can withstand large beam energy flux. Hence the removal of damaged gold coating without any damage to the substrate is important for re-coating

of these mirrors with fresh gold coatings. Thus, it is of importance to develop a technique for the cleaning of the gold layer of these mirrors without damage or modifications of the surface of the high optical quality substrate such as fused silica. There are several conventional cleaning methods for cleaning or coating removal including plasma cleaning, oxygen-discharge cleaning, chemical cleaning, electric discharge, and arc cleaning [194-197]. However, it has been observed that with these cleaning methods, sometimes the substrate surface is damaged or its morphology is modified making the re-coating of the mirrors difficult after cleaning process. The laser cleaning of gold layer is a potentially promising method, which may provide a more satisfactory solution. In this Section, we present the studies on laser cleaning process for the removal of 48 nm thick gold layer from fused silica mirror substrates for potential application in SR beamlines.

### 7.4.1 Experimental work

Figure 7.15 illustrates a schematic of experimental set-up for laser cleaning of gold layer. Fused silica mirror samples with 48 nm thick gold coating and dimensions of  $100 \times 60 \times 2 \text{ mm}^3$  were prepared. These samples were prepared without intermediate chromium layer using the technique proposed by Popescu [198].

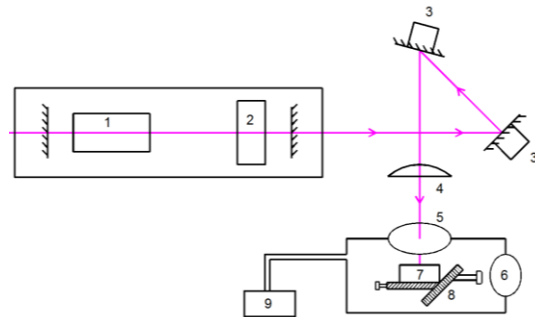


**Fig. 7.15.** Schematic of experimental set-up. (1. Laser pump chamber 2. AO Q-switch 3. X-Y scanner, 4. Flat field lens 5&6. Optical windows 7. Sample 8. Tilting screws, 9. Suction system).

A lamp-pumped acousto-optic (AO) Q-switched Nd:YAG laser providing pulses of ~100 ns duration, 10 mJ of energy at 2 kHz of repetition rate at a wavelength of 1064 nm was utilized for cleaning experiments. Samples were kept in a sealed and closed chamber having three antireflection (AR) coated optical windows for entry of laser beam and visual observation. Sample holder was fixed on a motorized translation stage and permits a precise repositioning of the sample. Angular tilting facility was incorporated with translation stage to perform the experiment at different incident angles of the laser beam. A suction system consisting of a vacuum pump of 200 l/min displacement rate and a particle filter prevents the redeposition of the ablated particles on the substrate. One of the key requirements for precise removal of surface layers with lasers is the high degree of control over the scanning speed of the focused laser beam. A constant and high scanning speed was achieved with orthogonal pair of scanner mirrors based on galvo-motors. The scanner mirrors can move the laser beam in the  $x$ - $y$  plane and a flat field ( $f$ - $\theta$ ) lens always keeps its focus in the same  $x$ - $y$  plane. Typical laser spot diameter at the focal plane was ~700  $\mu\text{m}$ . The experiments were performed with different percentage of spot overlapping and constant scanning velocity for a fixed area. The laser beam was moved in  $x$ -direction in the first pass and then in  $y$ -direction in the next pass on the sample. The laser scanning was carried out over an area of 48  $\text{cm}^2$  (6  $\text{cm} \times 8 \text{ cm}$  in  $x$ - $y$  plane) on the surface with a linear velocity of 280 mm/sec at 2 kHz pulse repetition rate and 80% spot overlapping.

#### **7.4.2 Result and analysis**

Figure 7.16 shows a view of the laser cleaned gold layer from the mirror samples. The 48 nm thick gold layer (film) was cleaned efficiently using ~100 ns duration laser pulses. It was

experimentally found that laser fluence in the range of 0.4-2 J/cm<sup>2</sup> permits evaporation of gold layer with a safety margin to avoid the damage of the underlying fused silica substrate.

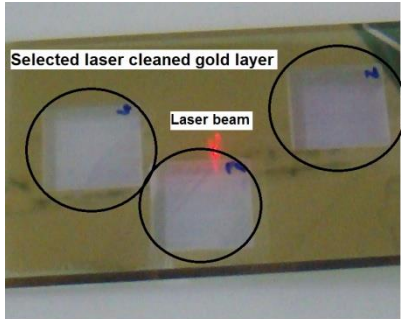


**Fig. 7.16.** A view of laser cleaned gold-coated mirror in selected areas.

**Table. 7.4.** Thermo-physical parameters of gold and fused silica.

Physical Property	Gold layer	Fused silica
T <sub>m</sub> (°C)	1063	1730
T <sub>v</sub> (°C)	2966	2230
C <sub>p</sub> (J/g°C)	0.13	0.07
L <sub>v</sub> (J/g)	1550	50.2
K (W/m°C)	318	1.38
k (cm <sup>2</sup> /s)	1.50	7×10 <sup>-3</sup>
a (%)	30	3.5
α (°K <sup>-1</sup> )	14.2×10 <sup>-6</sup>	0.55×10 <sup>-6</sup>
ρ(g/cm <sup>3</sup> )	16.4	2.23

The values of some important thermo-physical parameters of thin gold layer and bulk fused silica substrate are as given in Table 7.4, which has been used to select the optimum value of threshold fluence of laser beam [169,171]. Using Eq. (7.3) of Section 7.1, calculated value of  $t$  for thermal ablation of 48 nm thick gold film is of the order of 0.48 ns for a fluence of 0.5 J/cm<sup>2</sup>. Hence, it is difficult to achieve photo-thermal ablation using ps duration pulses as the interaction time of the laser pulses with the material, is less than the thermalization time. Moreover, gold has a weak electron-phonon coupling ability for fs and ps pulse laser excitation, the process which is important for thermal ablation [199]. Hence, ps pulses were not selected for gold layer cleaning.

Nanosecond pulse Nd:YAG lasers with pulse energies of the order of 10 mJ are easily available. The required threshold fluence can also be easily achieved for thermal ablation of gold with ns pulses. Further, it was observed that laser pulses of ~100 ns duration leave some amount of residual heat after thermal ablation of the gold layer, which changes the surface morphology of fused silica mirror and improves the root mean square (rms) surface roughness. This improvement in surface roughness is favourable for re-coating of mirror. The ablation depth per

pulse at the fluence level of  $0.5 \text{ J/cm}^2$  was found to be of the order of 10-15 nm per pulse, which is much higher than the value of  $\sim 3 \text{ nm}$  as calculated using Eq. (7.2). This difference may be due to the errors in the estimation of actual value of fluence and threshold fluence. Figure 7.17 shows variation of measured ablation depth as a function of fluence and Fig. 7.18 shows a plot of cleaning efficiency as a function of laser fluence. The results in Fig. 7.17 and 7.18 are for front side ablation. The ablation depth in each laser shot is limited due to the attenuation of incoming laser beam in laser produced plasma during ablation process.

It can be seen that the cleaning efficiency increases with increase in fluence and reaches a value of  $\sim 85\%$  at  $2 \text{ J/cm}^2$  fluence level. Further increase in fluence level above  $2 \text{ J/cm}^2$  results in damage of the substrate surface as the absorption of laser beam is limited only to the upper layer of gold up to a thickness up of 10-15 nm. Hence, a careful control of laser fluence is required for damage free gold layer cleaning of fused silica mirrors. The problem of substrate damage due to the high laser fluence was solved in our experiment by increase in the number of laser passes rather than by increase in laser fluence. More detailed studies about the damage of gold-coated fused silica surfaces at higher fluence levels have been reported by Natoli *et al.* [200].

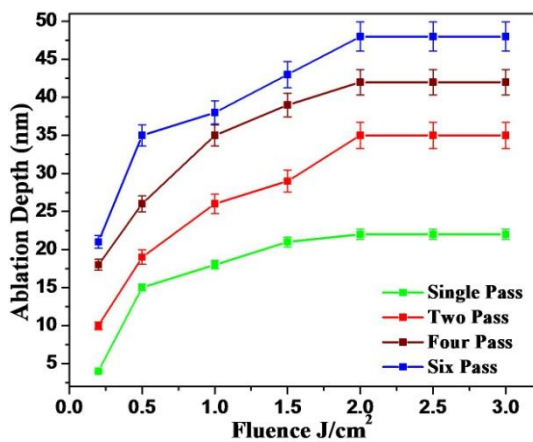


**Fig. 7.17.** Variation of ablation depth as a function of laser fluence with number of laser pulses as parameters.

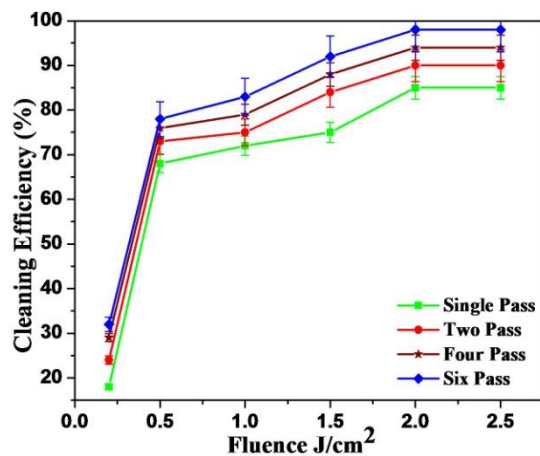


**Fig. 7.18.** A plot of cleaning efficiency versus laser fluence with number of laser pulses as parameter.

Laser spot overlapping has also been optimized during the experiment to achieve higher cleaning efficiency. The laser spot had a Gaussian spatial distribution at the focus of flat-field lens. A significant dependence of the laser cleaning on spot overlapping was observed during the experiments. An optimum value of spot overlapping was found to be 80%. With the spot overlapping value less than 80%, the cleaning efficiency reduced by ~10% for each 10% reduction in spot overlapping. For overlapping value higher than 80%, the value of cleaning efficiency did not change but cleaning speed reduced. Further, higher overlapping (>80%) increases heat deposition on the upper surface, which results in damage of the mirror substrate. With 80% value of spot overlapping, 48 cm<sup>2</sup> of surface area (60 mm × 80 mm in *x-y* plane) was cleaned in 3 minutes by six laser passes (three passes each in *x*- and *y*-directions) and the maximum cleaning efficiency was ~98%.

We had also studied the influence of suction on the cleaning efficiency. In the absence of suction some of the ablated gold particles tend to settle back on the surface due to random thermal motion. Figure 7.19 shows SEM image of single laser pass cleaned surface of the sample in the presence and absence of suction system. The suction system removes the ablated particles and a cleaner substrate is obtained.

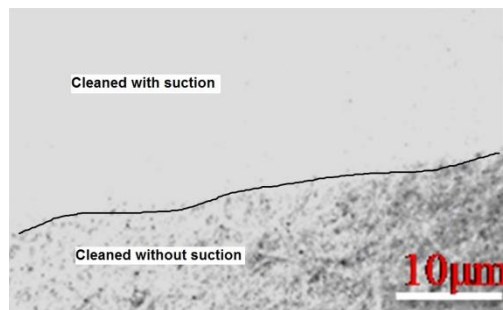


**Fig. 7.19.** SEM image of single laser pass cleaned surface of the sample, upper part shows cleaning in the presence of the suction system, and lower part shows image of the cleaned surface without suction system.

Laser cleaning of gold layer experiments were also carried out by irradiating the gold-coated substrate from the rear side of the substrate. The laser cleaning of gold was significantly less efficient in this case compared to the irradiation of the gold coating by laser beam from the front side. Fig.7.20 (a) shows that the cleaning from the front surface removes the gold particles completely. Fig. 7.20(b) shows that some gold particles still remain on the surface even after applying more number of laser passes during laser cleaning of the substrate from the rear surface.

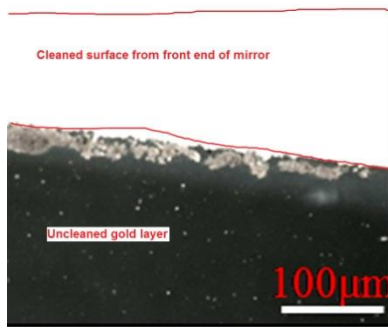


**Fig. 7.20 (a).** *Microscope image of the cleaned surface, when it was cleaned from the front surface. It shows a good cleaned surface in the upper part and lower part shows gold coated uncleaned surface.*



**Fig.7.20 (b).** *Microscope image of the cleaned surface, when it was cleaned from the rear surface. Some gold particles remain on surface (upper part) and lower part shows gold-coated uncleaned surface.*

This result can be explained with the help of an integrated two-temperature model and molecular dynamics method as given by Gan *et al.* [201] in the study of thermal ablation of 500 nm thick gold film. During the cleaning from the front side see Fig. 7.20 (a), the gold film is removed by the thermal ablation mechanism and the gold particles leave the surface layer by layer. Whereas, while cleaning from the rear surface, it is difficult for the gold particles to escape by thermal ablation since fused silica glass surface covers the gold layer from the rear end. Hence, in this case the gold particles are removed by the spallation mechanism rather than by thermal ablation. Spallation of gold particles is more probably in case of use of picosecond or

femtosecond laser pulses because of the generation of strong tensile stresses. However, it is difficult to achieve good clean quality and high laser cleaning efficiency in this irradiation geometry.

Experiments were also performed for the dependence of cleaning efficiency as a function of angle of incidence of the laser beam. The results are shown in Fig. 7.21, which indicates that the cleaning efficiency also depends on the angle of incidence of the laser beam. For single laser pass at 30° angle of incidence (with respect to surface and close to grazing incidence), a high value of cleaning efficiency (85%) was achieved as compared to the other angles. A visual difference in clean layer surface can be seen in the microscopic image of the surface (Fig. 7.22).

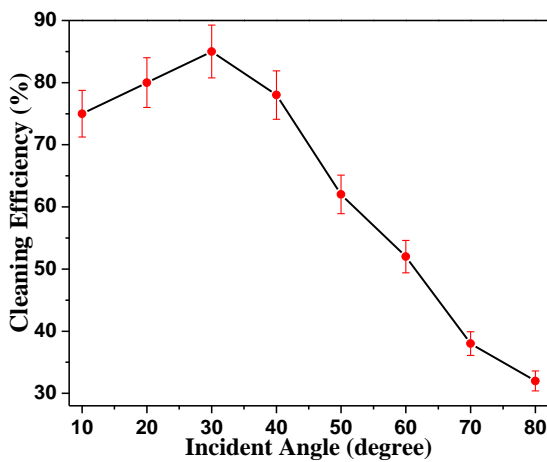


**Fig. 7.21.** Variation of gold layer cleaning efficiency as a function of angle of incidence.

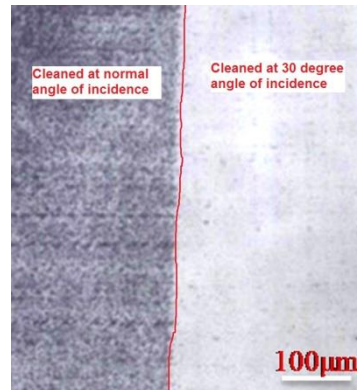


**Fig.7.22.** Optical microscope image showing the difference in cleaned layer for the normal incidence (left) and cleaned layer at 30° angle of incidence (right) with single pass of laser beam.

After six laser passes, the cleaning efficiency reaches to a value of ~98%. In addition, cleaning at small angle minimizes the risk of substrate damage as compared to laser cleaning at normal incidence due to reduced fluence level. A detailed analysis of angular laser cleaning of deposition has already been provided by Vereecke *et al.* and Watkins *et al.* [202,203] wherein

the maximum cleaning efficiency was observed at grazing incidence. However, in our case maximum cleaning efficiency was observed at 30° angle of incidence (close to grazing incidence), which may be due to ineffectiveness of suction force at angles less than 30°. Further, in our case the substrate is glass, on which particles have a tendency to slide on the surface instead of their rolling and it becomes much more difficult to remove them without sufficient suction force as compared to laser cleaning of deposition from other substrates.

The quality of laser cleaned surface was analyzed by angle-dependent SXR measurement using 130Å wavelength soft X-ray of SR beamline. Figure 7.23 shows the fit of experimental data in SXR curves for fused silica mirror before and after the gold layer cleaning. The circle in the SXR curve represents the experimental values of reflected intensity and the continuous line represents the fitted values [204]. Measurements were carried out for incidence angle (with respect to surface) in the range of 0°-70°. Fitting of the SXR curve shows that before laser cleaning, the gold layer thickness was 48 nm with surface roughness of 26 Å (as mentioned in Table 7.5). After laser cleaning the gold layer has removed completely and these mirrors can be re-used after re-coating of fresh gold layer.

**Table. 7.5.** Comparison of surface roughness obtained by angle-dependent SXR spectra of gold coated mirror sample before and after cleaning. (For 0° to 70° incidence angle and 13 nm soft X-ray wavelength)

	Thickness	Roughness $\sigma_{rms}$ (Å)	Refractive part of refractive index $\delta$	Absorptive part of refractive index $\beta$
Before laser cleaning				
Gold film	48 nm	26	$6.74 \times 10^{-2}$	$5.62 \times 10^{-2}$
Substrate	4 mm	8	$1.89 \times 10^{-2}$	$9.78 \times 10^{-3}$
After laser cleaning				
Gold film	Nil	Nil	Nil	Nil
Substrate	4 mm	5	$1.89 \times 10^{-2}$	$9.78 \times 10^{-3}$

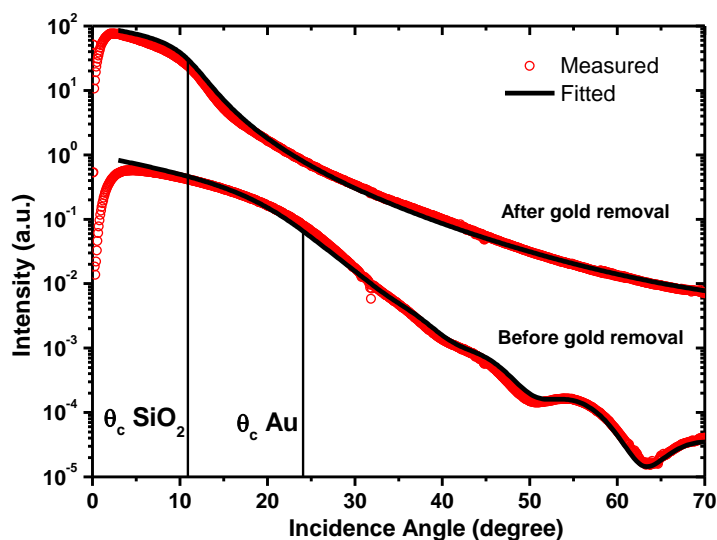


**Fig. 7.23.** Soft X-ray reflectivity (SXR) spectra of the sample before and after gold layer cleaning by using  $130\text{\AA}$  wavelength. Open circles represent the experimental data whereas continuous lines are corresponding to the best fit obtained using parameters given in Table 7.5. Curves are vertically shifted in the y-axis for the clarity. The vertical lines mark positions of the critical angle for Au film and fused silica substrate.

The SXR curve also shows interference fringes before cleaning caused by the waves reflected from the air-gold film interface and the gold film-substrate interface [205]. This curve shows that critical angle  $\theta_c$  is  $21.03^\circ$  for thin gold film [206]. After the gold layer cleaning, the critical angle  $\theta_c$  shifted from  $21.03^\circ$  towards a lower value of  $11.13^\circ$ , which matches well with the critical angle for fused silica. Further, the interface interference fringes have also disappeared. It clearly indicates that the gold layer was effectively removed from the fused silica surface. The rms roughness of the fused silica substrate was determined from the fitting parameters and was found to be  $8\text{\AA}$  before laser cleaning. This roughness improved to a value of  $5\text{\AA}$  after the laser cleaning process [205]. Details of the fitting parameters are given in Table 7.5. The possible reason for the improvement in rms roughness can be attributed to the fact that the calculated thermal diffusion length for 100 ns pulse duration is larger than the gold layer

thickness (48 nm), which may lead to the heating of the upper surface of the fused silica during laser cleaning and may improve the surface roughness. It was also observed that after laser cleaning, the exposure of these fused silica mirrors to the atmosphere results in the formation of an additional surface layer of 3-5 nm thickness due to the atmospheric effects.

XPS measurements, before and after laser cleaning of the gold layer have also been recorded. The XPS curve of the gold film has been fitted using two components, one with peak energy near 83 eV and the second having peak energy near 87.5 eV and is as shown in Fig. 7.24. After laser cleaning, it was found that the peaks of the gold layer disappear from the sample. It is clear from the XPS analysis that after laser cleaning process with ns pulses, the gold layer from the surface is removed completely.

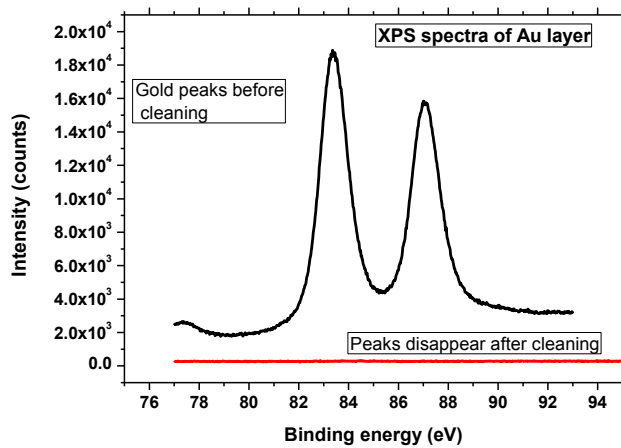


**Fig.7.24.** XPS spectrum of the gold layer shows that the peaks of gold disappear after laser cleaning process.

## 7.5 Conclusions

Short pulse Nd:YAG laser of 55  $\mu$ s pulse duration has been used effectively for cleaning of surface contamination of marble for potential applications in cleaning of historical buildings and artworks. It has also been tested for cleaning of surface contamination from zircaloy and

inconel for nuclear industry. The experimental results obtained using this laser showed that with optimization in the process parameters and laser parameters, this type of lasers have a good potential for efficient surface cleaning of contamination over a wide range of other materials like rocks, stainless steel, copper, niobium, titanium, and aluminium. Experimental results have been explained using theoretical description based on photo-thermal ablation mechanism.

Laser cleaning of 20 nm thick carbon layer from gold-coated surface of mirrors using ~100 ns pulse duration Nd:YAG laser has also been studied. From XPS and SXR data, it was found that pulsed Nd:YAG laser is highly effective in removal of carbon layer. SXR data confirmed that no damage to the gold coating has occurred during the laser cleaning of carbon layer. Dry laser cleaning with fiber optic beam delivery of Nd:YAG laser appears to be a promising technique for on-line cleaning of SR beamline components and optical elements without removal their position in the beamline. Dry laser cleaning is also very fast as compared to other conventional cleaning methods. Laser cleaning of 48 nm thick gold layer from X-ray mirror samples using ~100 ns pulse duration Nd:YAG laser has also been investigated. Analysis of laser-cleaned surface showed that ~100 ns duration laser pulses not only cleaned the gold layer effectively, but it also improved the rms roughness of fused silica substrate from a value of 8 Å to 5 Å without damaging its surface. Laser cleaning technique for gold layer removal from SR beamline mirror also meets the requirements of safety, efficiency, cost-effectiveness, and feasibility as compared to other conventional methods. In addition, high precision in cleaning of surface (precision in thickness of layer cleaned) is yet another advantage of short-pulse ns laser cleaning. Moreover, it is also possible to re-coat the laser cleaned mirror surface, so that it can be effectively used instead of replacing it with a new mirror in the SR beamline.

# Chapter 8

---

## Summary and scope for future work

In this dissertation, a detailed study on design and development of long and short pulse Nd:YAG lasers with high average and peak power has been carried out for potential applications in laser material processing. Investigations on laser pump chamber, laser resonator, and fiber optic beam delivery have been carried out. Further, thermal problems in the laser rod such as thermal lensing and stress-induced birefringence were investigated and resolved for improvement in the performance of the pulsed Nd:YAG lasers in terms of beam quality, slope efficiency and pulse-to-pulse stability. In order to enhance the ruggedness of Nd:YAG lasers for industrial environment, some important parameters like average output power, resonator stability, slope efficiency, beam quality, and pulse-to-pulse stability were also analyzed and improved successfully. Studies were also carried out for efficient coupling of laser beam to multimode optical fiber of core diameter in the range of 600  $\mu\text{m}$  to 200  $\mu\text{m}$  for long distance delivery (up to 150 m) of high power laser beam. Further, studies were also carried out on the application of pulsed Nd:YAG lasers for laser cutting in dry air and underwater environment for a variety of materials such as thick stainless steel, zirconium, and aluminium for nuclear and shipping industry. Detailed investigations were also carried out on the welding of aluminium and titanium

in inert gas environment. In addition, results and analysis is presented on laser drilling of rocks as well as laser cleaning of marble, inconel, carbon and gold layer for applications in science and engineering. Results of our studies have been summarized in Section 8.1 and scope for future work is provided in Section 8.2.

## **8.1 Summary of the important results**

In summary, study and development of rugged lamp pumped, long pulse Nd:YAG lasers of 250 W, 500 W, and 1 kW average power and their potential material processing applications has been presented. Pulse duration of these lasers can be varied in the range of 1-40 ms and repetition rate from 1-100 Hz. A maximum pulse energy of 540 J was achieved in 1 kW average power Nd:YAG laser with a slope efficiency of 5.4%. To the best of our knowledge, this is the highest slope efficiency and pulse energy at millisecond pulse duration reported in long pulse operation of flash lamp-pumped Nd:YAG lasers. These lasers have good beam quality in multimode operation, and hence efficient beam delivery through 400  $\mu\text{m}$  and 600  $\mu\text{m}$  core diameter optical fibers could be achieved. Delivery of up to 60 J of pulse energy through 200  $\mu\text{m}$  core diameter optical fiber with 90% transmission efficiency has been successfully demonstrated and used for micro-machining and welding applications. Further performance evaluation of 2% at. doped ceramic Nd:YAG rod was also carried out. Generation of up to 520 W of average output power in long pulse operation of ceramic Nd:YAG rod was achieved with a beam quality factor of  $M^2 \sim 47$  and a slope efficiency of 5.4%. The above performance parameters of ceramic Nd:YAG rods are comparable to that of single crystal Nd:YAG rods and hence the ceramic Nd:YAG rods can be used as a potential replacement for single crystal Nd:YAG rods. Laser beam from ceramic Nd:YAG rod was also delivered efficiently through a 400  $\mu\text{m}$  core diameter

optical fiber with a transmission efficiency of 90%. To the best of our knowledge, this is the highest average power, pulse energy, and efficiency reported in long pulse operation of flash lamp-pumped ceramic Nd:YAG lasers.

Further, study and development of a 22 kW peak power Nd:YAG laser with 55  $\mu\text{s}$  pulse duration and 1-20 Hz repetition rate as well as efficient beam delivery through an optical fiber has also been demonstrated and used for cleaning applications. A compact and robust laser pump chamber along with laser resonator was designed to achieve high peak power and good beam quality in multimode operation. An almost top-hat intensity distribution of laser beam profile was achieved after its beam delivery through a 200  $\mu\text{m}$  core diameter optical fiber, which has been found to be useful in more selective, uniform, and efficient laser cleaning. To the best of our knowledge, there are no published reports on  $\mu\text{s}$  pulse duration Nd:YAG laser with high peak power ( $\sim 22$  kW) and beam delivery through a small core diameter optical fiber of 200  $\mu\text{m}$  for laser cleaning applications.

It is well known that the polarization state of the laser beam has a strong influence on absorption in the material. For a linearly polarized beam the absorption is generally higher than for unpolarized or elliptically polarized beam. When a polarizer is placed in a Nd:YAG laser resonator to generate linearly polarized output, a significant reduction in the output power is observed due to thermally induced stress birefringence in Nd:YAG rod. Several schemes have been studied and analyzed to generate linearly polarized laser beam. A novel approach has been developed to compensate stress-induced birefringence and thereby reduce the depolarization loss by  $\sim 18\%$  using Glan-Taylor polarizer. Simpler optical schemes using quartz rotator and folded resonator geometries have also been used successfully to generate *p*-polarized average output

power of 215 W and 415 W in single and dual Nd:YAG rod resonators in long pulse operation. These results will be useful in nonlinear frequency conversion and laser material processing.

Studies were also carried out on laser cutting of thick section of SS 304 with thickness in the range of 4-20 mm using ms pulse duration Nd:YAG laser both in dry air as well as in underwater environment. There are several published reports on the use of CW lasers in the range of kilowatt power level for the cutting of the thick steel. We have demonstrated the laser cutting of thick section (up to 20 mm thick) of stainless steel in underwater conditions using long pulse Nd:YAG laser of only 500 W average power. This study on pulsed laser cutting technique in dry air and underwater environment will be useful in dismantling work in nuclear facilities and also in ship dismantling industries. Minimization of ejection of debris associated with decommissioning work in nuclear facilities is an important task as a large volume of contaminated debris may result in an increased radiological hazard. In view of this, laser cutting experiments for reduction of debris were also performed using laser cutting nozzle with half-imaging lenses made of GRADIUM glass and a substantial reduction in the amount of ejected debris was achieved.

Laser welding of 4 mm thick titanium and aluminium sheets were also performed successfully using 1 kW average power long pulse Nd:YAG laser. The microscopic analysis showed that the weld bead was uniform and no major porosities or inclusions were observed in the welded samples. It was also found that the ultimate tensile strength of weld joint is almost similar to that of the parent metal. Welded samples were also tested using helium leak detector for leak tightness of up to  $\sim 10^{-10}$  mbar.l/sec. These laser welded materials can be used for vacuum related applications.

Investigation on laser rock drilling and spallation using optical fiber coupled long pulsed Nd:YAG laser of 20 kW peak power has also been carried out. We have performed rock spallation by drilling holes on its upper surface for stress generation in the rock, which easily breaks the rock without melting or vapourization. It was found that this laser technique is cost effective and time saving as compared to other conventional drilling methods and it has potential applications in petroleum industries to damage the rocks for exploration of oil and natural gas wells.

Finally, some laser cleaning experiments have also been performed using short pulse (~100 ns) Nd:YAG laser to remove the surface contamination on marble and stone (beria gray sand stone, and shale) for conservation of historical buildings as well as removal of surface contamination from zircaloy and inconel for nuclear industry. Laser cleaned surface of inconel was also studied and analyzed using X-ray photoelectron spectroscopy (XPS). Cleaning of carbon contamination and gold layer from the optical elements of synchrotron radiation (SR) beamlines has also been performed successfully using nanosecond duration pulsed Nd:YAG laser. Since these optical elements including the substrates which are of special shapes are very costly, thus, it is desirable to develop a technique for the periodic cleaning of the coatings without damage or modifications to the underneath surface. Effect of different laser process parameters such as fluence energy, spot overlapping, angle of incidence, and number of laser passes has been studied for laser cleaning of optical elements. It was found that nanosecond pulses not only clean the surface contamination, but it also decreases the surface roughness of the substrate. Cleaning quality and efficiency has been analyzed using optical microscopy, SEM, XPS, and angle-dependent soft X-ray reflectivity (SXR) techniques. A laser cleaning efficiency of ~98% was achieved which is higher than that achieved by other conventional cleaning

techniques. This work provides an experimental base for further research work in laser cleaning of different materials.

## **8.2 Scope for future work**

Present work in this thesis describes the experimental studies on the development of various pulsed Nd:YAG lasers and its use in different material processing applications. However, there is a considerable scope for future work on studies and application of pulsed Nd:YAG lasers with longer pulse durations of the order of a few tens of ms and very high pulse energy of the order of hundreds of Joule for cutting and welding applications and generation of short duration  $\mu$ s pulses with still higher pulse energy for laser cleaning and drilling applications. Studies on reduction in thermal problems and birefringence compensation can be enhanced further to generate single mode polarized output with higher pulse energies with better focusing ability. Further study on highly Nd doped ceramic Nd:YAG rods in multi-rod and folded resonator geometries can also be explored for enhancement in pulse energy, average power and peak power for welding, cutting, and drilling of thick materials. Generation of linearly polarized laser beam with high pulse energy can be explored for laser grooving on metals for different industrial and technological applications. Underwater laser cutting and welding is also an area of extensive research involving many technological challenges, which can be explored further for various nuclear applications. Study on welding of dissimilar materials such as stainless steel and copper, niobium and copper, etc. using high power pulsed lasers will be an area of research with wide applications in the industry. Free-running microsecond duration Nd:YAG laser can be upgraded for the generation of tens of nanosecond duration pulses using electro-optic Q-switching

technique. These electro-optic Q-switched lasers will be useful in nuclear decontamination and other artwork conservation applications requiring very high peak powers.

## REFERENCES

- [1] Guenter Huber, Christian Kränkel, Klaus Petermann, “Solid-state lasers: status and future”, *Journal of Optical Society of America B* **27**, B 93 (2010).
- [2] Ed Gerstner, “Laser Physics: Extreme light”, *Nature* **446**, 16 (2007).
- [3] S.V. Usov and I.V. Minaev, “High-power impulse YAG laser system for cutting, welding and perforating of super hard materials”, *Journal of Materials Processing Technology* **149**, 541 (2004).
- [4] H. Gugel, A. Schuermann, W. Theisen, “Laser welding of NiTi wires”, *Materials Science and Engineering A* **481**, 668 (2008).
- [5] Reinhart Poprawe, “Tailored Light 1: High power lasers for production”, (Springer, 2012).
- [6] Moritz Andreaz, “Oral Laser Application”, (Springer, 2006).
- [7] W. Koechner, “Solid State Laser Engineering”, 5<sup>th</sup> ed. New York: Springer-Verlag (1999).
- [8] R. Iffländer, “Solid State Lasers for Materials Processing”, (Springer series in optical sciences, Springer-Verlag, Berlin, (1990).
- [9] R. Weber, B. Neuenschwander, H.P. Weber, “Thermal effects in solid-state laser materials”, *Optical Materials* **11**, 245 (1999).
- [10] O. Svelto, “Principles of Lasers”, 5th ed. New York: Springer-Verlag (2007).
- [11] Joseph T. Verdeyen, “Laser Electronics”, 3rd Edition: Prentice Hall Series in Solid State Physical Electronics (2010).
- [12] Amnon Yariv, Pochi Yeh, “Optical waves in crystals: propagation and control of laser radiation”, Wiley series in Pure and Applied Optics (2002).
- [13] W.M. Steen, “Laser Materials Processing”, Third ed., Springer London (2005).

- [14] J.F. Ready, D.F. Farson, "LIA Handbook of Laser Materials Processing", Orlando: Magnolia Publishing Inc. (2001).
- [15] W.W. Duley, "Thermodynamics and laser material processing", *Journal of Laser Applications* **17(1)**, 15-20 (2005).
- [16] D. Breitling, A. Ruf, F. Dausinger, "Fundamental aspects in machining of metals with short and ultra short laser pulses", *Proceedings of SPIE* **5339**, 49 (2004).
- [17] A.Z. Sahin, B.S. Yilbas, T. Ayar, "Laser Cutting Efficiency and Quality Assessments", *Comprehensive Materials Processing* **9**, 235 (2014).
- [18] Lv. Shanjin, Wang Yang, "An investigation of pulsed laser cutting of titanium alloy sheet", *Optics and Lasers in Engineering* **44**, 1067 (2006).
- [19] M. Kanskar, J. Cai, D. Kedlaya, T. Klos, M. Martin, D. Olson, Y. Xiao, S. H Macomber, "975nm surface-emitting distributed feedback (SE-DFB) laser and array", *22<sup>nd</sup> Annal Solid State Diode Laser Technology Review* **22**, 84 (2009).
- [20] See website <http://www.rofin.com/en/products>
- [21] See website <http://www.jklasers.com/nd-yag-pulsed-lasers>
- [22] See website <http://www.us.trumpf.com/products/laser-technology>
- [23] See website <http://www.lasag.com/en>
- [24] See website <http://www.uslasercorp.com>
- [25] P.P. Rajeev, S. Sengupta, A. Das, P. Taneja, P. Ayyub, P.K. Kaw, "Laser absorption in short-lived metal and nanoplasmas", *Applied Physics B* **80**, 1015 (2005).
- [26] Akio Ikesue, Yan Lin Aung, Takunori Taira, Tomosumi Kamimura, Kunio Yoshida, Gary L. Messing, "Progress in ceramic laser", *Annual Review of Material Research* **36**, 397 (2006).

- [27] N. Hodgson, H. Weber, "Optical Resonators fundamentals, advanced concepts and applications", Springer-Verlag, Berlin, (1997).
- [28] Th. Beck, N. Reng, H. Weber, "Optical fiber for material processing laser", Optics and Lasers in Engineering **34**, 255 (2000).
- [29] Koji Hirano and Remy Fabbro, "Possible explanations for different surface quality in laser cutting with 1 and 10  $\mu\text{m}$  beams", Journal of Laser Applications **24(1)**, 012006 (2012).
- [30] Paul Seiler, Klaus Wallmeroth, Kurt Mann, "The Nd:YAG laser: From a rod to a disk", Nature Photonics **4**, 285 (2010).
- [31] A.K. Nath, D. Hansdah, S. Roy and A. Roy Choudhury, "A study on laser drilling of thin steel sheet in air and underwater", Journal of Applied Physics **107**, 123103 (2010).
- [32] K. Abdel Ghany, M. Newishy, "Cutting of 1.2mm thick austenitic stainless steel sheet using pulsed and CW Nd:YAG laser", Journal of Materials Processing Technology **168**, 438 (2005).
- [33] B.N. Upadhyaya, P. Misra, K. Ranganathan, S.C. Vishwakarma, H.N. Golghate, A. Choubey, N. Muthukumar, R. K. Jain, G. Mundra, T. P. S. Nathan., "Beam Quality Considerations of high Power Nd:YAG Lasers", Optics & Laser Technology **34**, 193 (2002).
- [34] Menghua Jiang, Qiang Li, Hong Lei, Yongling Hui, Jiguo Wang, Chi Feng, Zhe Sun, "High average power and high pulse energy pulsed Nd:YAG laser", Proceedings of SPIE **8312**, 473 (2011).
- [35] Hideki Yagi, Takagimi Yanagitani, Ken-ichi Ued, "Nd<sup>3+</sup>:Y<sub>3</sub>Al<sub>5</sub>O<sub>12</sub> laser ceramics: Flash lamp pumped laser operation with a UV cut filter", Journal of Alloys and Compounds **421**, 195 (2006).

- [36] W. Koechner, "Absorbed pump power, thermal profile and stresses in a cw pumped Nd:YAG crystal", *Applied Optics* **9**, 1429 (1970).
- [37] Sungman Lee, Daewook Choi, Cheol-Jung Kim, Jun Zhou, "Highly efficient diode side-pumped Nd:YAG ceramic laser with 210 W output power", *Optics & Laser Technology* **39**, 705 (2007).
- [38] A. Hoffstadt, "High-average-power flash-lamp-pumped Ti: sapphire laser", *Optics Letters* **19**, 1523 (1994).
- [39] John Cloutier, "Alumina ceramics enhances laser pump cavities", *Laser Focus World* **10**, 34 (2007).
- [40] Noriah Bidin, Seyed Ebrahim Pourmand, Muhamad, Fakaruddin Sidi Ahmad, Ganesan Khrisnan, Nur Athriah, Mohd Taib, Nurul Nadia Adnan and Hazri Bakhtiar, "Temperature dependence of quasi-three level laser transition for long pulse Nd:YAG laser", *Optics & Laser Technology* **45**, 74 (2013).
- [41] A.S. Dalkilic, N.Kayac, A.Celen, M.Tabatabaei, O.Yıldız, W.Daungthongsuk, S.Wongwises, "Forced Convective Heat Transfer of Nanofluids - A Review of the Recent Literature", *Current Nanoscience* **8**, 949 (2012).
- [42] Dieter Schocker, Chapter 4 on Solid State Lasers by H. Weber in "Handbook of the Euro Laser Academy", Chapman & Hall, Cambridge, (1998).
- [43] K.P. Driedger, R.M. Ifflander, H. Weber, "Multi rod resonator for high power solid state lasers with improved beam quality", *IEEE Journal of Quantum Electronics* **24**, 665 (1988).
- [44] US Patent #4945489, 1990.
- [45] See website <http://www.gsilumonics.com>

- [46] V. Magni, “Resonators for solid state lasers with large volume fundamental mode and high alignment stability”, *Applied Optics* **25**, 107 (1986).
- [47] H.P. Kortz, R. Ifflander, H. Weber, “Stability and beam divergence of multimode lasers with internal variable lenses”, *Applied Optics* **20**, 4124 (1981).
- [48] B.N. Upadhyaya, S.C. Vishwakarma, A. Choubey, R.K. Jain, Sabir Ali, D.K. Agrawal, A.K. Nath, “A highly efficient 5 kW peak power Nd:YAG laser with time-shared fiber optic beam delivery”, *Optics & Laser Technology* **40**, 337 (2008).
- [49] Ambar Choubey, R.K. Jain, S.C. Vishwakarma, B.N. Upadhyaya, S.M. Oak, “Performance Improvement of long pulse Nd:YAG laser using advanced diffuse ceramic reflectors”, *Materials Focus* **2**, 362 (2013).
- [50] Ambar Choubey, S.C. Vishwakarma, Pushkar Misra, R.K. Jain, D.K. Agrawal, R. Arya, B.N. Upadhyaya, S.M. Oak, “A highly efficient and compact long pulse Nd:YAG rod laser with 540 J of pulse energy for welding application”, *Review of Scientific Instruments* **84**, 0731081 (2013).
- [51] Amit Sharma, Vinod Yadava, “Modelling and optimization of cut quality during pulsed Nd:YAG laser cutting of thin Al-alloy sheet for curved profile”, *Optics and Laser in Engineering* **51**, 77 (2013).
- [52] M.J. Torkamany, F.M. Ghaini, E.Papan, S.Dadras, “Process optimisation in Titanium welding with pulsed Nd:YAG laser”, *Science of Advanced Materials* **4**, 489 (2012).
- [53] Takunori Taira, “Ceramic YAG lasers”, *Comptes Rendus Physique* **8**, 138 (2007).
- [54] R. Lavi and S. Jackel, “Thermally boosted pumping of neodymium lasers”, *Applied Optics* **39**, 3093 (2000).
- [55] A. Ikesue, “Polycrystalline Nd:YAG ceramics lasers”, *Optical Materials* **19**, 183 (2002).

- [56] I. Shoji, T. Taira, A. Ikesue, "Ceramic lasers", IEICE Transactions C **J84-C**, 918 (2001).
- [57] D.C. Brown, "Ultrahigh-average-power diode-pumped Nd:YAG and Yb:YAG lasers", IEEE Journal of Quantum Electronics **QE-33**, 861 (1997).
- [58] T. Taira, A. Ikesue, K. Yoshida, "Diode-pumped Nd:YAG ceramics lasers", OSA TOPS on Advanced Solid-State Lasers **19**, 430 (1998).
- [59] M. Sekita, H. Haneda, Y. Yanagitani, S. Shirasaki, "Induced emission cross section of Nd:Y<sub>3</sub>Al<sub>5</sub>O<sub>12</sub> ceramics", Journal of Applied Physics **67**, 453 (1990).
- [60] A. Ikesue, I. Furusato, K. Kamata, "Polycrystalline transparent YAG ceramics by a solid state reaction method", Journal of American Ceramic Society **78**, 225 (1995).
- [61] T. Yanagitani, H. Yagi, M. Ichikawa, "Production of yttrium-aluminium-garnet fine powder", Japanese Patent 10-10133 (1998).
- [62] Jianren Lu, Ken-ichi Ueda, Hideki Yagi, Takagimi Yanagitani, Yasuhiro Akiyama, Alexander A. Kaminskii, "Neodymium doped yttrium aluminum garnet (Y<sub>3</sub>Al<sub>5</sub>O<sub>12</sub>) nano crystalline ceramics- a new generation of solid state laser and optical materials", Journal of Alloys and Compounds **341**, 220 (2002).
- [63] A. Heller, "Transparent ceramics spark laser advances", Science Technol. Rev. **4**, 10 (2006).
- [64] B. Bishop, "Northrop Grumman scales new heights in electric laser power, achieves 100 kW from a solid-state laser", Globe Newswire, March **18**, (2009).
- [65] Wenbin Liu, Jiang Li, Benxue Jiang, Di Zhang, Yubai Pan, "2.44 kW laser output of Nd:YAG ceramic slab fabricated by a solid-state reactive sintering", Journal of Alloys and Compounds **538**, 258 (2012).

- [66] A. Ikesue, Yan Lin Aung, T. Yoda, S. Nakayama, T. Kamimura, "Fabrication and laser performance of polycrystal and single crystal Nd:YAG by advanced ceramic processing", *Optical Materials* **29**,1289 (2007).
- [67] George Boulon, "Fifty years of advances in solid state laser materials", *Optical Materials* **34**,499 (2012).
- [68] Jasbinder Sanghera, Woohong Kim, Guillermo Villalobos, Brandon Shaw, Colin Baker, Jesse Frantz, Bryan Sadowski, Ishwar Aggarwal, "Ceramic laser materials: Past and present", *Optical Materials* **35**, 693 (2013).
- [69] Ambar Choubey, S.C. Vishwakarma, Sabir Ali, R.K. Jain, B.N. Upadhyaya, S.M. Oak, "Performance study of highly efficient 520 W average power long pulse ceramic Nd:YAG rod laser", *Optics & Laser Technology* **51**, 98 (2013).
- [70] Voicu Lupei, "Ceramic laser materials and the prospect for high power lasers", *Optical Materials* **31**, 701 (2009).
- [71] B. Richou, I. Schertz, I. Gobin, J. Richou, "Delivery of 10-MW Nd:YAG laser pulses by large-core optical fibers: dependence of the laser-intensity profile on beam propagation", *Applied Optics* **36**, 1610 (1997).
- [72] Zemin Wang, Xiaoyan Zeng, Weiling Huang, "Parameters and surface performance of laser removal of rust layer on A3 steel," *Surface and Coatings Technology* **166**, 10 (2003).
- [73] Yangsook Koh, Istvan Sárady, "Cleaning of corroded iron artefacts using pulsed TEA CO<sub>2</sub> and Nd:YAG-lasers", *Journal of Cultural Heritage* **4**, 129 (2003).
- [74] M.W. Turner, M.J.J. Schmidt, L. Li, "Preliminary study into the effects of YAG laser processing of titanium 6Al-4V alloy for potential aerospace component cleaning application", *Applied Surface Science* **247**, 623 (2005).

- [75] Giancarlo Calcagno, Erich Pummer, Manfred Koller, “St. Stephen's Church in Vienna: criteria for Nd:YAG laser cleaning on an architectural scale”, *Journal of Cultural Heritage* **1**, 111 (2000).
- [76] Anirudhha Kumar, Mark Sapp, Jay Vincelli, Mool C. Gupta, “ A study on laser cleaning and pulsed gas tungsten arc welding of titanium”, *Journal of Materials Processing Technology* **210**, 64 (2010).
- [77] Salvatore Siano, Fabrizio Margheri, Roberto Pini, Piero Mazzinghi, Renzo Salimbeni, “Cleaning process of encrusted marbles by Nd:YAG lasers operating in free-running and Q-switching regimes”, *Applied Optics* **36**, 7073 (1997).
- [78] Piero Mazzinghi, Fabrizio Margheri, “A short pulse, free running, Nd:YAG laser for the cleaning of stone cultural heritage”, *Optics and Lasers in Engineering* **39**, 191 (2003).
- [79] Constantin Fenic, Razvan Dabu, Aurel Stratan, Constantin Blanaru, Constantin Ungureanu, Catalin Luculescu, “Preliminary studies of material surface cleaning with a multi-pulse passively Q-switched Nd:YAG laser”, *Optics & Laser Technology* **36**, 125 (2004).
- [80] Fabrizio Margheri, Stefano Modib, Leonardo Masottic, Piero Mazzinghi, Roberto Pinie, Salvatore Siano, Renzo Salimbeni, “SMART CLEAN: a new laser system with improved emission characteristics and transmission through long optical fibres”, *Journal of Cultural Heritage* **1**, 119 (2000).
- [81] P. Wazen, “80 W average power of Q-switched Nd:YAG laser with optical fibre beam delivery for laser cleaning application,” *Journal of Cultural Heritage* **1**, 125 (2000).
- [82] R. Sundar, K. Ranganathan, S.M. Oak, “Generation of flattened Gaussian beam profile in a Nd:YAG laser with a Gaussian mirror resonator”, *Applied Optics* **47**, 147(2008).

- [83] X. Zhu, A. Schülzgen, H. Li, H. Wei, J.V. Moloney N. Peyghambarian, “Coherent beam transformations using multimode waveguides”, *Optics Express* **18**, 7506 (2010).
- [84] Andreas Kuhn, Ian J. Blewett, Duncan P. Hand, Julian D.C. Jones, “Beam quality after propagation of Nd:YAG laser light through large-core optical fibers”, *Applied Optics* **39**,6754 (2000).
- [85] R.S. Dutra, N.B. Viana, P.A. Maia Neto, H.M. Nussenzveig, “Polarization effects in optical tweezers”, *Journal of Optics A: Pure & Applied Optics* **9**, 221 (2007).
- [86] Baole Lu, Haowei Chen, Shuang Wang, Man Jiang, Zhaoyu Ren, Jintao Bai, “Red and green dual wavelength laser based on LD side pumped ceramic Nd:YAG and BBO electro optical Q-switch”, *Optics & Laser Technology* **50**, 163 (2013).
- [87] W.J. Suder, S.W. Williams, “Investigation of the effects of basic laser material interaction parameters in laser welding”, *Journal of Laser Applications* **24**, 032009 (2012).
- [88] V. G. Niziev, A. V. Nesterov, “Influence of beam polarization on laser cutting efficiency”, *Journal of Physics D: Applied Physics* **32**, 1455 (1999).
- [89] R.Weber, A. Michalowski, V.Onuseit, V.Rominger, T. Graf, “Effects of radial and tangential polarization in laser material processing”, *Physics Procedia* **12**, 21 (2011).
- [90] Zikui Bai, Aihua Wang, Changsheng Xie, “Laser grooving of Al<sub>2</sub>O<sub>3</sub> plate by a pulsed Nd:YAG laser: Characteristics and application to the manufacture of gas sensors array heater”, *Material Science and Engineering A* **435**, 418 (2006).
- [91] R. Fluck, M.R. Hermann, L.A. Hackel, “Birefringence compensation in single solid state rods”, *Applied Physics Letters* **76**, 1513 (2000).

- [92] S. Mondal, S.P. Singh, K. Hussain, Ambar Choubey, B.N. Upadhyaya, P.K. Datta, "Efficient depolarization-loss-compensation of solid state lasers using only a Glan-Taylor polarizer", *Optics & Laser Technology* **45**, 154 (2013).
- [93] Ion Moshe and Steven Jackle, "Correction of thermally induced birefringence in double-rod laser resonators-comparison of various methods", *Optics Communications* **214**, 315 (2002).
- [94] James Sherman, "Thermal compensation of a cw-pumped Nd:YAG laser", *Applied Optics* **37**, 7789 (1998).
- [95] W.A. Clarkson, "Thermal effects and their mitigation in end-pumped solid-state lasers", *Journal of Physics D: Applied Physics* **34**, 2381(2001).
- [96] R. Kandasamy, M. Yamanaka, Y.Izawa, S.Nakai, "Analysis of birefringence compensation using a quarter-wave plate in solid-state lasers", *Optical Review* **7**, 149 (2000).
- [97] Renzhong Hua, Satoshi Wada, Hideo Tashiro, "Principles and limitations of a quarter-wave plate for reducing the depolarization loss from thermally induced birefringence in Nd:YAG lasers", *Optics Communications* **175**, 189 (2000).
- [98] M. Frede, R. Wilhelm, M. Brendel, C. Fallnich, "High power fundamental mode Nd:YAG laser with efficient birefringence compensation", *Optics Express* **12**, 3581 (2004).
- [99] Sungman Lee, Mijeong Yun, Byung Heon Cha, Cheol Joong Kim, Sungsoo Suk, Hyun Su Kim, "Stability analysis of a diode-pumped, thermal birefringence-compensated two-rod Nd:YAG laser with 770-W output power", *Applied Optics* **41**, 5625 (2002).
- [100] Keisuke Furuta, Tetsuo Kojima, Shuichi Fujikawa, Jun-ichi Nishimae, "Diode-pumped 1 kW Q-switched Nd:YAG rod laser with high peak power and high beam quality", *Applied Optics* **44**, (2005) 4119.

- [101] Martin Ostermeyer, Guido Klemz, Philipp Kubina, Ralf Menzel, “Quasi-continuous-wave birefringence-compensated single and double rod Nd:YAG lasers”, *Applied Optics* **41**, (2002) 7573.
- [102] Ivan Mukhin, Oleg Palashov, Efim Khazanov, “Reduction of thermally induced depolarization of laser radiation in [110] oriented cubic crystals”, *Optics Express* **17**, 5496 (2009).
- [103] Ravi Bhusan, Koji Tsubakimoto, Hidetsugu Yoshida, Hisanori Fujita, Masahiro Nakatsuka, “Thermally induced birefringence compensation in high average power Nd:YAG laser”, *Japanes Journal of Applied Phycs* **46**, 1051 (2007).
- [104] R.C. Jones, “A new calculus for the treatment of optical systems”, *Journal of the Optical Society of America* **37**, 110 (1947).
- [105] A.E. Siegman, “Lasers”, University Science Books, California, (1986).
- [106] G. Ghosh, “Dispersion-equation coefficients for the refractive index and birefringence of calcite and quartz crystals”, *Optics Communications* **163**, 95 (1999).
- [107] W. Koechner, D.K. Rice, “Birefringence of YAG: Nd Laser Rods as a Function of Growth Direction,” *Journal of the Optical Society of America* **61**,758 (1971).
- [108] Ichiro Shoji and Takunori Taira, “Intrinsic reduction of the depolarization loss in solid state lasers by use of a (110)-cut  $Y_3Al_5O_{12}$  crystal”, *Applied Physics Letters* **80**, 3048 (2002).
- [109] Oliver Puncken, Henrik Tünnermann, James J. Morehead, Peter Weßels, Maik Frede, Jörg Neumann, Dietmar Kracht, “Intrinsic reduction of the depolarization in Nd:YAG crystals”, *Optics Express* **18**, 20461 (2010).

- [110] Henrik Tünnermann, Oliver Puncken, Peter Weßels, Maik Frede Jörg Neumann, Dietmar Kracht, “Linear polarized single-mode Nd:YAG oscillators using [100] and [110]-cut crystals”, *Optics Express* **19**, 12992 (2011).
- [111] Zhe Sun, Qiang Li, Menghua Jiang, Hong Lei, Yongling Hui, “Improvement of the linearly polarized output power in Nd:YAG laser with [110]-cut rod”, *Chinese Optics Letters* **10**, S11402 (2012).
- [112] A. Marrota and C.A. Arguello, “Dye ring laser narrowing and tuning using the optical activity dispersion of crystal quartz”, *Optics Communications* **13**, 226 (1975).
- [113] Hyun Su Kim, Sungman Lee, Do-Kyeong Ko, Gwon Lim, Byung Heon Cha, Hee-Jong Moon, Jongmin Lee, “Method to Enhance the Pump Efficiency of a Linearly Polarized Nd:YAG Laser”, *Journal of the Korean Physics Society* **39**, 869 (2001).
- [114] Ambar Choubey, Shyamal Mondal, Ravindra Singh, B.N. Upadhyaya, P.K. Datta, S.M. Oak, “Enhancement of *p*-polarized average power in long pulse operation of single rod Nd:YAG laser using a tilted 90° quartz rotator”, *Optics Communications* **330**, 61 (2014).
- [115] Q.Lu, N.Kugler, H.Weber, S.Dong, N.Muller, U.Wittrock, “A novel approach for compensation of birefringence in cylindrical Nd:YAG rods”, *Optics and Quantum Electronics* **28**, 57 (1996).
- [116] You Wang, Koichi Inoue, Hirofumi Kan, Takayo Ogawa, Satoshi Wada, “Birefringence compensation of two tandem-set NdYAG rods with different thermally induced features”, *Journal of Optics A: Pure & Applied Optics* **11**, 125501 (2009).
- [117] Binghua Su, Junwen Xue, Lu Sun, Huiyuan Zhao, Xuedan Pei, “Generalised ABCD matrix treatment for laser resonators and beam propagation”, *Optics & Laser Technology* **43**, 1318 (2011).

- [118] D.R. Hall, P.E. Jackson, "The Physics and Technology of Laser Resonators", Adam Hilger, Bristol, 1989.
- [119] Kimizo Ono, Katsuyoshi Sunage, Ken-ichi Yoshida, "Concave mirror laser beam waveguide for a carbon dioxide laser surgery system", *Applied Optics* **29**, 384 (1990).
- [120] Ambar Choubey, Shyamal Mondal, Ravindra Singh, B.N. Upadhyaya, P.K. Datta, S.M. Oak, "Generation of 415 W of  $p$ -polarized output power in long pulse operation of Nd:YAG laser using z-fold resonator geometry", *Optics & Laser Technology* **60**, 41 (2014).
- [121] Koji Yasui, "Efficient and stable operation of a high-brightness cw 500-W Nd:YAG rod laser", *Applied Optics* **35**, 2566 (1996).
- [122] Qing-Lei Ma, Yong Bo, Nan Zong, Qin-Jun Peng, Da-Fu Cui, Yu-Bai Pan, Zu-Yan Xu, "108 W Nd:YAG ceramic laser with birefringence compensation resonator", *Optics Communications* **285**, 5183 (2010).
- [123] Yih-fong Tzeng, "Parametric analysis of the pulsed Nd:YAG laser seam-welding process", *Journal of Materials Processing Technology* **102**, 40 (2000).
- [124] Ronny Pfeifer, Dirk Herzog, Michael Hustedt, Stephan Barcikowski, "Pulsed Nd:YAG laser cutting of NiTi shape memory alloys-Influence of process parameters", *Journal of Materials Processing Technology* **210**, 1918 (2010).
- [125] A.F.H. Kaplan, "An analytical model of metal cutting with a laser beam", *Journal of Applied Physics*, **79**, 8979 (1996).
- [126] J.Duan, H.C.Man, T.M.Yue,"Modelling the laser fusion cutting process: I. Mathematical modelling of the cut kerf geometry for laser fusion cutting of thick metal", *Journal of Physics D: Applied Physics*, **34**, 3727 (2001).

- [127] K.Tong, “Analytical model for laser fusion cutting of metals”, Laser Institute of America, Proceedings, **83**, 22 (1997).
- [128] A.F.H. Kaplan, “A model of deep penetration welding based on calculation of the keyhole profile”, Journal of Physics D: Applied Physics, **27**, 3727 (1994).
- [129] C. Lampa, A.F.H. Kaplan, J. Powell, C. Magnusson, “Analytical thermodynamic model of laser welding”, Journal of Physics D: Applied Physics, **30**, 451 (1997)
- [130] H. Ki, Mohanty, S. Pravansu, J. Mazumder, “Modeling of laser keyhole welding: Part I- Mathematical modeling, numerical methodology, role of recoil pressure, multiple reflections, and free surface evolution”, Metallurgy and Material Transaction A: Physics Metallurgy and Material Science **33**, 5623 (2002).
- [131] P. Solana, J. L. Ocana, “Mathematical model for penetration laser welding as a free-boundary problem”, Journal of Physics D: Applied Physics **30**, 111(1997).
- [132] R.K. Ganesh, A. Faghri, Y. Hahn, “Generalized thermal modeling for laser drilling process - I. Mathematical modeling and numerical methodology”, International Journal of Heat and Mass Transfer **40**, 345(1997).
- [133] Wolfgang Schulz, Urs Eppelt, Reinhart Poprawe, “Review on laser drilling I. Fundamentals, modeling, and simulation”, Journal of Laser Applications **25**, 012006 (2013).
- [134] E.G. Gamaly, “The physics of ultra-short laser interaction with solids at non-relativistic intensities,” Physics Reports **508**, 91 (2011).
- [135] D. Bergstrom, A. Kaplan, “Mathematical modelling of laser absorption mechanisms in metals: A review”, Proceedings of the 16th Meeting on Mathematical Modelling of Materials Processing with Lasers (M4PL16), Igls, Austria (2003).

- [136] Xudong Zhang, Wuzhu Chen, Eiji Ashida, Fukuhisa Matsuda, “Laser–material interaction and process sensing in underwater Nd:yttrium–aluminum–garnet laser welding”, *Journal of Laser Applications* **15**(4), 280 (2003).
- [137] Xudong Zhang, Eiji Ashida, Susumu Shono, Fukuhisa Matsuda, “Effect of shielding conditions of local dry cavity on weld quality in underwater Nd:YAG laser welding”, *Journal of Materials Processing Technology* **174**, 34 (2006).
- [138] A. Sanderson, C.S. Punshon, J.D. Russell, “Advanced welding processes for fusion reactor fabrication”, *Fusion Engineering and Design* **49**, 77 (2000).
- [139] W.J. Suder, S.W. Williams, “Investigation of the effects of basic laser material interaction parameters in laser welding”, *Journal of Laser Applications* **24**, 032009 (2012).
- [140] R.T. Brown, “Keyhole welding studies with a moderate-power, high-brightness fiber laser”, *Journal of Laser Applications* **20**, 201 (2008).
- [141] X. Jin, L. Li, Y. Zhang, “A study on fresnel absorption and reflections in the keyhole in deep penetration laser welding”, *Journal of Physics D: Applied Physics* **35**, 2304 (2002).
- [142] Solana, G. Negro, “A study of the effect of multiple reflections on the shape of the keyhole in the laser processing of materials”, *Journal of Physics D: Applied Physics* **30**, 321(1997).
- [143] Kenji Ikeda, Takashi Satoha, Mitsuaki Yoshikawa, Masaru Sato, “Development of laser associated cutting method for dangerous rock slopes”, *SPIE Proceedings* **67**, 3887 (2000).
- [144] Hara Kunio, Miyao Hidehiko, Nakazawa Masaharu, Tsukino Noriyuki, Wani Fumio, Okado Hikedi, Kataoka Shinichi, Nagura Yasumi, Saiki Hideo, “Development of Remote Dismantling of Nuclear Reactor with Laser transmitted through Optical Fiber 2”, *Journal of the RANDEC* **21**,50 (2000).

- [145] Kwan-Seong Jeong, Kune-Woo Lee, Hyeon-Kyo Lim, "Risk assessment on hazards for decommissioning safety of a nuclear facility", *Annals of Nuclear Energy* **37**,1751 (2010).
- [146] Federico Demaria, "Shipbreaking at Alang–Sosiya (India): An ecological distribution conflict", *Ecological Economics* **70**, 250 (2010).
- [147] B. Talei-Faz, F.P. Brennan, W.D. Dover, "Residual static strength of high strength steel cracked tubular joints", *Marine Structures* **17**, 291 (2004).
- [148] Gokdeniz Neser, Aynur Kontas, Deniz Unsalan, Esin Uluturhan, Oya Altay, Enis Darılmaz, Filiz Kucuksezgin, Nermin Tekog̃ul, Funda Yercan, "Heavy metals contamination levels at the Coast of Aliag̃a (Turkey) ship recycling zone", *Marine Pollution Bulletin* **64**, 882 (2012).
- [149] Lv. Shanjin, Wang Yang, "An investigation of pulsed laser cutting of titanium alloy sheet", *Optics and Lasers in Engineering* **44**, 1067 (2006).
- [150] G. Thawari, J.K. Sarin Sundar, G. Sundararajan, S.V. Joshi, "Influence of process parameters during pulsed Nd:YAG laser cutting of nickel-base super alloys", *Journal of Materials Processing Technology* **170**, 229 (2005).
- [151] W.O’Neill, J.T Gabzdyl, "New developments in laser-assisted oxygen cutting", *Optics and Lasers in Engineering* **34**, 355 (2000).
- [152] Koji Hirano, Remy Fabbro, "Possible explanations for different surface quality in laser cutting with 1 and 10  $\mu\text{m}$  beams", *Journal of Laser Applications* **24(1)**, 012006 (2012).
- [153] W.W. Duley, "Thermodynamics and laser material processing", *Journal of Laser Applications* **17(1)**, 15-20 (2005).

- [154] See website <http://www.lightpath.com/products/gradium-lenses.htm>
- [155] Ambar Choubey, R.K. Jain, Ravindra Singh, D.K. Agrawal, S.C. Vishwakarma, B.N. Upadhyaya, S.M. Oak, "Study on GRADIUM lens based fiber imaging for reduction of debris during Nd:YAG laser cutting and dismantling", *Materials Focus* **3**, 149 (2014).
- [156] Douglas R. Schmitt, Claire A. Currie, Lei Zhang, "Crustal stress determination from boreholes and rock cores: Fundamental principals", *Tectonophysics* **580**, 1 (2012).
- [157] Ambar Choubey, R.K. Jain, S.C. Vishwakarma, B.N. Upadhyaya, S.M. Oak, "Nd:YAG laser assisted drilling and spallation of rocks", *Advanced Science, Engineering and Medicine* **5**, 905 (2013).
- [158] Giancarlo Lanterna, Mauro Matteini, "Laser cleaning of stone artefacts: a substitute or alternative method", *Journal of Cultural Heritage* **1**, 29 (2000).
- [159] Yayun Ye, Xiaodong Yuan, Xia Xiang, Xiaofeng Cheng, Xinxiang Miao, "Laser cleaning of particle and grease contaminations on the surface of optics," *Optik* **123**, 1056 (2012).
- [160] Jie Zhang, Youneng Wang, Peng Cheng, Y. Lawrence Yao, "Effect of pulsing parameters on laser ablative cleaning of copper oxides," *Journal of Applied Physics* **99**, 064902 (2006).
- [161] Halina Garbacz, Elzbieta Fortuna-Zalesnaa, Jan Marczakb, Andrzej Kossc, Anna Zatorskac, Grazyna Z. Zukowskad, Tomasz Onyszczyka, Krzysztof J. Kurzydłowski, "Effect of laser treatment on the surface of copper alloys," *Applied Surface Science* **257**, 7369 (2011).
- [162] Pandora Psyllaki, Roland Oltra, "Preliminary study on the laser cleaning of stainless steels after high temperature oxidation", *Materials Science and Engineering A* **282**, 145 (2000).
- [163] J.D. Kelley, F.E. Hovis, "A thermal detachment mechanism for particle removal from surfaces by pulsed laser irradiation", *Microelectronic Engineering* **20**, 159 (1993).

- [164] Shin-Chun Hsu, Jehnming Lin, “Removal mechanisms of micro-scale particles by surface wave in laser cleaning”, *Optics & Laser Technology* **38**, 544 (2006).
- [165] T. Rivasa,, A.J. Lopez, A. Ramil, S. Pozo, M.P. Fiorucci, M.E. López de Silanes, A. García, J. R. Vazquez de Aldana, C. Romero, P. Moreno, “Comparative study of ornamental granite cleaning using femtosecond and nanosecond pulsed lasers”, *Applied Surface Science* **278**, 226 (2013).
- [166] Y.C. Guan, G.K.L. Ng, H.Y. Zheng, M.H. Hong, X. Hong, Z. Zhang, “Laser surface cleaning of carbonaceous deposits on diesel engine piston”, *Applied Surface Science* **270**, 526 (2013).
- [167] A. Leontyev, A. Semerok, D. Farcage, P.Y. Thro, C. Grisolia, A. Widdowson, P. Coad, M. Rubel, JET-EFDA contributors, “Theoretical and experimental studies on molybdenum and stainless steel mirrors cleaning by high repetition rate laser beam”, *Fusion Engineering and Design* **86**, 1728 (2011).
- [168] A.C. Tam, W.P. Leung, W.Zapka, W.Ziemlich, “Laser cleaning techniques for removal of surface particulates,” *Journal of Applied Physics* **71**, 3515 (1992).
- [169] E.G. Gamaly, A.V. Rode, B. Luther-Davies, “Ultrafast ablation with high-pulse-rate lasers Part I: Theoretical considerations,” *Journal of Applied Physics* **85**, 4213 (1999).
- [170] B.H. Christensen, K. Vestentoft, P. Balling, “Short-pulse ablation rates and the two temperature model”, *Applied Surface Science* **253**, 6347 (2007).
- [171] Boris Luk'yanchuk, “Laser Cleaning,” World scientific publisher, Singapore (2002).
- [172] Y.F. Lu, W.D. Song, Tee C.K., D.S.H. Chan, T.S. low, “Wavelength Effects in the Laser Cleaning Process,” *Japanes Journal of Applied Physics* **37**, 840 (1998).
- [173] P.N. Rao, Mohammed H. Modi, G.S. Lodha, “Optical properties of indium phosphide in the 50–200Å wavelength region using a reflectivity technique,” *Applied Optics* **49**, 5378 (2010).

- [174] L.Nevot, P. Croce, “Characterisation of surfaces by grazing X-ray reflection Application to the study of polishing some silicate glasses,” *Review of Physics Applications* **15**, 761 (1980).
- [175] L.G. Parratt, “Surface Studies of Solids by Total Reflection of X-Rays,” *Physical Review* **95**, 359 (1954).
- [176] P. Ortiz, V. Antúnez, R. Ortiz, J.M. Martín, M.A. Gómez, A.R. Hortal, B. Martínez-Haya, “Comparative study of pulsed laser cleaning applied to weathered marble surfaces”, *Applied Surface Science* **283**, 193 (2013).
- [177] A. Khedr, P. Pouli, C. Fotakis, M.A. Harith, “Cleaning of black crust from marble substrate by short free running Nd:YAG laser”, *AIP Conference Proceedings* **1172**, 91 (2009).
- [178] Vanessa Antúnez Pérez, María del Pilar Ortiz Calderón, José María Martín Ramirez, Rocio Ortiz Calderon, Maria Auxiliadora Gómez Morón, Francisco Gámez, Ana Rodriguez Hortal, Bruno Martinez-Haya, “Laser cleaning of graffiti, deposits and oxide stains on dolomitic marble: comparison with traditional methods”, In: *Proceedings of ninth conference on Lasers in the conservation of artworks (LACONA)*, London 7-10 September 2011.
- [179] T. Baldrige, G. Poling, E. Foroozmehr, R. Kovacevic, T. Metz, V. Kadekar, M. C. Gupta, “Laser cladding of Inconel 690 on Inconel 600 superalloy for corrosion protection in nuclear applications”, *Optics and Lasers in Engineering* **51**, 180 (2013).
- [180] S. Preuss, A. Demchuk, M. Stuke, “Sub-picosecond UV laser ablation of metals”, *Applied Physics A: Solids Surfaces* **61**, 33(1995).
- [181] A. Siatou, D. Charalambous, V. Argyropoulos, P. Pouli, “A comprehensive study for the laser cleaning of corrosion layers due to environmental pollution for metal objects of cultural value: preliminary studies on artificially corroded coupons”, doi:10.1155/2006/85324 *Laser Chemistry* **1**, 1(2006).

- [182] G. Srikantiah, P.R. Chappidi, "Particle Deposition and Fouling in PWR Steam Generators", Nuclear Engineering and Design **200**, 285 (2000).
- [183] J. Manjanna, S. Rangarajan, S.M. Velmurugan and S.V. Narasimhan, "Surface Analysis of Monel, Incoloy, and stainless steel exposed to ETA and LiOH at 150 °C", Corrosion Prevention & Control **3**, 18 (2002).
- [184] Ambar Choubey, S.C. Vishwakarma, D.M. Vachhani, Ravindra Singh, Pushkar Misra, R.K. Jain, R. Arya, B.N. Upadhyaya, S.M. Oak, "Study and development of 22 kW peak power fiber-coupled short pulse Nd:YAG laser for cleaning applications", Optics and Lasers in Engineering **62**, 69 (2014).
- [185] Amol Singh, Ambar Choubey, Mohammed H. Modi, B.N. Upadhyaya, S.M. Oak, G.S. Lodha, S.K. Deb, "Cleaning of carbon layer from the gold films using a pulsed Nd:YAG laser", Applied Surface Science **283**, 612 (2013).
- [186] Marjan Marin šek, "Ni-YSZ Substrate Degradation during Carbon Deposition", Boletín de la Sociedad Española de Cerámica y Vidrio **50**, 135 (2011).
- [187] Tao Chen, Wei Guo Wang, He Miao, Tingshuai Li, Cheng Xu, "Evaluation of carbon deposition behavior on the nickel/yttrium-stabilized zirconia anode-supported fuel cell fueled with simulated syngas", Journal of Power Sources **196**, 2461 (2011).
- [188] See website <http://cnx.org/content/m34549/1.2>
- [189] T.Ursby, J.Unge, R.Appio, D.T. Logan, F. Fredslund, C. Svensson, K. Larsson, A. Labrador, M.M.G.M. Thunnissen, "The macromolecular crystallography beamline I911-3 at the MAX IV laboratory", Journal of Synchrotron Radiation **20**, 648 (2013).

- [190] Y.Xi, B. Kou, H. Sun, J. Qi, J. Sun, J. Mohr, M. Börner, J.Zhao, L.X. Xu, T. Xiao, Y. Wang, “X-ray grating interferometer for biomedical imaging applications at Shanghai Synchrotron Radiation Facility”, *Journal of Synchrotron Radiation* **19**, 821 (2012).
- [191] M.E. Couprie, M. Billardon, M.Velghe, C.Bazin, M.Bergher, H.Fang, J.M. Ortega, Y.Petrof, R.Prazeres, “Optical properties of multilayer mirrors exposed to synchrotron radiation”, *Nuclear Instruments and Methodes A* **272**, 166 (1988).
- [192] A. Toyoshima, T. Kikuchi, H. Tanaka, J. Adachi, K. Mase, K. Amemiya, “In situ removal of carbon contamination from optics in a vacuum ultraviolet and soft X-ray undulator beamline using oxygen activated by zeroth-order synchrotron radiation”, *Journal of Synchrotron Radiation* **19**, 722 (2012).
- [193] Frank Barkusky, Armin Bayer, Stefan Döring, Peter Grossmann, Klaus Mann, “Damage threshold measurements on EUV optics using focused radiation from a table-top laser produced plasma source”, *Optics Express* **18**, 4346 (2010).
- [194] Kevin Raiber, Andreas Terfort, Carsten Benndorf, Norman Krings, Hans-Henning Strehblow, “Removal of self-assembled monolayers of alkanethiolates on gold by plasma cleaning”, *Surface Science* **595**, 56 (2005).
- [195] Kh. Gholivand, M. Khosravi, S.G. Hosseini, M. Fathollahi, “A novel surface cleaning method for chemical removal of fouling lead layer from chromium surfaces”, *Applied Surface Science* **256**, 7457 (2010).
- [196] A. Yerokhin, A. Pilkington, A. Matthews, “Pulse current plasma assisted electrolytic cleaning of AISI 4340 steel”, *Journal of Materials Processing Technology* **210**, 54 (2010).
- [197] F. Eggenstein, F. Senf, T. Zeschke, W. Gudat, “Cleaning of contaminated XUV-optics at BESSY II”, *Nuclear Instruments and Methodes A* **467** 325 (2001).

- [198] Violeta Popescu, Ioan Vida-Simiti, Nicolaie Jumate, “The characteristics of gold films deposited on ceramic substrate”, *Gold bulletin* **38**, 163 (2005).
- [199] S.I. Kudryashov, S.D. Allen, S. Papernov, A.W. Schmid, “Nanoscale laser-induced spallation in SiO<sub>2</sub> films containing gold nanoparticles”, *Applied Physics B* **82**, 523 (2006).
- [200] Jean-Yves Natoli, Laurent Gallais, Bertrand Bertussi, Annelise During, Mireille Commandré, Jean-Luc Rullier, Florian Bonneau, Patrick Combis, “Localized pulsed laser interaction with submicronic gold particles embedded in silica: a method for investigating laser damage initiation”, *Optics Express* **11**, 824 (2003).
- [201] Yong Gan, J.K. Chen, “An atomic-level study of material ablation and spallation in ultrafast laser processing of gold films”, *Journal of Applied Physics* **108**, 103102 (2010).
- [202] G. Vereecke, E. Rohr, M.M. Heyns, “Influence of beam incidence angle on dry laser cleaning of surface particles”, *Applied Surface Science* **157**, 67 (2000).
- [203] K.G. Watkins, Carmel Curran, Jong-Myung Lee, “Two new mechanisms for laser cleaning using Nd:YAG sources”, *Journal of Cultural Heritage* **4**, 59 (2003).
- [204] M.H. Modi, G.S. Lodha, M.K. Tiwari, S. Rai, C. Mukharjee, P. Magudapathy, K.G.M. Nair, R.V. Nandedkar, “Ion irradiation damage on tin side surface of float glass”, *Nuclear Instruments and Methods B* **239**, 383 (2005).
- [205] Ambar Choubey, Amol Singh, M.H. Modi, B.N. Upadhyaya, G.S. Lodha, S.M. Oak, “Study on effective cleaning of gold layer from fused silica mirrors using nanosecond pulsed Nd:YAG laser”, *Applied Optics* **52(31)**, 7540 (2013).
- [206] A.V. Vinogradov, N.N. Zorev, I.V. Kozhevnikov, I.G. Yakushkin, “Phenomenon of total external reflection of x rays”, *Soviet Physics JETP* **62**, 1225 (1985).

## Appendix-1

Since we can write a polarization state as a (Jones) vector, we use matrices,  $\mathbf{A}$ , to transform them from the input polarization,  $E_0$ , to the output polarization,  $E_1$ .

$$\underline{E}_1 = \mathbf{A} \underline{E}_0$$

This yields:

$$\begin{aligned} \underline{E}_{1x} &= a_{11} \underline{E}_{0x} + a_{12} \underline{E}_{0y} \\ \underline{E}_{1y} &= a_{21} \underline{E}_{0x} + a_{22} \underline{E}_{0y} \end{aligned}$$

For example, an x-polarizer can be written:

$$\mathbf{A}_x = \begin{bmatrix} 1 & 0 \\ 0 & 0 \end{bmatrix}$$

So

$$\underline{E}_1 = \mathbf{A}_x \underline{E}_0 = \begin{bmatrix} 1 & 0 \\ 0 & 0 \end{bmatrix} \begin{bmatrix} \underline{E}_{0x} \\ \underline{E}_{0y} \end{bmatrix} = \begin{bmatrix} \underline{E}_{0x} \\ 0 \end{bmatrix}$$

A y-polarizer:

$$\mathbf{A}_y = \begin{bmatrix} 0 & 0 \\ 0 & 1 \end{bmatrix}$$

A half-wave plate:

$$\mathbf{A}_{HWP} = \begin{bmatrix} 1 & 0 \\ 0 & -1 \end{bmatrix}$$

A half-wave plate rotates 45-degree-polarization to -45-degree,

$$\begin{bmatrix} 1 & 0 \\ 0 & -1 \end{bmatrix} \begin{bmatrix} 1 \\ 1 \end{bmatrix} = \begin{bmatrix} 1 \\ -1 \end{bmatrix}$$

$$\begin{bmatrix} 1 & 0 \\ 0 & -1 \end{bmatrix} \begin{bmatrix} 1 \\ -1 \end{bmatrix} = \begin{bmatrix} 1 \\ 1 \end{bmatrix}$$

A quarter-wave plate:

$$\underline{A}_{QWP} = \begin{bmatrix} 1 & 0 \\ 0 & \pm i \end{bmatrix}$$

$$\begin{bmatrix} 1 & 0 \\ 0 & \pm i \end{bmatrix} \begin{bmatrix} 1 \\ 1 \end{bmatrix} = \begin{bmatrix} 1 \\ \pm i \end{bmatrix}$$

**Jones Matrices for standard optical components:**

Horizontal linear polarizer  $\leftrightarrow$   $\begin{bmatrix} 1 & 0 \\ 0 & 0 \end{bmatrix}$

Vertical linear polarizer  $\updownarrow$   $\begin{bmatrix} 0 & 0 \\ 0 & 1 \end{bmatrix}$

Linear polarizer at  $+45^\circ$   $\nearrow$   $\frac{1}{2} \begin{bmatrix} 1 & 1 \\ 1 & 1 \end{bmatrix}$

Linear polarizer at  $-45^\circ$   $\searrow$   $\frac{1}{2} \begin{bmatrix} 1 & -1 \\ -1 & 1 \end{bmatrix}$

Quarter-wave plate,  
fast axis vertical

$$e^{i\pi/4} \begin{bmatrix} 1 & 0 \\ 0 & -i \end{bmatrix}$$

Quarter-wave plate,  
fast axis horizontal

$$e^{i\pi/4} \begin{bmatrix} 1 & 0 \\ 0 & i \end{bmatrix}$$

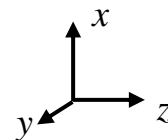
Homogeneous circular  
polarizer right  $\odot$

$$\frac{1}{2} \begin{bmatrix} 1 & i \\ -i & 1 \end{bmatrix}$$

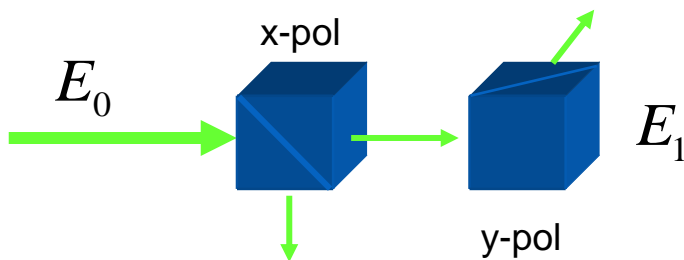
Homogeneous circular  
polarizer left  $\ominus$

$$\frac{1}{2} \begin{bmatrix} 1 & -i \\ i & 1 \end{bmatrix}$$

**Multiplying Jones Matrices:**



Crossed polarizers:



$$\underline{E}_1 = \mathbf{A}_y \mathbf{A}_x \underline{E}_0$$

$$\mathbf{A}_y \mathbf{A}_x = \begin{bmatrix} 0 & 0 \\ 0 & 1 \end{bmatrix} \begin{bmatrix} 1 & 0 \\ 0 & 0 \end{bmatrix} = \begin{bmatrix} 0 & 0 \\ 0 & 0 \end{bmatrix}$$

so no light leaks through.

## Appendix-2

### *Jones matrix analysis*

Jones matrices can also be used for an analysis of the working of tilted  $90^0$  QR in the resonator. Here, it works as a four-pass laser resonator for the generation of  $p$ -polarized laser beam with reduced depolarization losses. Here, the tilted  $90^0$  QR acts as a phase retarder as well as a Brewster's plate polarizer in its tilted position. If the transmission factor of polarized light through a Brewster's plate is ' $S$ ', then the Jones matrix for the Brewster effect of a tilted  $90^0$  QR can be written as

$$QR_B = \begin{bmatrix} S & 0 \\ 0 & 1 \end{bmatrix} \quad (\text{A})$$

For a single pass,  $S$  can be calculated by

$$S = \left( \frac{2n_e}{n_e^2 + 1} \right)^2 \quad (\text{B})$$

For a quartz crystal, the refractive index for an extraordinary ray ( $n_e$ ) is 1.5415 at 1064 nm and  $S$  has a value of 0.8328. At the Brewster angle, all the  $p$ -polarized light will pass through the  $90^0$  QR with phase retardation. The matrix of a phase retarder is given by

$$QR(\delta) = \begin{bmatrix} e^{-i\delta/2} & 0 \\ 0 & e^{i\delta/2} \end{bmatrix} \quad (\text{C})$$

Here, only the  $p$ -polarization has been allowed to oscillate (in the laboratory frame,  $y$ -direction) in the resonator. The phase  $\delta$  introduced by the  $90^\circ$  QR on an extraordinary (also  $p$ -polarized) beam incident normally on it is given by

$$\delta(y) = \frac{2\pi}{\lambda} (n_e - 1)(2y - d) \quad (\text{D})$$

where  $y$  is the entrance height of the beam on the  $90^\circ$  QR,  $d$  is the length of  $90^\circ$  QR in the  $z$ -direction. Single trip Jones matrix of a pumped Nd:YAG rod with the birefringence phase difference  $\Gamma$  can be written as

$$Rod(\Gamma) = \begin{bmatrix} e^{i\Gamma/2} & 0 \\ 0 & e^{-i\Gamma/2} \end{bmatrix} \quad (\text{E})$$

Further, if  $\theta$  is the angle between the laboratory frame and the thermally induced dielectric axes in the transverse plane of the rod, the transformation matrix is given by

$$R(\theta) = \begin{bmatrix} \cos \theta & \sin \theta \\ -\sin \theta & \cos \theta \end{bmatrix} \quad (\text{F})$$

When there is no birefringence compensating element or any polarizer in the resonator and only an Nd:YAG rod is placed in the resonator between mirrors, the round-trip Jones matrix for the resonator starting from the output coupler mirror can be written as

$$\begin{aligned} M_{Unpolarized} &= R(-\theta)Rod(\Gamma)Rod(\Gamma)R(\theta) \\ M_{Unpolarized} &= \begin{bmatrix} e^{i\Gamma} \cos^2 \theta + e^{-i\Gamma} \sin^2 \theta & -2i \sin \Gamma \cos \theta \sin \theta \\ -2i \sin \Gamma \cos \theta \sin \theta & e^{-i\Gamma} \cos^2 \theta + e^{i\Gamma} \sin^2 \theta \end{bmatrix} \end{aligned} \quad (\text{G})$$

Now, taking  $x$ -polarization (with respect to laboratory frame) as loss by inserting an intra-cavity polarizer having Jones matrix given by  $A_x$  as

$$A_x = \begin{bmatrix} 0 & 0 \\ 0 & 1 \end{bmatrix}$$

The uncompensated depolarized component  $E_x^{(Uncompensated)}$  is given by

$$\begin{bmatrix} E_x^{Uncompensated} \\ E_y^{Uncompensated} \end{bmatrix} = M_{Unpolarized} \begin{bmatrix} 0 & 0 \\ 0 & 1 \end{bmatrix} \begin{bmatrix} E_x \\ E_y \end{bmatrix} \quad (\text{H})$$

$$E_x^{Uncompensated} = -2i \sin \Gamma \cos \theta \sin \theta \quad (\text{I})$$

Hence, the uncompensated depolarization loss fraction for thermal birefringence in the transverse plane of the rod is given by

$$I_D^{Uncompensated} = E_x^{Uncompensated} E_x^{Uncompensated(\dagger)} = -\sin^2 \Gamma \sin^2 2\theta \quad (\text{J})$$

where,  $\Gamma = C_T P_h r^2 / r_0^2$  and  $C_T = 2n_0^3 \alpha C_B / \lambda K$

Here,  $K$  is the thermal conductivity of the laser rod,  $n_0$  is the index of refraction at the centre of the laser rod,  $r_0$  is the radius of the rod,  $P_h$  is the heat load dissipated in laser rod,  $\alpha$  is the coefficient of thermal expansion.  $C_B$  depends on Young's modulus, Poisson's ratio, and photo-elastic tensor elements of the Nd:YAG rod. Heat load dissipated in the rod ( $P_h$ ) is proportional to the electrical input power ( $P_E$ ) to the flash lamp and is given by  $P_E = K_0 I^2 t_p f$ . Here,  $I$  is the lamp current,  $t_p$  is the pulse duration,  $f$  is the pulse repetition rate,  $K_0$  is the lamp impedance parameter having a value of 18 for the flash lamp used in this experiment. The value of  $P_h$  has been selected as 10% of  $P_E$  for lamp pumped system.

The total uncompensated depolarization loss can be derived by integrating Eq. (J) over the cross-section of the Nd:YAG laser rod after placing the value of  $\Gamma = C_T P_h r^2 / r_0^2$  as

$$I_D^{Uncompensated} = \frac{1}{\pi r_0^2} \int_0^{2\pi} \int_0^{r_0} I_D^{Uncompensated} r dr d\theta = \frac{1}{4} [1 - \sin c(2C_T P_h)] \quad (\text{K})$$

Similarly, after birefringence compensation, the four pass Jones matrix would be the multiplication of all Jones matrices of the components in the path taken in appropriate order with

tilted  $90^\circ$  QR as a birefringence compensating element inside the resonator placed between the laser rod and output coupler mirror. Starting from the output coupler mirror, four pass Jones matrix in the birefringence compensated resonator (after passing tilted  $90^\circ$  QR and re-entering mirror) starting from the output coupler mirror can be written as

$$M_{Polarized} = Pass[1] \times Pass[2] \times Pass[3] \times Pass[4]$$

$$M_{Polarized} = [QR_B][QR(\delta)][R(-\theta)][Rod(\Gamma)] \times [Rod(\Gamma)][R(\theta)][QR_B]$$

$$\times [QR_B][R(-\theta)][Rod(\Gamma)] \times [Rod(\Gamma)][R(\theta)][QR_B][QR(\delta)] \quad (L)$$

$$M_{polarized} = \begin{bmatrix} e^{-i\delta} \{S^3 (\cos \Gamma + i \cos 2\theta \sin \Gamma)^2 - S \sin^2 \Gamma \sin^2 2\theta\} & \sin \Gamma \sin 2\theta \{-i(S^2 + 1) \cos \Gamma + (S^2 - 1) \cos 2\theta \sin \Gamma\} \\ S \sin \Gamma \sin 2\theta \{-i(S^2 + 1) \cos \Gamma + (S^2 - 1) \cos 2\theta \sin \Gamma\} & e^{i\delta} \{\cos^2 \Gamma - i \cos 2\theta \sin 2\Gamma - \sin^2 \Gamma (\cos^2 2\theta + S^2 \sin^2 2\theta)\} \end{bmatrix} \quad (M)$$

The compensated depolarized component  $E_x^{(Compensated)}$  is given by

$$\begin{bmatrix} E_x^{Compensated} \\ E_y^{Compensated} \end{bmatrix} = M_{Polarized} \begin{bmatrix} 0 & 0 \\ 0 & 1 \end{bmatrix} \begin{bmatrix} E_x \\ E_y \end{bmatrix} \quad (N)$$

Therefore,

$$E_x^{compensated} = \sin \Gamma \sin 2\theta \{-i(S^2 + 1) \cos \Gamma + (S^2 - 1) \cos 2\theta \sin \Gamma\} \quad (O)$$

and hence the depolarization loss factor will be

$$I_D^{compensated} = E_x^{compensated} \cdot E_x^{compensated(\dagger)} = \sin^2 \Gamma \sin^2 2\theta [(S^2 + 1)^2 \cos^2 \Gamma + (S^2 - 1)^2 \cos^2 2\theta \sin^2 \Gamma] \quad (P)$$

The total depolarization loss after birefringence compensation can be derived by integrating Eq.

(20) over the cross-section of the Nd:YAG laser rod after placing the value of  $\Gamma$  as

$$L_D^{Compensated} = \frac{1}{\pi r_0^2} \int_0^{2\pi} \int_0^{r_0} I_D^{Compensated} r dr d\theta$$

$$= \frac{1}{7364} \pi \left[ -8(S^2 - 1)^2 \sin c(2C_T P_h) - (3S^4 + 10S^2 + 3) \sin c(4C_T P_h) - 4C_T P_h (7S^4 + 2S^2 + 7) \right] \quad (Q)$$

The calculated numerical value of total uncompensated depolarization loss using Eq. (K) was 0.2463 and compensated depolarization loss using Eq. (Q) was 0.06 using the values of  $n_0=1.82$ ,  $\alpha=7.5\times 10^{-6}/^{\circ}\text{C}$ ,  $C_B=-0.0099$ ,  $\lambda=1064\text{ nm}$ ,  $K=14\text{ W/m}^{\circ}\text{K}$ ,  $r_0=4\text{ mm}$ , if  $P_h=500\text{ W}$ , and  $S=0.8328$  for QR. These values show that the depolarization loss is reduced significantly from a value of 24.6% to 6% after birefringence compensation using a tilted  $90^{\circ}$  QR and HR re-entering feedback mirror.